

GaAs-Based Semiconductor Optical Amplifiers with Quantum Dots as an Active Medium

vorgelegt von

Diplom-Physiker

Matthias Lämmlin

aus Müllheim

von der Fakultät II – Mathematik und Naturwissenschaften
der Technischen Universität Berlin
zur Erlangung des akademischen Grades

Doktor der Naturwissenschaften
– Dr. rer. nat. –

genehmigte Dissertation

Promotionsausschuss:

Vorsitzender: Prof. Dr. E. Schöll
Berichter / Gutachter: Prof. Dr. D. Bimberg
Berichter / Gutachter: Prof. Dr. N. N. Ledentsov

Tag der wissenschaftlichen Aussprache: 21.12.2006

Berlin 2007

D 83

Zusammenfassung

In dieser Arbeit über GaAs-basierte optische Halbleiterverstärker (SOA) mit InGaAs Quantenpunkten (QPen) als aktivem Material wird über die Herstellung und Charakterisierung solcher Bauelemente für optische Verstärkung im 1.3 μm Wellenlängenbereich berichtet.

Ein Teil der Arbeit befasst sich mit der Simulation und Modellierung der Verstärker, in der zentrale Bauelementeeigenschaften untersucht werden, die für das Design von schrägen Wellenleitern und Anti-Reflektionsbeschichtungen wichtig sind und die Aufschluss über das generelle Gewinn- und Sättigungsverhalten von Verstärkern geben. Dieser theoretische Teil der Arbeit beschäftigt sich mit den besonderen Eigenschaften (p-Dotierung, Alphafaktor, inhomogene Verbreiterung, Sättigungs- und Gewinnerholungsmechanismen) von QPen, die für SOA relevant sind. Gewinn, Gewinnsättigung, Bandbreite, sowie Polarisationsabhängigkeit und verstärkte spontane Emission von SOA werden diskutiert. Das Theoriekapitel schließt mit einer Betrachtung über die verfügbaren QP SOA Modelle, die eine exzellente Leistungsfähigkeit dieser Verstärker vorhersagen.

Ein neues Prozessierungsschema wurde entwickelt, bei dem durch den aktiven Wellenleiter hindurch geätzt wird, um eine starke Indexwellenführung zu erreichen. Ein neues Kontaktschema wurde realisiert, das erlaubt, die Kontakte von oben mit einem Tastkopf zu kontaktieren. Für den Wellenleiter wurde ein Konzept aus schrägem Wellenleiter in Kombination mit Anti-Reflektionsschichten angewendet. Die resultierende Reflektivität konnte mit der Hakki-Paoli Methode vermessen werden; es wurden Werte deutlich unter 10^{-3} erreicht.

Statische Messungen an den QP SOA ergaben einen Chipgewinn von 25 dB, eine Bandbreite von 30 nm und eine minimale Chipauschzahl von 4 dB, nahe am theoretischen Minimum von 3 dB. Kreuzgewinn- und Polarisationsmessungen bestätigten das Verhalten eines typischen inhomogen verbreiterten Gewinnmediums und entkoppelten QPen in einem rechteckigen Wellenleiter.

Dynamische Messungen zeigten ultraschnelle, unverzerrte Verstärkung von modengekoppelten Pulsfolgen mit Wiederholraten bis 80 GHz und minimalen Pulsbreiten von 710 fs. Mittels Pump-Probe-Spektroskopie wurde die Gewinnerholung nach zwei ultraschnellen 150 fs Pulsen vermessen, die eine vollständige Erholung des Grundzustandgewinns unter hohen Stromdichten zeigten. Die Kleinsignal-Kreuzgewinnmessungen demonstrierten Bandbreiten zwischen 1 und 3.5 GHz und damit das Potential für Multi-Wellenlängenverstärkung ohne Übersprechen der Kanäle außerhalb der homogenen Verbreiterung. 40 Gb/s Systemübertragungsmessungen wiesen eine fehlerfreie Verstärkung bis zu einer Bitfehlerrate von 10^{-12} nach und zeigten eine musterfreie Übertragung im linearen und schwach-gesättigten Bereich des QP SOA.

Die QP SOA sind auf dem neuesten Stand der Technik und zeigen das Potential für über 100 GHz Übertragung bei 1.3 μm Telekomwellenlängen. QPe als Gewinnmedium demonstrieren das Leistungsvermögen für zukünftige rein-optische Hochgeschwindigkeitsnetzwerke mit QP SOA als ultraschnelle Verstärkungselemente oder funktionale Elemente in rein-optischer Signalverarbeitung.

Parts of this work have been published:

- [1] M. Laemmlin, G. Fiol, C. Meuer, M. Kuntz, F. Hopfer, A. Kovsh, N. Ledentsov, and D. Bimberg, *Distortion-free optical amplification of 20–80 GHz modelocked laser pulses at 1.3 μm using quantum dots*, *Electronic Letters*, **42**, 697 (2006)
- [2] M. Laemmlin, G. Fiol, M. Kuntz, F. Hopfer, A. Mutig, N. Ledentsov, A. Kovsh, C. Schubert, A. Jacob, A. Umbach, and D. Bimberg, *Quantum dot based photonic devices at 1.3 μm : Direct modulation, mode-locking, SOAs and VCSELs*, *phys. stat. sol. (c)*, **3**, 391 (2006)
- [3] M. Laemmlin, G. Fiol, M. Kuntz, F. Hopfer, D. Bimberg, A. Kovsh, and N. Ledentsov. *Dynamical Properties of Quantum Dot Semiconductor Optical Amplifiers at 1.3 μm Fiber-Coupled to Quantum Dot Mode-Locked Lasers*. CThGG2, Technical Digest, Conference on Lasers and Electro-Optics (CLEO). Long Beach, USA: Optical Society of America (2006)
- [4] M. Laemmlin, G. Fiol, C. Meuer, M. Kuntz, F. Hopfer, N. Ledentsov, A. Kovsh, and D. Bimberg. *Self-organized quantum dots for 1.3 μm photonic devices*. 63500M, 6350, Workshop on Photonic Components for Broadband Communication 2006. Stockholm, Sweden: Proceedings of SPIE (2006)
- [5] M. Laemmlin, G. Fiol, C. Meuer, M. Kuntz, F. Hopfer, D. Bimberg, A. Kovsh, and N. Ledentsov. *Amplification of quantum dot mode-locked lasers with quantum dot semiconductor optical amplifiers at 20, 40 and 80 GHz*. II.2, International Workshop on Semiconductor Quantum dot based Devices and Applications. Paris (2006)
- [6] M. Laemmlin, D. Bimberg, A.V. Uskov, A.R. Kovsh, and V.M. Ustinov. *Semiconductor optical amplifiers near 1.3 μm based on InGaAs/GaAs quantum dots*. CThB6, 96, Conference on Lasers and Electro-Optics (CLEO). San Francisco, USA: Optical Society of America (2004)
- [7] M. Laemmlin, M. Kuntz, G. Fiol, D. Bimberg, A.R. Kovsh, and V.M. Ustinov. *InGaAs/GaAs quantum dot based photonic devices for direct modulation, mode-locking and optical amplification at 1.3 μm* . V.1, European Semiconductor Laser Workshop (ESLW). Särö, Sweden (2004)
- [8] S. Dommers, V.V. Temnov, U. Woggon, J. Gomis, J. Martinez-Pastor, M. Laemmlin, and D. Bimberg, *Complete ground state gain recovery after ultrashort double pulses in quantum dot based semiconductor optical amplifier*, *Applied Physics Letters*, submitted (2006)
- [9] D. Bimberg, G. Fiol, M. Kuntz, C. Meuer, M. Lämmlin, N. Ledentsov, and A. Kovsh, *High speed nanophotonic devices based on quantum dots*, *phys. stat. sol. (a)*, **203**, 3523 (2006).
- [10] D. Bimberg, M. Kuntz, and M. Laemmlin, *Quantum dot photonic devices for lightwave communication*, *Applied Physics a-Materials Science & Processing*, **80**, 1179 (2005)

- [11] A.V. Uskov, E.P. O'Reilly, M. Laemmlin, N.N. Ledentsov, and D. Bimberg, *On gain saturation in quantum dot semiconductor optical amplifiers*, Optics Communications, **248**, 211 (2005).
- [12] A.V. Uskov, E.P. O'Reilly, R.J. Manning, R.P. Webb, D. Cotter, M. Laemmlin, N.N. Ledentsov, and D. Bimberg, *On ultrafast optical switching based on quantum-dot semiconductor optical amplifiers in nonlinear interferometers*, IEEE Photonics Technology Letters, **16**, 1265 (2004)
- [13] D. Bimberg, M. Laemmlin, C. Meuer, G. Fiol, M. Kuntz, A. Schliwa, N. Ledentsov, and A. Kovsh. *Quantum dot amplifiers for 100 Gbit Ethernet*. Th.A2.2, International Conference on Transparent Optical Networks. Nottingham, UK (2006)
- [14] C. Meuer, M. Laemmlin, G. Fiol, M. Kuntz, D. Bimberg, N. Ledentsov, A. Kovsh, S. Ferber, C. Schubert, A. Steffan, and A. Umbach. *High Frequency Signal Amplification using Quantum Dot Semiconductor Optical Amplifiers at 1.3 μm* . We4.6.5, European Conference on Optical Communication (ECOC). Cannes, France (2006)

Contents

1	Introduction	9
2	Theory.....	13
2.1	Quantum dots.....	13
2.2	Amplifier theory	15
2.2.1	Basic concept of a semiconductor amplifier.....	15
2.2.2	Gain	16
2.2.3	Gain ripple	21
2.2.4	Amplified spontaneous emission and gain	23
2.2.5	Noise.....	24
2.2.6	Polarization properties of amplifiers	28
2.2.7	Higher order effects	30
2.3	Simulation and modeling of QD SOAs	32
2.3.1	Waveguide simulations	32
2.3.2	Reduction of facet reflectivity	35
2.3.3	Simulation of gain and saturation characteristics	40
2.3.4	Modeling of quantum dot semiconductor optical amplifiers.....	45
3	Processing and Fabrication.....	49
3.1	Growth of quantum dots	49
3.2	Epitaxial structure of QD SOAs	52
3.3	Processing of ridge waveguide devices	53
3.3.1	Processing steps evaluation	56
3.4	Post-processing: AR coating and mounting	63
3.4.1	AR coating and tilted facet	63
3.4.2	Mounting and packaging	66
4	General Device Characterization and Measurement Techniques.....	68
4.1	General device characterization.....	68
4.1.1	List of samples.....	68
4.1.2	Far field measurement	68
4.1.3	Determination of taper-facet coupling loss	73
4.1.4	Facet reflectivity measurement.....	75
4.1.5	Hakki-Paoli measurement	78
4.2	Measurement techniques for characterization of SOAs	83
4.2.1	Setup for SOA characterization.....	83
4.2.2	Gain measurement technique.....	84
4.2.3	Noise measurement technique	85
4.3	Dynamic characterization techniques.....	86
4.3.1	Amplification of mode-locked laser pulse trains.....	86
4.3.2	Double pump- and probe setup.....	86
4.3.3	Eye-pattern and BER measurement technique	87
4.3.4	Small signal cross gain modulation setup.....	89
5	Application Oriented Experiments with QD SOAs.....	91
5.1	Static amplification experiments with QD SOAs.....	91
5.1.1	QD SOA gain and ASE characterization.....	91
5.1.2	Noise figure of QD SOAs.....	94
5.1.3	Multi wavelength amplification and ASE cross gain modulation.....	95
5.1.4	Polarization dependence of QD SOAs	98
5.2	Dynamic amplification experiments with QD SOAs	99
5.2.1	Amplification of mode-locked laser pulse trains at 20 to 40 GHz	99

5.2.2	Double pulse pump- and probe measurements	105
5.2.3	Eye-pattern and bit-error-ratio measurements	107
5.2.4	Small-signal cross gain modulation of QD SOAs	109
6	Summary	112
7	Technical Annex	115
7.1	Abbreviations and acronyms.....	115
7.2	OSA calibration.....	116
7.3	Small signal modulation.....	117
7.4	On the use of the Brewster angle for reduced facet reflectivity of SOA	122
7.5	Fabry-Perot formulation of the amplifier gain.....	123
7.6	Considerations on contact metallization	125
8	Bibliography.....	127
9	Acknowledgement	143

« Put it before them briefly so they will read it, clearly so they will appreciate it, picturesquely so they will remember it and, above all, accurately so they will be guided by its light. »

Joseph Pulitzer

1 Introduction

The information society is constituted as a society where everyone can create, access, utilize and share information and knowledge. It is seen as the successor to the industrial society. Specific to this kind of society is the central position of information technology which allows the creation, distribution and manipulation of information and is regarded as a significant economic and cultural instrument [1]. The human prehistory can also be periodized into consecutive time periods, named for their respective predominant tool-making technologies or employed materials. The Stone Age is followed by the Bronze Age and the Iron Age. If one wishes, this classification can be expanded to the Silicon Age – with its dominance of electronics based on silicon. A paradigm change is necessary to describe the following period where the classification into material or elements is not possible. The next age will be the Nanotechnology Age¹, which in contrast to the material classes is defined by the change of material properties by the material (nanometer) size. The 21st century is technologically different from the 20th century where electrons could be considered the workhorses of technological progress. The 21st century is regarded as the century of photons. While the 18th century is called century of light (siècle des lumières), according to the more philosophical viewpoint of the so-called enlightenment, in our century light and its quantized particles, the photons are the symbol of modernity in information and communication technologies and a universal tool in many areas.

Considering the transitions from industry to information, silicon to nanotechnology, and electrons to photons, it is the combined field of nanotechnology and opto-electronics that works at the interface of these new societal concepts and that composes the framework of the subject of this thesis.

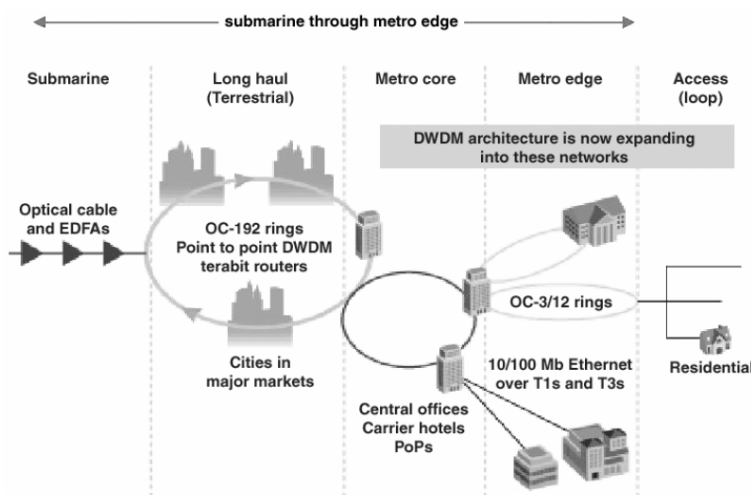


Fig. 1.1 Optical amplifiers are used throughout the optical network – from submarine through metro. From Agilent application notes [2].

dispersion of the fiber is zero, making this band ideal for high speed transmission in metro networks (Fig. 1.1) or in future 100 GBit Ethernet applications [4].

The wish to have instant and individual access to an ever growing amount of data has led to an exponentially increasing demand for transmission capacity to carry the fast growing data traffic. Fiber optics is ideal to transmit large amounts of data. The optical fiber wavelength range is divided in different regimes; the coarsest division are the 1.3 and 1.55 μm wavelength bands [3]. At 1.55 μm a standard single mode fiber has its absorption minimum, which predestines this range for long distance data transmission. At 1.3 μm the

¹ It could as well be the Bio Age, the Genetic Age, the Cloning Age or others, depending on which technology will have the most profound impact.

1 Introduction

The increase in data traffic, together with the advantages of fiber optics for data transmission, drive the development of optical components, especially those capable of all-optical processing without the need of complex opto-electro-optical conversion [5]. Due to the losses of the optical fiber and the signal power differences in network nodes, amplification and regeneration of the optical signal are essential processes and the reason for the adoption of optical amplifiers in fiber communication [6, 7], as depicted in Fig. 1.1. Optical amplifiers are used as functional blocks in the optical network: they are deployed as booster amplifiers directly after the transmitter to increase the optical power level, as in-line amplifiers to increase the regeneration lengths or to compensate for branching losses, and as pre-amplifiers to improve the sensitivity of the receiver. According to the ITU-T definition [8] the spectral bands can be divided in

O-band	E-band	S-band	C-band	L-band	U-band
1260-1360 nm	1360-1460 nm	1460-1530 nm	1530-1565 nm	1565-1625 nm	1625-1675 nm

and define the operating regions of the commercially available optical amplifiers:

- 1) Rare earth-doped fiber or waveguide amplifiers
Gain band: Erbium (C,L-band), Thulium (S,U-band), Praseodymium (O-band)
Based on fluoride, telluride and silica materials
- 2) Fiber Raman amplifiers
Gain band: 1.3 to 1.7 μm , tunable by the pump wavelength, if available
Realized as discrete or distributed pumped amplifiers
- 3) Semiconductor optical amplifiers
Gain band: 1.2 to 1.7 μm , tunable by the InGaAsP composition
Based on InP substrates

Although fiber amplifiers are available to amplify the optical signal in a large wavelength range with very good gain and noise performance, and are widely employed in the optical network [9, 10], they show some disadvantages creating the need for an alternative. Most fiber amplifiers are rather expensive and consume high power. Due to their dynamic properties, optical pumping, and large footprint they are not applicable for optical processing, not easily deployable in all fiber regimes, and not practicable for areal dense metro networks, respectively.

Semiconductor optical amplifiers (SOAs) are a viable low-cost alternative able to amplify and process optical signals in a wide range of bitrates at modest bias power requirements and in a small active volume [11-13]. SOAs lack from higher noise figures, polarization dependence of the gain, strong temperature dependence of the InP substrate and lower saturated output power as compared to fiber amplifiers. But SOAs have some specific advantages: In the saturated regime, SOAs exhibit nonlinear properties that can be used for wavelength conversion, optical regeneration and optical signal processing at bitrates up to 40 Gb/s [14-16]. They can be integrated with other active or passive optical components to generate more complex functionalities. Their on/off switching time is in the nanosecond range, which could be advantageous for optical packet switching [17] and their optical bandwidth is wide and can in principle be centered in the range of 1.2 to 1.7 μm by choosing the adequate material composition of the active layer to change the bandgap.

In order to omit the thermal problems of the InP substrate it would be desirable to use GaAs, which is in addition cheaper and available as large wafers. But there is no gain material at hand based on GaAs substrates in the O-band of the telecommunication window; in spite of a wide range of available semiconductors, many preferred wavelength-material combinations are not possible due to epitaxial mismatch of the involved materials.

It is at this point where nanotechnology with the alteration of material properties by the reduction of size, can be employed. Using nanometer-sized semiconductor material grains in a different semiconductor matrix the emission wavelength is widely tuned with the size of these so-called quantum dots (QDs). By means of this technology it is possible to achieve 1.3 μm emission from a material combination containing QDs, based on a GaAs substrate. Before portraying the advantages of QDs for SOAs a brief introduction to the concept of quantum dots is given.

Semiconductor nanostructures in which the carriers are confined, such that the DeBroglie-wavelength of the carriers (typ. 10 nm) is on the order of the extent of the confining potential, are classified in three categories according to the number of confined dimensions: Quantum wells (QWs) are structures that are nm-scaled in one dimension, usually in the epitaxial growth direction. So-called quantum wires cause a confinement in two dimensions, and hence the carriers can move freely only in one direction. The carriers in quantum dots, both electrons and holes, experience a three-dimensional confinement, if the QDs are nanometer-size islands of a low-bandgap semiconductor in a higher-bandgap matrix material. The energy levels in each dot become discrete, similar to electronic shells of an atom. In an ideal ensemble of equally sized uniform QDs one can expect a narrow gain spectrum and a large peak and differential gain [18]. Real QDs differ from this idealistic approach considerably, because they are very often grown in a self-organized manner being the most successful way to make QDs, yet results in an inhomogeneous broadening of the gain spectrum. The energy spectrum of a single QD is discrete, but due to the size dispersion resulting from the spontaneous nucleation process of the QDs, the energy levels of different QDs are spread over several tens of millielectronvolts. Usually the energy spectrum of self-organized grown InAs QDs includes several bound states, the ground state and the excited states. Although the intrinsic material gain of the QDs is large, only a small volume interacts with the optical mode. In order to improve the modal gain, the QD sheets can be stacked in several layers [19]. In the past years a lot of research has been carried out on quantum dots for optical communication. Further detailed descriptions of QDs and of devices based on them can be found in several books and review articles (e.g. [20-31]).

In all-optical high speed networks deploying the O-band, photonic devices based on QDs might play a decisive role due to their unique optical properties at 1.3 μm [32]. For next-generation networks in metropolitan areas the demand for inexpensive ultrafast amplifiers is even larger than that for lasers. QD based SOAs offer potential advantages due to their special gain medium: the inhomogeneous broadening results in a wide gain spectrum, the emission peak is tunable by changing the size of the QDs, the emission polarization can be engineered by vertical coupling, the temperature stability should be improvable by the confinement of the carriers in the dots, fast switching is likely due to a low linewidth enhancement factor, and the saturated output power can be large because of new saturation mechanisms [33].

QD based devices have already demonstrated excellent properties that confirm the usefulness of QDs for amplifiers. SOAs based on QDs at 1.3 μm have shown ultrafast gain recovery dynamics with recovery times of 140 fs, many times faster than conventional SOAs based on bulk and QW material on InP [34, 35], promising operation faster than 200 Gb/s. Cold carrier tunnel injection [29] and p-type modulation doping [36] have been proposed and applied to further improve the frequency response of QD devices. With QD SOAs pattern effect free amplification up to 40 Gb/s and efficient wavelength conversion based on four-wave mixing was demonstrated [37-40]. In the 1.55 μm regime, ultrawide gain spectra up to

1 Introduction

120 nm, large penalty-free output power as large as 23 dBm and small pattern effects of QD and quantum dash² SOAs based on InP have been presented [41-44].

Nevertheless, there are still challenges for QDs that have to be investigated and unraveled. The change of the polarization by coupling of the QDs brings about a coupled electronic state that might reduce the gain. The inhomogeneous broadening of the QDs causes a wide bandwidth, but also a reduction of the gain per wavelength, thereby resulting in small saturation power level. Theoretical predictions confirm the fast recovery of a single short pulse as described before, but expect the gain recovery to be incomplete after amplification of a pulse train with high repetition rates, implying pattern effects and questioning the possibility of ultrafast high repetition rate operation of QD SOAs [45]. These challenges have driven the research on QD SOAs in the project described here.

In this thesis the physics and applications of quantum dot SOAs based on GaAs semiconductor substrates are described. My work presented here provides a comprehensive characterization of quantum dot based amplifiers at 1.3 μm including the design, processing, fundamental device properties, static analysis of the gain properties and experiments on the dynamic behavior of the quantum dot gain medium.

The thesis is organized as follows: Chapter 2 is devoted to the theory and modeling of QDs and SOAs. It serves as an introduction to some of the unique properties of QD devices and explains fundamental attributes of semiconductor optical amplifiers. Chapter 3 describes the growth of the quantum dots and the waveguide structure, and gives details on the processing of the SOAs as well as post-processing like anti-reflection coating and packaging. In chapter 4 the key measurement techniques for cw and dynamic experiments are introduced and basic device properties like far field, reflectivity and coupling loss are qualified. The main results of the thesis are presented in chapter 5. There, first, the cw amplification properties including amplified spontaneous emission (ASE), linear gain, saturation, noise, and polarization are discussed. Then the dynamic properties of the QD SOAs are evaluated with experiments on pulse train amplification, gain recovery, cross gain modulation, and data pattern amplification in a system test bed. Chapter 6 provides a summary of the thesis. A technical annex and the bibliography are given in chapters 7 and 8.

² Quantum dashes are laterally elongated “dots” that combine properties of quantum wires and dots.

2 Theory

2.1 Quantum dots

The concept of quantum dots has been described in the introduction. The nanostructures used in this work are InGaAs QDs that were grown with the intention to shift the wavelength to the 1.3 μm wavelength range, maximize their gain, and improve their thermal as well as dynamic performance. The QD epitaxial growth details are described in section 3.1.

QDs as a gain medium show advantages and peculiarities compared to QW and bulk gain material connected to their discrete energy of states. Those that are important for the performance of amplifiers are reviewed here briefly.

The size, form and material dispersion gives rise to a large inhomogeneous broadening which is an advantage for applications like wavelength division multiplexing that require a broad gain spectrum. By using chirped QD multilayers or combining ground state (GS) and excited state (ES) gain spectra, the spectral bandwidth can be enlarged considerably. Quantum dash amplifiers at 1.55 μm have been reported with an ultrawide gain spectrum up to 120 nm [43]. Yet, there is a trade-off between gain bandwidth and the value of the gain at a given wavelength as there are only a finite number of states in a particular QD device to deliver gain.

The Gaussian distribution of the QD sizes and the discrete density of states result ideally in a symmetric gain spectrum of the GS and in turn in a low linewidth enhancement factor α or low chirp. For QDs the linewidth enhancement factor is a parameter which is under constant discussion. It is directly connected to the chirp, i.e. the change of emission wavelength during a change of the carrier density. The physical origin of this shift is related to the coupling of the real and imaginary parts of the complex susceptibility in the gain medium. A variation of gain due to a change of carrier density N leads to a variation of the refractive index that modifies the phase of the optical mode in the laser cavity. The coupling strength is defined by the linewidth enhancement factor as

$$\alpha = -\frac{2\pi}{\lambda} \frac{\partial n_r / \partial N}{\partial g_{\text{mat}} / \partial N} \quad (2.1)$$

where n_r is the real part of the complex refractive index, λ the photon wavelength, and g_{mat} the material gain [20]. In the ideal case of a perfect Gaussian energy distribution the gain spectrum is perfectly symmetric around the peak gain energy and $\alpha = 0$, i.e. chirp-free. Yet, due to the influence of the carrier density and thermal effects due to heating the linewidth enhancement factors is neither constant nor zero. Values between 0 and 10, and even negative values have been reported depending on the measurement method and the operating condition [46-48].

The temperature dependence of the laser threshold current measured by the characteristic temperature T_0 can be much better than for QWs because the electronic levels in the conduction band of the QDs are spaced more than the Boltzmann energy kT at room temperature, which translates to a nearly constant population distribution. Yet, due to a larger effective mass of the holes their level separation is much smaller than the electron level spacing. Therefore, the injected hole distribution will be thermally broadened resulting in a thermal degradation for increasing temperature. By building in an excess hole concentration

2 Theory

(p-type modulation doping), the effect of the closely spaced hole energy levels can be countered, so that the ground state transition of the QDs is always filled by holes. The temperature dependence of gain is then governed by the electron energy levels, which are widely spaced in energy. By forcing a large hole population, the quasi-Fermi level is pushed deeply in the band and a constant hole occupation of the gain state is ensured over a broad temperature range [49]. P-doping enhances the carrier capture and relaxation through carrier scattering or by an increased capture rate in charged dots. Moreover, p-doping has been shown to reduce the temperature sensitivity of the devices [31, 49, 50]. P-doping increases the characteristic temperature T_0 , making QD laser thresholds independent up to elevated temperatures, thereby eliminating the need for active cooling and temperature control. Most of the samples studied in this thesis were p-doped in the active region.

In the application of QD SOAs for ultrafast optical signal processing the gain recovery dynamics in the presence of a pulse sequence is very important. When an optical signal pulse with a wavelength resonant to the GS is amplified due to stimulated recombination of the GS excitons, the next pulse in the sequence can only be amplified if the gain has recovered. Indeed, a time constant of 140 fs, corresponding to the fastest recovery process, has been reported indicating an upper limit of the signal pulse frequency of some THz [35, 51, 52].

This fast relaxation from ES to GS is a result of two features: the large energy splitting between the dot levels which ensures slow thermal excitation of carriers, and a high WL carrier density resulting in fast Auger-assisted relaxation. The ultrafast gain recovery is enabled by the ES level, which acts as a nearby carrier reservoir for the GS level. Since the process of carrier capture into the dot is slower than intradot relaxation, the ES level recovers on a longer time-scale (~picoseconds). The rate of refilling the WL is essentially determined by the injection current and the spontaneous recombination rate of the WL (~nanoseconds) [45]. Considering only the ultrafast gain recovery following a single pulse excitation the conclusion is possible that the QD amplifier allows for ultrafast all-optical signal processing in the Tb/s range. However, due to slow refilling of the WL level, this is in question. The gain is seen to recover almost completely after the first pulse; however, after each of the following pulses the gain would recover a little less and reach a smaller absolute value. Hence, an amplified pulse train would undergo a considerable gain saturation, stronger with increasing pulse rate. Experimental evidence that additional relaxation processes make possible an ultrafast amplification of pulse trains is demonstrated in sections 5.2.1 and 5.2.2.

Due to the presence of a carrier reservoir in the ES and the wetting layer (WL), QD amplifiers have the potential for a large saturation output power [44]. Under high inversion the WL acts as carrier reservoir for the QD states and a higher rate of stimulated emission can be supported before the gain is saturated. Gain saturation in QD SOAs occurs through carrier depletion in the whole QD structure and spectral hole burning due to stimulated recombination. Increasing the pump current density in a QD SOA can eliminate the gain saturation mechanism due to carrier depletion, and hence increases the saturation power [53]. In section 2.2.2 the saturation power of QDs will be discussed further.

Therefore, because of the properties of QDs, for SOAs deploying these nanostructures

- a wide spectral bandwidth is expected,
- the unique dependence on the linewidth enhancement factor and consequently regions of decoupled gain and refractive index propose interesting cross gain and phase characteristics,

- p-doping could result in even faster relaxation mechanisms, and furthermore improve the temperature performance of the devices,
- ultrafast gain relaxation can help to build SOAs working at high speed, and
- their saturation output power could be larger than for conventional SOAs as the dominant saturation mechanism is spectral hole burning at large pump current.

2.2 Amplifier theory

2.2.1 Basic concept of a semiconductor amplifier

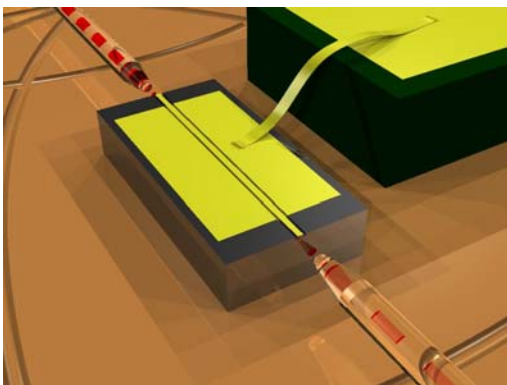


Fig. 2.1 Sketch of a semiconductor optical amplifier with current injection to the active region and coupling light in and out of the waveguide with optical fibers. Courtesy of M. Kuntz.

An optical amplifier is conceptually a gain medium through which light is transmitted and amplified by stimulated emission. The carrier population in the active region of the SOA waveguide is inverted by electrical pumping. An input signal coupled to this waveguide travels along the device and experiences amplification by stimulated emission. At the opposite end the amplified light exits the semiconductor chip. A semiconductor optical amplifier is very similar to a semiconductor laser with the main difference that the resonator of the laser is removed. Ideally, an optical mode is traveling only once through the SOA which is also called traveling wave amplifier (Fig. 2.1).

Light can be generated and amplified by stimulated emission from electron-hole recombination in an active semiconductor region. The high carrier densities needed for this condition are created in a

semiconductor by optical excitation or preferably current injection. Therefore, a structure is needed that is able to confine and guide light in a dielectric waveguide and that provides a carrier injection and confinement as well. Coincidentally, the so-called double heterostructure [54, 55] combines both features and thus is highly suitable as a structure for lasers and amplifiers.

A pn-heterojunction is used for carrier injection and confinement. It is realized by a narrow-gap semiconductor, which can be p-, n-type or undoped, that is sandwiched between two higher-gap p- and n-type semiconductor layers. The carriers that are injected into the active region are prevented from diffusing out by means of the potential barrier due to the difference between the energy gaps of the active layer and the doped claddings. This structure does not only inject and confine electrons and holes at the heterojunction, also the index of refraction of the lower-gap region is larger than for the higher-gap material. This makes a three-layer vertical waveguide in which two types of transverse optical modes (transverse electric TE and transverse magnetic TM) can propagate (e.g. [56]). The energy band diagram, the refractive index distribution and the fundamental mode of a double heterostructure³ at forward bias are depicted in Fig. 2.2.

Only a fraction of the optical mode overlaps with the active region, which could be bulk material, quantum wells or quantum dot layers. This fraction is described by the confinement factor, which is discussed in the next section.

³ including two QD layers in the active region

2 Theory

The optical mode must be also guided in the transverse direction of the device to achieve single transverse mode operation and the current should be confined to the gain region in lateral direction for efficient carrier injection. Typically the transverse waveguide mechanisms are distinguished in

- gain guiding (only the top contact and the current path define the lateral guiding),
- weak index guiding (a ridge profile with insulating layer confines the mode due to overlap of the optical mode with the edge of the ridge) and
- strong index guiding (most often so-called buried heterostructures with the two dimensional waveguide realized by refractive index steps in vertical and lateral direction).

The design of the structures for amplifiers has followed the development of semiconductor lasers. A good transverse guiding is important for amplifier performance due to an improved overlap of the propagating optical mode with the gain medium. For strongly index guided amplifiers a lower amplified spontaneous emission and lower noise can be expected as a smaller fraction of the isotropically emitted ASE is guided in the waveguide.

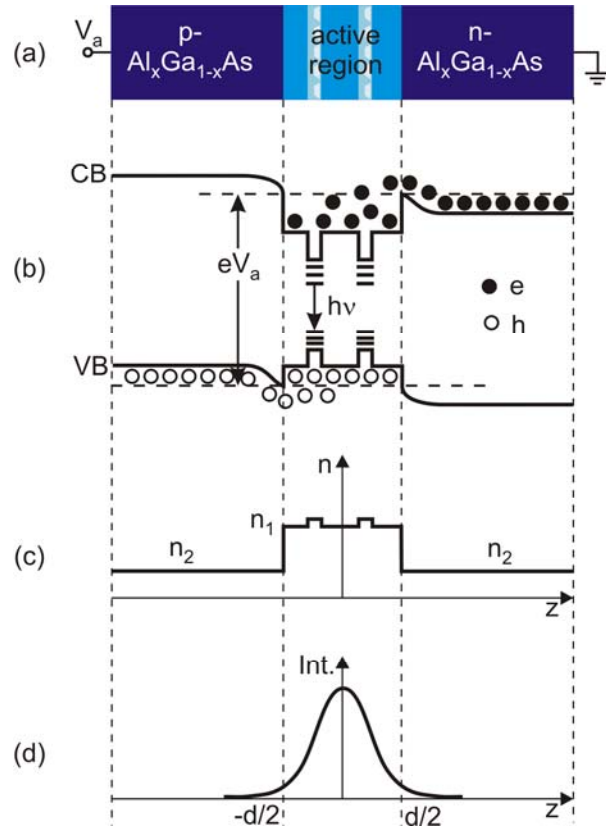


Fig. 2.2 (a) Schematic in vertical growth direction z of a GaAs/AlGaAs pn-heterojunction with two QD layers in the active region. (b) Energy band edges of a forward-biased double heterostructure. Electrons and holes are trapped in the potential well formed by the conduction/valence band (CB/VB) edge discontinuity and are then captured in the wetting layer and QD states. (c) Spatial profile of the index of refraction which creates a dielectric waveguide in the active region layer. (d) Intensity profile of the fundamental optical mode in a three-layer waveguide.

2.2.2 Gain

The gain of an amplifier is its most important characteristic. It is further described by the gain saturation and the according figure of merit, the saturation output power. The gain bandwidth illustrates the spectral dependence of the gain. As only parts of the optical mode overlap with the active medium, the gain is classified in material gain and modal gain, and their dependence is given by the confinement factor.

First we will describe some general relations for the gain of an optical amplifier, then we will give some details for conventional (bulk and QW) and for QD SOAs. Let us consider an amplifier as a single element with a gain G defined as the ratio

$$G = \frac{P_{\text{out}}}{P_{\text{in}}} \quad (2.2)$$

where $P_{\text{in}} = P(z=0)$ and $P_{\text{out}} = P(z=L)$ are the optical input and output power of the amplifier.

This ratio (2.2) is a number, if the given optical powers are in linear units, i.e. commonly in Milliwatts {mW}. Very often a large power range is of interest and the linear units are converted into a logarithmic unit system that is defined by

$$P\{\text{dBm}\} = 10 \cdot \log\left(\frac{P\{\text{mW}\}}{1 \text{ mW}}\right), \text{ and} \quad (2.3)$$

$$\text{dB} = 10 \cdot \log\left(\frac{P_1\{\text{mW}\}}{P_2\{\text{mW}\}}\right) \quad (2.4)$$

for the optical power in decibel per 1 mW {dBm} and the linear ratio converted in logarithmic scale decibel {dB}.

The amplifier equation [57]

$$\frac{dP}{dz} = gP \quad (2.5)$$

relates the optical power P at a distance z from the input at $z=0$. For constant gain g equation (2.5) has the solution $P(z) = P_{\text{in}} \exp(gz)$ which for a length L of the amplifier medium results in the amplifier gain

$$G = \exp(gL). \quad (2.6)$$

The optical gain depends on the wavelength or frequency of the incident signal and on the local intensity of the signal. The most general model to discuss basic behavior of the gain is a homogeneously broadened two-level system with a gain coefficient

$$g(\omega) = \frac{g_0}{1 + (\omega - \omega_0)^2 T_2^2 + P/P_s} \quad (2.7)$$

where g_0 is the maximum value of the gain, ω is the optical angular frequency of the incident signal, ω_0 is the atomic transition angular frequency, P the optical power of the signal being amplified, P_s is the saturation power of the gain medium and T_2 is the dipole relaxation time⁴.

This relation shows that the amplifier gain G and the optical gain g are frequency or wavelength dependent and given by $G(\omega) = \exp(g(\omega)L)$. Both are maximum at the angular frequency $\omega = \omega_0$, but $G(\omega)$ decreases faster than $g(\omega)$ because of the exponential dependence.

⁴ with a typical value of 0.1 ps in a semiconductor.

2 Theory

Gain bandwidth

Using equation (2.7) we can discuss general amplifier characteristics like gain bandwidth, amplification and output power within the model of a homogeneously broadened two-level system. For low powers ($P/P_s \ll 1$) the gain coefficient is given by

$$g(\omega) = \frac{g_0}{1 + (\omega - \omega_0)^2 T_2^2} \quad (2.8)$$

which is maximum for $\omega = \omega_0$ and the gain spectrum is given by a Lorentzian profile that is characteristic for the assumed two-level system. The actual gain spectrum will deviate from this form depending on the gain medium that is deployed in the amplifier. In general the optical gain bandwidth $\Delta\nu_g$ is defined as the full-width-at-half-maximum (FWHM) of the gain spectrum and for the special case of equation (2.8) it is given by

$$\Delta\nu_g = \Delta\omega_g / 2\pi = 1/\pi T_2. \quad (2.9)$$

Using equation (2.6) the FWHM of $G(\omega)$, known as the amplifier bandwidth $\Delta\nu_a$ can be related to the FWHM of $g(\omega)$, the optical gain bandwidth $\Delta\nu_g$, by

$$\Delta\nu_a = \Delta\nu_g \left(\frac{\ln 2}{g_0 L - \ln 2} \right). \quad (2.10)$$

Typical values for a bulk SOA are $T_2 \sim 0.1$ ps which results in $\Delta\nu_g \sim 3$ THz or assuming $G = 25$ dB, $\lambda = 1.55$ μm we calculate $\Delta\nu_a \sim 0.4$ THz and $\Delta\lambda \approx \Delta\nu c/\nu_0^2 = 3.3$ nm.

On the basis of this model, we would find for typical values of the QD SOA ($G = 20$ dB, $\Delta\lambda = 30$ nm) a dipole relaxation time of $T_2 \sim 10$ fs. Therefore, it is clear that this simplistic model of a homogeneously broadened two-level system does not apply to QD amplifiers with inhomogeneously broadened gain spectrum.

We can only conclude from equation (2.10) that the amplifier bandwidth is smaller than the optical gain bandwidth due to the exponential dependence in (2.6) and the value depends on the amplifier gain which is true for all gain media independent of the assumed model.

Gain saturation

The saturation power of an amplifier is an important parameter, which influences linear and non-linear properties. With a high saturation power a linear amplification at large output power is possible, while a low saturation power allows for high non-linearity and hence efficient interaction between optical signals. The underlying principle of gain saturation is that because of energy conservation at larger input power the light cannot be amplified linearly all the time. At some point the light output would exceed the total power supplied to the device, i.e. the gain must saturate. Gain saturation occurs also in lasers: After the laser is above threshold the output power increases linearly with the current. But at very large drive currents the light output will grow slower and will finally saturate when the carrier refill time is identical with the stimulated recombination time. Gain saturation is immanent in

equation (2.7) where g is reduced when P becomes comparable to P_s and therefore, the amplifier gain G decreases when P becomes large. From equations (2.7) and (2.5) in the case of the signal input at maximum gain ($\omega = \omega_0$) follows

$$\frac{dP}{dz} = \frac{g_0 P}{1 + P/P_s}, \quad (2.11)$$

which is solved using the same boundary conditions as before: $P_{in} = P(z=0)$ and $P_{out} = P(z=L)$. For the large signal gain the following implicit equation is obtained:

$$G = G_0 \exp\left(-\frac{G-1}{G} \frac{P_{out}}{P_s}\right) \quad (2.12)$$

where $G_0 = \exp(g_0 L)$ is the unsaturated gain for small input power. As a figure of merit the 3-dB saturation output power P_{sat}^{3dB} is defined as the output power at which the gain decreases to half of its unsaturated value. Using equation (2.12) we find with its relation to P_s by calculating $G(P_{sat}^{3dB}) = G_0 / 2$

$$P_{sat}^{3dB} = \frac{G_0 \ln 2}{G_0 - 2} P_s \stackrel{G_0 > 100}{\approx} \ln 2 \cdot P_s. \quad (2.13)$$

A more general definition of the saturation output power can be used if the gain is very small (on the order of or smaller than 3 dB), then $G_{sat}^{out} = (G_0 + A) / 2$ with $A = \exp(-\alpha_{WG} L)$, i.e. the point halfway between the unsaturated and the completely saturated gain. According to [58] the saturation output power P_{sat}^{out} and the saturation power P_s are connected by

$$P_{sat}^{out} = \frac{\ln 2}{1 + \frac{\alpha_{WG}}{g}} P_s \quad (2.14)$$

with the waveguide losses α_{WG} and the modal gain g . Using this generalized definition of the saturation output power, a SOA with small device gain can still achieve a large saturation output power.

With the last equations a general description of the saturation behavior of amplifiers is at hand and the saturation output power as a figure of merit of the SOA performance is connected to the intrinsic saturation power of the gain medium.

For bulk and QW material it is usually assumed that the peak gain depends on first order linearly on the carrier density N

$$g = (\Gamma a / V)(N - N_0) \quad (2.15)$$

2 Theory

with the confinement factor Γ , the differential gain coefficient $a = dg/dN$, the active volume V and the transparency carrier density N_0 . The carrier density changes with the injection current I and the optical signal power P according to the rate equation

$$\frac{dN}{dt} = \frac{I}{q} - \frac{N}{\tau_e} - \frac{a(N - N_0)}{\sigma_m h\nu} P \quad (2.16)$$

if the number of photons is expressed by the optical power. Here, τ_e is the carrier lifetime, σ_m the effective cross section of the waveguide mode, h is Planck's constant and ν is the frequency of the signal. For times longer than τ_e or in continuous wave (cw)-operation we get a stationary solution for $dN/dt = 0$. Using the solution in the above equation the gain saturation is described by

$$g = \frac{g_0}{1 + P/P_S} \quad (2.17)$$

With the small signal gain given by $g_0 = (\Gamma a/V)(I\tau_e/q - N_0)$ and the saturation power P_S defined by

$$P_S = \frac{h\nu\sigma_m}{a} \frac{1}{\tau_e} \quad (2.18)$$

for bulk or QWs as gain medium.

For QDs it is not possible to find an analytical solution, but approximations can describe the saturation power. Using a 2-level rate equation model the relation between cw power and inversion of the active states can be found, from which the saturation power in the limit of high inversion P_S^{HI} can be approximated [59] with

$$P_S^{\text{HI}} = \frac{h\nu\sigma_m}{a} \left(\frac{1}{\tau_C} - \frac{1}{\tau_G} \right) \quad (2.19)$$

where τ_C is the characteristic capture time (~ 2 ps) and τ_G is the spontaneous recombination carrier lifetime of the GS (~ 1 ns). This is valid under high current density where both, the QD states and the WL band edge are completely filled. The GS carrier lifetime is much larger and can be neglected in equation (2.19), hence, in this limit the gain saturation is only determined by the QD-WL spectral hole burning and limited only by the transport time into the active states. The saturation power can not be increased by further increasing the current injection because the capture time is not affected by it.

Comparing the expression for bulk resp. QWs and QDs we find them similar in structure, but as the capture time τ_C is much smaller than the carrier lifetime τ_e we can expect a much larger saturation power for QDs than for conventional materials. It should be noted that the approximation for the QDs assumes that the WL band edge is completely filled. This is not always achievable in real devices due to start of lasing or thermal degradation of the device.

Confinement factor

As previously described the optical mode overlaps only partly with the region of the active medium. The fraction of the optical mode that has an overlap with the active medium is the optical confinement factor Γ . This factor is different for bulk, QW and QD material. For a typical device dimension of $2000 \times 4 \mu\text{m}^2$ with a QD density of several 10^{10} cm^{-2} per layer, we can estimate about 10^7 quantum dots in an active zone with ten layers. Depending on the broadening, the peak material gain can be high. Yet, the overlap of the optical mode with the QD array is small. For a QD array it is on the order of total dot volume to total waveguide volume. It can be separated in an in-plane and a vertical part

$$\Gamma = \underbrace{\frac{N_D A_D}{A}}_{\text{in-plane}} \cdot \underbrace{\frac{1}{A} \int \int_A \int_{\text{dot}} |E(z)|^2 dz}_{\text{vertical}} \bigg/ \underbrace{\int_{-\infty}^{\infty} |E(z)|^2 dz}_{\text{vertical}} \quad (2.20)$$

with the area coverage with dots consisting of the number of QDs N_D of average in-plane size A_D for an area A . The vertical confinement factor is given by the vertical overlap of QDs and optical mode represented by the optical field E , averaged over the plane of area A and integrated along the vertical direction z [20]. Typical values of the total optical confinement factor for QDs are $\Gamma = 10^{-3} - 10^{-4}$.

The confinement factor relates the material gain g_{mat} of QDs, which is difficult to measure, to the modal gain g , which can be accessed via experiment and for which most of the general formulas in this section hold. The modal gain is defined as

$$g = \Gamma g_{\text{mat}} \quad (2.21)$$

In QDs it is typically one order of magnitude lower than the maximum modal gain in QWs due to the lower confinement factor and the larger spectral width. Because of the low modal gain QD devices require a low cavity loss. It typically ranges between 2 and 10 cm^{-1} and has its origin in free-carrier absorption and defect center scattering.

For a rectangular shaped waveguide the confinement factors of the TE and TM polarized optical mode are different. This is one reason why the gain for TE and TM modes is different and the semiconductor optical amplifiers generally exhibit a polarization dependence of the gain. The optical properties of the amplifying material have a polarization dependence itself; this is discussed in detail in section 2.2.6.

Using the definitions and equations derived in this section, the gain, its bandwidth, the saturation behavior and the difference of material and modal gain of an amplifier can be understood and applied to the measurement results on a SOA.

2.2.3 Gain ripple

The residual reflectivity of the chip facets has an impact on the gain of the amplifiers [60, 61]. An ideal amplifier should have no reflectivity at the end facets yielding a perfect traveling wave device. In practice, even with several means of reducing the reflectivity, as seen in chapter 2.3.2, some residual reflectivity forms an optical cavity. Therefore, the gain of the

2 Theory

device is modulated at the longitudinal modes of the cavity because the gain is higher at the modes and lower in between the modes.

For an amplifier with facet reflectivities $R_{1,2}$ the gain is given by [11]⁵

$$G = \frac{(1 - R_1)(1 - R_2)G_s}{(1 - \sqrt{R_1 R_2} G_s)^2 + 4\sqrt{R_1 R_2} G_s \sin^2 \phi}, \quad (2.22)$$

$$\text{where } \phi = \phi_0 + \frac{g_0 L \alpha}{2} \left(\frac{P}{P + P_s} \right), \phi_0 = \frac{2\pi L n}{\lambda} \quad (2.23)$$

with G_s the single-pass gain, $\phi_{(0)}$ the (nominal) phase shift, L the length, n the index, α the linewidth enhancement factor, g_0 the unsaturated gain, $P_{(s)}$ the total internal (saturation) power, and λ the wavelength.

The $\sin^2 \phi$ term is responsible for the modulation of the output signal at the longitudinal cavity modes as depicted in Fig. 2.3a. A change in the second term of ϕ results in a shift of the cavity modes. For $\sin^2 \phi = 1$ (gain minimum G_{\min}) and $\sin^2 \phi = 0$ (gain maximum G_{\max}) we can calculate the gain ripple ξ

$$\xi = \frac{G_{\max}}{G_{\min}} = \left(\frac{1 + G_s \sqrt{R_1 R_2}}{1 - G_s \sqrt{R_1 R_2}} \right)^2. \quad (2.24)$$

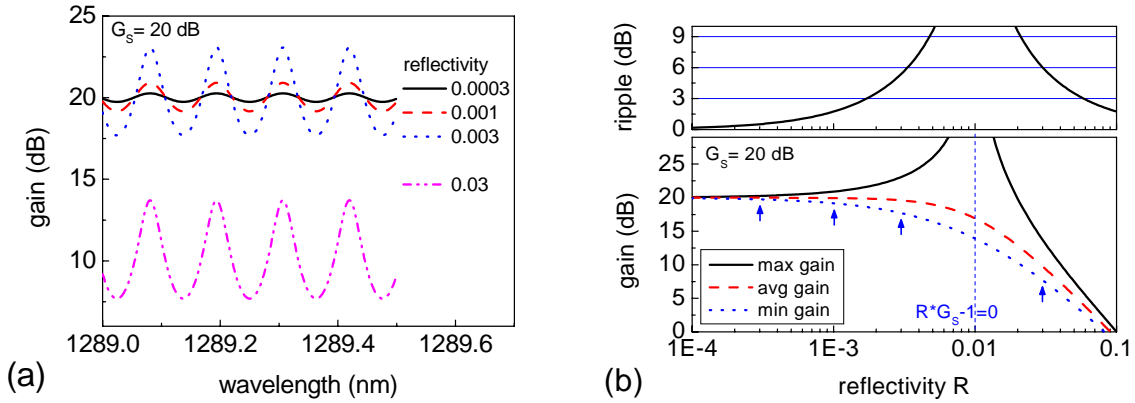


Fig. 2.3: Simulation of the gain function (eq. (2.22)) for typical amplifier parameters (length 2 mm, $n_{\text{eff}} = 3.68$, $\lambda_{\text{center}} = 1290$ nm, $P = -10$ dBm, $P_{\text{sat}} = 5$ dBm, $G_s = 20$ dB). (a) Gain vs. wavelength for various reflectivities and (b) gain and ripple vs. reflectivity for $\sin^2 \phi = 1$ (minimum gain), 0 (maximum gain) and $\frac{1}{2}$ (average gain). The arrows denote the reflectivity values for which the gain function is plotted in (a).

Fig. 2.3 and Fig. 2.4 show the various aspects of equation (3.10) in a graphical representation. Typical values which fit to experiments have been used for the parameters. This helps to understand the basic dependencies of a SOA on facet reflectivity and gain. For the maximum value of the gain when $\sin \phi = 0$ we find a singularity for $(1 - R G_s) = 0$ (Fig. 2.3b). This indicates that gain and reflectivity are interdependent; a larger gain necessitates also a smaller

⁵ see also Technical Annex 7.5

reflectivity. From Fig. 2.4b we conclude that for the facet reflectivity a value $R \ll 1/G_s$ must be achieved in order to realize a traveling wave amplifier with low gain ripple.

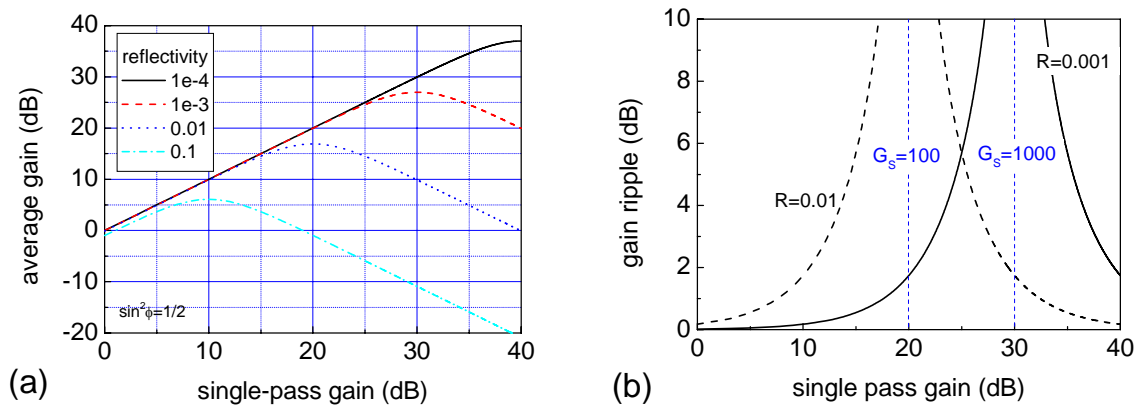


Fig. 2.4: (a) Average gain for $\sin^2 \phi = 1/2$ in eq. (2.22) vs. single-pass gain G_s for various facet reflectivities. Note that with the deviation from linear dependency the gain ripple degrades to large values as can be seen in graph (b). (b) Amplifier ripple vs. single-pass gain for two different reflectivities. The ripple degrades when the denominator of eq. (2.22) is zero, i.e. $RG_s = 1$.

The gain ripple which is also observed in the ASE spectrum has a strong influence on the amplifier performance. It is observed in the gain vs. wavelength spectrum as well in the gain vs. current measurement. The latter is coherent if we consider the following dependencies: a change in current or current density is generally accompanied by a change in carrier density ($dI \propto (dn)^2$). The carrier density is coupled to the refractive index which in turn has a direct relationship with the wavelength via $n = \lambda^2 / 2L\Delta\lambda$. An experimental observation of this dependence will be shown in chapter 5.1.1.

The ripple, which stems from the residual reflectivity of the Fabry-Perot cavity, was discussed in detail as it causes a wavelength dependent deterioration of the performance of the device. It is on the other hand also an important device property, and the ASE ripple is easily measured and contains valid information on the quality of the device.

From its measurements the gain-reflectivity product can be identified with the Hakki-Paoli method (chapter 3.4.1), which allows extracting information on gain and reflectivity. If one of both is known, this is a simple way to get the information of the complementing property. If the gain-reflectivity product data is available for different device stadiums, i.e. before and after anti-reflection coating, it is possible to deduce the reflectivity spectrum.

2.2.4 Amplified spontaneous emission and gain

The exact measurement of the optical gain requires a sophisticated setup and is rather time consuming. Often companies use the fact that a large part of the relevant information may be derived from the amplified spontaneous emission spectrum of the optical amplifier.

The output power vs. current characteristics (P-I) of an optical amplifier is less distinct compared to a laser. The P-I curve exhibits a soft turn-on which is a result of amplification of the spontaneous emission. A high resolution ASE spectrum shows the modulation of the intensity at the longitudinal mode spacing caused by residual reflectivity of the facets as

2 Theory

discussed in chapter 2.2.3. For bulk and quantum well based amplifiers the amplified spontaneous emission spectrum shifts to the blue (shorter wavelengths) with increasing current. This is primarily due to the filling of the band with injected electrons and holes [57]. The optical gain, current and ASE are related and can be calculated as described for bulk and QWs in [11, 62, 63]. A gain proportional to the carrier density, a parabolic gain wavelength characteristic and a peak wavelength that is a function of the carrier density are assumed giving a good approximation for the characteristics of bulk and QW SOAs. The most important result is the proportionality of ASE and gain from which we can expect a similarity in their spectrum and their absolute value of the gain ripple.

For QDs no such simple relations can be given for gain and ASE because a sophisticated model is needed that describes the properties of QDs and their surrounding WL and barrier material. Such a model has been implemented by Berg [59] showing the crucial role of ASE in QD SOAs, especially for long (>5 mm) devices at high current densities. The interrelation of ASE and gain for QD SOAs will be experimentally investigated in section 5.1.1.

2.2.5 Noise

Within the amplifying section of a SOA the ground state can recombine through stimulated emission caused by a signal photon or spontaneously with random direction and phase. Some of the spontaneously emitted photons will be amplified which results in amplified spontaneous emission (ASE). This and other contributions of the noise degrade the overall performance of the amplifier as it they are added to the input and amplified signal. In this section the noise properties are analyzed in detail to understand the different roles of the individual noise contributions.

For an optical amplifier the following general consideration from [64] applies. The total ASE power P_{ASE} or the ASE density ρ_{ASE} summed over all modes in an optical bandwidth B_0 equals to

$$P_{ASE} = 2n_{sp}hv(G-1)B_0 \quad \text{or} \quad \rho_{ASE} = 2n_{sp}hv(G-1) \quad (2.25)$$

with the spontaneous emission factor n_{sp} as a measure of the quality of inversion of the optical amplifier given by

$$n_{sp} = \frac{N_2}{N_2 - N_1} \quad (2.26)$$

with $N_{1,2}$ the occupation probability of the ground and the excited level.

Intensity/Photocurrent noise

Discussions about the basic conversion of light intensity into electrical current by an optical receiver can be found in many books and articles [7, 13, 64-67]. In order to understand the noise figure, this discussion is reviewed shortly at this point. The average photocurrent generated in a photodetector by an optical source is $i_{dc} = \Re\langle P \rangle$ with average power $\langle P \rangle = \overline{E^2(t)}$ where the detector responsivity is defined as $\Re = \eta q / hv$ [A/W] with q the

charge of the carriers. The light collection quantum efficiency η includes all optical losses that are part of the optical receiver.

Not only is the average optical power, but also intensity noise is present in the amplifier which is a significant limiting factor in optical communication systems. The amplitude of the optical field noise is directly converted by the photodetector into electrical noise, while the phase noise can be converted to intensity noise via interference effects. The following intensity noise types are commonly encountered in optical systems and result in a contribution to the noise figure:

- Shot noise
- Signal-spontaneous beat noise
- Spontaneous-spontaneous beat noise
- Interference noise

For the following equations the variables are listed further below. We consider an amplified signal light together with ASE incident on a detector with their total electric field expressed as⁶

$$E(t) = \sqrt{2GP_{in}} \cos(\omega_0 t) + \sum_{k=-B_0/2\delta\nu}^{B_0/2\delta\nu} \sqrt{2\rho_{ASE}\delta\nu} \cdot \cos((\omega_0 + 2\pi k\delta\nu)t + \Omega_k) \quad (2.27)$$

Hence,

$$\begin{aligned} i(t) &= \overline{\Re E^2(t)} \\ &= \Re GP_{in} \quad (\text{signal}) \\ &+ 4\Re \sum_{k=-B_0/2\delta\nu}^{B_0/2\delta\nu} \sqrt{GP_{in}\rho_{ASE}\delta\nu} \cdot \cos(\omega_0 t) \cos((\omega_0 + 2\pi k\delta\nu)t + \Phi_k) \quad (\text{sig-sp beat noise}) \quad (2.28) \\ &+ 2\Re \rho_{ASE} \delta\nu \cdot \left[\sum_{k=-B_0/2\delta\nu}^{B_0/2\delta\nu} \cos((\omega_0 + 2\pi k\delta\nu)t + \Phi_k) \right]^2 \quad (\text{sp-sp beat noise}) \end{aligned}$$

and application of trigonometric addition theorems and symmetry arguments yields

$$\begin{aligned} i(t) &= \Re GP_{in} \quad (\text{signal}) \\ &+ 2\Re \sqrt{GP_{in}\rho_{ASE}\delta\nu} \sum_{k=-B_0/2\delta\nu}^{B_0/2\delta\nu} \cos(2\pi k\delta\nu t + \Phi_k) \quad (\text{sig-sp beat noise}) \quad (2.29) \\ &+ 2\Re \rho_{ASE} \delta\nu \cdot \sum_{k=0}^{B_0/\delta\nu} \sum_{j=0}^{B_0/\delta\nu} \cos((k-j)2\pi\delta\nu t + \Phi_k - \Phi_j) \quad (\text{sp-sp beat noise}) \end{aligned}$$

The first term is simply the detected signal. It has an underlying shot noise process with the variance or noise power spectral density

$$\sigma_{i_{\text{sig-shot}}}^2 = 2q\Re P_{\text{sig}} \quad (2.30)$$

⁶ (Factor $\sqrt{2}$ arises from normalization, because $\overline{\cos^2(t)} = 1/2$).

2 Theory

The phase of the ASE fluctuates randomly, thus the second and third term fluctuate accordingly, which results in noise. Because these terms have no correlation, they can be treated individually and the noise power of each term is given by the variance $\sigma_i^2 = \langle i^2 \rangle - \langle i \rangle^2$. Assuming that the ASE is wavelength independent around the signal wavelength, the power density of the signal-spontaneous beat noise is evaluated to

$$\sigma_{i_{\text{sig-sp}}}^2 = 4\Re^2 G P_{\text{sig}} \rho_{\text{ASE}}^{\parallel} . \quad (2.31)$$

For the spontaneous-spontaneous beat noise (third term) the dc current $I_{\text{sp}}^{\text{dc}} = \Re \rho_{\text{ASE}} B_0$ is obtained for $k = j$. This results in a shot noise of $\sigma_{i_{\text{sp-shot}}}^2 = 2q\Re \rho_{\text{ASE}} B_0$. By organizing the remaining sum terms according to their frequency one obtains the power density near dc of

$$\sigma_{i_{\text{sp-sp}}}^2 \simeq 2\Re^2 \rho_{\text{ASE}}^2 B_0 \quad (2.32)$$

For amplifiers that are polarization dependent, i.e. they have a different single-pass gain for TE and TM polarization, ASE $\rho_{\text{ASE}}^{\parallel}$ (copolarized with the signal) has to be accounted for. This leads to a polarization dependent noise figure.

Noise Figure

The so-called noise figure is explicitly defined as [2, 68]:

The decrease of the signal-to-noise ratio (SNR), at the output of an optical detector with unitary quantum efficiency, due to the propagation of a shot-noise-limited signal through the optical amplifier expressed in dB.

Therefore, the noise figure of an amplifier describes the degradation of the SNR between the input and the output of the amplifier. The noise factor F is the linear representation of the noise figure NF with the following relation

$$\text{NF} = 10 \log(\text{F}) \quad (2.33)$$

and the noise factor is defined in terms of electrical signal-to-noise ratios by

$$\text{F} = \frac{\text{SNR}_{\text{in}}}{\text{SNR}_{\text{out}}} \quad (2.34)$$

Using the above derived contributions of the signal shot noise, the signal-spontaneous beat noise, the spontaneous-spontaneous beat noise, the spontaneous shot noise and the contribution from multi-path interference noise, we obtain $\text{SNR}_{\text{in}} = i_{\text{dc}}^2 / \sigma_{i_{\text{sig-shot}}}^2 = (\Re P_{\text{sig}})^2 / (2q\Re P_{\text{sig}})$; $\text{SNR}_{\text{out}} = i_{\text{dc,out}}^2 / (\sigma_{i_{\text{sig-shot}}}^2 + \sigma_{i_{\text{sig-sp}}}^2 + \sigma_{i_{\text{sp-sp}}}^2 + \sigma_{i_{\text{sp-shot}}}^2 + \sigma_{i_{\text{MPI}}}^2)$ $= (G\Re P_{\text{sig}})^2 / (2qG\Re P_{\text{sig}} + 4\Re^2 G P_{\text{sig}} \rho_{\text{ASE}}^{\parallel} + 2\Re^2 \rho_{\text{ASE}}^2 B_0 + 2q\Re \rho_{\text{ASE}} B_0 + \sigma_{\text{MPI}}^2)$ which equals a noise factor of

$$\begin{aligned}
 F &= \frac{1}{G} + \frac{2\eta\rho_{\text{ASE}}^{\parallel}}{G\hbar\nu} + \frac{\rho_{\text{ASE}}^2 B_{\text{sp-sp}}}{2\hbar\nu G^2 P_{\text{sig}}} + \frac{P_{\text{ASE}}}{G^2 P_{\text{sig}}} + \text{factor} \cdot \sigma_{\text{MPI}}^2 \\
 &= F_{\text{sig-shot}} + F_{\text{sig-sp}} + F_{\text{sp-sp}} + F_{\text{sp-shot}} + F_{\text{MPI}}
 \end{aligned} \tag{2.35}$$

$$\text{with } F_{\text{MPI}} = \frac{2P_{\text{sig}}}{\hbar\nu\pi} \frac{\Delta\nu}{f^2 + \Delta\nu} \sum_i (p_i G_{\text{cav},i})$$

where G is the gain at the signal wavelength,
 η is the collection quantum efficiency,
 ρ_{ASE} is the unpolarized optical power density of spontaneous emission,
 $\rho_{\text{ASE}}^{\parallel}$ is the with the signal copolarized ASE density,
 $\nu = \frac{c}{\lambda}$ is the signal frequency, with speed of light c and wavelength λ ,
 $B_{\text{sp-sp}} \cong \frac{c\Delta\lambda}{(\lambda_0)^2}$ is the equivalent optical bandwidth of the ASE in Hz,
 P_{sig} is the optical input power,
 P_{ASE} is the integrated ASE power over wavelength,
 $p_i G_{\text{cav},i}$ is the effective resonator gain of the i^{th} resonator which takes the polarization state of the signals into account,
 $\Delta\nu$ is the FWHM of the source linewidth, and
 f is the base band frequency.

The noise factor due to multipath interference (MPI), F_{MPI} , is generated by the beating between the output signal and one or more doubly reflected replicas of the output signal. Two or more reflection points inside the amplifier are necessary to generate MPI noise. MPI noise cannot be derived from the ASE as measured on an optical spectrum analyzer. It must be measured after a broadband optical-to-electrical conversion on an electrical spectrum analyzer.

For most cases the signal-spontaneous beat noise contribution is dominant while ASE shot noise and multiple path interference contributions are neglected.

Using the first two terms of (2.35) and (2.25) with $\rho_{\text{ASE}}^{\parallel} = 1/2\rho_{\text{ASE}}$ and assuming $G \gg 1$ we find for $n_{\text{sp}} = 1$ the minimum value for the noise factor $F = 2n_{\text{sp}} = 2 \hat{=} 3\text{dB} = \text{NF}$.

For perfect population inversion ($n_{\text{sp}} = 1$), there is no stimulated absorption, and a quantum-limited noise figure is achieved. For imperfect population inversion, on the other hand, stimulated absorption occurs, which increases the noise figure. This consideration indicates that the stimulated absorption causes noise figure degradation. For semiconductor amplifiers n_{sp} ranges from 1.4 to more than 4 depending both on the pumping rate and the operating wavelength.

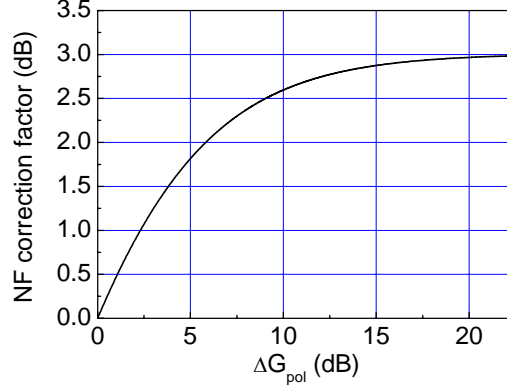


Fig. 2.5: Correction of the noise figure for TE modes vs. polarization dependence of the amplifier gain showing a maximum correction of 3 dB for large polarization difference for TE/TM modes.

The polarization dependence of an amplifier is defined as $\Delta G_{\text{pol}} = 10 \log(G_{\text{TE}}/G_{\text{TM}})$. If $\Delta G = 0$, i.e. the amplifier is polarization independent, then the only polarization dependent part of the noise figure yields $F_{\Delta G=0} = \rho_{\text{ASE}}/G_{\text{h}\nu}$. According to [69] the correction of the noise figure for TE modes is

$$\frac{F_{\text{TE}}(\Delta G)}{F_{\Delta G=0}} = \frac{2}{1 + \frac{\rho_{\text{ASE,TM}}}{\rho_{\text{ASE,TE}}}} \approx \frac{2}{1 + \frac{G_{\text{TM}}}{G_{\text{TE}}}} \quad (2.36)$$

using the fact that $\rho_{\text{ASE}} = \rho_{\text{ASE,TE}} + \rho_{\text{ASE,TM}}$ and the proportionality of formula (2.25) with $\rho_{\text{ASE,TE/TM}} \sim G_{\text{TE/TM}}$ for large gain. As can be seen on Fig. 2.5, the corrective factor is as high as 3 dB for strongly polarized SOAs.

In summary, the elaborate derivation of the noise figure allows an insight in the different contributions, their physical origin and their weight in the noise figure. Using equation (2.35) we are able to derive the noise figure of an amplifier, which is described by method in section 4.2.3 and the measurement in section 5.1.2. It was shown that the noise figure is sensitive on the polarization dependence of the gain, which must be taken into account when measuring the noise figure.

2.2.6 Polarization properties of amplifiers

The polarization properties of SOAs are of interest for the performance of these elements in optical systems. In data transmission systems where SOAs can be deployed as booster, in-line or pre-amplifiers polarization insensitive operation is demanded for the latter two applications.

For the two polarization states we adhere to the definition given in chapter 2.3.2. In the case of the transverse-magnetic (TM)-mode the polarization is aligned with the z-direction. For the transverse-electric (TE)-mode the polarization vector is along the xy-plane.

The polarization sensitivity of SOAs results at first from the difference of the confinement factor for the TE- and TM-modes in the waveguide which contribute to the different TE and TM signal amplification. Additionally, the gain medium can amplify the two polarizations

differently. This is the case for QW SOAs where different quantization levels for heavy hole (HH) bands (which are the dominant part of the optical gain for the TE-mode) and light-hole (LH) bands (which are the part of the optical gain for the TM-mode) lead to a polarization sensitivity of the gain medium. In bulk material HH and LH are degenerate in the valence band which results in a polarization insensitive material gain. For the design of polarization insensitive SOAs many approaches exist which have been successfully implemented for bulk and QW SOAs.

- a) A thick active layer reduces the difference in the confinement factor between TE- and TM-mode (mostly realized for bulk)
- b) An anisotropic gain coefficient of the active layer compensates the difference in the modal confinement factor. In QW SOAs the HH and LH energies can be shifted by strain which results in a polarization insensitive amplifier [70-74].
- c) A non-planar waveguide structure (more square-like) results in a comparably large confinement-factor, but a very narrow waveguide and large coupling losses.

QDs as an active medium offer potential advantages with regards to polarization because their electronic wavefunctions can be tailored to some extent by growth. Detailed eight-band k-p modeling to calculate the electronic structure of QDs has been carried out by A. Schliwa [75]. With information on size, shape and composition of the QDs it is possible to compute the single- and multi-particle states, oscillation strength and polarization of optical transitions. In general single QDs show a dominant transition to the heavy hole projection of the hole state which is transverse electrically polarized. The optical transition to the light hole projection would be transverse magnetic, but has only a small contribution for a single dot which is mainly due to the biaxial strain distribution in the disk like QD.

Calculations of the polarization anisotropy of quantum dots show a strong anisotropy between the TM and the TE polarization direction. The reason is – similar to the quantum wells – the different position of the HH- and LH-bands. A typical hole ground state of a pyramidal InAs QD shows 89% HH- and only 8.4% LH-contribution. This situation changes fundamentally in layered structures. We start with a short description about the reason for HH-LH splitting.

Possible deformations of a cubic unit cell are a volume change (hydrostatic strain, $\varepsilon_{\text{hydro}}$) or a change of the axial ratio. The latter is the biaxial strain ($\varepsilon_{\text{biax}}$) defined by $\varepsilon_{\text{biax}}(\mathbf{r}) = \varepsilon_{xx}(\mathbf{r}) + \varepsilon_{yy}(\mathbf{r}) - 2\varepsilon_{zz}(\mathbf{r})$ with $\varepsilon_{xx,yy,zz}$ the strain along the crystal directions and \mathbf{r} the radial vector. This biaxial strain determines the relative energetic position of HH- to LH-band (at the Γ -point):

$$\begin{aligned} V_{\text{HH}}(\mathbf{r}) &= a_v \varepsilon_{\text{hydro}}(\mathbf{r}) + b/2 \varepsilon_{\text{biax}}(\mathbf{r}) \\ V_{\text{LH}}(\mathbf{r}) &= a_v \varepsilon_{\text{hydro}}(\mathbf{r}) - b/2 \varepsilon_{\text{biax}}(\mathbf{r}) \quad \text{with } b|_{\text{InAs}} < 0 \end{aligned} \quad (2.37)$$

In a single QD (Fig. 2.6 red) we have $\varepsilon_{xx}(\mathbf{r}) + \varepsilon_{yy}(\mathbf{r}) < 2\varepsilon_{zz}(\mathbf{r})$, $\varepsilon_{\text{biax}}(\mathbf{r}) < 0$ and therefore, the HH-band lies energetically above the LH-band. In layered structures we have the blue coded situation in Fig. 2.6: $\varepsilon_{xx}(\mathbf{r}) + \varepsilon_{yy}(\mathbf{r}) > 2\varepsilon_{zz}(\mathbf{r})$, $\varepsilon_{\text{biax}}(\mathbf{r}) > 0$, meaning HH-band and LH-band move towards each other and possibly change their energetic position. HH-fractions of a hole wavefunction emit solely TE-polarized light, while LH-fractions are dominantly TM-polarized.

2 Theory

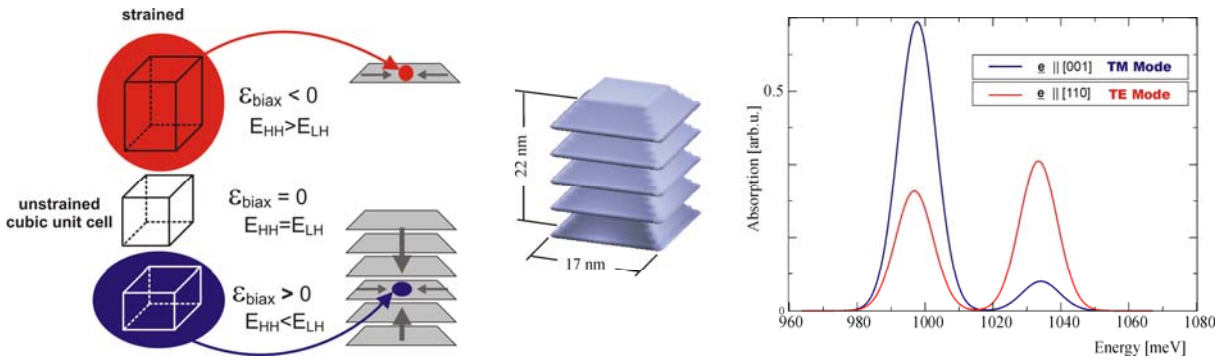


Fig. 2.6: (left) Deformation of the cubic unit cell in a single QDs [red] and in layered QDs [blue]. (middle) Scheme of five closely stacked coupled QDs used as input structure for eight-band k-p calculations. (right) This structure results in an inverted optical absorption of the QD structure preferring TM polarization. Courtesy of A. Schliwa [75].

If the quantum dots are stacked closely on top of each other preserving an electronic coupling (Fig. 2.6 middle) the biaxial strain within the QDs changes sign and it is possible to achieve a stronger TM absorption in this structure as can be observed in the according calculation to this structure in Fig. 2.6 (right). The TM preference for closely stacked QD structures has been also found experimentally in CdSe submonolayer superlattices with vertical correlation of quantum dots [76], in InGaAs QD structures with 20 layers [77], and for an inhomogeneous thermal strain induced effect at higher temperature [78].

From the above considerations we find that the polarization properties of QDs can be manipulated by using layered structures. Parameters to be considered should be

- number of the QD-layers,
- distance of these layers and the
- composition in the QD.

It should be noted that with such a coupling the QD-stack would be a single quantum mechanical object with probably only one exciton, resulting in a small gain as compared to decoupled stacked QD materials. Further, the wavelength division multiplexing properties of these QD SOAs would probably be degraded by this coupling through cross-gain-modulation. A possible way out would be a layered structure with alternate bigger and smaller QDs. The smaller ones would pass on the strain while being outside the interesting gain region. The larger QDs would be spatially separated by the smaller ones, therefore no coupled states exist and they can be treated as separate quantum mechanical objects with one exciton each. Combining these results with an adequate modeling of the waveguide shows the roadmap to achieve polarization insensitive QD SOAs.

2.2.7 Higher order effects

SOAs can be used in both linear and nonlinear operation. In the latter they can perform all-optical signal processing because of their strong nonlinearities and their fast dynamics. The properties of SOAs allow realizing a large number of different functions. Therefore SOAs are devices with a large application area.

The main physical effects behind the realized functionalities are listed here and some examples of functionalities and applications are given to each effect without wishing to be exhaustive.

Linear effects

- **Optical gain**
The signal is amplified by stimulated emission
Function: booster-, inline-, pre-amplification
- **Amplified Spontaneous Emission (ASE)**
Consists of spontaneously emitted photons amplified along the active waveguide
Function: broadband light source

Non-linear effects

- **Self Phase Modulation (SPM)**
Modulation of the output signal phase caused by refractive index changes induced by the power variations of the same signal
Function: waveform shaping, chirp compensation
- **Self Gain Modulation (SGM)**
Modulation of the signal gain induced by the variation of the signal input power
Function: waveform distortion compensation
- **Cross Gain Modulation (XGM)**
Gain modulation induced by one optical signal that affects the gain of all the other optical beams propagating in the SOA
Function: wavelength conversion, multiplexing, label swapping, clock recovery
- **Cross Phase Modulation (XPM)**
Refractive index changes induced by one optical beam affecting the output phase of all the other signals propagating along the SOA
Function: add/drop multiplexing, optical sampling, wavelength conversion, regeneration
- **Four-Wave mixing (FWM)**
Beating of two or more signals propagating along the SOA generates beams at new optical frequencies
Function: optical sampling, demultiplexing, wavelength conversion, XOR gate

The optical gain and ASE were described in previous sections. Here, we will present some details on XGM as this effect was studied with our QD SOAs by experiments (section 5.2.4). The other effects will not be further reviewed.

XGM results from gain saturation in a SOA. If two signals with different wavelengths, usually a strong pump and a weak probe signal, are present in an amplifier this effect occurs. In saturation the available gain is distributed between the two wavelengths and the changes due to the pump wavelength have an inverse effect on the gain which is available for the probe wavelength. Thereby, data can be transferred from one wavelength to the other, so-called wavelength conversion, but on the other hand the effect is unwanted for amplification of multiple wavelengths where a cross talk between the channels occurs by XGM.

The maximum operation speed of the wavelength converter based on XGM is limited due to the gain recovery time, which results from the change of the total carrier density in the active region of bulk or QW SOAs. An ultrafast gain recovery time has been reported for QD SOAs [52] which would predict a faster operation with XGM. There have been already reports on XGM with quantum dot SOAs where wavelength conversion by XGM without patterning of a 10 Gbit/s data signal was experimentally demonstrated [40]. Other papers reported a small-signal 3dB XGM bandwidth of 1.5 GHz with an InP-based 1550 nm quantum dash SOA [79] and a bandwidth of 3.5 GHz in a p-doped QD SOA at 1.3 μm [80] which is comparable to the structures introduced in this thesis.

2 Theory

The XGM can be tested with a small-signal measurement where a strong saturating pump signal is modulated by an electro-optical modulator. The modulation amplitude is much smaller than the signal amplitude to achieve a small-signal modulation which is transferred in a gain modulation which in turn is probed by the second wavelength cw signal. The small signal conversion efficiency from the pump to the probe wavelength is given by [57]

$$\eta = \left| \exp \left(\frac{-gL}{\tau_s/\tau_{se} + 1 + i2\pi f\tau_s} \right) - 1 \right| \quad (2.38)$$

where τ_{se} is the spontaneous emission carrier lifetime and τ_s is the stimulated emission carrier lifetime which can be deduced from

$$\frac{1}{\tau_s} = \frac{P_p}{E_{sat}} \quad (2.39)$$

with the probe power P_p and the saturation energy $E_{sat} = P_{sat} \cdot \tau_{se}$. Typical XGM bandwidths are in the range of 1-10 GHz, depending on the optical power of the probe as seen from the above formula.

The XGM effect is very interesting as it allows wavelength conversion. According to the dynamic properties of QD SOAs even parallel wavelength conversion with two or more wavelengths seems feasible: A fast XGM operation based on spectral hole burning can be realized within the homogeneous broadening of the wavelength sub-ensemble, while the inhomogeneous broadening is dominated by carrier depletion resulting in a small XGM bandwidth, and thereby a small interdependence of neighboring wavelengths.

2.3 Simulation and modeling of QD SOAs

2.3.1 Waveguide simulations

In order to understand basic properties of the optical waveguide, simulations with a pure optical modeling tool were done.

The BPM-CAD (beam propagation method - computer aided design) program [81] allows calculating the two-dimensional mode of a waveguide profile and is able to simulate the transmission of this mode in a waveguide with a beam propagation method. The ridge waveguide profile of the SOA is simulated using a 2D mode solver which calculates the optical near field, modal distribution and the effective refractive index of the ridge waveguide structure. The simulation tool accounts only for optical influences via a complex refractive index, while current injection, carrier densities and thermal effects are not included. Fig. 2.7(a) shows a typical result of the mode solver featuring the optical mode and the underlying ridge waveguide profile for a deeply etched 2 μm mesa. The modeled structure has to be simplified compared to the epitaxial structure of the sample (see section 3.2). No capping layer is included, the graded layers and the QD layers are approximated with an averaged refractive index.

The optical mode is well confined within lateral extension of the waveguide while it leaks into the cladding in vertical direction. This can be expected from the index step which is much larger in lateral ($\Delta n_{\text{lat}} = 1.73$) than in vertical ($\Delta n_{\text{vert}} = 0.17$) direction. A cross section of the first order optical mode in lateral direction is shown as intensity plot in Fig. 2.7(b) for 2 and 4 μm ridge width. The corresponding power mode width $2w_p$ measured at $1/e$ is 1.25 and 2.4 μm , respectively. These results point out a large lateral confinement and a strong index guiding of the deeply etched waveguide.

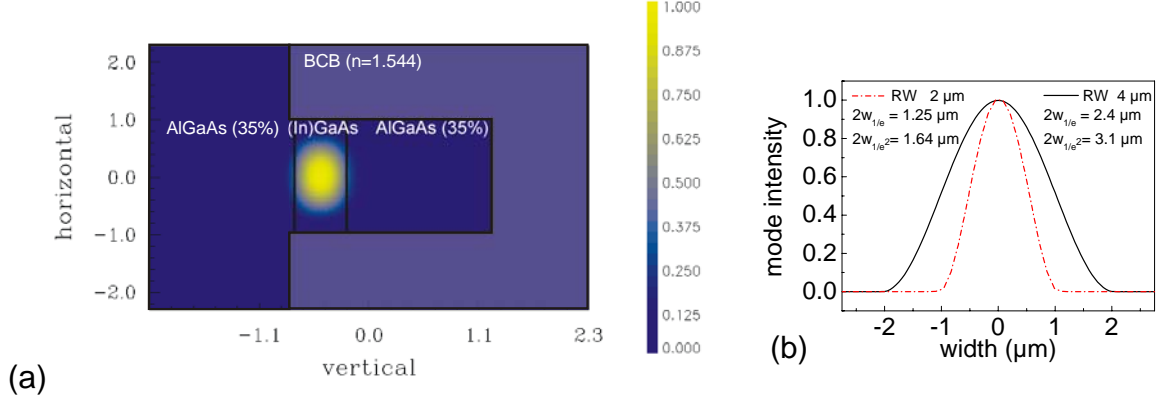


Fig. 2.7: (a) Ridge waveguide profile (2 μm) and calculated two dimensional optical mode. Picture is rotated by 90° . (b) Comparison of first order optical mode (horizontal cut of 2D mode) for ridge widths of 2 and 4 μm . (Parameters for sample DO520)

Although the mode solver calculates higher order modes that are guided laterally in the 2 and 4 μm ridges, we find mostly single mode like emission in our far field measurements, with an exception for a 4 μm ridge with angled facets (see section 4.1.2). The transverse modes with their shape, but also their relative intensity (which are not calculated by the mode solver) determine the shape of the far-field. We assume a first order mode intensity with two-dimensional Gaussian shape

$$I(x, y) = |E_0|^2 e^{-2\left(\frac{x}{w_x}\right)^2} e^{-2\left(\frac{y}{w_y}\right)^2} \quad (2.40)$$

where w_x and w_y are the beam waist diameters of the mode in lateral and vertical direction. From the waist diameters the far-field divergence characterized by its divergence angles $\theta_{x,y}$ is calculated by

$$\theta_x = \frac{\lambda}{\pi w_x}, \quad \theta_y = \frac{\lambda}{\pi w_y}. \quad (2.41)$$

For our structure (DO57) with waveguide dimensions $0.4 \times 4 \mu\text{m}^2$ we calculate 15° and 63° for lateral and vertical far-field divergence, respectively. Due to the large far-field divergence in vertical direction the structures experience a large coupling loss, since most fiber coupling optics have a numerical aperture below 0.5, corresponding to a full acceptance angle of 50° . We measured a vertical far field angle of 55° (section 4.1.2) which does not coincide exactly with the calculated value. This is due to the limitation of the model, which does not include the influence from carrier densities and thermal effects. In Fig. 2.8(a) the simulated far field angle is plotted for various waveguide thicknesses. It can be lowered below 40° , but the according waveguides are certainly not single mode. In order to achieve such large

2 Theory

waveguides which support only the first order mode, special concepts like large optical cavities, photonic band gap crystals or so-called tilted cavity have to be applied [82-85].

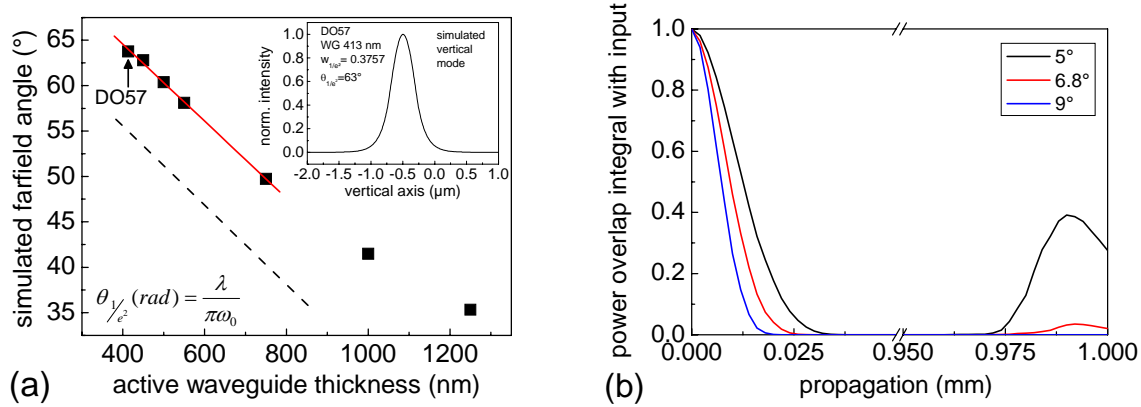


Fig. 2.8: (a) Simulated far field angle vs. height of waveguide core. The first point represents the waveguide of sample DO57. The red line is a linear fit. The dashed line estimates the far field angle of real devices, according to the far field measurement of DO57 ($\theta_{\text{meas}} = 55^\circ$). (b) From the simulation of the tilted waveguides the overlap integral between input mode and propagated mode was calculated. The overlap at the end of the waveguide (1 mm propagation) gives a measure of how much of the mode is back reflected and guided (sample structure DO520 4 μm).

The results of these simulations are both important for the conception of SOA-waveguides for improved far field and coupling-characteristics, and also for the design of modulated lasers with an advanced current guiding for improvement of the RC-characteristic of the device. The latter results have been described in detail in the thesis of Kuntz [86]. The improvement of the far field by waveguide design started from the standard TU laser processing, which uses a weakly index-guided waveguide. These structures have shown difficult coupling issues as the gain-guiding is not effective for the input mode, while successful SOA-technology has been implemented with InP buried-heterostructures, which facilitates one or more overgrowth processes. But overgrowth technology of (Al)GaAs structures⁷ has not been established up to now due to the oxidation problems of the AlGaAs cladding layers.

We have proposed a unique system of a deeply etched waveguide – making use of the spatially lateral uncoupled QDs that allow etching through the active region – in combination with a planarization of the lateral waveguide with SiO_2 as filling material. We have compared these simulations with shallow etched structures where we found a distinct change in the guiding properties from weakly (and therefore also gain) guiding to strong index guiding. The strong index guided structures are favorable for characterization of SOAs because the guiding of the optical mode is more independent of device operating conditions like current density, optical power and gain saturation.

A measure to reduce the back coupling into the waveguide of the optical mode after reflection at the facet is designing the waveguide with an angle to the facet normal. We have simulated the mode coupling of such a tilted waveguide with the beam propagation simulation tool. The input of the mode solver consists of the geometry of the cross sectional waveguide structure and the corresponding dielectric constants. The eigenvalues, i.e. the effective index of refraction, and the eigenfunctions, i.e. the optical modes, of the electromagnetic wave equations are computed. The solution is then propagated along a discretized, finite spatial grid for the given wavelength of 1.3 μm . The tool can only simulate forward propagation, therefore, reflection at a tilted facet can only be simulated through a sharp bend, i.e. a kink at

⁷ the 1.3 μm devices are based on GaAs

double angle, in the waveguide. Simulations of the optical field intensity along the sharply bent waveguide were conducted for tilt angles from 1° to 10° . The devices have a defined length of $500\ \mu\text{m}$, which on the one hand assures to investigate a real propagating mode and on the other hand keeps the computational time in a reasonable range. The lateral starting point of the input mode was $-50\ \mu\text{m}$, it then propagated for $500\ \mu\text{m}$, was “reflected” and propagated for another $500\ \mu\text{m}$.

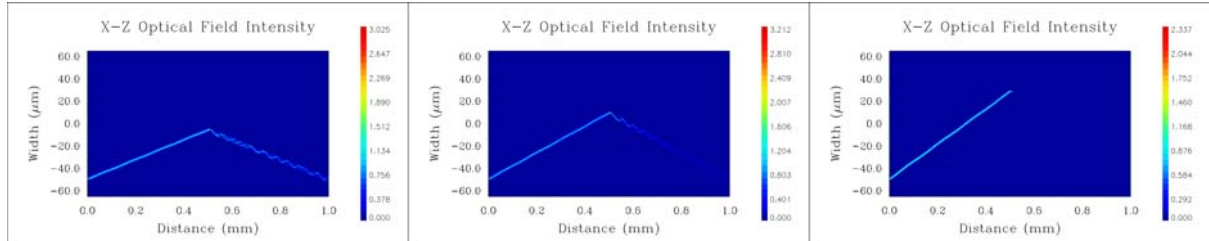


Fig. 2.9: BPM-CAD simulation of tilted waveguide. The reflection at the angled end facet was modeled by a sharp bend after $500\ \mu\text{m}$. From left to right: tilt 5° , 6.8° , 9° . Note, width scale and length scale are not the same (sample structure DO520 $4\ \mu\text{m}$).

The simulations were done for weakly index-guided and strongly index-guided structures. In the first case we observed a strong suppression of the reflected optical mode at tilt angles larger than only one degree. The situation changed dramatically for the strongly index-guided buried waveguides which indicate a strong guidance of the optical mode back into the tilted waveguide up to angles of eight degrees (Fig. 2.9). We also found a lateral reflection of the mode within the waveguide (the mode propagates zigzag like), which could explain the lateral components that we have observed in measurements of the far field of tilted structures (section 4.1.2).

From the simulation of the tilted waveguides the overlap integral between input mode and propagated mode was calculated. The overlap at the end of the waveguide gives a measure of how much of the mode is back reflected and guided. At the input side the overlap reduces quickly because the optical mode is at a different lateral position due to the waveguide tilt. As shown in Fig. 2.8(b) at 5° there is a considerable overlap at the end (which is also at $-50\ \mu\text{m}$) with the input mode. This overlap reduces for 6.8° and eventually vanishes at 9° . Although the overlap at 6.8° is well below 5%, this residual back coupling is enough to even allow lasing from these tilted devices as described in section 4.2.2. The evaluation of the reflectivity of tilted structures is continued in the next section.

Simulations of the optical waveguide help to understand basic properties of the ridge waveguides. Details on the ridge waveguide mode were calculated that provide input to the lateral and vertical design of the waveguide. Studies on the influence of waveguide tilt determine important design rules for the processing of the SOAs.

2.3.2 Reduction of facet reflectivity

In order to realize a traveling wave amplifier the reflectivity of the semiconductor crystal facets, which form a Fabry-Perot cavity, has to be reduced.

Various measures can be applied to decrease the facet reflectivity which is typically 0.32 for a GaAs semiconductor crystal calculated by the Fresnel formula with a refractive index $n_{\text{GaAs}} = 3.25$. Anti-reflection (AR) coatings, buried facets or window structures, and tilted waveguides can be deployed to achieve low facet reflectivity.

One-layer anti-reflection coating

Using one dielectric layer a reflection $R = 0$ can be theoretically achieved with a coating with thickness $d = \lambda/4$ and an index of refraction $n_{AR} = \sqrt{n_1 n_3} = \sqrt{n_1}$ for the semiconductor-air interface ($n_3^{\text{air}} = 1$) [56]. Yet,

- 1) the necessary material with n_{AR} is not always available (e.g. $n_{AR} = 1.8 - 1.9$ for $n_1 = 3.2 - 3.8$),
- 2) the consideration holds only for plane waves and does not apply fully for the fundamental mode in a waveguide,
- 3) due to the critical nature of the thickness requirements an in-situ monitoring is necessary during coating, and
- 4) the minimum reflectivity is only valid for one wavelength.

Multi-layer anti-reflection coating

Two or more dielectric layers are superior to one-layer AR coatings as they offer more flexibility in designing them to available refractive indices, wavelength and bandwidth. In the following a derivation for the calculation of multi-layer AR coatings is given which allows simulating the reflectivity of given dielectric layers on a semiconductor facet.

The definition of the polarization state of a wave propagating in an optical medium is found to be different in various textbooks. Here, we adhere to the following definition.

Consider a plane, time-harmonic electromagnetic wave propagating through a layered medium. In the case when the wave is linearly polarized with its electric vector parallel to the plane of incidence we shall speak of a *transverse electrical wave* (denoted as TE or p-polarized); when it is linearly polarized with its magnetic vector parallel to the plane of incidence (or electric vector perpendicular (German: senkrecht)) we shall speak of a *transverse magnetic wave* (denoted as TM or s-polarized).

A homogeneous dielectric medium can be described by a characteristic matrix. Following the derivation of [56] the propagation of a plane monochromatic wave through this medium is then described with the matrix

$$M(z) = \begin{bmatrix} \cos \beta & -\frac{i}{p_j} \sin \beta \\ -ip_j \sin \beta & \cos \beta \end{bmatrix} \quad (2.42)$$

Here,

$$p_{j,\text{TM}} = \sqrt{\frac{\epsilon}{\mu}} \cos \theta_j \quad \text{for TM}, \quad p_{j,\text{TE}} = \sqrt{\frac{\mu}{\epsilon}} \cos \theta_j \quad \text{for TE} \quad (2.43)$$

$$\beta = \frac{2\pi}{\lambda_0} n_j h_j \cos \theta_j \quad \text{with} \quad \theta_j = \sin^{-1} \left(\frac{n_1}{n_j} \right) \sin \theta_1 \quad \text{from Snell's law} \quad (2.44)$$

with θ the angle of incidence with respect to the facet normal, i, j the numbers of consecutive layers and h the layer height. For a homogeneous dielectric film which is assumed to be non-magnetic ($\mu = 1$) the refractive index is $n = \sqrt{\mu\epsilon} = \sqrt{\epsilon}$.

Propagation through several dielectric layers is described by the multiplication of the corresponding matrices (2.42). From the resulting matrix the reflection coefficient of the layer structure is calculated as

$$r = \frac{(m_{11} + m_{12}p_{\text{last}})p_{\text{first}} - (m_{21} + m_{22}p_{\text{last}})}{(m_{11} + m_{12}p_{\text{last}})p_{\text{first}} + (m_{21} + m_{22}p_{\text{last}})} \quad (2.45)$$

with $p_{\text{first/last}}$ for the first and last layer, respectively, and the reflectivity given by $R = r \cdot r^*$.

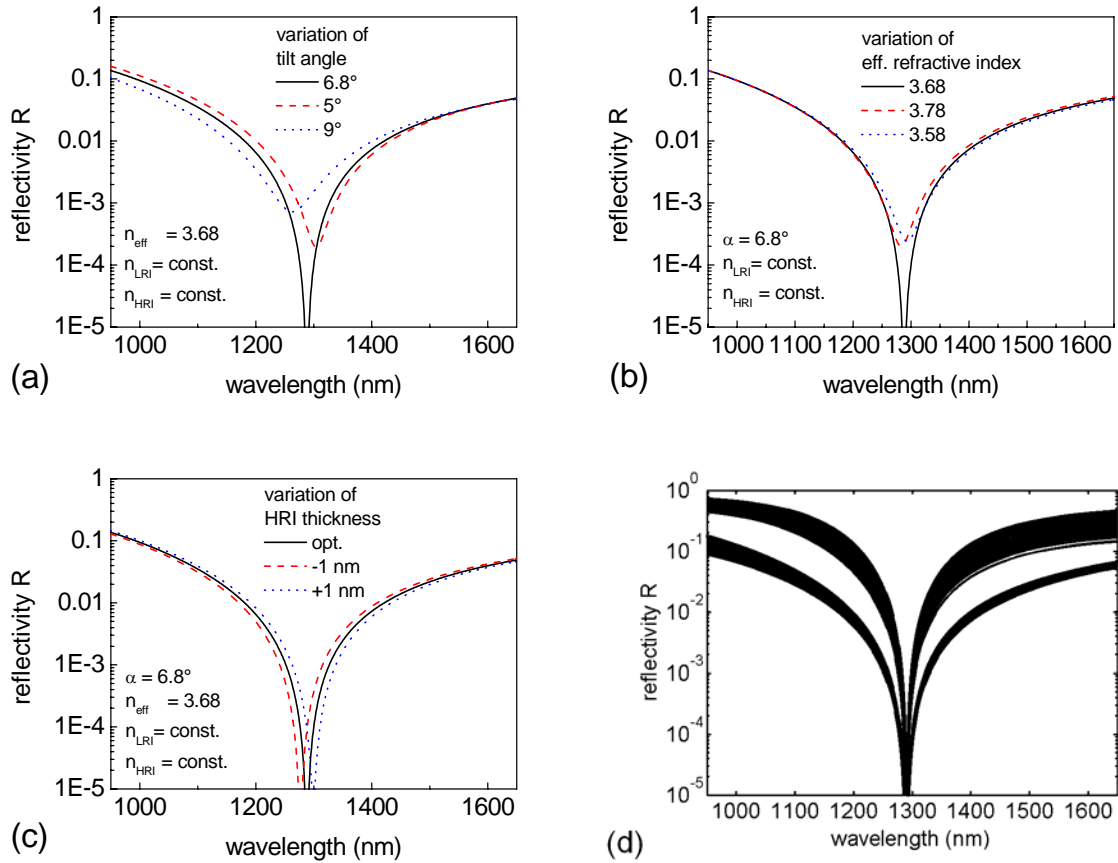


Fig. 2.10: (a)-(c) two-layer AR coating reflectivity simulation for variation of tilt angle, effective refractive index, dielectric layer thickness with typical parameters of sample DO520 for TE polarization: center wavelength $\lambda = 1290$ nm, tilt angle $\alpha = 6.8^\circ$, LRI and HRI used as dielectric layers. As a rule of thumb: 1 nm change in layer thickness results in 10 nm shift of the center wavelength. (d) four-layer AR coating reflectivity for DO520: shown are all simulated four-layer thickness combinations with $R_{\text{min}}(1290 \text{ nm}) < 10^{-6}$.

A deeper evaluation of the facet reflectivity must consider the modal character of the light wave. Therefore, the above consideration lacks from the approximation of plane waves, but gives a good qualitative picture of the influence of layer height and effective refractive index. By implementation of the formulas (2.42) to (2.45) in Matlab [87] a simulation of a double layer anti-reflection coating was carried out to evaluate the optimum parameters for the coating of the samples at the Ferdinand Braun Institut für Höchstfrequenztechnik (FBH).

2 Theory

The FBH considers its AR coatings as intellectual property. Therefore, no details on the coating materials and their layer thicknesses may be published in this thesis. The AR coatings consist of a dielectric two-layer system with a low and a high refracting material. All other details are for internal use only. Here, we will denote the low refractive material with *LRI* and the material with high refractive index *HRI*.

The effective refractive index of the optical mode in the waveguide is either evaluated theoretically by using an optical mode solver for the lateral structure of the ridge waveguide or it is simply calculated from the optical spectrum of the device from the Fabry-Perot cavity resonances using $n = \lambda^2/2L\Delta\lambda$.

Note, if the waveguide is tilted, $\theta > 0$, the reflectivity of a multilayer AR coating has a strong dependence on the polarization of the mode. The optimization of the layer system can only be done for TE or TM polarization. Fig. 2.10(a-c) shows the dependence of a **two layer AR coating** for variation of tilt angle, effective refractive index and dielectric layer thicknesses for TE polarization. All parameters have a strong influence on the position and the depth of the minimum reflectivity. This demonstrates how carefully the AR coating has to be designed and experimentally processed.

The simulation for a **four layer AR coating** (Fig. 2.10d) exhibits many combinations of four thicknesses to achieve a minimum reflectivity for the available material combination LRI/HRI/LRI/HRI. We find a bimodal distribution of layer combinations which all achieve reflectivities below 10^{-6} , but show a difference in their bandwidth $\Delta\lambda \approx 70$ or 20 nm at $R = 10^{-3}$. Even the larger bandwidth does not exceed the bandwidth of the two layer AR coating which is approximately the same at $R = 10^{-3}$. Therefore, as no improvement is expected from a four layer coating and due to the costly coating process no experiment with a four layer coating was conducted.

Buried facet or window structure

The idea of this approach is to extend the beam waist of the fundamental mode after the waveguide by a window structure with no index guiding in front of the facet. The Gaussian beam waist is

$$w^2(z) = w_0^2 \left(1 + \left(\frac{\lambda z}{\pi w_0^2} \right)^2 \right) \quad (2.46)$$

with dependence on the distance z from the spot size of the beam waist w_0 . The extension of the beam waist leads to a reduction of the reflectivity R to

$$R_{\text{eff}} = \frac{R}{1 + (d\lambda/\pi w^2)^2} \quad (2.47)$$

for a length d of the buried facet region [88]. Using typical values ($\lambda = \lambda_0/n = 1.3/3.7 \mu\text{m}$, $w_0 = 0.8 \mu\text{m}$, $R = 0.32$) from our structures we find a possible reduction of 6 dB for a window length of $10 \mu\text{m}$. But, although a longer region would result in a further decreased reflectivity, the beam would extend and eventually strike the top (metallized) surface of the device,

producing multi peak in the far field pattern and a reduction in coupling efficiency. This is estimated to be at $d > 11 \mu\text{m}$ for a typical structure height of $2 \mu\text{m}$.

Tilted waveguide/facet

The idea of reducing the facet reflectivity by angled facets (Fig. 2.11a) for InP based traveling wave laser amplifiers was introduced by Zah et al. [89]. A following detailed calculation of the reflection loss from tilted end mirrors shows a strong dependence on waveguide width d and its determining effective refractive indices n_1 and n_2 of the active and cladding regions, respectively. In the waveguide the mode field is approximated by a field of the form $E_y = A_y \exp\left(-\left(x/w\right)^2\right)$ with the half width of the mode w at $1/e$ and the corresponding width of the power $w_p = w/\sqrt{2}$. In this Gaussian approximation of the fundamental waveguide mode an analytical formula for the reflectivity of a tilted waveguide is found [90, 91]

$$R = R_f(\theta) \exp\left[-\left(\frac{2\pi n_2 w \theta}{\lambda}\right)^2\right] \quad (2.48)$$

where R_f is the Fresnel reflection of a plane wave that is reflected from a tilted dielectric interface between the amplifier facet and air. For a TE wave the Fresnel reflectivity is [56]

$$R_f(\theta) = \left(\frac{n_{\text{air}} \cos \theta - n_1 \sqrt{1 - \frac{n_1^2}{n_{\text{air}}^2} \sin^2 \theta}}{n_{\text{air}} \cos \theta + n_1 \sqrt{1 - \frac{n_1^2}{n_{\text{air}}^2} \sin^2 \theta}}\right)^2 = \left(\frac{\cos \theta - n_1 \sqrt{1 - n_1^2 \sin^2 \theta}}{\cos \theta + n_1 \sqrt{1 - n_1^2 \sin^2 \theta}}\right)^2 \quad (2.49)$$

with the tilt angle θ and the effective refractive index n_1 of the core waveguide. The Fresnel reflectivity has only small impact on the decrease of the resulting reflectivity for angles below 10° . In the technical annex 7.4 the influence of the Fresnel reflectivity and the potential use of the Brewster angle is evaluated.

With a BPM simulation of our ridge waveguide system we can calculate the width of the mode for various ridge waveguide widths (see chapter 2.3). Table 1 summarizes the typical values that have been used and calculated for structure DO520. Using the formulas (2.48) and (2.49) we can compute the dependence of the reflectivity on the tilt angle for various ridge widths for typical values of our ridge waveguide system (Fig. 2.11b).

Increasing the ridge width would lead to a stronger decrease of the reflectivity, yet, higher order modes will be supported by these waveguides. Although the effective reflection of the fundamental mode decreases with tilt of the waveguide the effective reflection of the higher order modes increases, especially for larger ridge widths, which in turn leads to a reduction of fiber coupling efficiency.

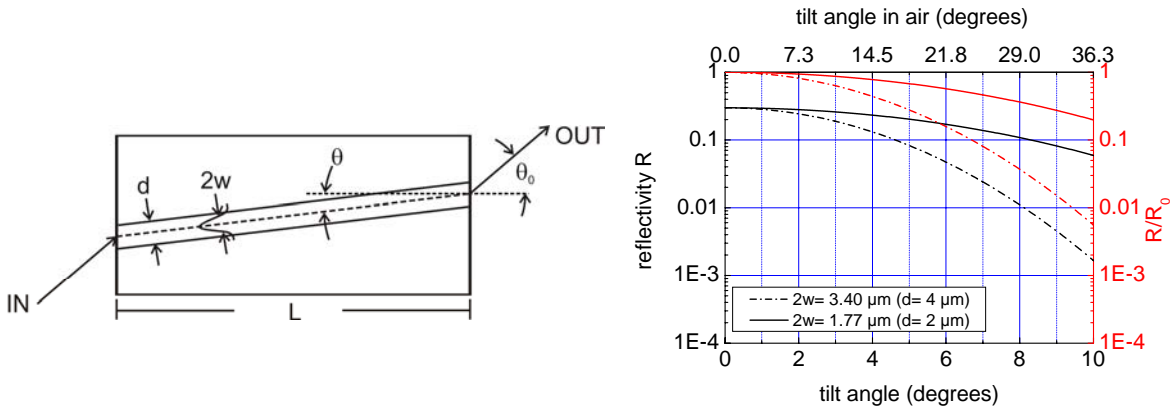


Fig. 2.11: (a) Sketch of tilted waveguide from top view (b) reflectivity (left ordinate) and relative loss (right ordinate) of a tilted waveguide calculated from equation (2.48) with parameters from Table 1.

The use of the Brewster angle for facet tilt giving low reflectivity and polarization selection is an intriguing idea which is not feasible for GaAs based SOAs due to an extreme output angle and other impracticalities. This is described in detail in the technical annex 7.4.

Table 1: Parameters of lateral mode of the sample DO520. Simplified lateral waveguide structure BCB / GaAs (width d) / BCB ($n_2 = 1.544$ / $n_1 = 3.41$ / $n_2 = 1.544$). Wavelength used in calculations $\lambda = 1.29 \mu\text{m}$. BCB is Benzocyclobutene.

Ridge width d (μm)	Field mode width $2w$ (μm)	Power mode width $2w_p$ (μm)
2	1.73	1.25
4	3.40	2.40

These simulations provide the input for design considerations to realize a traveling wave amplifier. The means of reduction of the crystal facet reflectivity like anti-reflection coatings, tilted waveguides or facet windows have been discussed in detail. Buried facet or window structures will not be realized as their effect is too small in comparison to the difficulties that arise from them. It was shown that two-layered AR coatings are optimum; while one-layer AR is too restrictive and 4-layer AR coatings do not show significant improvements. The analysis of the tilted facet demonstrated the trade-off between low reflectivity and larger output tilt angle of the optical mode.

2.3.3 Simulation of gain and saturation characteristics

There are several approaches to model the characteristics of a SOA. Among them are the use of rate equations based on photon statistics [62], the active Fabry-Perot formulation (chapter 7.5) [92] and traveling wave equations [93].

An accurate analysis will require consideration of the interaction between the injected carrier density, the material gain and the electric field amplitude point by point within the cavity. Some of these approaches assume a uniform gain and electric field profile which is often not true in SOAs.

Here, we will focus on the so-called Transfer Matrix Method (TMM) following the derivation of [94] which allows to implement traveling-wave equations and a z -dependence in the model. The transient responses of amplifiers cannot be determined efficiently as a very wide frequency range will be required for accurate solutions in the analysis. For the steady-state operation the TMM will be suitable for the studies of gain, saturation and noise characteristics. In this section we apply the TMM to analyze the longitudinal traveling fields in SOAs. To start off, a simple gain and carrier recombination model is included in the TMM which could be extended and adapted to a more special gain model, e.g. for quantum dots.

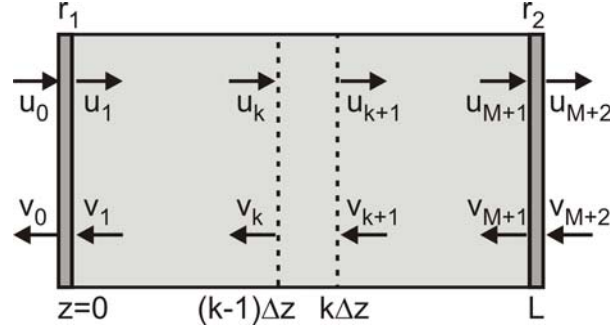


Fig. 2.12: Schematic illustration of the TMM: one dimensional cavity with reflectivities $R = rr^*$ and a non-uniform gain profile along z -direction.

We describe the SOA as a one-dimensional cavity with an effective index n_{eff} and length L . The cavity, build by two reflectivities $R_{1,2} = r_{1,2}r_{1,2}^*$, is divided into M sections with length Δz each. An electric field u and v is traveling in the $+z$ - and $-z$ -direction, respectively, as depicted in Fig. 2.12. For each subsection k of the device we define accordingly, the material gain coefficient g_m in a linear model or parabolic model [61] (Fig. 2.13a)

$$g_{mk} = A(n_k - n_0) \quad \text{or} \quad g_{mk} = an^2 + bn + c \quad (2.50)$$

With the differential gain coefficient A and constants a , b , and c . The modal gain g for a simple buried heterostructures design is defined as

$$g_k = \Gamma(g_{mk} - \alpha_{ak}) - (1 - \Gamma)\alpha_{ck}, \quad (2.51)$$

and the carrier density n is related to the optical fields and the current density j via the rate equation

$$\frac{j}{ed} = R_k + \frac{\Gamma g_{mk}}{E} \left[|u_{k+1}|^2 + |v_{k+1}|^2 \right] \quad (2.52)$$

with the recombination rate $R_k = A_{nr}n_k + Bn_k^2 + Cn_k^3$ and the photon density $S_k = \left[|u_{k+1}|^2 + |v_{k+1}|^2 \right] \cdot n_{\text{eff}}/cE$. All parameters are listed in Table 2 with values from [94] for a typical buried-heterostructure SOA based on InP at $1.55 \mu\text{m}$. The recombination rate is given with contributions of non-radiative processes such as recombination at defect sites (proportional to n) and Auger recombination involving transfer of the excitation energy to a carrier and relaxation via phonons (proportional to n^3) which is a significant contribution at long wavelengths [95] and the recombination rate has a contribution of a radiative process, so-called bi-molecular recombination (proportional to n^2).

2 Theory

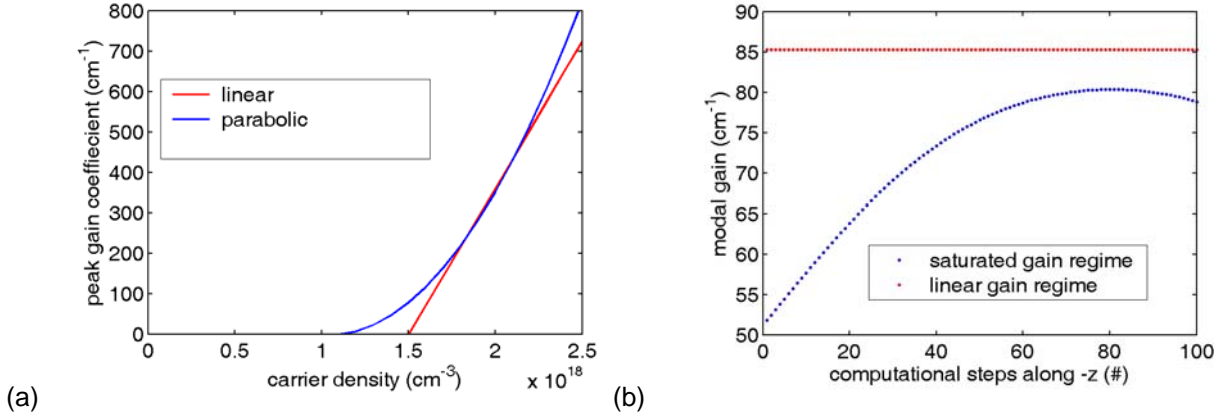


Fig. 2.13: (a) Difference of linear or parabolic gain model for the peak gain coefficient. After [61]. (b) Calculated modal gain along the length of the amplifier (in $-z$ -direction) for linear and saturated gain regime.

The implementation of the TMM is straightforward, e.g. in Matlab [87]. When following these steps the gain vs. output power characteristic of the amplifier is calculated:

- Set an initial value of P_{out} . This determines the output field u_{M+2} by $P_{\text{out}} = |u_{M+2}|^2 Wd$, while we consider no in-going field at $z = L$ and therefore $v_{M+2} = 0$.
- Compute u_{M+1} and v_{M+1} by executing the transfer matrix formalism for the facet reflectivity at $z = L$

$$\begin{bmatrix} u_{M+1} \\ v_{M+1} \end{bmatrix} = \frac{1}{\sqrt{1-r_2^2}} \begin{bmatrix} 1 & r_2 \\ r_2 & 1 \end{bmatrix} \begin{bmatrix} u_{M+2} \\ v_{M+2} \end{bmatrix} \quad (2.53)$$

- Substituting Eqns. (2.50) and (2.51) in (2.52) we get a defining polynomial equation from which we can find the roots for n_k . Now we can calculate the modal gain using Eqns. (2.50) and (2.51). The transfer matrix method computes the fields u_k and v_k from the following equation by using $k = M, \dots, 1$

$$\begin{bmatrix} u_k \\ v_k \end{bmatrix} = \begin{bmatrix} \exp(-g_k \Delta z/2 + i\beta_z \Delta z) & 0 \\ 0 & \exp(g_k \Delta z/2 + i\beta_z \Delta z) \end{bmatrix} \begin{bmatrix} u_{k+1} \\ v_{k+1} \end{bmatrix} \quad (2.54)$$

- Repeat the step (c) until $k = 1$ and u_1 and v_1 are determined. The modal gain g , the carrier density n and the field amplitude u are plotted for each computational step in Fig. 2.13(b) and Fig. 2.14(a) and (b), respectively.
- We account for the facet reflectivity by applying

$$\begin{bmatrix} u_0 \\ v_0 \end{bmatrix} = \frac{1}{\sqrt{1-r_1^2}} \begin{bmatrix} 1 & -r_1 \\ -r_1 & 1 \end{bmatrix} \begin{bmatrix} u_1 \\ v_1 \end{bmatrix} \quad (2.55)$$

to receive u_0 and v_0 . In order to calculate the input power we use $P_{in} = |u_0|^2 Wd$. (From boundary conditions and absence of spontaneous emission we should find $v_0 = 0$.)

(f) The amplifier gain is given by

$$G = \frac{P_{out}}{P_{in}} = \left| \frac{u_{M+2}}{u_0} \right|^2. \quad (2.56)$$

(g) In order to calculate a range of P_{out} repeat the steps (a) to (f). This is shown in Fig. 2.15 as a function of input and output power for different bias currents.

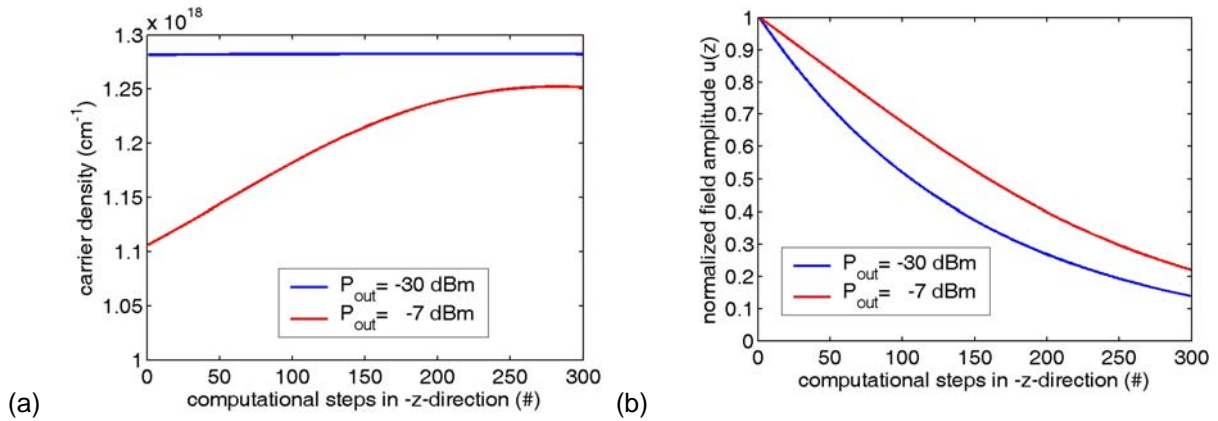


Fig. 2.14: Carrier density (a) and field amplitude $u(z)$ (b) along the length of the amplifier (in $-z$ -direction) for linear and saturated gain regime. (at $I/I_{th} = 0.81$ with $I_{th} = 4.88$ mA).

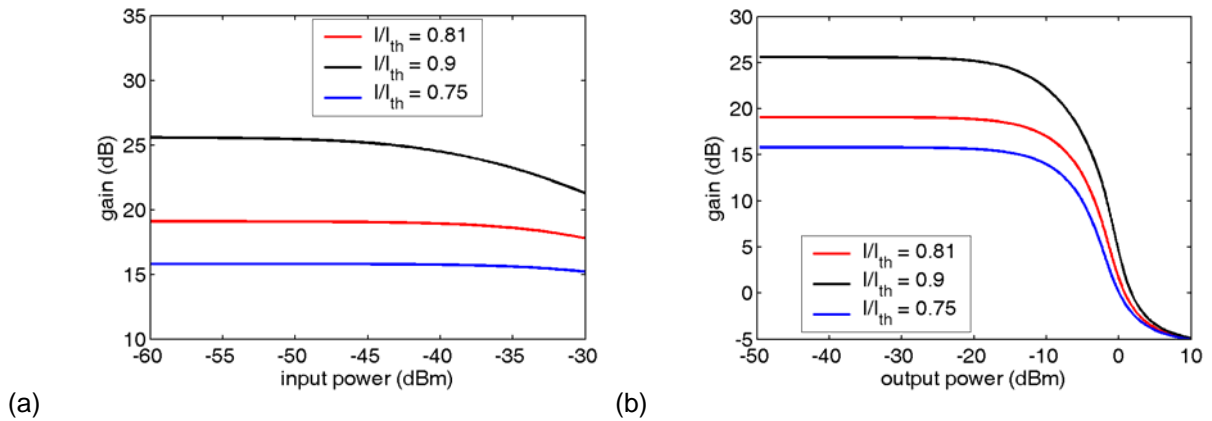


Fig. 2.15: Typical gain dependence plotted as a function of input power (a) and output power (b) for different bias currents calculated with the TMM.

Even if we assume a reduction of the facet reflectivities the amplifier will show an onset of lasing at high current densities. The lasing threshold can be deduced from the lasing condition that the gain equals all losses, or $g - \alpha = 0$. Using Eqns. (2.50) and (2.51) the threshold carrier density is given by

$$n_{th} = n_0 + \frac{\alpha_a}{A} + \frac{1 - \Gamma}{\Gamma A} \alpha_c + \frac{1}{\Gamma A} \frac{1}{2L} \ln \left(\frac{1}{R_1 R_2} \right) \quad (2.57)$$

2 Theory

and the threshold current density is found by eq. (2.52) with the photon density assumed to be zero at the lasing threshold (as no spontaneous emission is included in the model).

In this implementation of the model the computational direction is in the minus z -direction. It is straightforward – by using inverted matrices – to implement the calculation in $+z$ -direction which offers the possibility to start with an input power into the SOA.

The TMM model has several limitations and approximations which are collected here:

- the current density is uniform over z which is only true in the approximation of high serial resistance
- no gain compression from thermal effects and renormalization due to high carrier densities is implemented
- no effect of the carrier density on the refractive index which is valid unless the amplifier is heavily saturated and the carrier density distribution is strongly non-uniform
- no spontaneous emission is considered because its contribution is negligible for gain and saturation characteristics (not for noise) for current densities below the lasing threshold. A detailed formulation of the spontaneous emission with TMM is reported in [96]
- the propagation constant β has no modal dependence
- although the model is kept rather simple, it is very sensitive on the values of the parameters and it is already strongly dependent on the gain model (linear or parabolic) that is used

Table 2: Parameters from [94] used in the showcase modeling presented in this section.

Parameter	Symbol	Value-Unit
Facet reflectivity	R	$3.6 \cdot 10^{-3}$
Differential gain coefficient	A	$4.63 \cdot 10^{-16} \text{ cm}^2$
Transparency carrier density	n_0	$8.31 \cdot 10^{-17} \text{ cm}^{-3}$
Confinement factor	Γ	0.5
Loss in active waveguide region	α_a	25 cm^{-1}
Loss in cladding region	α_c	50 cm^{-1}
Thickness of active region	d	$0.2 \cdot 10^{-4} \text{ cm}$
Width of active region	W	$1.5 \cdot 10^{-4} \text{ cm}$
Length of active region	L	$500 \cdot 10^{-4} \text{ cm}$
Non-radiative recombination coefficient	A_{nr}	10^{-8} s^{-1}
Radiative recombination coefficient	B	$10^{-10} \text{ cm}^3 \text{ s}^{-1}$
Auger recombination coefficient	C	$7.5 \cdot 10^{-29} \text{ cm}^6 \text{ s}^{-1}$
Effective refractive index	n_{eff}	3.5
Photon energy	$E = hc/\lambda$	$1.28 \cdot 10^{-19} \text{ J}$
Wavelength	λ	$1.55 \cdot 10^{-6} \text{ m}$
Propagation constant	$\beta_z = 2\pi n_{eff}/\lambda$	$0.142 \cdot 10^6 \text{ cm}^{-1}$

The way the TMM was described here, it does not work for QDs. The model for material and modal gain must be adapted, and the simple model with the recombination rate (with non- and radiative processes and Auger recombination) is not sufficient to describe the interdependency of barrier, WL, ES and GS of a QD gain medium.

Here we have used the TMM only to describe the general dependency of amplifier characteristics like carrier density, modal gain and field amplitude on the z-position along the length of the device. It was shown that in the linear regime modal gain and carrier density are constant while the field amplitude is small at the input and large at the output of the SOA as it is expected for the exponentially amplified signal power in the device. The saturated regime displays a strong decrease of the modal gain and the carrier density with increasing propagation through the amplifier which is also expected due to the increased carrier recombination at larger powers and the direct dependency of the modal gain on carrier density as assumed in this model. Using the complete TMM we were able to simulate the typical gain saturation for large input powers as it is depicted in Fig. 2.15. As the input power and consequently also the output power is increased, the gain starts to saturate and eventually the amplifier is forced towards transparency where the gain is completely depleted and the net “gain” is completely determined by the total waveguide loss.

In order to apply this model to simulate QD amplifiers and explain and predict their behavior considerable effort would have to be made and all approximations implicit in the model, e.g. a constant current along the device, have to be checked whether they are still valid. The next section introduces the modeling of QD SOAs as it is done with extensive manpower by other groups.

The transfer matrix method was applied to study the propagation of an optical field through an amplifier. In this modeling the general gain and saturation behavior of a SOA was illustrated to understand the propagation dependent mechanisms of the carrier density and the modal gain along the device.

2.3.4 Modeling of quantum dot semiconductor optical amplifiers

To model QD based SOAs it is necessary to develop a detailed theoretical understanding of the QD properties. The modeling can start off with available information like material, size and shape of the QDs. The shape of QDs is often either lens shape or truncated pyramid like. The modeling of the individual QD wavefunction, eigenenergy, strain and piezo-electric fields can be done with numerical methods with a large level of physical detail. Very successfully the 8-band k-p method has been applied to calculate the atomlike state spectrum of QDs and the influence of shape, strain and piezo-electric fields on electronic and optical properties of QDs [75, 97-99].

It is possible to compute the single- and multi-particle states, oscillation strength and polarization of optical transitions. These simulations help for instance to simulate numerically the polarization properties of a combined ridge waveguide with the active gain medium, namely quantum dots. For each part of the problem several different approaches are known. The polarization properties of a ridge waveguide are often tackled with a mode solver for the cross section of the device and a beam propagation method to describe the propagation of the mode(s) through the waveguide. The polarization properties of the gain medium are mainly determined by the recombination probabilities of the involved excitons and their fraction of HH- and LH-contribution. This can be computed by detailed k-p-calculations as it was

2 Theory

described in section 2.2.6. On the whole we seek for a numerical solution which combines the various effects on the polarization of the amplified light from the waveguide and the gain medium. Ideally we would like to have a tool that predicts

- the TE/TM polarization fraction of the light output from the complete device or
- the polarization dependent gain of the SOA subject to ridge waveguide dimensions and composition as well as QD parameters like stacking distance, strain, Indium content and the like.

Such a complete simulation tool is not available to date and could not be developed in the framework of this project.

A reduction of the complexity in modeling of the QD gain medium can be achieved by the use of phenomenological key parameters like single dot gain, volume, confinement energy, and capture times, averaged over the QD ensemble. For such a modeling of QD devices a rate equation approach is widely used ranging from rather simple models to more complex models [59, 86, 100-105]. Alternatively, the master equation approach [22, 106, 107] or the use of Bloch equations [108] can be applied. These models are able to include the position dependence within the device with a stepwise calculation similar to the TMM approach introduced in section 2.3.3.

Theoretically many device properties have been predicted that fuel the interest in QD SOAs and promise excellent performance of these amplifiers. Some of these theoretical findings are reviewed here without intending to be exhaustive.

Full scale modeling of the QD gain and an implementation of this active medium in SOAs considering ASE, cw and dynamic processes with a multi population rate equation model is presented in detail in the thesis of Berg [59]. A comprehensive paper of Sugawara et al. develops and displays a theory of optical signal amplification and processing by QD SOAs [104]. The linear optical response as well as the incoherent and coherent nonlinear response of the devices with arbitrary spectral and spatial distribution of quantum dots in the active region are calculated. The incoherent nonlinear response is due to the incoherent spectral hole burning and the reduction in the carrier density by the stimulated emission, while the coherent nonlinearity is due to the dynamic spectral hole burning caused by the population beating at the electronic states resonant to the multimode light and the carrier density pulsation caused by the carrier relaxation dynamics. From the QD SOAs low power consumption, high saturation power, broad gain bandwidth, and pattern-effect-free operation under gain saturation is expected. Pattern-effect-free wavelength conversion by XGM with low frequency chirping and symmetric highly-efficient 1 to 2 THz wavelength conversion by the non-degenerate FWM is predicted for signal processing devices which realize high speed of 40 to 160 Gb/s. For the high-speed optical signal processing the nonlinear optical response due to the spectral hole burning has the main effect on the amplifier performance. The findings of this paper are supported by various results that have been published before and after it.

The ultrafast gain recovery of QDs is explained by a comprehensive numerical model where the QD excited state carriers are found to act as a reservoir for the optically active ground state carriers resulting in an ultrafast gain recovery as long as the excited state is well populated. But modulation limitations in the self-assembled quantum-dot devices when pulses are injected into the device at high-repetition frequencies are predicted because the response of the QD amplifiers is found to be limited by the wetting-layer dynamics [45]. The interplay of the carrier reservoir for the QDs and the fast carrier relaxation gives rise for different unique properties of the quantum dot based SOAs compared with conventional devices based

on bulk or quantum well material. QD devices may be operated in regimes of high linearity, i.e. with a high saturation power, but can also show strong and fast nonlinearities by breaking the equilibrium between discrete dot states and the continuum of wetting layer states [109]. The gain saturation due to carrier depletion can be eliminated by increasing the SOA pump current density. At high pump currents, gain saturation in QD SOAs is then due to spectral hole burning. As a result, the saturation power for cw amplification can be enhanced by two orders in magnitude in QD SOAs [53].

Qasaimeh describes wavelength conversion based on four-wave mixing and cross gain conversion in quantum dot semiconductor optical amplifiers. The model takes into account the effect of the multidiscrete QD energy levels and the wetting layer. The high FWM conversion efficiencies at high detuning frequency are attributed to the discreteness of the energy levels, where carrier escape from the ground state significantly affects the performance of the amplifier. The small-signal cross gain conversion efficiency shows strong dependence on the escape and relaxation lifetimes between the ground and excited states [110, 111]. Uskov et al. model QD SOAs which allow for high-speed cross-gain modulation without pattern effects. This is attributed to instantaneous gain modulation by change of the photon density which is possible due to the spectral hole burning effects in the regime with maximum linear gain. The maximum bit-rate at modulation bit-rates much higher than the interband relaxation rate for this pattern-effect free XGM grows with increasing pump current density of the QD SOA [37]. Bilenca and Eisenstein describe the XGM via the noise properties of linear and nonlinear QD amplifiers by considering the impact of the inhomogeneously broadened gain and the fast carrier dynamics under a saturating signal. The optical noise spectrum at the amplifier output comprises broad-band ASE which in saturation contains an added spectral hole due to a nonlinear noise-signal interaction. This spectral hole stems from saturation of the inhomogeneously broadened gain and the narrower portion is due to a distributed nonlinear interaction between the saturating signal propagating down the amplifier axis and the amplifier noise. The most important characteristics of the optical and electrical noise spectra are determined by the degree of inhomogeneous broadening and by the fast carrier dynamics of QD amplifiers. The fast dynamics causes a very wide noise spectral hole which has important potential consequences for all optical signal processing [112].

40-Gbit/s dynamic performance of QD amplifiers was calculated and compared with bulk SOAs. The results demonstrate that quantum dot SOAs can process multiple-wavelength high bit-rate optical pulse trains over 40 Gbit/s under gain saturation. Functions like regeneration, reshaping, multiple-wavelength processing, wavelength conversion, and demultiplexing of high-bit-rate patterned optical signals, which meet with the demand of next-generation broadband all-optical photonic networks are promised [113]. With interferometers containing quantum dot SOAs ultrafast cross phase modulation and digital signal processing with low dependence on the specific random data pattern is possible [114]. Furthermore, high-bit-rate signal processing up to 160 Gb/s and a new scheme of 3R regenerator are envisioned based on the spectral hole burning properties of the inhomogeneously broadened QD ensemble and its unique gain saturation character. The theory includes spatial isolation of quantum dots, carrier relaxation and excitation among the discrete energy states and the wetting layer, grouping of dots by their optical resonant frequency under the inhomogeneous broadening, and the homogeneous broadening of the single-dot gain, which are all essential to the amplifier performance. Switching functions can be realized by the cross gain modulation between two wavelength channels when the channel separation is within the homogeneous broadening, allowing the possible application of a quantum dot based 3R (re-amplification, re-shaping, re-timing) regenerator [115].

2 Theory

It is beyond the scope of this thesis to implement a full scale modeling of QD SOAs. This last part of the theory chapter has given a review on available models for QD amplifiers and has subsumed important results that predict excellent performance of QD based SOAs in comparison to conventional SOAs.

3 Processing and Fabrication

3.1 Growth of quantum dots

The idea and advantages of using QDs as an active medium have been described in the introduction and section 2.1. The growth of quantum dots is a broad field [23] and will be only briefly summarized in this thesis. In general we would like to make use of QDs as a gain medium for SOAs in order to achieve an emission wavelength of 1.3 μm based on a GaAs substrate, realize a moderate gain comparable to QW devices, attain a broad wavelength bandwidth and improve the dynamic properties of SOAs.

For the growth of semiconductor material in general, several growth techniques exist. Most commonly the structures are grown by molecular beam epitaxy (MBE) [116] and metal organic chemical vapor deposition (MOCVD) [117, 118]. Using MOCVD, established as commercial large-scale fabrication technology for electronic and optoelectronic semiconductor devices in Europe, very high deposition rates can be achieved, and since no UHV is needed like in MBE a larger throughput is yielded. But MOCVD growth is rather difficult to control as the reactants are supplied as organic or hydride precursors that are thermally cracked by the heated substrate susceptor making the fraction of reactants in the gas phase a function of temperature. The choice of precursor molecules, total pressure and total gas flow are additional parameters that have to be controlled in contrast to MBE. In MBE, growth conditions can very accurately be defined, controlled, and monitored. The reactants can be supplied in elemental form by molecular beams that are directed perpendicularly onto a heated substrate placed in a UHV chamber. The growth process is controlled by substrate temperature and molecular flows only. In-situ monitoring of the growth is available with reflection high-energy electron diffraction (RHEED). Although QD self-organization has been investigated using both, MOCVD and MBE, the samples used for measurements in this thesis were grown by MBE as they were the only available samples with emission wavelength in the 1.26 – 1.31 μm regime.

The methods to fabricate nanostructures with size dimensions below the DeBroglie wavelength and to achieve an electronic confinement in three dimensions can be divided into three categories [20].

1) The inclusion of nano-sized semiconductor material (often CdS and CdSe) in a glass matrix leads to a quantum dot material class that is frequently used for color filters⁸. The QDs in a glass matrix are usually surrounded by an isolating material, therefore, these QDs can not be deployed easily in opto-electronic functions. They are sometimes used to characterize the properties of single dots.

2) Lithography, substrate patterning and etching techniques build the second category which allow to tailor the shape and size of QDs with the help of e-beam lithography [119]. Although the idea of having full control on the formation of the nanostructures is intriguing and highly desirable for many applications the etching processes often cause roughness and damage to the crystalline structure of the QD semiconductor material. This fact and also the difficulties in having a large scale production of these kind of QDs on a full wafer by the use of e-beam lithography have narrowed down the use of this tailor-made QDs.

3) So-called self-assembled or self-organized QDs have proven to be the most versatile and reliably grown nanostructures used for opto-electronic devices. Island like growth is distinguished by the associated surface strain energies into Frank-van-der-Merve growth

⁸ One of the earliest applications of nanotechnology (without people actually knowing it was nanotechnology), was the use of nanoparticles in red church windows.

3 Processing and Fabrication

(layer by layer), Stranski-Krastanow growth (layer and island) and Vollmer-Weber growth (3D islands). In the Stranski-Krastanow growth mode a semiconductor material with a lattice mismatch to the substrate is deposited on it. First one or more complete monolayers grow, and then three-dimensional islands start to organize (often in connection with a growth interruption). The deposited film can not grow further than a couple of monolayers epitactically due to the lattice mismatch to the substrate, a different symmetry or different orientation of the substrate and the film. If the elastic deformation energy is larger than the adhesion forces of the deposited material the growth changes from layers to islands.

Stranski-Krastanow grown QDs are prevalent in the category of self-organized QDs for optoelectronic devices, such as lasers and SOAs. As described before the QDs grown in this mode have a thin film beneath them. Depending on the thickness of this layer it is referred to as wetting layer or quantum well. In the latter case the dots are embedded in a QW and the structures are named dots-in-a-well or DWELL structure. After the formation of the dots they are usually overgrown with a high bandgap material that acts as a barrier (often the substrate material is used) or by another QW that is meant to shift the emission of the dots. Then further layers of QDs can be grown on top of the buried QD layer.

Self-organized QDs offer several advantages, e.g.

- a large number of QDs is created in one step without lithography
- QDs can be covered epitactically by the host material without interface defects
- their size can be controlled by controlling the amount of deposited material
- the emission wavelength depends on the size of the dots and can be controlled to a certain extent for the same material system
- techniques of doping, energy band modification from planar layer growth can in principle be applied to QD growth.

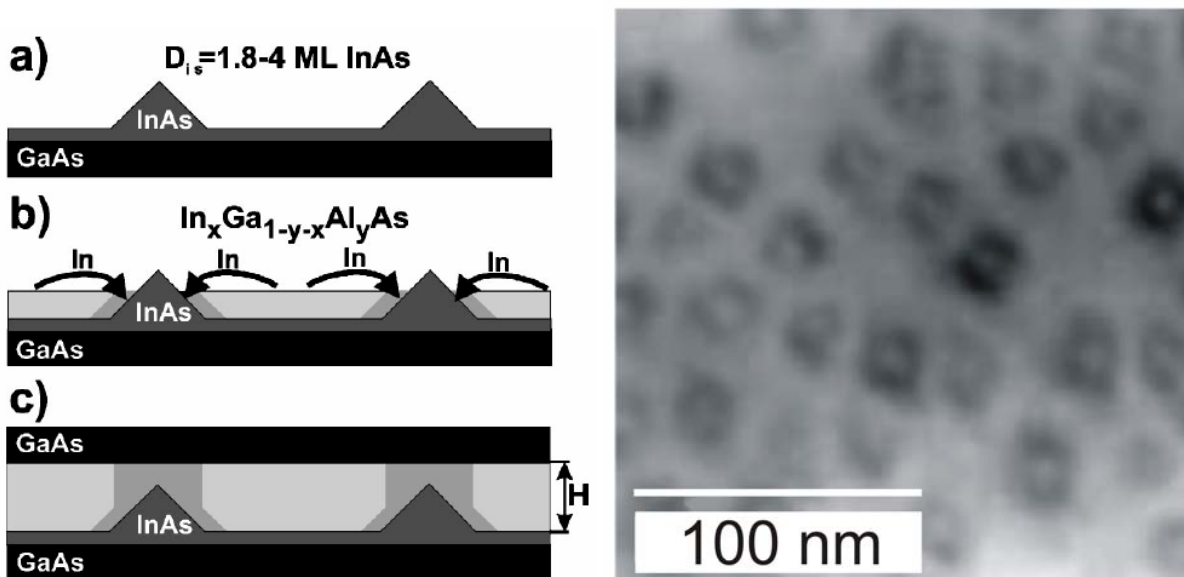


Fig. 3.1: (left) Schematic diagram of activated alloy phase separation for QDs in a dot-in-well (DWELL) scheme. (a) After an initial deposition of InAs quantum dots are formed, (b) the alloy layer decomposes partially due to strain-driven surface migration of indium, thereby enriching the QDs with In and causing a wavelength red shift and (c) the final structure of one QD layer after GaAs capping. Courtesy of M. Maximov [120].

(right) Plan-view TEM (transmission electron microscopy) image of single layer of QDs formed by 2.5 monolayers InAs deposition followed by overgrowth with a 5 nm thick $\text{In}_{0.15}\text{Ga}_{0.85}\text{As}$ layer prior to GaAs deposition. From [19].

MOCVD grown InAs QDs in a GaAs matrix emit at a wavelength of 1.1 μm at room temperature [121-123]. There has been continuous effort to extend the emission wavelength over the last years. The concept of overgrowth with an InGaAs quantum well and subsequent decomposition of the QW lead to devices with emission wavelength between 1250 and 1300 nm [19, 124-143]. For applications in the telecommunication O-band emission wavelengths in the range of 1260 to 1360 nm would be desirable. This would also facilitate the investigation of the QDs as gain medium in a SOA because standard measurement equipment (tunable laser, amplifier, photodetector, power meter, spectrum analyzer) is available in this wavelength regime.

The main samples used in this thesis were grown by MBE at the company NL Nanosemiconductor, Dortmund. Fig. 3.1 shows their schematic DWELL structure and a transmission electron micrograph of one sample that was grown with identical parameters as the samples utilized.

Detailed description of the QD growth of the investigated samples

QDs were grown by MBE on a GaAs substrate using the material combination InAs/InGaAs. Plain InAs QDs formed by deposition of 2.5-3 monolayers (ML) of InAs usually emit at about 1.2 μm . To extend the emission wavelength into the infrared to 1.3 μm the QDs can be covered by an InGaAs layer. By this means the bandgap of the surrounding material decreases, the strain of the QDs is reduced, In out-diffusion from the QDs is inhibited, and most significantly a phase separation in the cover layer lead to a shift of the emission spectrum. The latter effect, the activated alloy phase separation (Fig. 3.1 left), stems from the nucleation of InAs molecules at the elastically relaxed island as this is energetically favorable. This leads to an increase of the volume of the islands and thereby to the red shift.

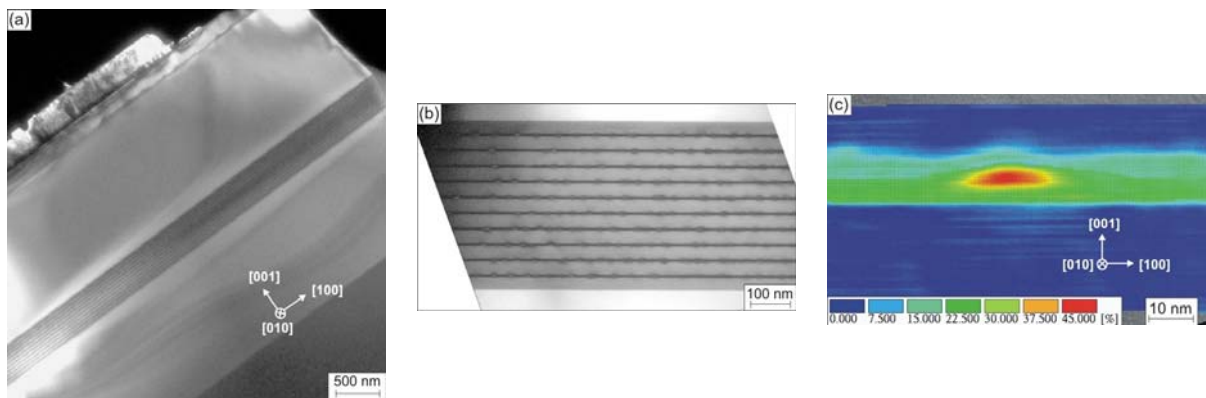


Fig. 3.2: TEM images of cross-section of sample DO520: (a) and (b) 002 dark-field, (c) typical CELFA (Composition Evaluation by Lattice Fringe Analysis) color-coded map of In concentration. The measured maximal In concentration in the island is not true because with CELFA evaluation the In concentration is averaged through the thickness of the TEM sample. But from the map the island shape and size, and the true In concentration in the wetting layer can be seen. Courtesy of D. Litvinov, University Karlsruhe.

The conditions of growth like temperature, rate, V-III ratio, thicknesses and In content in the InGaAs layer must be carefully optimized [19, 120]. The QDs were directly grown on the GaAs matrix at 485 $^{\circ}\text{C}$ by depositing 2.5 monolayers of InAs at a growth rate of 0.083 monolayers/s. The QDs were covered with a 5 nm thick $\text{In}_{0.15}\text{Ga}_{0.85}\text{As}$ layer. This resulted in a peak emission of the QDs at 1.28 μm and a surface density of the dots of $3\text{-}5 \cdot 10^{10} \text{ cm}^{-2}$ (Fig. 3.1 right). Cross section transmission electron microscopy (TEM) images

3 Processing and Fabrication

of the sample DO520 are presented in Fig. 3.2 showing the active quantum dot layers between the AlGaAs-claddings (a), the 10 QD stacks including their wetting layer (b), and an image of a quantum dot which was enhanced by image evaluation to show its composition contrasts (c).

3.2 Epitaxial structure of QD SOAs

The SOAs in this work all have an epitaxial structure that is similar to a laser structure with a separate optical confinement (SC) double heterostructure (DHS).

The samples are grown by solid source MBE in a Riber 32P machine on n-doped GaAs (100) substrates. After oxide desorption, a 300 nm GaAs buffer layer at 600 °C for surface smoothness is grown. Then a 15 nm Al-content-graded layer is prepared in front of the Si-doped 1.5 μm thick lower cladding layer with Al_{0.35}Ga_{0.65}As. Subsequently, the substrate temperature is lowered to ~480 °C for deposition of the active QD layers. The core waveguide consists of 10 or 15 QD layers as described in the previous section with 33 nm GaAs spacer layers. The upper cladding, again grown at 600 °C, is a C-doped 1.5 μm Al_{0.35}Ga_{0.65}As layer that is terminated with a 15 nm thick graded layer and a 200 nm thick p-doped GaAs contact layer. The complete structure is depicted schematically in Fig. 3.3.

The Al content of the cladding layers was 35 % to achieve a broadening of the photonic mode and a better overlap with the outer quantum dot layers. The cladding layer thickness was chosen to be large enough to avoid any leakage of the photonic mode into neighboring GaAs layers.

The samples (designed as laser structure) were p-doped between the quantum dot layers to improve the laser properties like temperature stability of the threshold current and the dynamic characteristics [36].

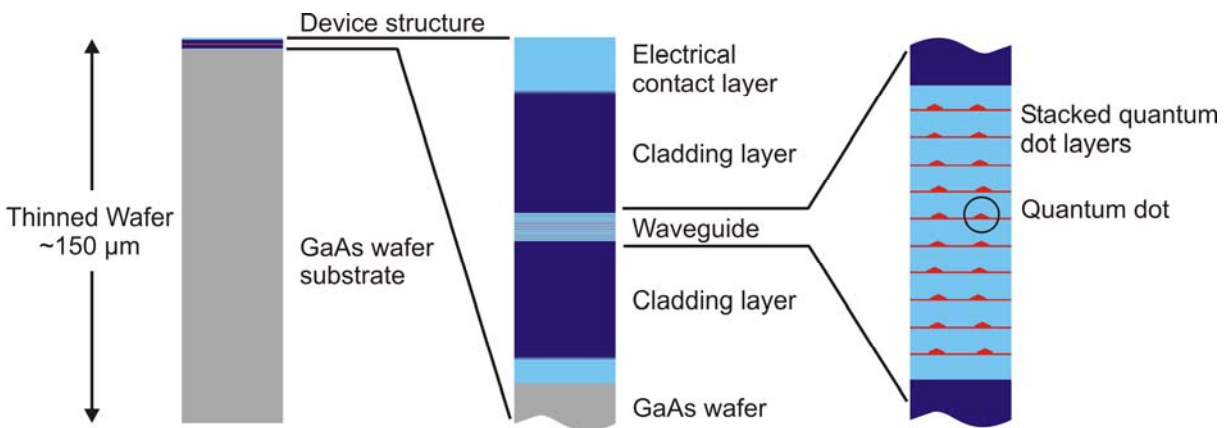


Fig. 3.3: Sketch of the epitaxial structure of a QD SOA. From left to right the layers are expanded to scale of their thickness. Courtesy of M. Kuntz [86].

The thickness of the spacer layer between the QD stacks needs to be optimized. To release the accumulated strain of each QD layer relatively thick spacer layers are required [144, 145], otherwise correlation effects between the QDs of adjacent layers appear (site correlation and anti-correlation, intermixing of electronic levels, change of photoluminescence efficiency etc.) [146-157]. The intermixing of the electronic levels of vertically stacked QDs leads to the formation of minibands (beneficial for carrier transport) and has an influence on the polarization dependence characteristics of the stacked QDs [76, 77] (section 2.2.6).

On the other hand, a large distance reduces the contribution of the outer layers to the modal gain. With a spacer thickness of 33 nm it was possible to stack up to 15 QD layers without

degradation of the optical properties of the waveguide. The QD stacks of the samples investigated in this work are uncoupled.

3.3 Processing of ridge waveguide devices

The devices described here have their application in data transmission in the 1.3 μm optical transmission window of glass fibers. A good coupling of these devices to and from optical fibers is mandatory and also the optical mode has to be guided within the devices for low optical loss and large overlap with the active region. This implies a two-dimensional wave confinement along the device and a single mode operation of this waveguide. Therefore, the SC DHS epitaxial device structure has to be further processed in order to introduce lateral optical confinement and a current supply to the active layer.

There are various concepts for active waveguide devices. Most commonly buried-heterostructure waveguides or ridge waveguides are deployed. The buried-heterostructure concept implies an etch and re-growth step of the epitaxial structure. This process, which is often utilized for InP-based devices, is not available for the usually used $\text{Al}_x\text{Ga}_{1-x}\text{As}$ claddings of GaAs-based heterostructures. This is because of the oxidation of the claddings after etching which inhibits the re- and over-growth. For all devices we have applied the ridge waveguide concept due to its versatility and its relatively simple processing scheme. The ridge waveguide conception (section 2.2.1) can be distinguished in shallow and deeply etched mesa, i.e. stopping the etching in the upper cladding layer or etching through the active layer and the core waveguide, respectively.

For shallow ridge waveguides wet and dry etching can be used for typical etch depths of 1.5 μm resulting in a weak lateral index guiding of the optical mode which is enhanced during device operation by gain guiding. As the optical confinement in the growth direction is stronger these devices exhibit a strong far-field ellipticity and as a consequence large coupling losses to a symmetrical optical fiber (section 4.1.3). An advantage of the weak guiding is the suppression of higher lateral modes [158], but there are also several delicate implications for SOAs. Due to the fraction of gain guiding the ASE of the SOA is guided in a different way than the signal yielding coupling problems, difficulties in determination of coupling losses and the problem that the influence of gain guiding and the suppression of ASE by the signal are not differentiable.

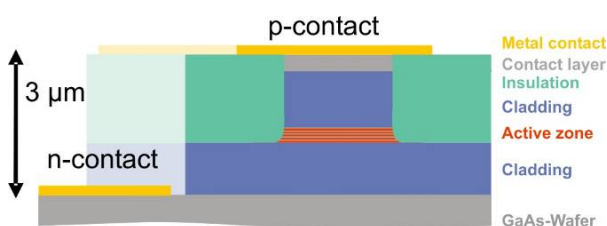


Fig. 3.4: Sketch of a deeply etched ridge waveguide structure with top n-contact.

Deeply etched ridge waveguides are single mode only below a ridge width of 4 μm (for our material combination) and require an etch depth of typically more than 2 μm , therefore, only dry etching can be applied due to their etch isotropy and steep etch profiles as compared to wet etchants. By etching through the active layer a strong index guiding of the optical mode is achieved and additionally a direct fixed current path to the active layer is created. Because of these

advantages the deeply etched ridge waveguide structure has been employed for all devices presented in this thesis.

QD wafer material for 1.3 μm was only limited available. Therefore, the processing was coordinated to the need of realizing different narrow stripe device categories like directly modulated lasers, mode-locked lasers and SOAs in only one processing run. The contact isolation for high speed operation, the contact pad scheme and multisectionability had to be

3 Processing and Fabrication

customized for this need. We have developed a self-aligning processing scheme (Fig. 3.4) employing

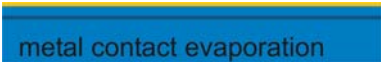
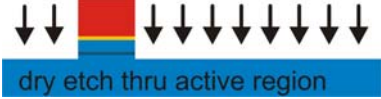
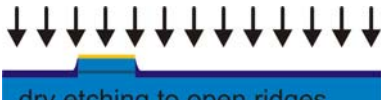
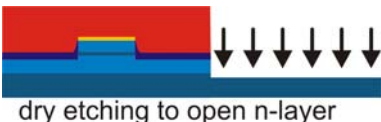
- dry etching the mesa through the pre-metallized wafer (which allows for narrow ridges down to 1 μm width without lithography alignment requirements for the metallization of the ridge),
- etching within the same step through the active layer creating deeply etched strong index guided waveguides and a stringent current path,
- the combination of isolation and planarization of the structure by the use of spin-on-glass or a spin-on polymer to achieve a large capacitance for directly modulated lasers,
- on top lying p- and n-contacts in a ground-signal-ground (GSG) configuration for the ease of contacting with a high-frequency capable probe-head and bar testing or for wire-bonding of individual devices, and
- the option of creating multisection devices from the same mask set by an additional etch step to create trenches along the ridge contacts.

The versatility of this concept allows processing of directly modulated high-speed lasers, multisection mode-locked lasers, SOAs with and without waveguide tilt, and is extendable for multisection SOAs.

The processed samples were the basis for results of our group and of our project partner groups. In addition to results based on QD SOAs, which are subject of this thesis, we have joint publications based on the other samples. We have achieved repetition rates of 5-80 GHz, picosecond pulse generation and the amplification of these ultrafast and -short pulses for QD mode-locked lasers [159-165]. Directly-modulated lasers based on quantum dot material were applied in various experiments showing 10 Gb/s data modulation, 5 and 10 Gb/s data transmission up to elevated temperatures and the influence of feedback sensitivity on relaxation oscillations [166-172]. Additionally, the results on the samples based on the processing described in this section have been collected and presented in a number of review papers [32, 33, 173-177].

The schematic processing steps for a ridge waveguide structure with ground-signal-ground top contacts are depicted in Table 3. A detailed description and evaluation of these processing steps follows in the next section.

Table 3: Schematic processing steps for ridge waveguide structure with top n-contacts

No.	Process description	Mask layout	Cross section of wafer
1	The wafer is grown by MBE as described previously. In general only a part of the wafer is processed. First, the wafer surface is cleaned thoroughly. mask set →		
2	A metal contact is evaporated on top of the wafer to provide a contact to the ridges without the need of mask alignment.		
3	The first lithography step defines the mesa structure for the ridge waveguides.		
4	By dry etching through the metal layer, the top cladding and the core waveguide, the deeply etched ridge waveguide is formed.		
5	An insulation step provides electrical insulation, passivation of the ridge edges and additional planarization of the structure.		
6	Dry etching reduces the overall height of the insulation and uncovers the ridge contacts.		
7	This lithography step is followed by dry etching to open the n-layer and to remove the insulator on that part of the wafer that will be scribed and broken.		
8	Another negative lithography defines the top contacts and the metal is evaporated on the n-layer.		
9	This final negative lithography prepares the bond pads which extend the ridge contacts. Then metal evaporation and sputtering follows.		
10	The completed top structure consists of a deeply etched ridge waveguide with a ground-signal-ground (GSG) contact pad design. Further processing and fabrication steps follow.		

3.3.1 Processing steps evaluation

The following processing steps have evolved over a series of different samples and processing runs. Here, for each step some general considerations are given and competitive techniques are evaluated. In the box the detailed processing parameters and steps are given for the sample DO520 (DO453 is similar in most steps).

(1) Wafer growth and cleaning

The growth of the epitaxial structure is described in chapter 3.2. After growth the wafers are sent to us and processed into ridge waveguide devices. Due to transport, storing and handling some dust and particles as well as some possible oxide layer have to be removed of the wafer surface which is done with a combination of solvents and an acid dip.

Solvent cascade
Acetone (70°C, 5 min.), Isopropanol (5 min.), dry with N₂
HCl dip
HCl:H₂O = 1:4 (stir well), 60 s
H₂O-cascade
1. beaker H₂O dest. (15 s), 2. beaker H₂O dest. (15 s),
3. H₂O-cascade (5 min. or resistivity below 16-18 MΩ), dry with N₂

(2) Metal contact and rapid thermal annealing

First the (part of the) wafer is covered with a metal contact which will serve as a direct contact on the ridge without the need of extensive re-alignment procedures. In general a Schottky-like metal-semiconductor contact is realized which can be converted to an ohmic contact by rapid thermal annealing (RTA) of the contact. The metal evaporation is discussed in more detail in the technical annex 7.6.

Metallization
E-beam: Ti/Pt 30/40 nm, 0.8-1.2/0.8-1.2 Å/s @ ~8x10⁻⁴ mbar
Veeco: Au 200 nm, 2.5-3 Å/s @ 6x10⁻⁶ torr
Liftoff
NMP 70 °C 20 min. (if necessary ultrasonic treatment), Isopropanol 5 min., dry with N₂
RTA
N₂-ofen 390 °C, 3 min.

(3) Mesa lithography

Positive contact lithography defines the mesa for the ridges. Narrow ridge widths from 1 to 4 μm have been realized. The lithography mask needs to have an accuracy that is below 100 nm otherwise these deviations will be translated via lithography and etching into a rough sidewall of the ridge. Depending on the used photoresist different spinning and baking procedures have to be followed before exposure, which have to be optimized for each resist. At the edge of the wafer a “bead” of photoresist builds up during spinning⁹. In order to have a direct contact of the lithography mask and the wafer with photoresist this bead has to be removed. This can be done either carefully by hand using a cotton swab with acetone or by an exposure and

⁹ Happens more pronounced for pieces of wafers than for complete wafers.

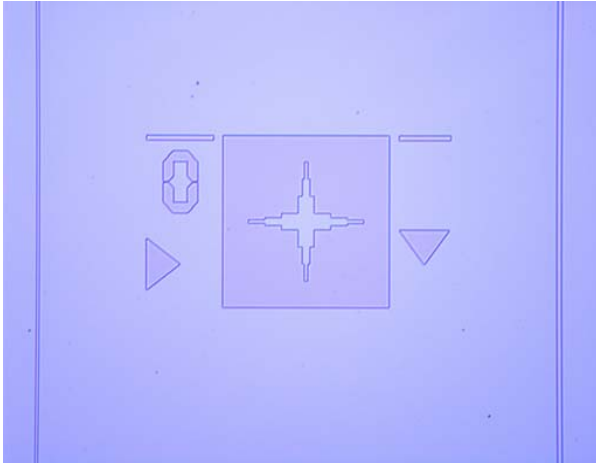


Fig. 3.5: Microscope picture of positive lithography for definition of the ridges with 2 μm (left) and 4 μm (right). In the middle the alignment mark is shown with feature sizes on the order of one micrometer.

development step of the wafer edge while covering the center. After baking the wafer should rest for a couple of minutes to allow the photoresist to resorb water from air humidity. It is exposed with a Süss MA6 mask aligner at 320 nm wavelength and 6 mW/cm² power. Then the resist is developed, possibly baked and cleaned with a soft oxide plasma.

Ridge widths of 1, 1.5, 2, 4, 8 and 10 μm have been successfully fabricated in various process runs. Due to reasons of yield and single mode operation the mask diversity has been reduced to a texture of 2/2 and 4/4 μm double ridges (see Fig. 3.10). Results on the far field characteristics of various ridge widths and etch depths are presented in section 4.1.

Positive lithography AZ701MIR
 HCl dip 120s, solvent cascade, prebake 5 min. 120°, spin MA-P 1250 rpm 30 s, bake 2 min. 100°
 Edge removal: expose 40 s, develop AZ351B:H₂O (1:4) 30 s
 Mesa litho: expose 20 s, develop AZ351B:H₂O (1:4) 45 s, plasma P2 5 min. 150 W
 XP2 profiler: resist height ~1100 nm

(4) Etching of mesa

For the definition of the narrow mesa structures wet and dry etching can be applied. Early samples were wet etched shallowly, i.e. the process was stopped within the upper cladding layer. Depending on the etchant mixture, the process has a more or less pronounced lateral etch component which causes the sidewalls of the mesa to become tilted and rough. Wet etching is difficult and unstable to control for ridge widths below 4 μm and for etch depths larger than 2 μm .

Dry etching provides a powerful tool to achieve vertical and smooth sidewalls with high aspect ratios. Therefore, the processing was adjusted to the use of *chemically assisted ion beam etching* (CAIBE) and *reactive ion etching* (RIE). By this means the self-aligned processing scheme could be implemented as it is possible to etch through the top metal layer with CAIBE. The dry etching process with an Oxford Plasma Ionfab 300 Plus CAIBE system was described in detail in [178]. In principle, accelerated Ar ions provide the mechanical isotropic sputtering part of this etching process and Cl₂ is the chemical component which etches anisotropic and selectively. By adjusting the two components smooth etch profiles with little surface damage and a high semiconductor-photoresist selectivity can be achieved. CAIBE is used to etch the top metallization and the (Al)GaAs semiconductor layers.

The plasma etching system Sentech SI 591 provides a versatile etch process in which argon ions are generated inside the ion source and are accelerated into a broad parallel beam, and to a defined energy, by the extraction grids on the front of the source. If one uses an inert gas such as argon, the process is relatively slow, and the heat that is generated must be removed with care. With a RF ion source gases such as Cl₂, F₂, CF₄, and O₂ are cracked in the ion source and extracted into the ion beam. The process that results is partially chemical, as the ions react with the surface, and partially physical, as the reaction products are sputtered away

3 Processing and Fabrication

by the energy of the ion flux. RIE is used to etch and re-structure dielectric and polymer insulation layers.

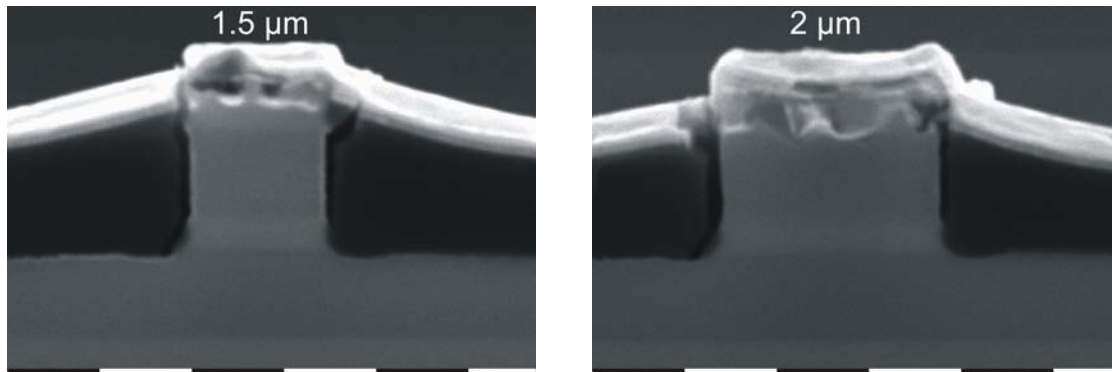


Fig. 3.6: Examples of dry etched laser mesas with 1.5 μm (left) and 2 μm (right) widths – looked at by cross section REM. The mesa is etched through the active layer (slightly lighter part of the ridge) and stopped in the lower cladding. Adjacent to the mesa is the isolation (which has cracked from the mesa due to the high energy electrons from the REM) and on top is the metallization.

With CAIBE the mesa is etched through the metal, the upper cladding, the waveguide with active region into the lower cladding as shown in Fig. 3.6. Etching through the active region without a re-growth step is not feasible for all active media. Due to the localization of the carriers in the quantum dots there is a reduced lateral diffusion length of $L_D \approx 50$ nm, and there are no generated recombination defects at the side walls from through etching. We have compared the performance of shallowly and deeply etched lasers of the same material and found no significant difference in waveguide losses, internal efficiency and threshold current density [86]. As the deeply etched devices provide strong index guiding of the optical mode and efficient suppression of current spreading this device structure was implemented for the SOAs which are presented in this thesis. Strong index guiding combined with the small stripe width yields a low asymmetry of the far-field (down to ellipticity 1.2) which in turn results in a larger coupling efficiency into optical fibers. For the directly modulated lasers, which were also produced in the same process run, suppression of current spreading in the QD layers achieves an improvement of the electrical high-frequency characteristics of laser diodes by reducing parasitic capacitances [166].

CAIBE dry etching	etch through metallization, cladding, active layer, stop in n-cladding
Liftoff processor	processor + NMP ¹⁰ 70° + O ₂ plasma 600W
XP2 Profiler	record the height profile of the mesa

(5) Insulation and planarization

In order to electrically insulate the side wall of the mesa and the bottom of the etched wafer from the top contact an insulation needs to be applied. The simplest solution would be a thin (100-300 nm) dielectric layer such as SiO₂ or Si₃N_x sputtered onto the structure. But as the samples are deeply etched, it is necessary to planarize the mesa structure before depositing the top contact pads. Due to the steep sidewall achieved by dry etching the contact pad would have no electrical contact between the top of the ridge and the lower side part of the structure. There are two material classes available that provide electric insulation, planarization properties, and the ease of applying the material by a spin on process. We have investigated

¹⁰ N-Methyl-2-pyrrolidone (NMP) is a good solvent and is used to dissolve polymers of the photo resist.

the properties of spin-on-glass (SOG) which is a dielectric material that is applied in liquid form. The film fills narrow spaces and planarizes the surface. The SOG from Honeywell Electronic Materials showed good planarization and adhesion to the wafer. By varying the spinning parameters the thickness could be controlled and curing (at 425 °C for 60 min.) of the material resulted in a stable dielectric SiO₂-like layer. Yet, in the further processing steps various problems arose. Due to the large aspect ratio of the ridges the covering height on ridges of different widths were varying to a large degree (making the back-etching difficult to control), the films exhibited large stress (see Fig. 3.6 were the SOG cracked from the ridge side walls due to charging from the scanning electron microscope (SEM) electron beam), the SOG layers showed non-uniform etching behavior (both with wet and dry etching), the SOG shrank during curing leaving a gap between the SOG and the mesa, and in further lithography steps the resist did adhere badly to the material.

We then changed the process to use a polymer (Benzocyclobutene (BCB), Cyclotene 3022-46 by Dow Chemicals). This material provides also an insulating layer and planarizes structures with feature heights larger than micrometers. It also acts as a low refractive index material (n=1.54) to provide the lateral index step to the ridge waveguide. Although BCB has certain drawbacks (ball-bonding on contacts lying on BCB is difficult without having the contact additionally plated), it showed an overall better performance than SOG.

BCB spin 1500 rpm, pre-bake 100 °C 2 min., cure 250 °C 60 min. in inert gas box oven

(6) Back structuring of insulation on the mesa

The planarization step covers the whole structure. The ridges have to be uncovered to access the contacts. Through the spin-on process the BCB is thinner on top of the ridges than adjacent of them. Therefore, the ridges are uncovered by etching the complete wafer with RIE (see (4)) until the ridges are free from BCB. This is ensured by measuring the ridge conductance along the structure with a needle probe.

RIE dry etching	etch structure to open ridges, 50 W 30 Pa 8 min.
Ridge contact	conductance measured with needle probes

(7) Uncovering the n-substrate

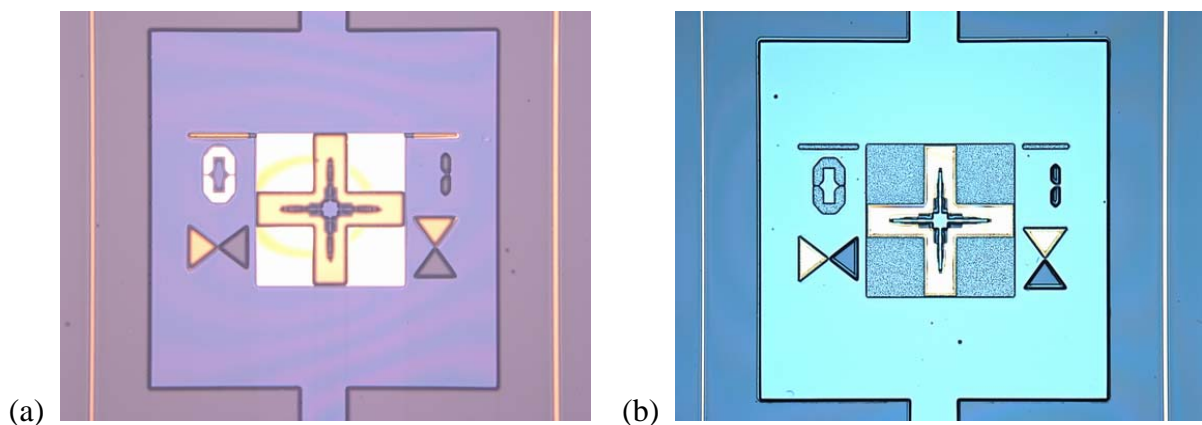


Fig. 3.7: (a) Microscope picture of ridges (2/4 μm) and alignment mark. The darker blue structure around the ridges is the isolation (BCB) which is removed in the center part (lighter blue) and on the ridges. (b) Microscope picture of top structure with alignment mark where the n-substrate (green) has been uncovered by etching through the isolation (blue) and the n-cladding.

3 Processing and Fabrication

The contacts of the device are designed in a GSG-configuration. For the n-contact a region between the mesas has to be opened and the BCB insulation has to be removed. Additionally, in this step the insulator on that part of the wafer that will be scribed and broken is removed. A lithography step defines the regions that are to be opened and the BCB is etched with RIE (Fig. 3.7a). The same lithography is repeated before the semiconductor is etched by CAIBE through the cladding into the n-substrate on which the n-contact will be placed (Fig. 3.7b).

Negative lithography MaN440 Spin MA-N 3000 rpm 30 s, bake 5 min. 90°, expose 8s, develop MaD532 45s, plasma P2 5min. 150W RIE dry etching etch structure to remove BCB, 50 W 30 Pa 24 min. Negative lithography MaN440 Spin MA-N 3000 rpm 30 s, bake 5 min. 90°, expose 8s, develop MaD532 45s, plasma P2 5min. 150W CAIBE dry etching etch semiconductor into substrate, 21 min., nom. 2 μm Removal of resist residue flood exposure 3 min., develop MaD532 5 min., NMP 5 min., Isopropanol 5 min.
--

(8) Definition of top n-contact

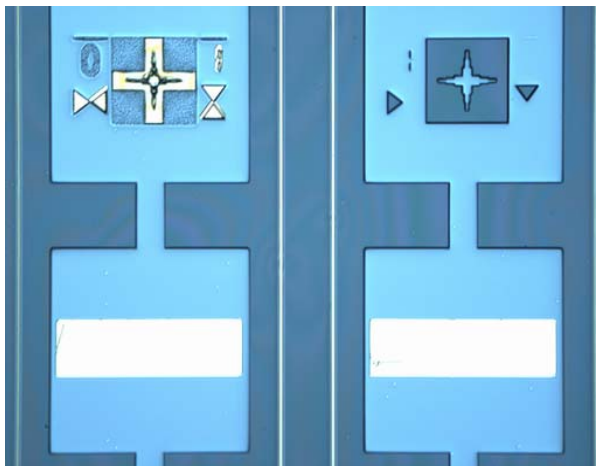


Fig. 3.8: Microscope picture showing part of the processed top structure with two alignment markers and two metal n-contacts (white) which have been evaporated on the substrate (blue-green) in between the double ridge structure (white stripes) and the isolation (blue).

Topside n-contacts (Fig. 3.8) offer the possibility to contact the devices via high-frequency capable probe-head which also makes fast bar-testing feasible. These n-contacts can be alternatively contacted with wire-bonding. It is also possible to use the backside n-contact (see step (10)) of the devices. The contacts are evaporated onto the opened substrate after a lithography has defined the contact area and the oxide layer was removed with an etch treatment. For the contact a metal combination is used that acts as adhesive layer to the semiconductor, bonding between the primer and the top layer, and as accessible contact for bonding, respectively.

Negative lithography MaN440 Spin MA-N 3000 rpm 30 s, bake 5 min. 90°, expose 8s, develop MaD532 60s, plasma P2 5min. 150W HCl dip remove oxide, HCl:H ₂ O = 1:4 (stir well), 60 s, H ₂ O-cascade Metallization Veeco: Ni/Au:Ge/Au 8/80/200 nm, 1-3 Å/s @ 6x10 ⁻⁶ torr Liftoff NMP 70 °C 10 min. (if necessary ultrasonic treatment), Isopropanol 5 min., dry with N ₂
--

(9) Definition of p-contact

The contact layer should provide a good electrical and physical contact to the layer beneath, i.e. an ohmic contact of low resistivity and a stable cohesive power for ultrasonic bonding with a wire bonder. For directly modulated lasers, the pad size should be as small as possible and neighboring pads should be spaced as far apart as possible in order to introduce no parasitic limitation on the device. Modeling of parasitic influences of the contact metallization showed that a bond pad size of $200 \times 100 \mu\text{m}$ is both suitable for bonding and for high frequency modulation up to 10 GHz [86]. Fig. 3.9 shows a microscopic view of GSG-contact structure with p-contact pads and top-side n-contacts. The pitch between the p- and n-contact pads is $250 \mu\text{m}$.

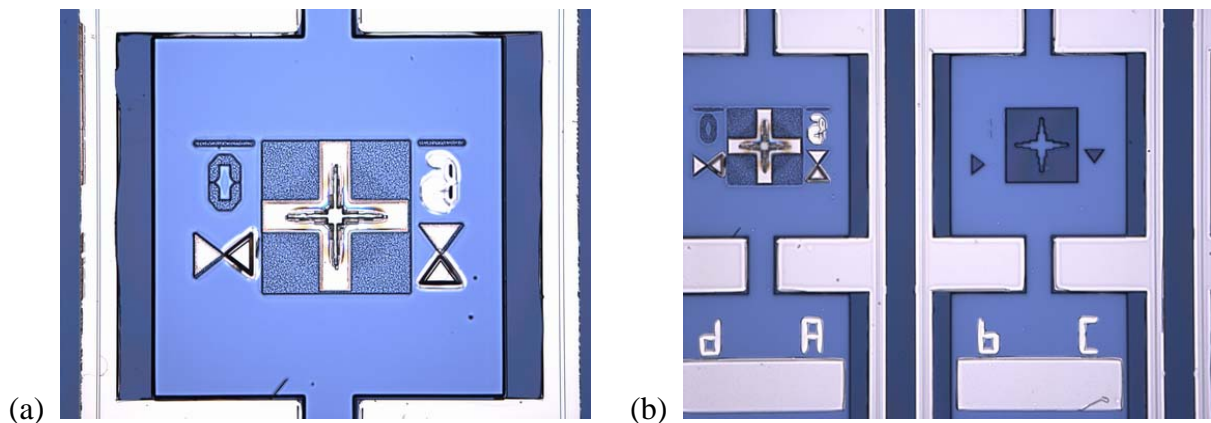


Fig. 3.9: (a) Microscope picture of ridges ($2/4 \mu\text{m}$) with top metallization (white) and alignment mark after the top structure is finished. (b) Larger view of the structure in (a) showing part of the processed top structure with two alignment markers and two metal n-contacts (white) which have been evaporated on the substrate (blue) in between the double ridge structure with top metallization and bond pads (white) and the isolation (dark blue). The mesas run vertically, with twin mesas of $4/4$ and $2/2 \mu\text{m}$ width, coded with A/b and C/d.

2x
Negative lithography MaN440
Spin MA-N 3000 rpm 30 s, bake 5 min. 90° , expose 8s, develop MaD532 60s, plasma P2 5min. 150W
HCl dip
remove oxide, HCl:H ₂ O = 1:4 (stir well), 60 s, H ₂ O-cascade
Metallization
1. run: Veeco: Cr/Au 20/350 nm, 1-3 Å/s @ 6×10^{-6} torr 2. run: Sputtering: Ti/Au 10/200 nm
Liftoff
NMP 70°C 20 min. (if necessary ultrasonic treatment), Isopropanol 5 min., dry with N ₂

3 Processing and Fabrication

(9a) Gap etching for multi-contact structure

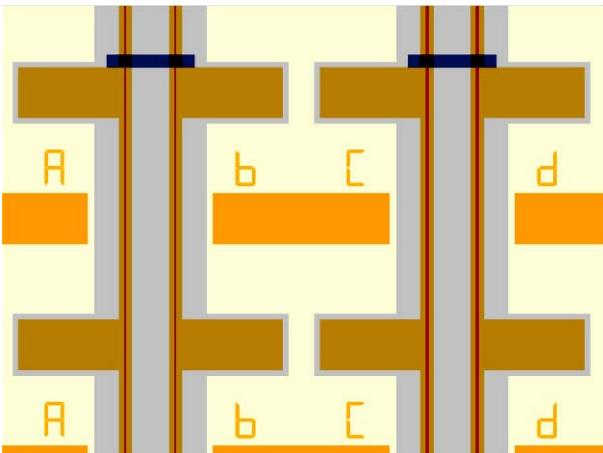


Fig. 3.10: Schematic mask picture showing the mesa (red) (2/2 and 4/4 μm), insulation layer (grey), n-contact (orange) and the p-contact (brown). In order to create multisection devices a gap (blue) can be etched to separate the contacts.

Fig. 3.10 shows the complete mask set including the gap definition for a multi-sectional contact scheme. This was applied for mode-locked lasers with a gain and absorber section. It can be also used for multi-section amplifiers. Separate sections of 1 mm length can be biased individually. Depending on at which length the devices are cleaved the minimum possible length of the absorber and gain section is 100 and 500 μm , respectively. Insulation between the sections was achieved by removal of the metallization and the p-GaAs contact layer by dry etching. Quantum dot based mode-locked lasers produced by this method have achieved repetition rates of 5-80 GHz, picosecond pulse generation, and the amplification of these ultrafast and -short pulses was demonstrated [159-165].

Negative lithography MaN440

Spin MA-N 3000 rpm 30 s, bake 5 min. 90°, expose 8s, develop MaD532 45s, plasma P2 5min. 150W CAIBE dry etching

etch through Au contact and GaAs contact layer into p-cladding

(10) Completed top structure and further processing steps

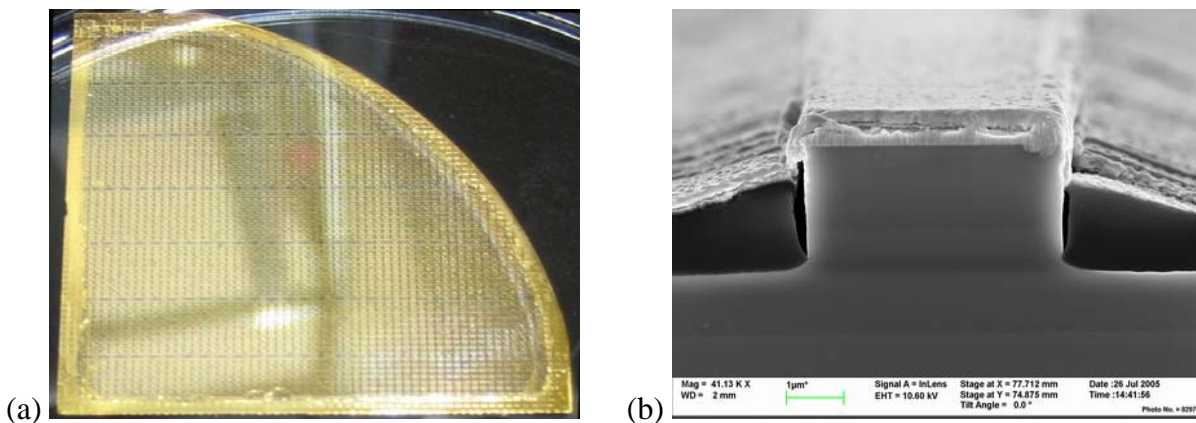


Fig. 3.11: (a) Finished quarter 3''-wafer DO520 (no ridge tilt) after processing before scribing and cleaving. The fine structure of the contact pads is visible (larger shadows and white spots are due to reflections during photography). (b) REM picture (by ZELMI) of the facet of a 4 μm ridge waveguide deeply etched through the active layer with BCB isolation adjacent to the ridge and top contact metallization.

After the top structure of the wafer is completed (Fig. 3.11a) the backside of the wafer is prepared. In order to be able to cleave the wafer it has to be thinned from its original thickness of 450 μm to 120-140 μm . An additional metal contact is evaporated on the backside if the

topside n-contact cannot be used. A combination of Ni/Au:Ge/Au for the backside contact of the n-doped substrate side provides good ohmic contact. Ni serves as the adhesive layer between semiconductor and metal. Although these contacts show a good ohmic contact, they are not usable for die-bonding on a diamond heat spreader (see technical annex 7.6). Finally the wafer is thermally annealed to convert the Schottky-like metal-semiconductor contact to an ohmic contact.

The wafer is divided into bars and devices by scribing the wafer with a diamond facet. Then the wafer is cleaved by breaking it at the scribed positions. In this procedure which is done partly before and partly after the anti-reflection coating (section 3.4.1) the facet may not be damaged, i.e. the scribing should not be carried out across the edge of the wafer. Fig. 3.11(b) shows the facet of a cleaved device after completed processing.

Backside treatment of wafer	mount sample topside with wax on glass plate remove oxides: HF-dip 1 min.
Thinning	$\text{H}_2\text{SO}_4:\text{H}_2\text{O}_2:\text{H}_2\text{O} = 1:8:10$ (4.6 $\mu\text{m}/\text{min.}$, 70 min.) $\sim 130 \mu\text{m}$
Backside contact	Veeco: Ni/Au:Ge/Au 8/80/200 nm, 1-3 $\text{\AA}/\text{s}$ @ 6×10^{-6} torr
RTA	N_2 -Ofen 390 $^\circ\text{C}$, 3 min.

3.4 Post-processing: AR coating and mounting

3.4.1 AR coating and tilted facet

As described in section 2.3.2 there are several means to reduce the crystal facet reflectivity. We have applied anti-reflection (AR) coatings on straight waveguides and AR coatings in combination with a waveguide tilt. These measures are presented in this section.

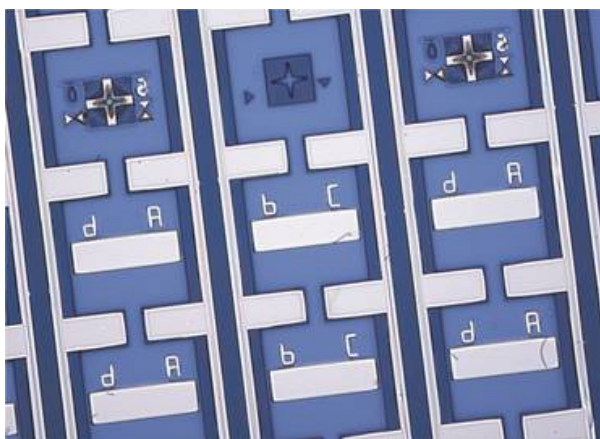


Fig. 3.12: Section of a bar (1.5 mm device length, DO520) with 8 ridge waveguides that have been processed with an angular displacement of 6.8° .

It is expected that the combination of AR and tilt gives a lower reflectivity. On the other hand, it is very useful to compare the device performance (lasing threshold, waveguide losses) before and after AR coating, i.e. as a laser and as an amplifier. The Hakki-Paoli method (section 4.1.5) is normally applied to perpendicular waveguides because it is difficult to estimate the influence of the tilt on the lasing characteristics. It is very difficult to measure effective facet reflectivity of a tilted ridge waveguide as the methods rely on perpendicular back-reflection from the device facet (section 4.1.4).

From the processing point of view it is straightforward to displace the ridge waveguides with an angle to the facet normal. Only in the first lithography step the mesa mask is not aligned with the crystal axis, but is applied with the desired angle between facet normal and ridge direction. All following

3 Processing and Fabrication

processing steps are with respect to the alignment marks defined by the first lithography and hence automatically angled. See Fig. 3.12(a) as an example for a tilted waveguide structure.

For the AR coating we have applied the 2-layer concept because of the expected spectrally broad AR and the flexibility in use of materials with unmatched index of refraction. With the available sputtering machine at the institute we have applied $\text{SiO}_2/\text{SiN}_x$ layers to a sample to test our own capabilities. The refractive indices of the materials were measured with an ellipsometer in a calibration procedure. The effective refractive index of the ridge waveguide was calculated with a mode solver [81] and the nominal optimum thicknesses for the desired minimum wavelength were calculated according to section 2.3.2.

As we can see from Fig. 3.13(a) the resulting reflectivity spectrum does not match the simulation. The reason for the high minimum value is that the effective refractive index is not determined accurately with the mode solver as compared to the experimental determination through the Fabry-Perot cavity spacing (see section 2.3.2). Moreover, the minimum is shifted by 30 nm from the targeted wavelength. This is due to the insufficient thickness control of the sputter machine which is dependent on the position of the sample with respect to the thickness monitor and there is a lag of up to 3 nm after the process is shut of. Because of these imponderabilities we have not pursued the AR coating at our institute.

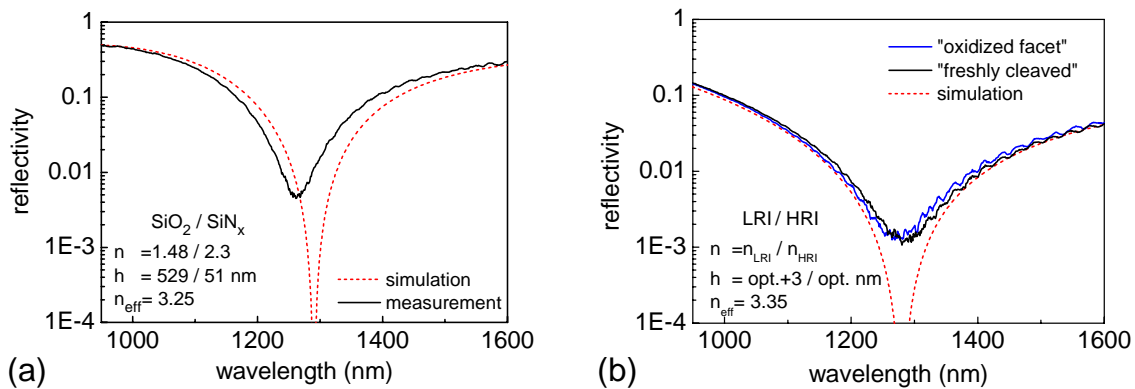


Fig. 3.13: (a) AR coating with $\text{SiO}_2/\text{SiN}_x$ double layer and simulation for nominal refractive indices and layer thicknesses (fabricated at TUB). (b) Difference for freshly cleaved and oxidized facet: AR coating with LRI/HRI double layer and corrected simulation for layer thicknesses plus 3 nm oxide layer (fabricated at FBH).

Further AR coatings were done in collaboration with the Ferdinand Braun Institut für Höchstfrequenztechnik (FBH). The FBH considers its AR coatings as intellectual property. Therefore, no details on the coating materials and their layer thicknesses may be published in this thesis. The AR coatings consist of a dielectric two-layer system with a low and a high refracting material. All other details are for internal use only. Here, we will denote the low refractive material with *LRI* and the material with high refractive index *HRI*.

The FBH has an evaporation machine available with good calibration and reproducibility. A precise thickness monitor is implemented and after the deposition of the first layer, its thickness is measured with an ellipsometer and the second layer is adapted accordingly if necessary. In spite of these measures the thickness uncertainty is ± 1 nm. The material combination used here is LRI/HRI. For some deposition runs a reference sample coating was available on a Si wafer.

It was unclear whether an oxide layer on the facet exists after cleaving, which would shift the AR-coating minimum. Two samples were coated to check the influence of an oxide layer:

- a) *Sample 1* with $2/4$ μm ridges was cleaved and tested before and after the AR-coating. The facet was exposed to air for oxidation for approximately 17 hours before coating.

b) *Sample 2* (from edge of wafer) was freshly cleaved before the AR-coating. The facet was exposed to air for approximately 15 minutes.

Fig. 3.13(b) shows the measured AR spectrum of the facet of the two bars. There is - within the error margin - no difference seen due to the longer oxidation time. The measured spectrum was compared with the transfer-matrix simulation of the AR-coating for different effective indices and layer thickness. Compared to the nominal thicknesses of the layers there is a shift of the spectrum which would correspond to about 3 nm of oxide on the facets (even the freshly cleaved one). We conclude that either even after 15 minutes the facets build up an oxide layer of about 3 nm or there is a systematic error in the thickness monitoring of the sputtered layers. For the subsequent AR coating of a laser bar we have taken the 3 nm into account, calculated the LRI/HRI layers for thicknesses $t_{\text{LRI}}/t_{\text{HRI}}$ nm and set a nominal coating thickness of $(t_{\text{LRI}}-3)/t_{\text{HRI}}$ nm.

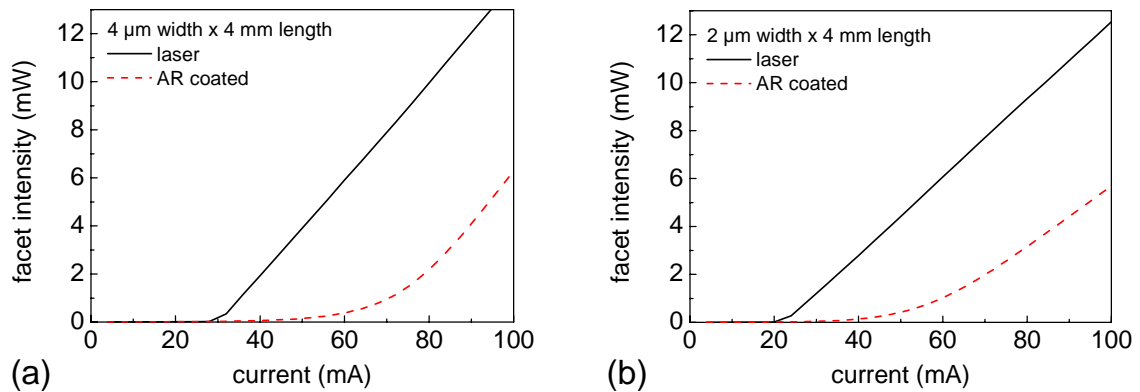


Fig. 3.14: Facet light output before and after AR coating for a 4 mm long sample (DO453) with 4 μm (a) and 2 μm (b) width. The threshold current is shifted by a factor 2-3 and the typical sharp bend of the laser is softened by the ASE of the amplifier. Yet, due to their length and the insufficient AR coating the amplifiers show lasing above 80 and 60 mA, respectively.

The lasing threshold shifted as can be seen by the comparison of the power-current curves before and after coating in Fig. 3.14. As this sample is very long, lasing is not fully suppressed by the AR coating and the devices show a – due to the contribution of ASE – softened lasing kink and a linear power dependence for larger currents. Therefore, these SOAs should be only operated at currents below the onset of lasing and gain measurements at high pump current are impractical.

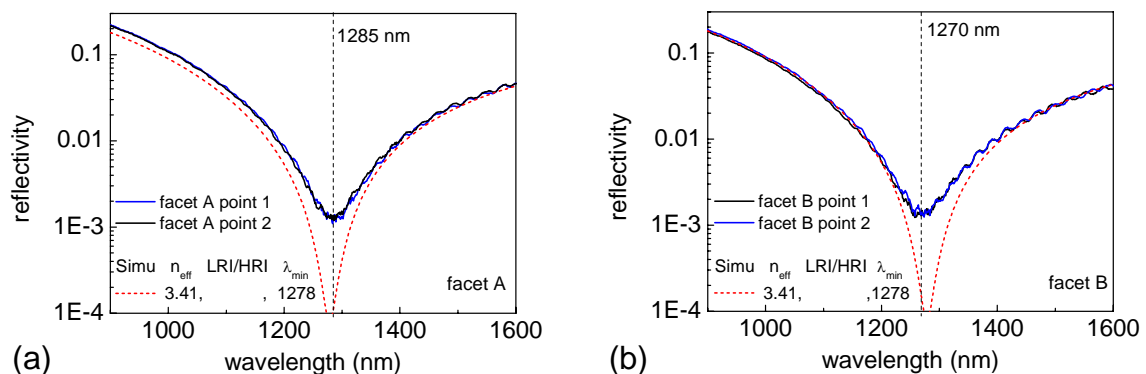


Fig. 3.15: Comparison of front (a) and back (b) facet AR coating of SOA (DO453) with the same nominal layer thicknesses as indicated by the simulated AR spectrum.

The original lasing wavelength of DO453 is between 1280-1290 nm depending on the length of the device. Front and back facet of the devices are nominally coated the same. Their measured spectra (Fig. 3.15) do not coincide exactly with the simulation. From the coating of

3 Processing and Fabrication

facet A to facet B there is a shift of the spectral minimum of approximately 15 nm which is consistent with the uncertainty of ± 1 nm in the coating process.

A discussion on the method and limitation of the measurement of the facet reflectivity is given in section 4.1.4. Via the measurement of the gain and its ripple it is as well possible to extract information on the quality of the AR coating as described in the context of the Hakki-Paoli method (section 4.1.5).

Another AR coating run was done in collaboration with the Technion, Israel. The effective refractive index was calculated from the modal structure ($n_{\text{eff}} = 3.386$) and the reflectivity was simulated by a tool that includes the modal character of the wave in contrast to the plane wave approximation of the transfer matrix method. The simulated thicknesses were 110.7 nm and 110.4 nm. The actual coating consists of two layers, Ta_2O_5 ($n = 2.21$, $t_1 = 116$ nm) and Al_2O_3 ($n = 1.59$, $t_2 = 105$ nm) which were optimized by measuring the output power of some contacted devices during interruption of the coating. The devices exhibit an increase of the threshold current by more than 3 times, yet, they still show a gain ripple as large as 5 dB.

3.4.2 Mounting and packaging

For the usual chip and bar testing the cleaved and AR-coated devices are placed on a submount for heat dissipation and secure handling.

Two methods have been employed which differ if the devices are individually wire-bonded or contacted with the probe head: For individual devices the chips were die-bonded on a diamond heatspreader (see also technical annex 7.6) which itself was bonded on a commercial Kyocera submount with a ceramically isolated bond pad for ball-wedge wire-bonding. For contacting the devices with a probe head a bar with several devices was aligned and glued with silver epoxy on a simple copper piece that was prepared to fit the chip size and had a mounting hole to screw the heatsink on the temperature controlled copper finger between the coupling tapers (section 4.2.1, Fig. 4.16).

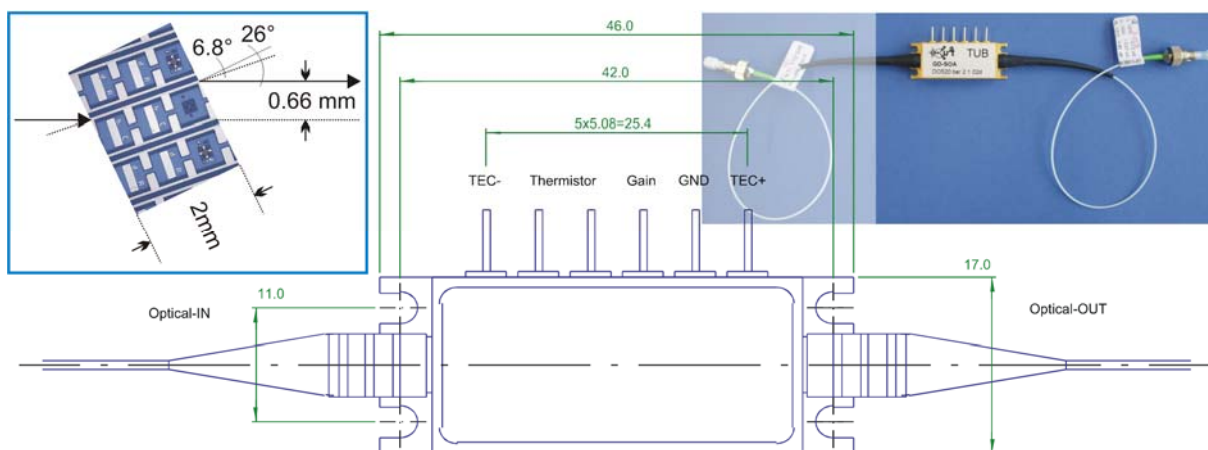


Fig. 3.16: Module package sketch showing optical input and output fibers and the electrical contact pins for bias voltage and cooling control (dimensions in mm). The inset left shows the angular configuration of the tilted chip for in- and out coupling. The inset on the right is a picture of the QD SOA module with fiber pigtails and APC/PC connectors.

For devices with a tilted ridge waveguide (Fig. 3.12) the output is refracted by an angle approximately given by Snell's law. When mounting these chips and coupling light in and out, the angular displacement of the chip and the offset of the tapers have to be taken into

account. For a 2 mm long SOA with tilt angle $\alpha = 6.8^\circ$, we find an output angle of $\beta \approx 26^\circ$ (see section 4.1) and a resulting fiber displacement of $d = L \cdot \sin(\beta - \alpha) / \cos \alpha \approx 0.66$ mm as depicted in the inset of Fig. 3.16.

Two chips were packaged into a module in cooperation with u²t photonics, Berlin, a leading supplier in ultrafast photodetectors with expert knowledge in packaging opto-electronic devices. The tilted QD SOAs were placed in a modified prototype package which is otherwise used for modulators (Fig. 3.16).

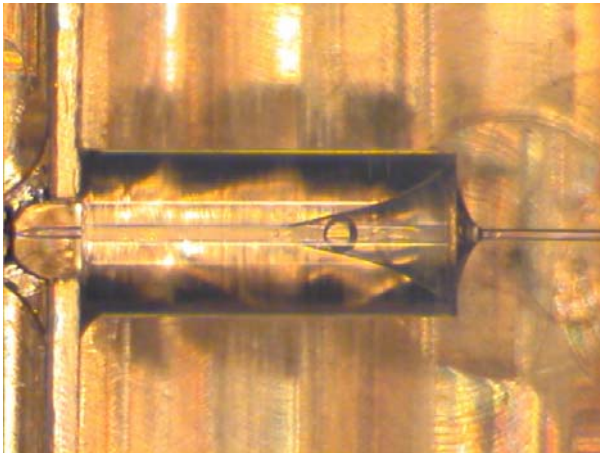


Fig. 3.17: Fiber-chip coupling in the module featuring a glass ferule with a tapered fiber in front of the chip facet (left border of the picture).

As the chips feature no spot size converter of the optical mode and the coupling efficiency to the ridge waveguide structure with cleaved fibers is very low (section 4.1.3) tapered fibers with a small focus were employed. Due to the small adjustment tolerance of the coupling with tapered fibers an extremely stable, yet adjustable coupling scheme is needed. We used a glass ferule that carries the tapered fiber. This combination is actively aligned in front of the SOA facet (Fig. 3.17) and fixed with a UV-curing adhesive which introduces a degradation of the coupling efficiency by 10-30 %. The submounts were modified to account for the angled facets of the chip and the resulting offset for the input and output fiber. In order to have a temperature control the submounts

including the fiber coupling were placed on a peltier element and controlled by a temperature resistor. After biasing the module the temperature settles quickly and without excessive swing.

This packaged module has been deployed extensively in the characterization of cw and dynamic properties of the QD SOA as it allows stable and completely reproducible measurements at constant temperature and over long time, and furthermore is easily portable and pluggable.

4 General Device Characterization and Measurement Techniques

The device performance with regard to far field, coupling losses, facet reflectivity and gain-reflectivity product should be assessed before the measurement of the cw and dynamic gain characteristics. These preliminary general device characterizations are presented in the first part of this chapter together with the corresponding measurement techniques.

The implementation of measurement techniques for the characterization of SOAs was one of the goals of this thesis. In the second part the setups and measurement techniques for gain, noise, pump probe, bit error ratio and XGM measurements are introduced and described. The corresponding results will be discussed in full detail in chapter 5.

4.1 General device characterization

4.1.1 List of samples

Table 4 lists all samples with their key properties that were used in this work. The wafer Ioffe4915 was grown at the Ioffe Physico-Technical Institute, St. Petersburg. The wafers starting with DO were grown by NL Nanosemiconductor, Dortmund. The samples of the Ioffe4915 wafer did not show positive fiber-to-fiber gain and are only considered in the far field measurements. DO75 is a laser structure with no AR coating. The sample was used for M^2 - and far field measurements. Its epitaxial structure is comparable to DO520. Samples DO453 and DO520 are considered the workhorses of this thesis, all cw and dynamic gain investigation were done with these sample structures.

Table 4: List of sample structures that are presented in this work.

Wafer	QD layers	Peak λ	AR	Tilt	Etching	Widths	Lengths
loff4915	5	1270 nm	No	7°	Shallow	6 μm	2 mm
loff4915	5	1270 nm	Yes	No	Shallow	4 μm	2 mm
loff4915	5	1270 nm	Yes	No	Deep	4 μm	2 mm
DO75	10	1270 nm	No	No	Deep	1/2/4 μm	1 mm
DO453	15	1280 nm	Yes	No	Deep	2/4 μm	2/4 mm
DO520	10	1290 nm	Yes	6.8°	Deep	2/4 μm	2 mm

4.1.2 Far field measurement

For a SOA the far field characterizes the modal structure of the waveguide and indicates with what efficiency light can be coupled to and from the device. Therefore, the far field is the starting point in the assessment of the amplifier performance.

The far field of an optical source is characterized by two methods in this section: 1) The deviation from an ideal Gaussian mode is described by the so-called M^2 -factor and its measurement gives a figure of merit that characterizes the quality of the beam. 2) The direct

measurement of the far field either in the principal axis or two-dimensionally scanned results in the divergence angles along the horizontal and vertical axis or in a 2D image of the far field.

M²-measurements

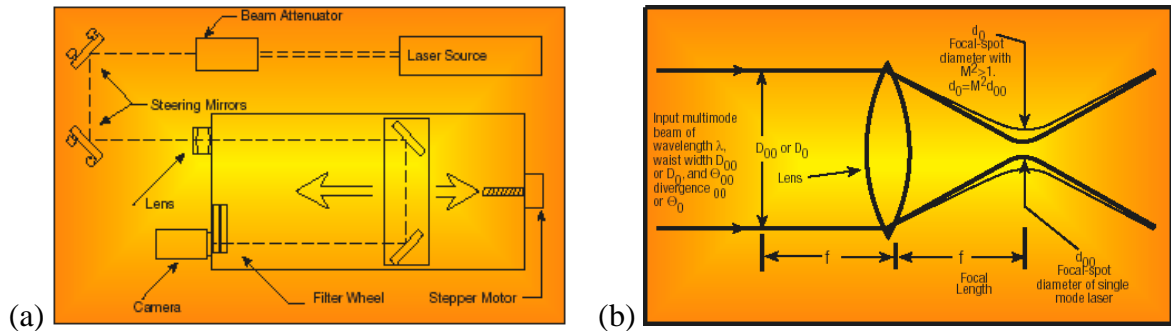


Fig. 4.1: (a) Setup of M²-measurement. (b) Measurement parameters for characterization of beam quality. From www.spiricon.com

For a pure unfocused Gaussian beam the beam divergence θ_{00} is given by $\theta_{00} = 4\lambda/\pi D_{00}$ with the Gaussian waist width D_{00} . For an actual non-Gaussian beam this equation is modified by the factor M^2 , the beam propagation ratio, which defines the deviation from an ideal Gaussian beam [179]. The focused spot width is $d_{00} = 4\lambda f/\pi D_{00}$. For the distorted beam with waist width D_0 and focal spot diameter d_0 the defining equation for M^2 is given by

$$d_0 = M^2 \cdot 4\lambda f/\pi D_0 \tag{4.1}$$

with the focal length f . To determine M^2 a series of measurements has to be taken which is semi-automated with the setup sketched in Fig. 4.1a. The beam is directed via mirrors to the setup and is imaged with a lens onto the camera chip as seen in Fig. 4.2. Then the distance between lens and chip plane is scanned to measure the beam waist at various distances from the focal spot.

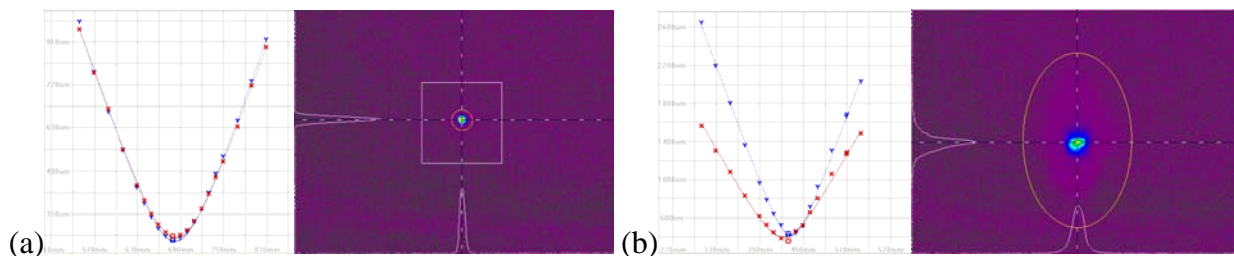


Fig. 4.2: M²-measurements showing the beam width vs. position and a representative camera picture of the mode at one measurement point (a) output of a single mode fiber and (b) facet output of a deeply etched laser. Vertical axis: red dots, horizontal axis: blue dots.

We have tested the setup with a commercial pigtailed laser diode at 1270 nm with an output >2 dBm from the butt fiber. The output of the cleaved single mode fiber is expected to be ideally Gaussian.

4 General Device Characterization and Measurement Techniques

The camera is very insensitive in the IR wavelength regime above 1270 nm. Therefore, no devices with an emission wavelength in that region and a low output power such as an amplifier with only ASE output could be characterized with the M^2 -setup. It was possible to measure the M^2 -factor for a deeply etched laser of the wafer DO75¹¹ which emits at 1270 nm (output >0 dBm), and is structurewise comparable to the sample DO520.

Table 5: M^2 -measurements for the output of a single mode fiber (SMF) and the output of a deeply etched laser (QDL) at 30 mA.

Device	M^2_x	M^2_y	Astigmatism	Asymmetry
SMF, 9 μm core	1.13	1.11	0.06	1.04
QDL, 2 μm ridge	5.64	8.19	0.51	1.20

The measurements of beam width vs. position for a given run are shown in Fig. 4.2. After a few points are measured the software calculates an extrapolated curve fit. This curve is used to double the frequency of measurements in the waist region, following the ISO 11146 procedure [179]. The results of these measurements are summarized in Table 5 and Fig. 4.3a. As expected, the output of the single mode fiber shows a close-to-ideal behavior with $M^2 = 1.1$ and negligible astigmatism and asymmetry of the focused beam. The output of the QD laser shows a strong deviation from the Gaussian mode indicated by the M^2 -values of 5.6 and 8.2 for horizontal and vertical axis, respectively. The rectangular shape of the waveguide is reflected in the asymmetry and astigmatism of the beam focus. Fig. 4.3a shows the M^2 -values for different bias currents of a 2 μm and a 4 μm laser. It can be clearly seen that the beam propagation ratio M^2 is lowered for current densities above 5 kA/cm^2 to values of approximately 2.5 and 3.5 for horizontal and vertical axis, respectively. This is attributed to the enhanced guiding of the mode in the device under large bias current.

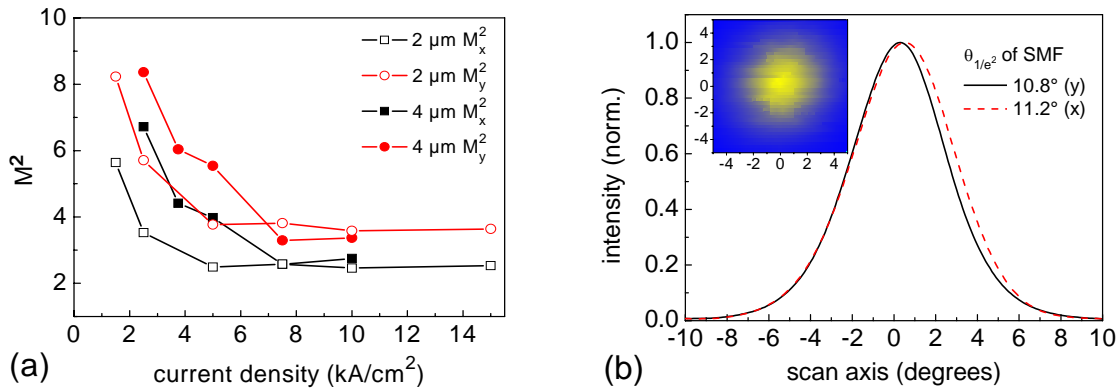


Fig. 4.3: (a) Current dependence of M^2 -factor of the deeply etched QD laser (DO75) for 2/4 μm ridge width and vertical (y) and horizontal (x) axis. (b) Far field of a cleaved single mode fiber with 9 μm core. The inset shows a color coded 2D scan.

Direct far field measurements

The far field of a ridge waveguide device gives direct information of the quality and shape of the output beam.

¹¹ For a sample list see section 4.1.1 Table 4.

The far field measurement setup was build during this thesis and consists of a sample holder which sits in the center of two axial stepper motors that allow rotation in the lateral and vertical plane of the device. At some distance a photodiode measures the light intensity for each angular configuration. In combination with a beam chopper and a lock-in amplifier the intensity can be measured for very low values. By scanning both stepper motors the 1D horizontal and vertical far field or the two-dimensional representation of the far field can be recorded. When aligning the sample, the facet of the device must be adjusted to be right in the center of rotation.

To assess the measurement setup the symmetrical far field of a cleaved single-mode fiber was measured and is shown in Fig. 4.3b for both, 1D and 2D scan. The measured beam divergence angle fits exactly to the core width of $9\ \mu\text{m}$.

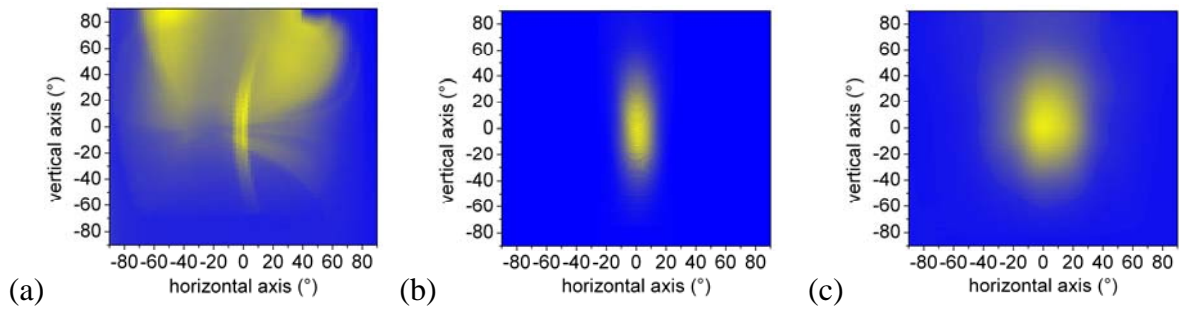


Fig. 4.4: Comparison of two-dimensional far field patterns of (a) a SOA structure with shallow waveguide with tilt 7° and width $6\ \mu\text{m}$, (b) a deeply etched laser with no tilt and width $4\ \mu\text{m}$, and (c) a SOA with same structure as [b] with additional AR coating.

The typical far field patterns of a

- shallow waveguide structure (below threshold, tilt 7° , width $6\ \mu\text{m}$),
- a deeply etched laser (lasing, width $4\ \mu\text{m}$), and
- a deeply etched SOA (below threshold, width $4\ \mu\text{m}$, AR)

are compared in Fig. 4.4.

The latter two structures only differed by the AR coating, therefore, the change in the far field is attributed to the isotropic emission of the ASE and the weaker guiding as there is no input and amplified mode in the amplifier. Fig. 4.4a shows the distorted 2D far field of a SOA, where several causes contribute to this complex pattern. With a ridge width of $6\ \mu\text{m}$ the waveguide is clearly multimode, the tilt introduces multiple reflections, and the shallow ridge does not guide the isotropic ASE efficiently. Such a device structure would be difficult to couple with a fiber because there are multiple intensity maxima, and the coupling efficiency to the symmetric circular mode of a single mode fiber would be very low.

Deep etching of the waveguide decreases the ellipticity of the far field from an initial ratio of 1:10 for a shallowly etched laser to 1:3.5 for a deeply etched laser of the same epitaxial structure and also $4\ \mu\text{m}$ stripe width (Fig. 4.5a). This wafer had an Aluminum content of 75% in the $\text{Al}_x\text{Ga}_{1-x}\text{As}$ waveguide claddings which resulted together with the waveguide thickness of $230\ \text{nm}$ in a vertical divergence angle θ_{1/e^2} of 60° . Using 35% $\text{Al}_x\text{Ga}_{1-x}\text{As}$ and a thickness of $360\ \text{nm}$ this value was reduced to 54° .

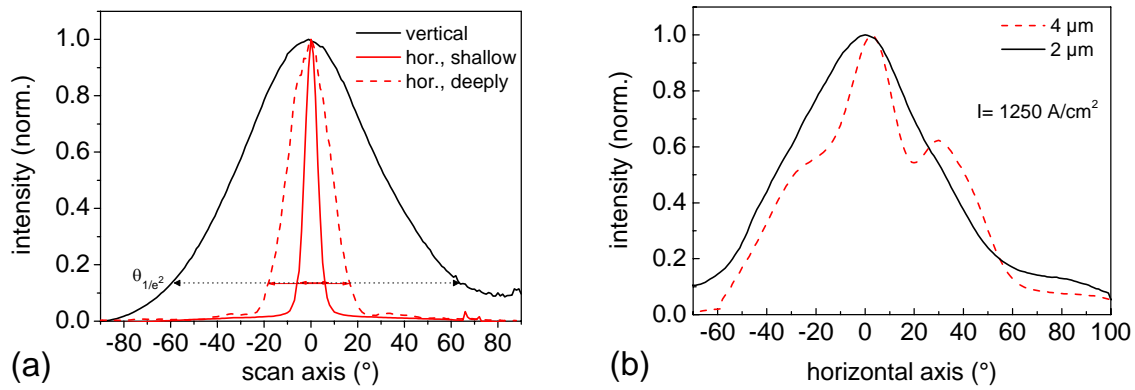


Fig. 4.5: (a) Comparison of xy far field for shallow and deeply etched laser (Ioffe4915 $4\ \mu\text{m} \times 2\ \text{mm}$). The divergence angle θ_{1/e^2} is 60° , 17.5° , 6° for the vertical, horizontal deeply and horizontal shallow profile, respectively. (b) Horizontal far field scan of ASE output of 2 and $4\ \mu\text{m}$ ridge waveguide SOA (DO520) with 6.8° tilt, deeply etched.

For the latter sample the dependence of the far field on ridge width was studied. By decreasing the ridge width to $1\ \mu\text{m}$, we attained a close to symmetric far field which should improve the coupling due to a matched mode profile between device and fiber taper (Fig. 4.6). On the other hand, this narrow ridge is associated with a large divergence which demands a large numerical aperture of 0.6 to collect the output beam. Such coupling optics are expensive (aspheric lenses), difficult to fabricate (fiber tapers), and show a low alignment tolerance. It would be more useful to use a ridge width of 2- $4\ \mu\text{m}$ while reducing the vertical divergence of the device. This cannot be simply done by enlarging the waveguide thickness, because it would support higher order modes as opposed to the single mode structure used here. Concepts like large optical cavity (LOC) or longitudinal photonic band crystal (PBC) structures for a larger vertical mode necessitate a complete redesign of the epitaxial structure, yield in general a lower overlap with the active region, but could not be applied within the framework of this thesis.

The coupling loss due to the asymmetry of the optical mode can be estimated from the ellipticity ratio. The minimum (ideal) coupling loss α_{ellip} of an asymmetric far field with ellipticity $\varepsilon = w_x/w_y = \theta_y/\theta_x$ to a symmetrical optical fiber is [180]

$$\alpha_{\text{ellip}} = \left(\frac{\varepsilon - 1}{\varepsilon + 1} \right)^2 \quad (4.2)$$

with $w_{x,y}$ and $\theta_{x,y}$ the horizontal and vertical mode width and divergence angle, respectively. The deep mesa mode (DO520) with $4\ \mu\text{m}$ ridge width has an ellipticity of 3 (Fig. 4.6a). For the calculated first order mode of this structure this corresponds to a minimum coupling loss of 25% or 1.25 dB. Yet, for real coupling losses other effects are predominant, such as a non-matching numerical aperture, non-ideal Gaussian or multi-mode emission or displacement of the coupling optics in angle or distance. The coupling of the SOAs to tapered fibers will be described in detail in section 4.1.3.

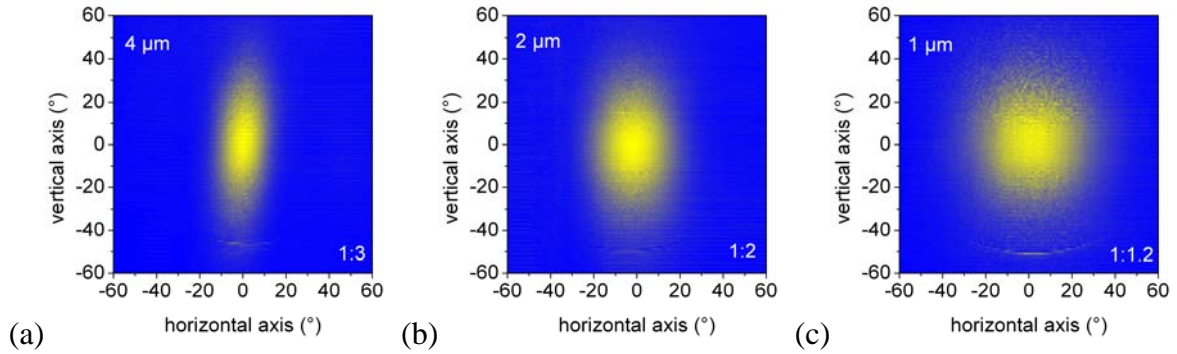


Fig. 4.6: Far fields of deeply etched ridge waveguides (DO75, $\text{Al}_{0.35}\text{Ga}_{0.65}\text{As}$, waveguide $t=360$ nm, vertical divergence 54°) with different ridge width, aspect ratio and horizontal divergence angle: (a) $4\ \mu\text{m}$, 1:3, 17.5° , (b) $2\ \mu\text{m}$, 1:2, 29° , $1\ \mu\text{m}$, 1:1.2, 45°

The introduction of a waveguide angle has a strong influence on the far field as additional lateral reflections within the waveguide can occur which introduce deviations from ideal single mode behavior. For a straight waveguide of $4\ \mu\text{m}$ width the horizontal far field is Gaussian (Fig. 4.5a), while the horizontal profile degrades from an ideal profile for a deeply etched waveguide with 6.8° tilt (Fig. 4.5b). This was explained in section 2.3.1 with lateral reflections that showed up after reflection at the tilted facet. The $4\ \mu\text{m}$ output shows several peaks indicating multi-mode emission in contrast to the $2\ \mu\text{m}$ device which is not Gaussian either, but features only one maximum. Note, due to the tilt and additional AR coating the devices do not lase, therefore, the far field is broadened by the isotropic emitted ASE which is not guided as strongly as a lasing mode.

Two measurement techniques, M^2 - and direct far field measurements, have been established, and benchmarked with the ideal Gaussian emission of a single-mode fiber. These measurements allow the characterization of the far field of our laser and SOA structures.

The M^2 -measurements have shown that even for deeply etched strong index guiding lasers, the guiding of the mode is considerably enhanced at large current densities and the M^2 -value decreases from 8 to approximately 3.

The direct comparison of the far fields have demonstrated that the concept of etching through the active waveguide greatly improves the far field, and therefore also the coupling efficiency to a SMF.

4.1.3 Determination of taper-facet coupling loss

In order to use and characterize a SOA chip, light has to be coupled in and out of the ridge waveguide. Free space optics would be an option, yet rather unpractical as most signal sources, components and characterization units are fiber based. Therefore, the chips are fiber-to-fiber coupled (see section 4.2.1 for the auto-alignment setup) with single-mode fibers (SMF). This coupling is deteriorating the overall efficiency of the device because light is lost at each coupling point. The fiber-facet coupling decreases the gain, increases the noise figure and causes other problems like instabilities, feedback or residual reflectivities. So as to determine the characteristics of the chip and the material itself, the coupling losses have to be measured and de-embedded from the fiber-to-fiber results.

4 General Device Characterization and Measurement Techniques

As described in section 4.1.2 the ridge-waveguide devices have a large divergence angle necessitating a large aperture for coupling. A cleaved single-mode fiber has an acceptance angle of 11° (Fig. 4.3b) which causes coupling losses larger than 10 dB for our structures. A focusing optic is needed to lower the loss. Coupling lenses would introduce aberrations and other losses, therefore fibers with a built-in lens are the best choice. Fibers with graded index-lenses, microlenses or tapers are available. Tapered fibers, i.e. fibers which are drawn under an electric arc to form a round tip at the end, achieve the smallest focus spot sizes (down to $2\ \mu\text{m}$) and were used throughout this work.

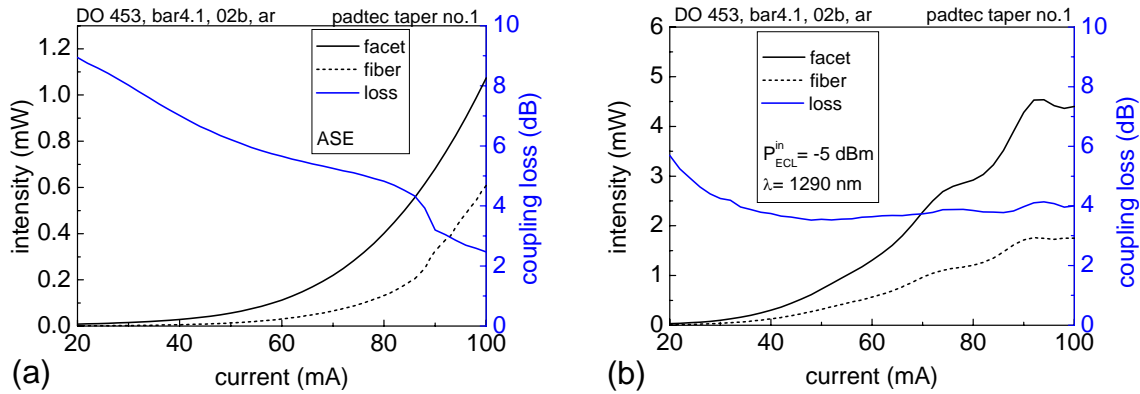


Fig. 4.7: (a) Coupling loss calculated from ASE and lasing output power at facet in comparison to power in fiber. (b) Output coupling loss for guided amplified light with an input power of -5 dB.

The measurement of the coupling loss by comparison of the facet ASE emission with the power in fiber is insufficient as it is pictured in Fig. 4.7(a): The coupling loss decreases with an increase of ASE power with current because the amplified part of the light experiences more guiding than the isotropic emitting spontaneous emission. Also, the feedback of the taper might lead to an enhanced lasing at lower currents, thereby artificially lowering the coupling loss. A more accurate method is the determination of the output coupling loss while an input signal is present that is being amplified by the SOA (Fig. 4.7b). Only at low currents where the gain is low the coupling loss is not a constant. For currents above 40 mA the coupling loss is the same with an accuracy of ± 0.5 dB. The absolute value of the coupling loss depends on taper and device structure like tilt, etching and width. The best value we have achieved is 4.0 ± 0.5 dB in a combination with a Padtec taper and the sample DO453. The results for other tapers are summarized in Table 6.

Table 6: Coupling losses of different used tapers with structure DO453 (4 mm x 4 μm SOA, straight) and structure DO520 (2 mm x 4 μm SOA, 6.8° tilt)

Taper identifier	Coupling loss (dB) to structure DO453	Coupling loss (dB) to structure DO520	Lasing threshold of structure DO453 measured in combination with Padtec taper
IzM blau	6.5 ± 0.5	6.5 ± 1.0	90 mA
Padtec no.1	4.0 ± 0.5	6.0 ± 0.5	85 mA
Padtec no.2	4.0 ± 0.5	6.0 ± 0.5	85 mA
Nanonics 5 μm	4.5 ± 1.0		80 mA

By this method we have determined the output coupling losses. Although one would expect from simple optical mapping arguments that the coupling losses for input and output are symmetrical and therefore the same, this is not entirely clear and was verified by the following measurements.

- 1) By using alternately two different tapers for the input (leaving the same for the output) a difference in the linear gain and in the noise figure (both of them directly proportional to the difference in input coupling efficiency) should be observable. For alternately IZM and Padtec taper we measured 2 ± 0.5 dB difference for the linear gain and the noise figure which agrees within the error margins with the difference of these tapers in output coupling loss. This supports the presumption of symmetry.
- 2) The input coupling loss can also be calculated via the measurement of the overall loss in the long wavelength tail of the gain spectrum. At 1370 nm the gain and absorption of the quantum dot gain medium is assumed to be negligible ($G_{\text{QD}}(1370\text{nm}) \approx 0$). The measured losses are caused by input coupling $\alpha_{\text{in,coupl}}$, output coupling $\alpha_{\text{out,coupl}}$ and waveguide α_{WG} losses. The latter were determined by lasers of different length of the identical wafer and structure ($\alpha_{\text{WG}}^{\text{DO453}} = 3.5\pm 1.7$ dB, $\alpha_{\text{WG}}^{\text{DO520}} = 1.7\pm 0.8$ dB). Using the relation $G(\lambda) = G_{\text{QD}} - \alpha_{\text{WG}} - \alpha_{\text{out,coupl}} - \alpha_{\text{in,coupl}}$ we find for the input coupling losses of the IZM taper 7.0 ± 2.6 dB and the Padtec taper 4.5 ± 2.2 dB which matches with the values we have measured for their output coupling losses (Table 6).

The module as described in section 3.4.2 is fiber-pigtailed, i.e. two fibers are permanently coupled to the chip. The fibers are mounted with a glass ferule in front of the chips and aligned via photocurrent feedback. They are fixed with a UV-curing adhesive. During fixation the fiber shifts vertically and horizontally due to strain which results in deterioration of the coupling efficiency by 10 to 30 %. In a separate experiment the 1dB-alignment tolerances of the coupling were measured. For tapered fibers the tolerance is about ± 0.25 μm which is a factor of 8-10 lower than for cleaved fibers, yet, with a much better coupling efficiency.

We conclude that it is sufficient to determine the coupling loss from the output as this is easier, more accurately and in agreement with the input loss. Once the coupling losses are identified they can be de-embedded from the fiber-to-fiber gain and noise measurements to get values of the SOA chip.

4.1.4 Facet reflectivity measurement

Section 2.3.2 has described the various means to reduce the facet reflectivity of the amplifiers. In section 3.4.1 it was shown how these means are realized. In order to check the quality of the applied measures it is necessary to accurately determine the effective reflectivity of the waveguide. In this part the direct measurement of the reflectivity from the facet or an according reference sample is illustrated.

To measure the reflectivity of a facet, the fraction of an incident signal that is reflected from the facet has to be determined. There are elaborate schemes to measure the micro-reflectance with a spatial resolution on the order of the waveguide dimensions [181]. Yet, such a setup was not available at our or collaborating institutes and the build-up would have been beyond the scope of this work. We have used simplified methods to measure the reflectance of the GaAs facet of the device requiring a spatial resolution of only about 50 μm , as depicted in Fig. 4.8(a). Setup 1 (Fig. 4.8b) works with a tapered fiber or a fiber with a micro-lens to focus and collimate the light onto and from the facet. Due to the back-reflection within the taper the

noise level of the measurement can be as high as the value of reflectivity to be measured. An idea to circumvent the problem of noise from back-reflection would be to use setup 2 (Fig. 4.8b) with a dual fiber collimator. But a perfectly symmetric component would be needed which was not available and the setup allowed no efficient collimation. Therefore, the measurements were accomplished with setup 1 under consideration of the noise problem.

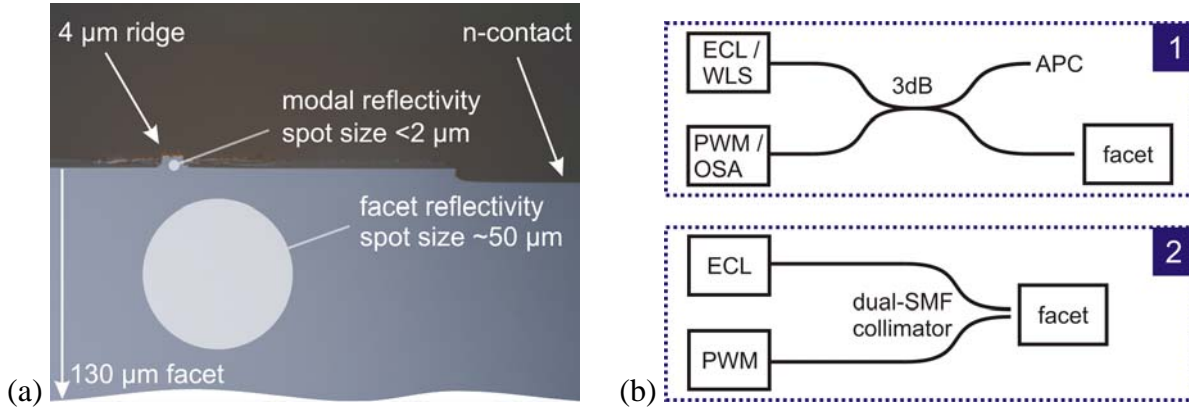


Fig. 4.8: (a) Microscope picture of a sample facet (cross section with deeply etched 4 μm ridge and uncovered n-contact). The circles indicate the measurement spots for modal (waveguide) and facet (GaAs) reflectivity. (b) Setup schematic for reflectivity measurement of AR-coated facet. Setup [1] uses an external cavity laser (ECL) with single mode fibers or a white light source (WLS) with multi mode fibers as signal source which is back-reflected through the 3 dB coupler into the power meter (PWM) or optical spectrum analyzer (OSA). The second output of the coupler is terminated with an angled facet connector (APC). Setup [2] uses a dual single mode fiber collimator to focus and collect the light onto and from the facet.

Fig. 4.9 depicts the method and limitation of the reflectivity measurement. Using a white light source the signal is focused with a multi-mode fiber including a micro-lens onto the facet. The reflected light is picked up with the same micro-lens and analyzed after the 3 dB coupler with an optical spectrum analyzer (Fig. 4.9a).

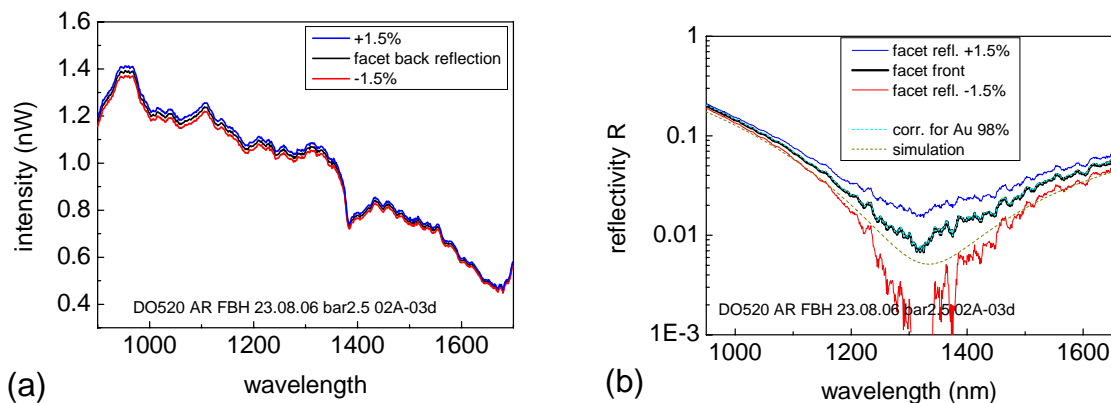


Fig. 4.9: (a) Measurement of back reflection from facet (black curve) and variation of measurement values by $\pm 1.5\%$ which is roughly the measurement uncertainty. In the measurement the signal is optimized for maximum intensity. (b) Comparison of the calculated reflectivity from the measurement plotted in [a] showing the strong influence on the accuracy. This is because from the back reflection signal the zero measurement is subtracted which is of the same magnitude; any low reflectivity value can be achieved by a bad optimization in [a]. Therefore, this measurement gives only an indication on the shape of the reflectivity spectrum and the position of the minimum wavelength. The correction of the Au standard from 100% to 98% does not have a significant influence on the result.

The focus point of the fiber lens is optimized with regards to the maximum intensity in the OSA. Besides the facet reflectivity, a spectrum from a gold plated surface (as reference for 98%) and the back-reflection from the fiber taper (as zero) are recorded. The spectrally resolved reflectivity is then calculated by $R(\lambda) = I_{\text{facet}}/I_{\text{Au}} - I_{\text{zero}}/I_{\text{Au}}$ with the measured OSA intensities $I_{\text{facet/Au/zero}}$ for the back reflection of the facet, the gold standard and the micro-lens, respectively.

Any misalignment is directly translated in a strong influence on the minimum value of the reflectivity because of the procedure to calculate it by subtraction of the zero measurement (Fig. 4.9b). Therefore, this measurement method is only correct for reflectivity values well above the noise floor and gives only an indication on the shape of the reflectivity spectrum and the position of the minimum wavelength.

For some AR coatings a reference sample on a Si wafer was deposited in parallel to the sample. This Si wafer was measured in a reflectometer setup at FBH and the measured data can be used for fitting the thicknesses of the layers by simulation. The result of this procedure is shown in Fig. 4.10(a). A good agreement between measurement and simulation is achieved for LRI/HRI layer thicknesses of $t_{\text{LRI}}/t_{\text{HRI}}$ nm for the front facet which differs considerably from the nominal (optimum) thicknesses of $(t_{\text{LRI}}+0.8)/(t_{\text{HRI}}+2)$ nm. The back facet layers are closer to the ideal thicknesses. The geometrical average of the front and back facet was calculated for the effective refractive index of the structure and the tilt angle was taken into account. The resulting reflectivity shows two minima (Fig. 4.10b) which are similar the reflectivity derived from the Hakki-Paoli measurement on the same structure presented in section 4.1.5 (Fig. 4.15b). The position of the minima has in both cases a distance of 25 nm, but the absolute position differs by 15 nm indicating that the measurement of the Si reference sample is not perfectly accurate, too. Note, the difference of 15 nm correspond to a thickness of about 1.5 nm of the layers. This difference between sample and reference could stem from a different tooling factor for different positions in the deposition unit.

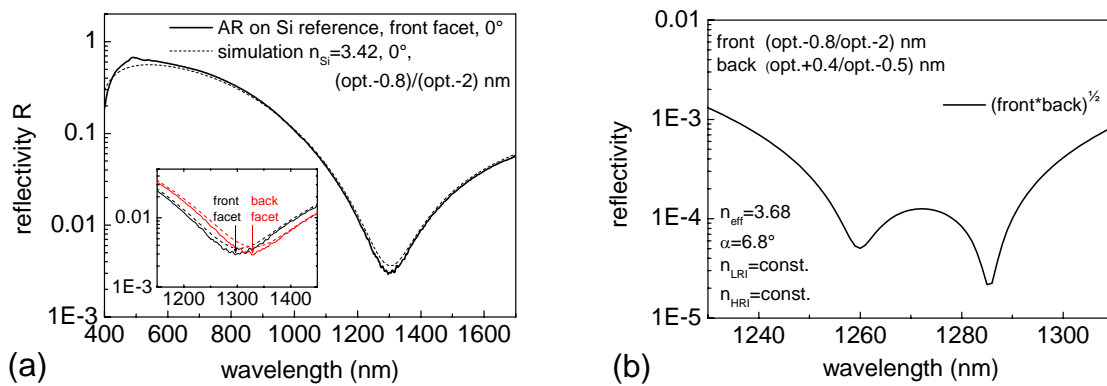


Fig. 4.10: (a) Reflectometer measurement of AR coated Si reference at 0° incidence. The simulation was fitted to the shape of the measurement by varying the layer thicknesses. The inset shows the reflectivity of front and back facet of the bar (DO520) which are shifted by 30 nm due to deposition tolerances. (b) Using the fitted thicknesses of the dielectric layers of the front and back facets the geometrical average reflectivity is calculated, now with the parameters for the effective refractive index of the sample and the angle of 6.8° . “opt.” denotes the theoretically optimum thickness of the layer.

In conclusion, it is found that for tilted waveguides it is very difficult to measure directly the effective waveguide reflectivity as only the vertical back-reflection from the facet or a

reference sample can be measured. The effective reflectivity can then be calculated using the reflectivity simulation tool, but with a large error margin.

The information that is contained in the spectral ripple of the emission of the amplifier can be extracted with the Hakki-Paoli method as described in the next section. It is possible to determine the effective reflectivity indirectly with this method using an additional spectral gain measurement.

4.1.5 Hakki-Paoli measurement

The reflectivities of the facets of a semiconductor device result in a Fabry-Perot-like cavity. In conjunction with the gain of the semiconductor medium this results in a modulation of the emission spectrum of the device. Therefore, the modulation comprises information about the reflectivity and the modal gain of the device – generally speaking this information is accessed with the so-called Hakki-Paoli method [182].

Determination of the effective index of refraction

Due to the facet and sidewall reflectivities the emission spectrum of a laser or an amplifier shows lateral and longitudinal modes. If the device is laterally single mode, then $2Ln = m\lambda$, with $m \in \mathbb{N}$ holds for the longitudinal modes for a Fabry-Perot cavity of length L , refractive index n and the wavelength λ defined in vacuum. With $f_m = c/\lambda_m = mc/2Ln$, c is the speed of light, we can find the mode distance from

$$\Delta f = f_m - f_{m-1} = \frac{c}{2Ln} \Rightarrow |\Delta\lambda| = \frac{\lambda^2}{2Ln}. \quad (4.3)$$

Using the Fresnel formula (7.6) the reflectivity R of an interface air-semiconductor can be calculated under vertical incidence by $R = (n_1 - n_2)^2 / (n_1 + n_2)^2$ with the refractive index of the semiconductor material n_1 and of air n_2 . This is of course only valid for uncoated facets. The reflectivity of an AR coated facet can be characterized with the Hakki-Paoli method.

Derivation of the gain-reflectivity product with the Hakki-Paoli method

The spectrum of the spontaneous emission below the lasing threshold is measured in high resolution. The minima $P_{\min}^{\lambda_i}$ and maxima $P_{\max}^{\lambda_i}$ of the spectrum stem from the destructive and constructive interference of the lightwave that is being reflected between the facets. From this Fabry-Perot modulated ripple a relation for the gain spectrum can be deduced [182]

$$g(\lambda_i) - \alpha = \frac{1}{L} \ln \left(\frac{\sqrt{P_{\max}^{\lambda_i}} - \sqrt{P_{\min}^{\lambda_i}}}{\sqrt{P_{\max}^{\lambda_i}} + \sqrt{P_{\min}^{\lambda_i}}} \right) - \frac{1}{2L} \ln(R_1 R_2) \quad (4.4)$$

which applies for the modal gain g and the internal losses α for a device with length L and the facet reflectivities R_1, R_2 for each ripple i . The so-called gain-reflectivity product $\rho(\lambda)$ is defined by

$$\rho(\lambda) = \sqrt{R_1(\lambda)R_2(\lambda)} \cdot G_s(\lambda) \quad (4.5)$$

and can be calculated from the minima and maxima of the measured spectrum, as Hakki-Paoli gain-reflectivity product $\rho_{HP}(\lambda)$ with

$$\rho_{HP}(\lambda_i) = \frac{\sqrt{\gamma(\lambda_i)} - 1}{\sqrt{\gamma(\lambda_i)} + 1} \cong \frac{\sqrt{P_{\max}^{\lambda_i}} - \sqrt{P_{\min}^{\lambda_i}}}{\sqrt{P_{\max}^{\lambda_i}} + \sqrt{P_{\min}^{\lambda_i}}} . \quad (4.6)$$

Here, G_s is the single-pass gain and the amplitude ratio is given by $\gamma(\lambda_i) = (P_{\max}^{\lambda_i} + P_{\max}^{\lambda_{i+1}})/2P_{\min}^{\lambda_i}$. After the coating of facets the new reflectivity R' can be calculated from the new gain-reflectivity product $\rho'(\lambda)$ with

$$R' = \frac{\rho'(\lambda)}{\rho(\lambda)} R . \quad (4.7)$$

This is only true if $G'(\lambda) \approx G(\lambda)$, i.e. the shift of the gain spectrum due to band filling must be small.

From a single measured gain-reflectivity product an upper boundary of the facet reflectivity can be estimated if the chip gain of the device was measured separately. The single-pass gain G_s equals the chip gain only in the case of vanishing reflectivities R (see section 2.2.3). For a non-ideal traveling wave amplifier G_s can be larger than the actual device gain, therefore

$$R = \rho(\lambda)/G_s(\lambda) \leq \rho(\lambda)/G_{\text{mean}}(\lambda) = R_{\max} . \quad (4.8)$$

Here, G_{mean} is the averaged chip gain of the measured spectrum with gain ripples. In [13] a simple formula is given

$$R = \frac{G_{\max} - G_{\min}}{4G_{\max}G_{\min}} \quad (4.9)$$

to calculate the reflectivity R directly from the highly resolved chip gain spectrum with minimum and maximum gain values $G_{\text{min/max}}$.

1) Measurement of the gain of a laser below threshold with the Hakki-Paoli method

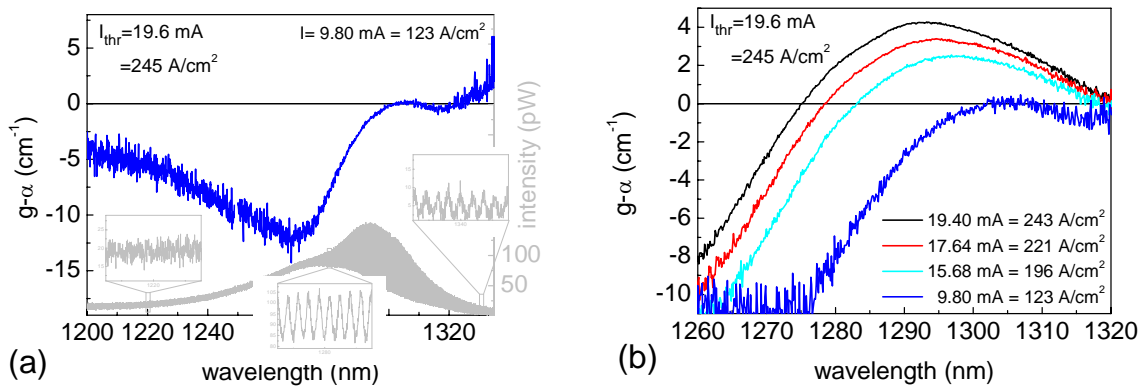


Fig. 4.11: (a) High resolution laser spectrum below threshold (grey) and gain spectrum (blue) calculated according to eq. (4.4) with an automated analysis to deduce the spectral minima and maxima. The insets depict the valid regions of the method with a true modulation in contrast to noise at 1220 nm and 1330 nm. (b) Laser gain spectrum of sample DO453 (4 μm x 2 mm) for different currents below threshold.

The measurement of the gain of a laser with the Hakki-Paoli method below threshold is limited by the resolution and sensitivity of the available optical spectrum analyzer and the extent of gain modulation. Fig. 4.11(a) depicts these limits. For a 2 mm long laser the mode spacing is 0.11 nm. In order to resolve the minimum and maximum of the modes the resolution should be about an order of magnitude better¹². If the signal is within the noise floor of the OSA, the gain cannot be deduced (see inset at 1330 nm of Fig. 4.11a), or if the gain is too small to cause significant modulation ((see inset at 1220 nm of Fig. 4.11a), the automatic analysis of the peak values must fail. Assuming a crystal facet reflectivity of 30% the gain can be easily calculated from the gain-reflectivity product. The gain of a laser of sample structure DO453 is shown in Fig. 4.11(b) for current values below threshold. It features the typical shift of the gain maximum to shorter wavelengths due to the band filling for larger current density.

2) Reflectivity determination using gain-reflectivity spectrum before and after AR coating

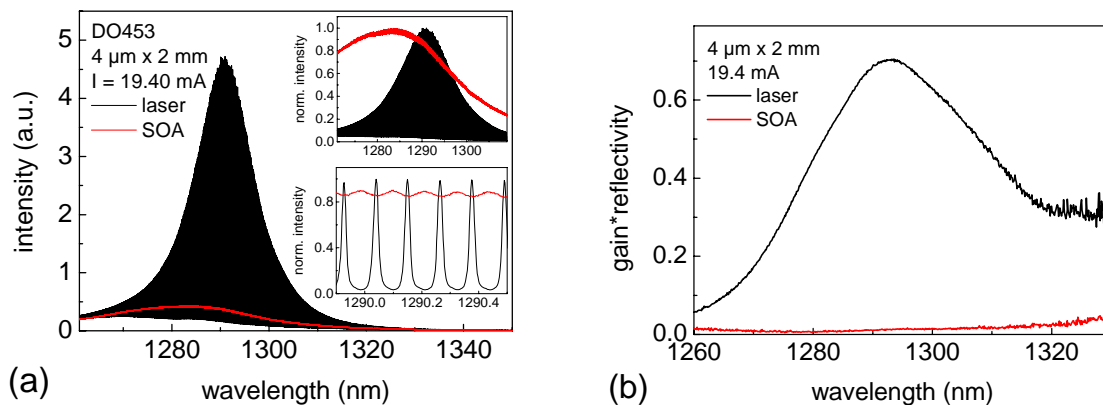


Fig. 4.12: (a) Spectra of device before (laser) and after AR coating (SOA) at the same current. Insets show the normalized spectra displaying the spectral shift of the maximum and a section of the spectrum presenting the modulation due to the reflectivity of the facets. (b) Gain-reflectivity product calculated from spectra in [a].

¹² which in this case is the minimum resolution setting of the optical spectrum analyzer (OSA) with 0.01 nm.

The Hakki-Paoli method is applied as described above to derive information on the facet reflectivity of an AR coated device using equation (4.7). The spectra of the laser (before coating) and the SOA (after coating) are taken at the same current (Fig. 4.12a). The shift between the maxima of the spectra shows a different band filling and therefore, a different carrier density within the laser and the SOA. This indicates that $G_s^{\text{laser}}(\lambda)$ is not equal to $G_s^{\text{SOA}}(\lambda)$ at the same current which is a prerequisite to apply equation (4.7). What happens, if we ignore this and shift the SOA spectrum by 8 nm to match the spectral peak with that of the laser, is depicted in Fig. 4.13a. The facet reflectivity spectrum, which we get from this procedure, seems to be of the wrong shape and magnitude.

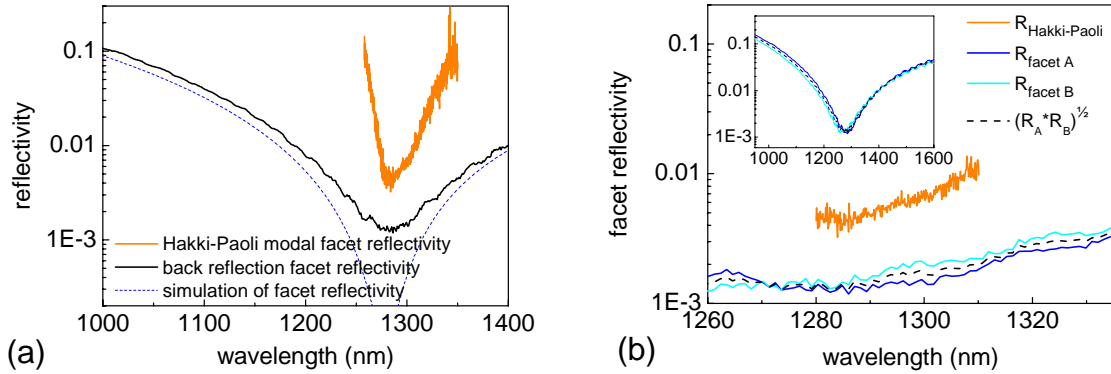


Fig. 4.13: (a) Comparison of the derivation of the facet reflectivity with the Hakki-Paoli method or the measurement of the back reflection (section 4.1.4). (b) Reflectivity of the facets measured by back reflection (section 4.1.4) and Hakki-Paoli. The averaged reflectivity from back reflection is used to calculate the gain by dividing the measured gain-reflectivity product.

3) Gain determination using gain-reflectivity spectrum and measured reflectivity

On the other hand it is possible to divide the gain-reflectivity product of the SOA (Fig. 4.12b) either by the reflectivity calculated from the back reflection spectrum or the reflectivity derived from the Hakki-Paoli method (both in Fig. 4.13b). We obtain the gain spectrum of the SOA (Fig. 4.14a) within the error margin of the measured back reflection spectrum (for discussion see section 4.1.4) or the error margin of the Hakki-Paoli method (as discussed above). The values depend on the accuracy of the reflectivity measurement.

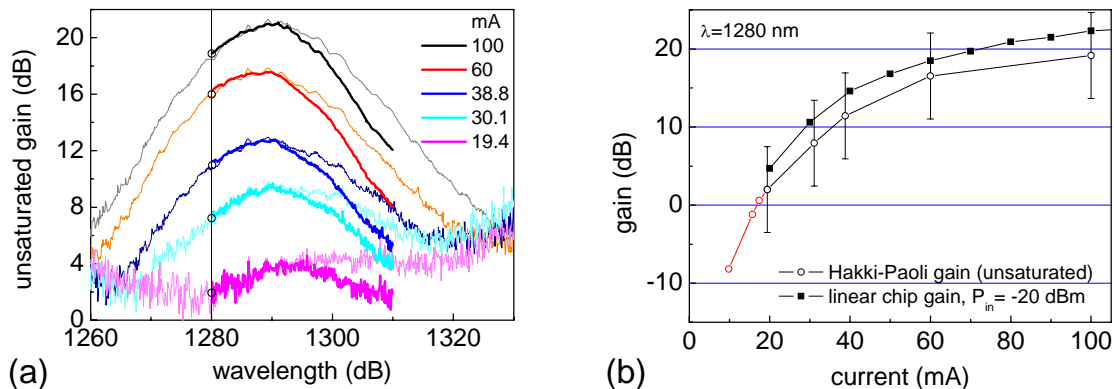


Fig. 4.14: (a) SOA gain spectrum of sample DO453 ($4 \mu\text{m} \times 2 \text{mm}$) for different currents. The gain derived by the reflectivity from back reflection (thin lines) was corrected by 5.5 dB to match with the gain from Hakki-Paoli (thicker lines). The values at 1280 nm are plotted in Fig. b. (b) Comparison of SOA gain vs. current for measurement with Hakki-Paoli method or direct input signal ($\lambda_{in}=1280 \text{ nm}$, $P_{in}=-20 \text{ dBm}$). Red data points are from the laser gain spectra (Fig. 4.11b).

In Fig. 4.14(a) the gain values deduced from back reflection measurements were corrected (lowered by 5.5 dB) to match with the gain peak of the Hakki-Paoli measurement. The shape of the gain curves is similar, but deviates considerably at wavelengths above 1310 nm and low currents. This is attributed to the noise level of the ASE measurement as discussed in Fig. 4.11(a). At 1280 nm we have taken the gain values and plotted them in comparison with a direct measurement where the gain was measured fiber-to-fiber ($P_{in}=-20$ dBm, $\lambda=1280$ nm) and the coupling losses were subtracted (Fig. 4.14b). The two methods yield within the error margin the same results for the amplifier gain.

Although the Hakki-Paoli method promises to directly access the gain of an amplifier, the error introduced by the unknown reflectivity spectrum makes the method too elaborate while at the same time too inaccurate.

4) Reflectivity determination using gain-reflectivity spectrum and measured gain spectrum

Another way to benefit from the information of the gain-reflectivity product is to combine it with a spectral gain measurement (section 4.2.2) and infer from this the reflectivity spectrum according to equation (4.8).

It is also possible to use equation (4.9) and calculate the reflectivity directly from the minima and maxima of the measured net gain, corrected by the fiber coupling losses. Both calculations are presented in Fig. 4.15 showing a good agreement. The reflectivity of sample DO520 (Fig. 4.15b) varies in the range of 10^{-4} - 10^{-3} exhibiting two minima at 1277 and 1305 nm which correspond the shifted minima of the front and back facet AR coating. The minima are also clearly visible in the ASE spectrum where the ripple nearly vanishes.

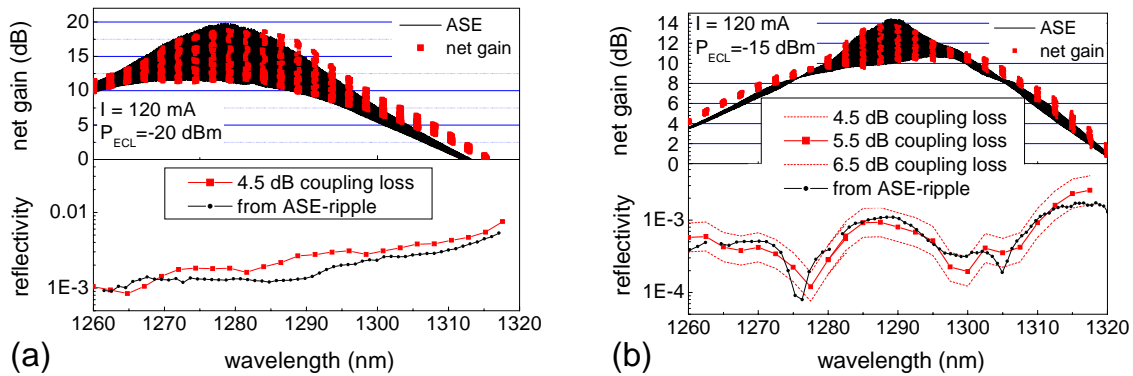


Fig. 4.15: Reflectivity calculation by equations (4.8) and (4.9) using the measurement of the high resolution ASE spectrum and the net gain measurement. From the net gain the coupling losses are subtracted and a mean gain can be calculated by averaging the ripple. (a) Sample DO453 (4 μ m x 2 mm), no tilt, AR fabricated by FBH. (b) Sample DO520 (4 μ m x 2 mm), 6.8° tilt, AR fabricated by FBH.

In summary, the Hakki-Paoli method is a versatile tool to access the information of either gain or reflectivity of a SOA. In order to calculate one of the two, additional information must be available: a second gain-reflectivity spectrum at another operation point, the reflectivity spectrum or the gain spectrum. All combinations have been evaluated in this section.

The best results were achieved with calculating the reflectivity from the gain-reflectivity product by division with the measured gain spectrum. This gives a valuable information as the reflectivity of a tilted facet is not otherwise easily measurable, like it was discussed in the previous section. Minimum reflectivity values of 10^{-4} of the combined AR-coated and tilted waveguide sample have been derived.

4.2 Measurement techniques for characterization of SOAs

4.2.1 Setup for SOA characterization

In order to characterize the QD SOAs on a chip and bar level a set up was built that allows to contact individual devices with a ground-signal probe-head and to access the ridge waveguide with tapered fibers to couple light in and out of the SOA. The setup is shown in Fig. 4.16:

- Two micrometer-piezoelectric stages control the positioning of the tapered fibers in front of the facet and the ridge waveguide. A part of the output light is used as feedback to allow for auto-coupling. Input and output fibers are both scanned in a narrow circle around the optimum coupling position with two different frequencies. With a lock-in type method a deviation from the best coupling, i.e. the largest output signal, is detected and the position of each taper is adjusted individually back to the optimum. The z-position of the taper, i.e. the distance between fiber and facet, is adjusted manually. It does not vary a lot with changing current and does not need to be optimized continuously – as it is necessary for the x- and y-position.
- The chip heatsink is mounted on a Cu finger which is extended from the temperature controlled peltier heater reservoir. It acts as a fast responding heat sink and allows adjusting the temperature in a range from 0 – 80 °C.
- The SOA chip is contacted via its top contacts with a high-frequency capable probe-head. The setup is constructed in a way that also wire bonded samples and samples with a bottom-side n-contact can be mounted and contacted. The setup can handle device lengths ranging from below 500 μm to over 10 mm.
- The coupling of the fiber to the ridge is done manually until an initial light power level is reached which allows for feedback coupling. As the fiber-taper distances are often below 10 μm , a high resolution microscope is used to observe the initial coupling process.

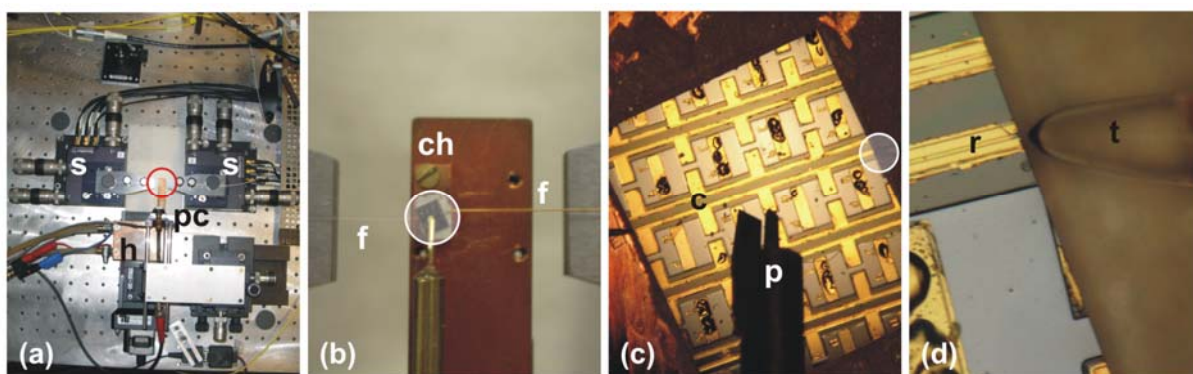


Fig. 4.16: Setup for device characterization – from left to right each picture shows enlargement of circled area: (a) two micrometer-piezo stages [s] for fiber-alignment, copper heatsink [h] with mounting finger including water cooling and peltier heater, probehead chuck [pc], (b) chip-heatsink [ch] on mounting finger, two coupling fibers [f], (c) SOA chip [c], probehead [p], (d) edge of device ridge [r] and tapered fiber [t].

With the ability to couple light in and out of the device all sorts of fiber based measurements can be conducted using all accessible signal sources and fiber based characterization equipment. We are able to scan the bias current and the temperature of the device, the cw input signal wavelength can be swept throughout the O-band, and the signal power level can be set from -50 to +5 dBm. An automated optimization of the input signal polarization is

available in the fully Labview [183] implemented measurement control panel which operates all equipment via general purpose interface bus (GPIB) interfaces.

The signal sources and analysis equipment used are described for each type of measurement in the following sub-sections.

4.2.2 Gain measurement technique

For the measurement of the device gain one could in principle compare the integrated input and output power to get $G = P_{out}/P_{in}$. Yet, if the noise level is comparable to the signal level a considerable error is introduced by this definition. In most cases the noise floor of the input signal is low and does only have to be taken into account for noise measurements (see next section), but the ASE level can be close to the signal level for low input power and has to be deduced from the integrated output power. We follow the standardized measurement specification given by the DIN norm [184].

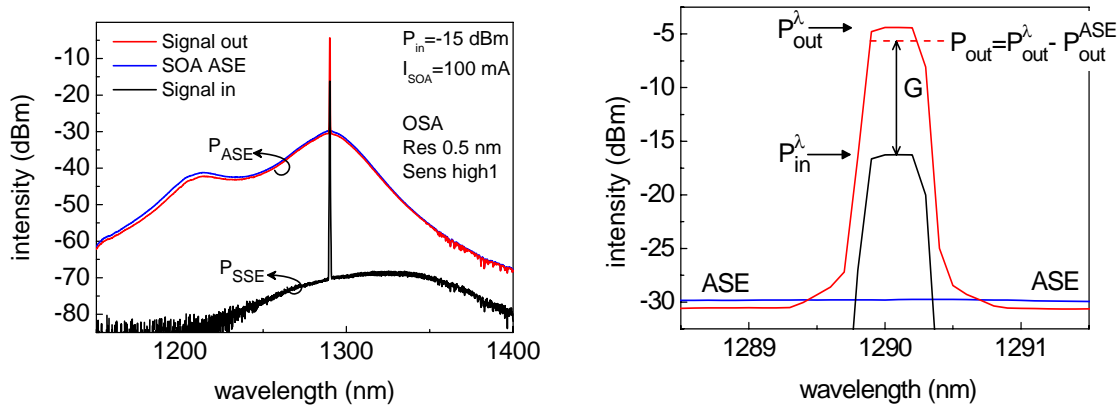


Fig. 4.17: Procedure for determination of accurate SOA gain. (a) Spectra of input and output signal and of ASE. If the noise levels are close to the signal levels they have to be subtracted from the peak values as depicted in (b). [ECL power -15 dBm, OSA span 300 nm, OSA center 1250 nm, OSA resolution 0.5 nm, OSA sensitivity high1, SOA current (DO520) 100mA]

The small signal amplification is defined within in the linear operation of the SOA. This can be verified by plotting G vs. P_{in} . The linear region requires that P_{in} is in the region in which the gain is largely independent of P_{in} . The small signal gain at the wavelength λ is calculated by

$$G = \frac{P_{out} - P_{ASE}}{P_{in}} \quad (4.10)$$

in linear units. The gain is given in decibels by using

$$G[dB] = 10 \log(G_{lin}) \quad (4.11)$$

and can be used to calculate the modal gain of an amplifier of length L or convert units from cm^{-1} to dB and vice versa

$$G[dB] = 10 \log \left(e^{g[cm^{-1}] \cdot L[cm]} \right) = 10 \log e \cdot g[cm^{-1}] L[cm]. \quad (4.12)$$

The measurement principle is depicted in Fig. 4.17 where the associated signal levels of the source spontaneous emission (SSE), ASE, input and output signal are plotted vs. wavelength. Usually, for each gain measurement data point a spectrum of the output signal – such as the red graph in Fig. 4.17(b) – is taken and evaluated for signal and ASE level.

4.2.3 Noise measurement technique

For a quantitative measure the noise figure of a SOA (chapter 2.2.5) can be evaluated by two methods:

- Using an optical spectrum analyzer (OSA) to measure the gain and the spectrally resolved ASE to calculate the noise figure terms of equation (2.35) except the noise contribution from multi path interference.
- Measuring the electronic noise with an electrical spectrum analyzer (ESA) and a broadband optical photodetector to evaluate the total noise figure including the multi path interference term. Note: this part is strongly dependent on the base frequency, linewidth of the source and polarization match of the multiple reflections.

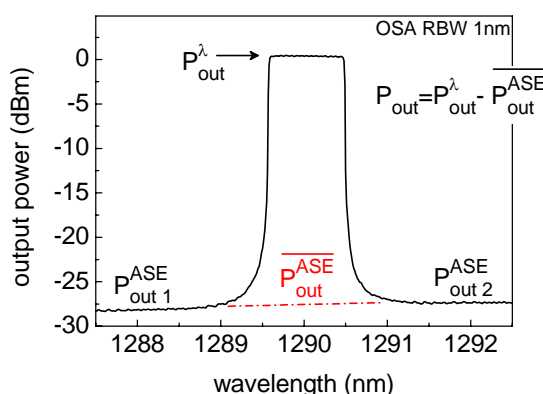


Fig. 4.18: Procedure for determination of accurate signal power from OSA measurement: Interpolation of the ASE levels and subtraction of this value from the peak power. (Here shown for the output power levels. Same procedure applies for input signal with signal spontaneous emission power).

Optical spectrum analyzer method

There are two alternate ways [185] to determine the signal-spontaneous noise figure with an OSA: the method of direct ASE-interpolation (DI) and the polarization extinction with interpolation method. Although the DI method has some limitations for a strongly wavelength dependent ASE spectral gradient and for large signal input power it is used here for its simpler setup and its satisfactory accuracy. The noise factor is calculated according to

$$N = \frac{P_{ASE}}{G h \nu B_0} + \frac{1}{G} - \frac{P_{SSE}}{h \nu B_0} \quad (4.13)$$

with the last term performing a subtraction of the amplified signal spontaneous emission P_{SSE} . As the measurement of P_{ASE} and P_{SSE} at the signal wavelength is not possible due to the presence of the signal peak, interpolation is required to estimate the noise powers at the signal

wavelength (Fig. 4.18). A detailed discussion on the calibration of the OSA and the determination of resolution bandwidth for this measurement is found in the technical annex 7.2.

Electrical spectrum analyzer method

With this method [186] the electrical noise is measured directly using a modulated signal that is amplified with the SOA and characterized in an electrical spectrum analyzer. It is based straight on the definition of the noise factor including all relevant noise contributions (chapter 2.2.5). Yet, it is strongly dependent on the base frequency, linewidth of the source signal and polarization match of the multiple reflections, which makes the method delicate in handling and interpreting of the results.

As all necessary information for the optical spectrum analyzer method is collected in our standard gain measurement we have not applied the ESA method to determine the noise factor.

Influence of coupling efficiency on noise figure

The coupling efficiency between the amplifier and the coupling fibers is very important for the noise figure. With $P_{\text{out}} = \eta_1 \eta_2 G P_{\text{in}}$ one can describe the signal output power of the amplifier under consideration of the input η_1 and output η_2 coupling efficiencies, respectively. For the ASE output power in fiber we use $\eta_2 P_{\text{ASE}}$ and thus, the signal-to-ASE ratio

$$\text{SNR}_{\text{out}} = \eta_1 \eta_2 G P_{\text{in}} / \eta_2 P_{\text{ASE}} = \eta_1 G P_{\text{in}} / P_{\text{ASE}} . \quad (4.14)$$

This shows that the output SNR is only dependent on the input coupling efficiency¹³. In order to realize a low-noise fiber-to-fiber coupled SOA it is important to reduce the input coupling loss.

4.3 Dynamic characterization techniques

4.3.1 Amplification of mode-locked laser pulse trains

The setup of this measurement is described in the context of the experiment in section 5.2.1.

4.3.2 Double pump- and probe setup

The gain dynamics in the amplifier are measured in collaboration with the group of U. Woggon, Universität Dortmund, by a femtosecond pump-probe technique with heterodyne detection as described in [187, 188] (see Fig. 4.19). Using an optical parametric oscillator pumped by a 75 MHz repetition rate Ti:Sapphire laser, tunable pump and probe pulses are

¹³ The input SNR is - by definition - independent of the coupling efficiency as it is measured before the coupling.

generated. From the pump pulse, pairs of 150 fs long Fourier-limited pulses with equal energies of the order of 0.1 pJ are generated using a Michelson interferometer [189].

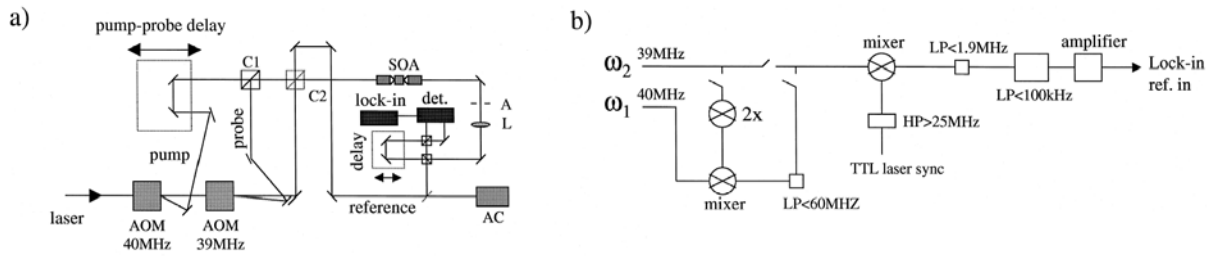


Fig. 4.19: (a) Experimental set-up for pump-probe technique with heterodyne detection. C1 and C2: broadband non-polarizing cube beam-splitters; A: 200 mm aperture, L: lens, AC: autocorrelator, SOA: semiconductor optical amplifier. (b) Scheme of the electrical mixing to generate the reference signal for lock-in. LP: low-pass filter, HP: high-pass filter. From [187].

The delay of these pairs can be set in a picosecond time range and the measurements are performed for 5 ps time delay. Two different wavelengths can be set, 1.3 μm (QD ground state) and 1.2 μm (QD excited state). The probe transmission with and without the pump, T and T_0 , are measured and the total gain is defined as $G = 10 \log(T/T_0)$. Then the temporal evolution of the gain change $\Delta G(\tau)$ induced by the two pump pulses in the ground and the excited states for different bias current is measured.

4.3.3 Eye-pattern and BER measurement technique

The system type measurements at 40 Gb/s with a pseudo random bit sequence (PRBS) optical data pattern were done in collaboration with the group of C. Schubert, Fraunhofer Institut für Nachrichtentechnik Heinrich-Hertz-Institut. Only two measurement sessions were available to characterize the QD SOA. For reasons of transportability and ease of alignment the QD SOA module (DO520 2mm x 4 μm , 6.8° tilt) was deployed. For all measurements the module was set at 17 °C. Eye-patterns and bit error ratio (BER) were recorded and tested.

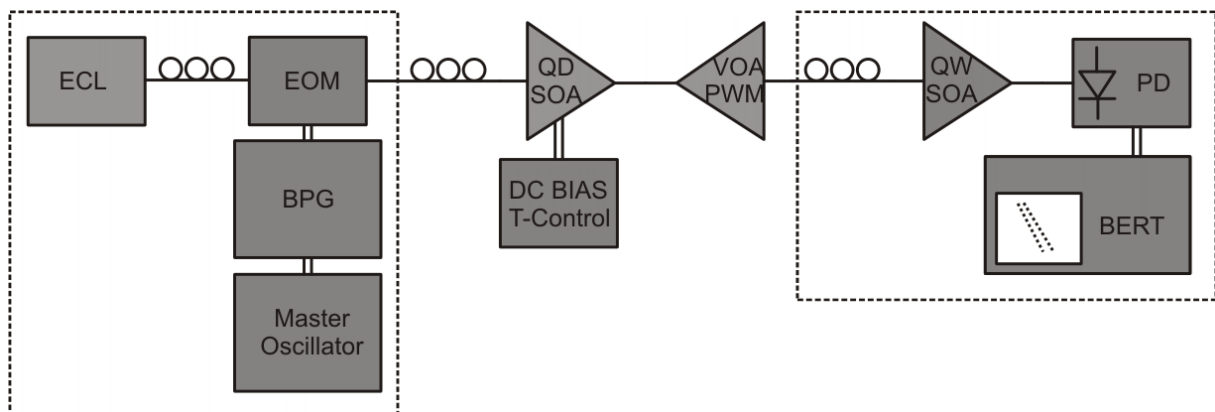


Fig. 4.20: Schematic setup for BER-Testing with a receiver unit containing an optical preamplifier. Referred to as “setup 1”. For measurement of the eye-diagrams the right part of the setup was replaced by a sampling oscilloscope with a precision timebase. Abbreviations given in Table 7.

For the two sessions different setups were used which are depicted in Fig. 4.20 and Fig. 4.21. All abbreviations are written out in Table 7. The data signal was generated by modulating a cw ECL signal ($\lambda=1290$ nm) with an electro-optical modulator (EOM) that was driven by a non-return-to-zero (NRZ) PRBS having a word length of $2^{31}-1$ generated by a BPG at 40 Gb/s

of the master oscillator. The amplified signal was either recorded by a sampling oscilloscope with a precision timebase (Agilent Infiniium DCA 86100B, 86107A, 86118A) for the eye-diagram or tested with a SHF EA44 BERT for evaluation of the BER.

Setup 1

Due to sensitivity problems on the receiver side – because of the QD SOA operating at a wavelength of 1.3 μm while the setup is optimized for 1.55 μm - an optical preamplifier (QW SOA) was used. The QD SOA was driven in polarization optimized booster configuration, i.e. directly following the modulator with -5.8 dBm constant input power amplified to +2.4 dBm by the QD SOA, i.e. the SOA was working in the saturation regime. The amplified pulses were attenuated by adjusting a VOA to set the receiver optical power. A back-to-back measurement is necessary to evaluate the characteristics of the setup without the QD SOA. This was done by extracting the QD SOA and setting the input power at the QW SOA at the same level as before. One would expect an improvement of the BER in the back-to-back configuration, but the BER deteriorated¹⁴ to a minimum value of only 10^{-4} . Comparing the eye-diagrams for both configurations showed also a better eye opening and jitter with the QD SOA.

Setup 2

As the back-to-back measurement was not feasible with setup 1 we used a modified scheme during the second session. Here the cw signal of the ECL was boosted with a QW SOA to compensate for losses in the EOM and have a larger modulated signal available that could be adjusted by the VOA in front of the QD SOA. The sensitivity problems on the receiver side were reduced by the use of an electrical broadband amplifier in front of the BERT. A constant input power of -1 dBm was amplified to +4.8 dBm, i.e. the QD SOA was also working in the saturation regime.

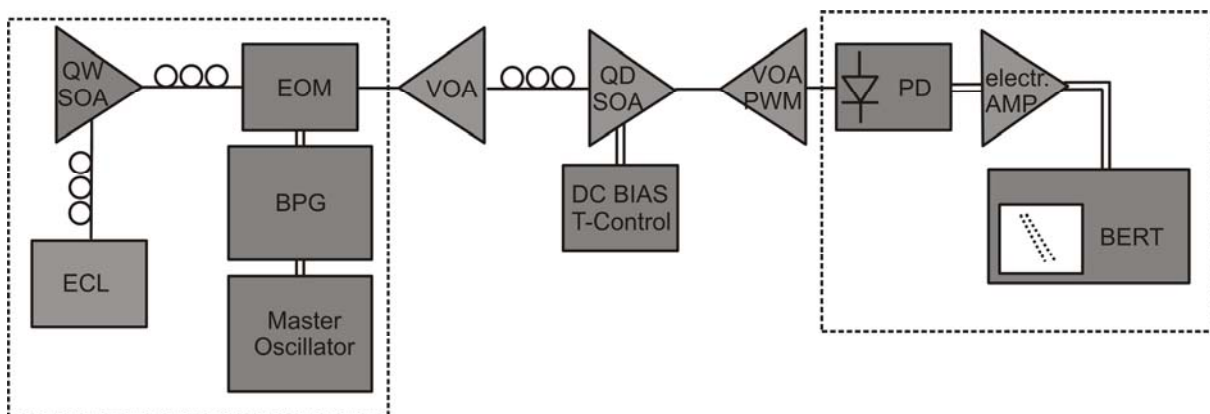


Fig. 4.21: “Setup 2” allows adjustment of input power, additionally, only the QD SOA influences the high speed optical properties. Abbreviations given in Table 7.

¹⁴ This is possibly due to a back-reflection of the signal in the system, deteriorating the EOM which has an automatic bias point control.

Table 7: Abbreviations used in schematic setup of Fig. 4.20, Fig. 4.21 and Fig. 4.22

AMP	Electrical amplifier	EOM	Electro optical modulator
ATT	Attenuator	MUX	Multiplexer
BERT	Bit error ratio tester	PD	Photodetector
BPG	Bit pattern generator	PWM	Powermeter
CWDM	Coarse wavelength division multiplexer	QD SOA	Quantum dot SOA
DC BIAS	Direct current bias	QW SOA	Quantum well SOA
DEMUX	De-Multiplexer	T-Control	Temperature control
ECL	External cavity laser	VOA	Variable optical attenuator

4.3.4 Small signal cross gain modulation setup

To measure the small-signal cross gain modulation (XGM), a small-signal modulated pump with high-power and a low power cw probe at a different wavelength are injected into the QD SOA. The modulation signal is generated and analyzed by a network analyzer (HP8722C 40 GHz Network Analyzer). The pump signal from an optically boosted distributed feedback (DFB) laser diode is sinusoidally modulated using a LiNbO₃ Mach-Zehnder modulator (Avanex SD40 – as characterized in the technical annex 7.3). A tunable ECL with operating wavelengths from 1260 nm to 1370 nm and an adjustable output power is used as the probe signal. Polarization controllers are used to align the polarization of the pump and probe signals with the optimum polarization of the EOM and SOAs. Pump and probe signal are merged with a CWDM MUX which also truncates the modulated ASE background of the pump signal. The output probe signal, cross gain modulated by the pump signal, is filtered with a CWDM DEMUX and converted in an electrical signal using a high-speed detector (u2t photonics). Finally, the small-signal XGM response is preamplified and analyzed with the network analyzer. The abbreviations are given in Table 7.

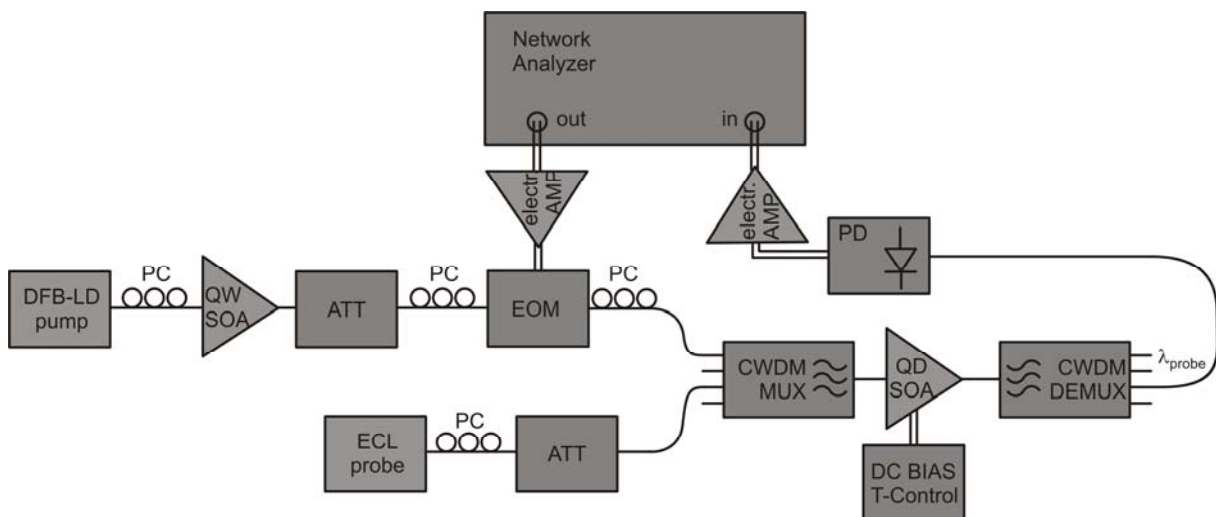


Fig. 4.22: Sketch of the dynamic XGM-setup with a fixed strong pump signal generated by a DFB laser diode amplified by a QW SOA and a variable probe signal provided by a tunable ECL. The small signal modulation of the pump wavelength is generated and the cross gain modulated signal is analyzed with a network analyzer. The CWDM multiplexer and de-multiplexer provide coupling of the signals and filtering within the channel bandwidth of 20 nm, thereby reducing the crosstalk of the modulated ASE. Abbreviations given in Table 7.

4 General Device Characterization and Measurement Techniques

The modulation power of the network analyzer and the optical probe power have been set to -10 dBm. The power for all pump wavelengths 1270, 1290 and 1310 nm is +1 dBm (Fig. 4.23a). The measured traces have been divided by the back-to-back measurement trace in order to cancel out the frequency response of the electrical amplifiers and the EOM (Fig. 4.23b). The measurement was performed and the network analyzer was calibrated in the frequency range 0-5 GHz as the main dynamic was expected in this region.

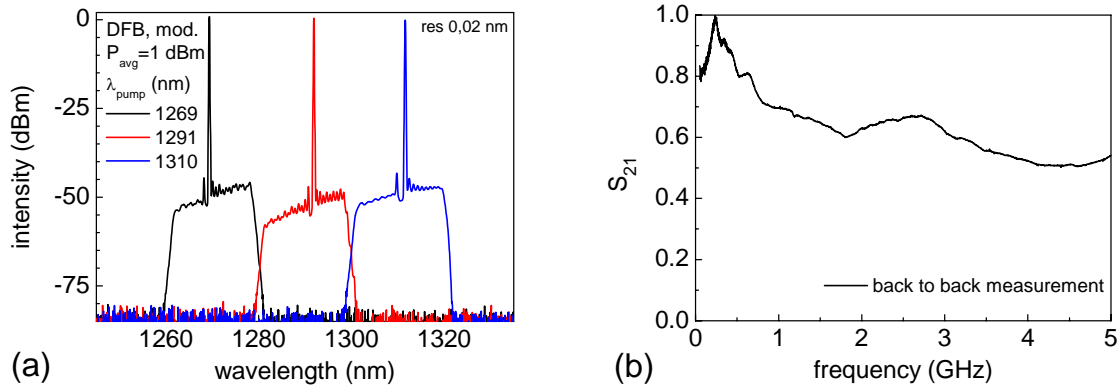


Fig. 4.23: (a) Spectra of three different input DFB lasers after amplification with QW SOA and after CWDM MUX filter truncating each spectrum at ± 10 nm around its center. (b) Small-signal measurement of the directly modulated signal. This back-to-back measurement is used to deconvolute the influence of EOM and electrical amplifier response from the XGM measurement.

5 Application Oriented Experiments with QD SOAs

5.1 Static amplification experiments with QD SOAs

The detailed characterization of two different samples (DO453 and DO520) as described in sections 3.2 and 4.1.1 is presented in this chapter. The cw characteristics are important to assess the operating conditions for the dynamic experiments in chapter 5.2.

5.1.1 QD SOA gain and ASE characterization

Without an input signal an amplifier emits amplified spontaneous emission (ASE) when a current is applied to the pn-structure, i.e. we observe the electroluminescence of the device. The ASE spectrum is a good measure of the position of the gain peak, FWHM of the gain curve and the gain ripple, because the ASE is proportional to the amplifier gain as described in section 2.2.4. Fig. 4.15 shows the measured gain and the corresponding ASE as a function of the wavelength. The correlation between ripple, peak and gain roll-off is good. A departure between ideal correlation of ASE and gain ripple is observed. It may be due to the gain ripple since the gain measurements are carried out at specific wavelengths whereas the ASE represents an average over the spectrum.

Fig. 5.1(a) shows a series of ASE spectra for different currents. For low currents the SOA emits solely from the inhomogeneously broadened ground state (GS) at 1290 nm with a spectral FWHM of 25 nm, for larger currents the excited state (ES) at around 1210 nm turns on and eventually dominates the emission. At 1100 nm we observe the onset of the wetting layer emission. A good homogeneity of the QDs is indicated by the spectral width of 25 nm. The ES group involves the recombination of electrons and holes in excited states. Transparency (i.e., one exciton on average) is reached for the GS transitions at a lower injection current than for the ES transitions, and the GS gain saturates for currents larger than 120 mA.

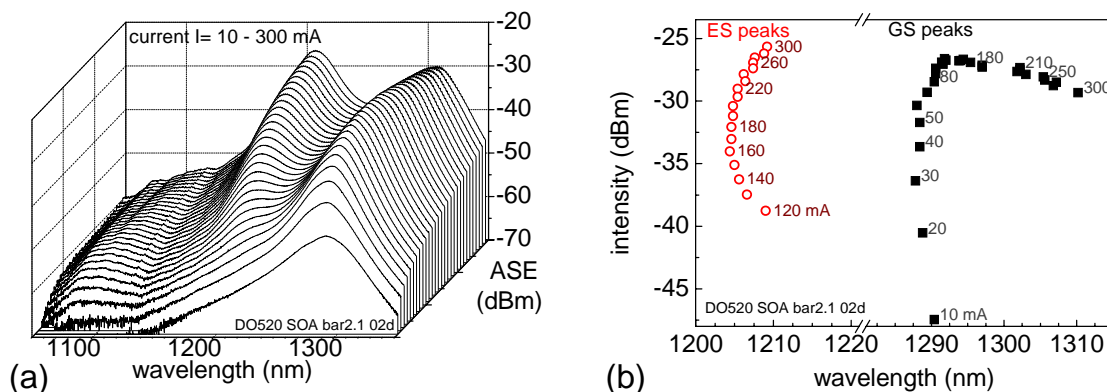


Fig. 5.1: (a) ASE spectra for different bias current showing ground state (GS), excited state (ES) and the onset of WL state emission. (b) Spectral position of the GS and ES peaks for different bias current.

In Fig. 5.1(b) the spectral position of the GS and ES peaks is plotted. With increasing current the GS first shifts to higher energies, then starts to shift slowly to the red, and for large currents exhibits a strong wavelength shift to the red. The ES shows the same general trend.

This behavior is attributed to a band filling effect with a renormalization of the bandgap and a thermal shift due to heating of the gain section, respectively. The ground state clearly saturates while the excited state shows no saturation at this current level.

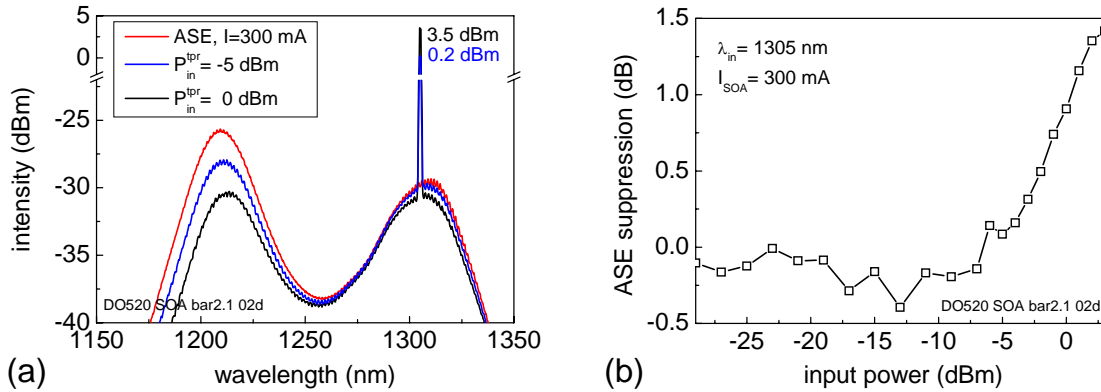


Fig. 5.2: (a) ASE spectrum and ASE combined with amplified signal for two input powers saturating the amplifier at $I=300$ mA. Note, the intensity scale features a break. (b) Suppression of ASE, measured as difference between saturated and unsaturated ASE level at the signal wavelength $\lambda=1305$ nm for various signal input powers. For input powers larger than -5 dBm the SOA starts to saturate.

If an external optical signal is injected into the SOA the signal is amplified by the gain that is available at its spectral position. If the signal saturates the available gain, the replenishment of the carriers will be from other states, thereby decreasing the ASE over a large wavelength region. This is examined in Fig. 5.2 where the ASE is compared for no and saturating optical injection. The saturation is not only observed in the ground state but has a strong impact on the ES emission, too. The ASE is suppressed only for input powers larger than -5 dBm while it is constant in the region below (Fig. 5.2b). This characterizes the two main operation regimes of an optical amplifier

- the linear region where the output is directly proportional to the input of the amplifier or in other words the gain is constant, and
- the non-linear region where we observe a saturation of the gain and the relation between input and output is non-linear.

Measuring the ASE with a high resolution spectrometer displays the spectral ripple due to the residual reflectivity of the facets which build a Fabry-Perot cavity modulating the longitudinal optical mode. In Fig. 5.3 a section of the ASE spectrum was measured with a resolution of 0.01 nm for increasing current. A difference in current of $\Delta I=10$ mA yields a shift of $\Delta\lambda=0.1$ nm. This explains why the gain-current graph (Fig. 5.3b) exhibits a modulation although the measurement was conducted at a fixed wavelength. The occurrence of ripple in the gain-current characteristics has also been discussed in section 2.2.3. The sample (DO520) has a tilted ridge waveguide and an additional AR-coating. By this means the lasing action is successfully suppressed. Still, the measurements show a residual ripple up to 4 dB which is disturbing for the device performance. In the same manner as the gain is saturated, the gain ripple is also reduced as it can be seen in the figure for various input powers.

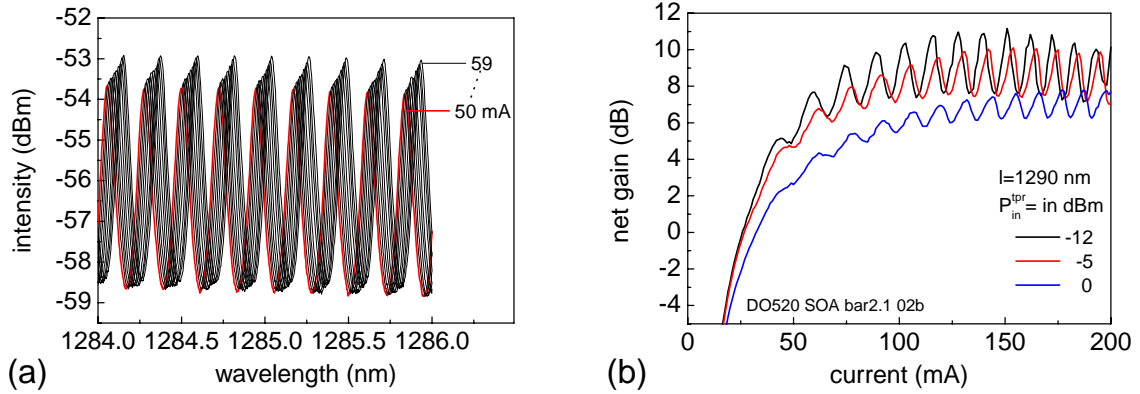


Fig. 5.3: (a) Shift of ASE ripple for different currents. (b) Gain vs. current showing ripple which are more or less pronounced depending on the input power.

Gain as a function of current is important because the optimum driving conditions of the amplifier are derived by this measurement. The optical gain is found to increase with increasing current, then it saturates. This is because only a limited amount of QDs is available that can be inverted and contribute to the gain. We have also found the optical gain to decrease with temperature from a net gain of 12.5 to 3.5 dB in the range from 15 to 80 °C. Reasons for this could be a non-radiative recombination which increases with temperature. This causes a reduction of gain or a carrier redistribution over a wider range, and less carriers participating at the gain at the given wavelength.

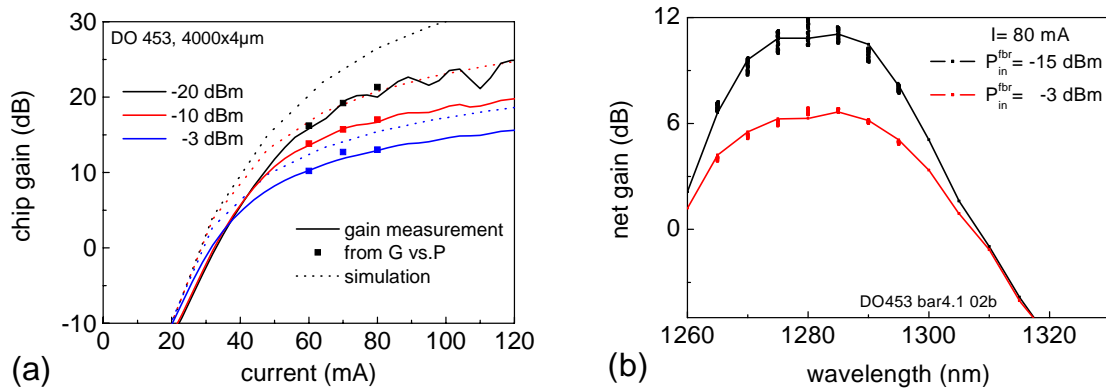


Fig. 5.4: (a) Current dependency of chip gain for various input powers at $\lambda=1280$ nm. The broken lines show corresponding simulated curves according to a rate equation model [Courtesy of M. Kuntz [86]]. (b) Spectrally resolved net gain of the same chip as in [a]. The line shows the result if one data point is taken every 10 nm. Only if a subscan of 50 points with a stepwidth below the Fabry-Perot spacing is measured, the gain ripple is resolved (shown as discrete data points).

The gain-current dependency (de-embedded for chip gain) for various input powers at $\lambda=1280$ nm is shown for the sample DO453 with 4 mm length in Fig. 5.4(a). The measured data (solid lines) is compared with measurement points from the gain vs. power graph (Fig. 5.6a) which coincides well. The broken lines show corresponding simulated curves according to a rate equation model [86] with parameters that have been extracted from laser characterization. The simulated values overestimate the measured data, but agree with the general shape of the curves. The deviations between model and measurement stem from the error in subtraction of the coupling losses to get the chip gain, from the gain ripple which is not included in the model, and from the limitation of the model which is not spatially resolved along the amplifier length.

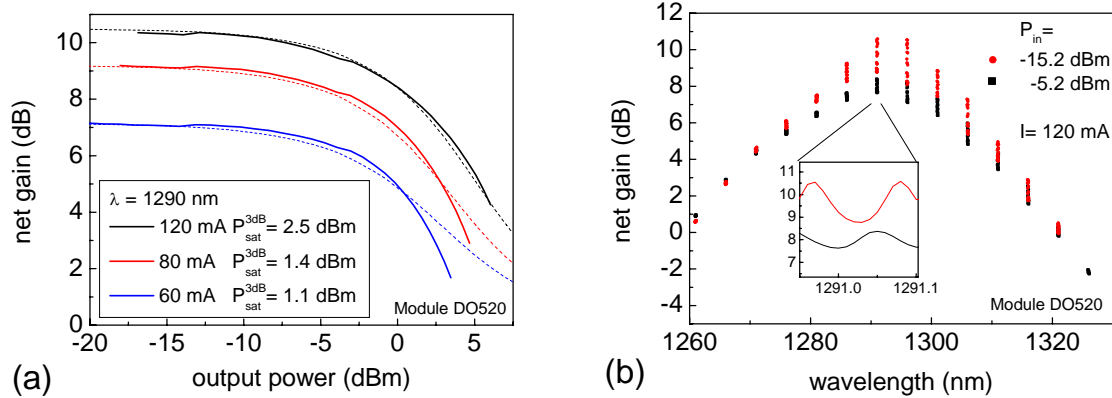


Fig. 5.5: (a) Module net gain vs. output power for three bias currents. The broken lines are fits from equation (2.12) with linear gain and saturation output values as fitting parameters. (b) Spectrally resolved net gain of the QD SOA module. A subscan of 50 points with a stepwidth below the Fabry-Perot spacing is measured and the gain ripple is resolved (shown as discrete data points). Inset shows one subscan region.

As discussed in the theory part, the optical gain decreases with increasing optical input power (which is the same mechanism as for the saturation in gain as a function of current). The module net gain as a function of output power is presented in Fig. 5.5(a) for three bias currents. The broken lines are fits from equation (2.12) with linear gain and saturation output values taken from the measurement as fitting parameters. The fits agree nicely with the measured data for large gain and low input power. The deviation for larger input/output powers has its origin in the implicit function which was used to generate the fit, because it approaches zero (0 dB) for large output powers. If we do not consider the net gain but the actual chip gain, as it was done in Fig. 5.6(a) for DO453, data and fit show a better agreement for large output power.

Fig. 5.4(b) and Fig. 5.5(b) summarize the spectrally resolved net gain of the samples DO453 and DO520. A subscan with a stepwidth below the Fabry-Perot spacing was measured and the gain ripple of the devices is clearly resolved. For both structures we find a FWHM of the spectral bandwidth of about 30 nm slightly dependent on the saturation condition. This is a rather small value comparable to typical QW devices. This result indicates that these QDs are relatively homogeneous in contrast to other QD or QDash samples where much larger inhomogeneities and bandwidths have been reported [41, 42, 190].

In this section the full cw gain characterization of our QD SOAs was shown. The typical gain saturation behavior of SOAs was observed and compared with theory. The spectral width of 30 nm is surprisingly small as compared to other inhomogeneously broadened gain media.

5.1.2 Noise figure of QD SOAs

The theoretical concept of the noise figure was introduced in detail in part 2.2.5 and the measurement method needed to evaluate this parameter was described in section 4.2.3. In order to evaluate the chip performance the coupling losses were de-embedded from the results. For the employed ridge waveguide-tapered fiber combination a 4 dB coupling loss for each facet of the chip (DO453) was found that was added to the measured net gain or net noise figure. For three different bias currents the gain was evaluated at 1280 nm with respect to the output power (Fig. 5.6a). A maximum chip gain of 25 dB at 80 mA in the linear regime and a 3dB-saturation output power of 4 dBm at 60 mA was found. In Fig. 5.6(a) the broken

lines are fits from equation (2.12) with linear gain parameters from the measurement and assumed 5 dBm saturation output power. The fits agree nicely with the measured data for 60 and 70 mA. For 80 mA a considerable departure of the measurement from the fit is found. This is explained by the saturation through lasing as the chip showed lasing at currents starting from 80 mA due to insufficient AR coating for the 4 mm long device.

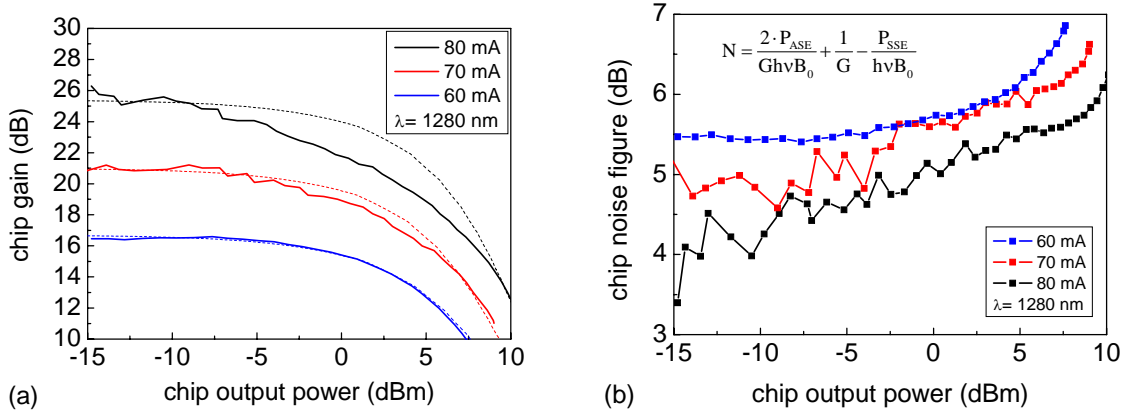


Fig. 5.6: (a) Chip gain vs. chip output power for three bias currents. The broken lines are fits from equation (2.12) with linear gain and saturation output values as fitting parameters. (b) Chip noise figures corresponding to the measurement range in [a], calculated with the formula stated in the graph [Sample DO453 4mm x 4 μ m, AR].

The corresponding noise figure of the SOA was measured with an optical spectrum analyzer method using direct amplified spontaneous emission interpolation. We have accounted for the polarization sensitivity (see section 2.2.5) of the device and, hence, we find the noise figure dependence on input power and bias current as shown in Fig. 5.6(b). The noise figure is increasing for larger input power and for smaller current. This behaviour is expected because in both cases the input SNR is about constant while the SNR within the device gets smaller as 1) for the current range 80-60 mA the ASE decreases much less than the gain and thus the signal power and 2) for saturating input power the gain drops while the ASE decreases only a little by suppression (Fig. 5.2b). A minimum chip noise figure of 4 dB is yielded at 80 mA which is close to the theoretical limit of 3 dB at large gain.

For the QD SOA module with structure DO520 we achieve a net noise figure of 8-12 dB including the fiber coupling losses. This is in the range of commercial devices, which have a much smaller coupling loss due to their buried heterostructure design.

5.1.3 Multi wavelength amplification and ASE cross gain modulation

In order to assess the coarse wavelength division multiplexing (CWDM) feasibility of the QD gain medium we have performed multi-wavelength amplification measurements with the SOA module using DFB lasers in CWDM wavelengths at 1270 nm, 1290 nm and 1310 nm. A positive net gain for simultaneous amplification in all three channels was achieved. The gain measured at each wavelength is compared for only one wavelength present in the device with three simultaneously amplified wavelengths. The resulting gain saturation is shown in Fig. 5.7(a) for amplification in the linear and non-linear regime at low and high output power, respectively. Negligible multi-wavelength saturation (<0.3 dB) is observed in the linear regime while the gain saturation of the SOA prevails over the complete spectrum in the non-linear regime.

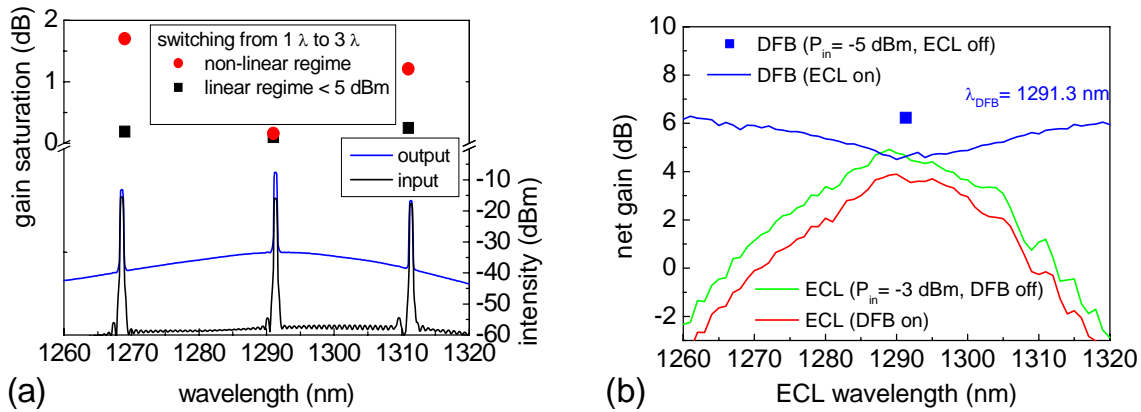


Fig. 5.7: (a) Bottom: Spectra of three CWDM DFB lasers before and after amplification at 1270, 1290 and 1310 nm. Top: Gain saturation, i.e. difference of gain for amplification of one or three wavelengths simultaneously, for linear and non-linear gain regime. (b) The cross-gain saturation is mapped between DFB laser at fixed wavelength 1291 nm and ECL scanned from 1260 to 1320 nm in the non-linear regime of the SOA.

This is also found when an external cavity laser is tuned from 1260 to 1320 nm with respect to a fixed DFB-laser wavelength to find the influence of the distance of two signals present in the amplifier. We observe no suppression of the gain if both signals operate in the linear regime, i.e. the both wavelengths are amplified independently no matter how close they are. The situation changes if the input signals saturate the amplifier. Fig. 5.7(b) presents the case where the power of both wavelengths independently leads to a gain saturation of the device. If both signals are amplified, the gain of each of the two wavelengths is suppressed further and this suppression is found to be present over the whole spectral bandwidth of the SOA with a maximum as large as 2 dB when the wavelengths are close to each other. This is attributed to carrier depletion of the shared carrier reservoir.

In the linear regime of the SOA at low input power no influence of the CWDM wavelengths is found, which shows the potential for pattern effect free multi-wavelength data transmission.

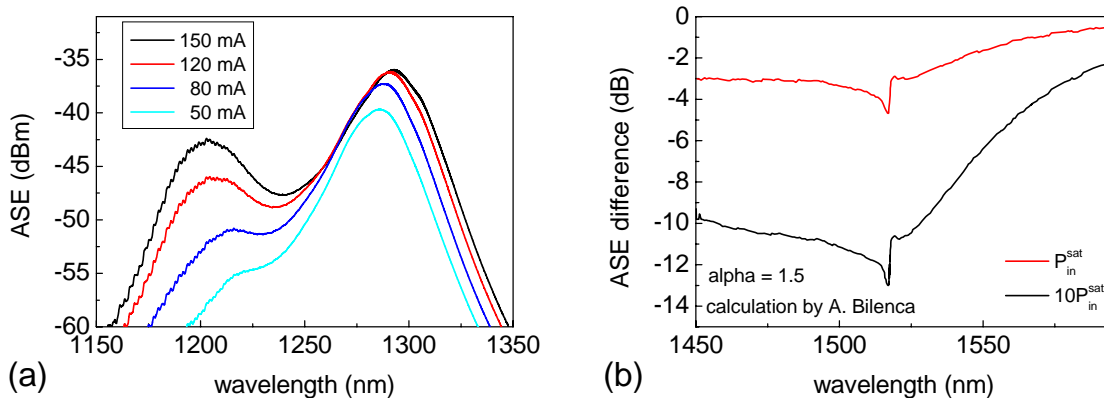


Fig. 5.8: (a) ASE spectra of module at various bias currents. (b) Calculation of ASE difference for strongly saturating signal for a quantum dash amplifier. [Adapted from modeling of A. Bilenca [112]. Courtesy of G. Eisenstein.]

The cross gain modulation can be assessed by measurement of the ASE suppression due to a saturating input signal. As a motivation the theoretical investigation on noise properties of quantum dot SOAs at 1.55 μm is considered [112]. The ASE of an optical amplifier is related to the carrier distribution in energy, the gain spectrum, and the saturation properties which in turn are strongly affected by the gain inhomogeneity and the gain dynamics. The noise is

determined in saturation by the deterioration of the population inversion and nonlinear interactions between the saturating signal and the noise. Fig. 5.8(b) shows that a coherent spectral hole is formed whose width and depth are determined by the medium response time and the injected power level. A spectral hole with two parts is observed near the input wavelength. The first hole results from saturation of the inhomogeneously broadened gain and its width depends on the degree of overlap between adjacent QD groups and on the input power. The narrower (and deeper) portion is due to a distributed nonlinear interaction between the saturating signal propagating down the amplifier axis and the amplifier noise. The noise properties are governed by two important characteristics of QD gain media: the inhomogeneous gain broadening and the fast carrier dynamics.

To investigate the dependence on various input wavelengths we have chosen two bias currents: a) 50 mA where mainly the GS is populated and b) 150 mA where the GS is saturated and the ES is populated (see Fig. 5.8a). The input wavelengths correspond to values below (1270 nm), at (1290 nm) and above (1310 nm) the QD gain maximum. The input power was varied between -11 and +5 dBm. For 50 mA bias (Fig. 5.9 upper row) we obtain a picture that is similar to the above presented theoretical calculation. The ASE difference shows an asymmetry where the long wavelength tail is not so strongly affected by the saturation as the wavelengths shorter than the input wavelength. A large saturation of the GS up to 6 dB at the gain maximum was observed for strongly saturating input power of +5 dBm. The occurrence of a narrow spectral hole (if any) can not be seen due to the presence of the signal wavelength in the spectra.

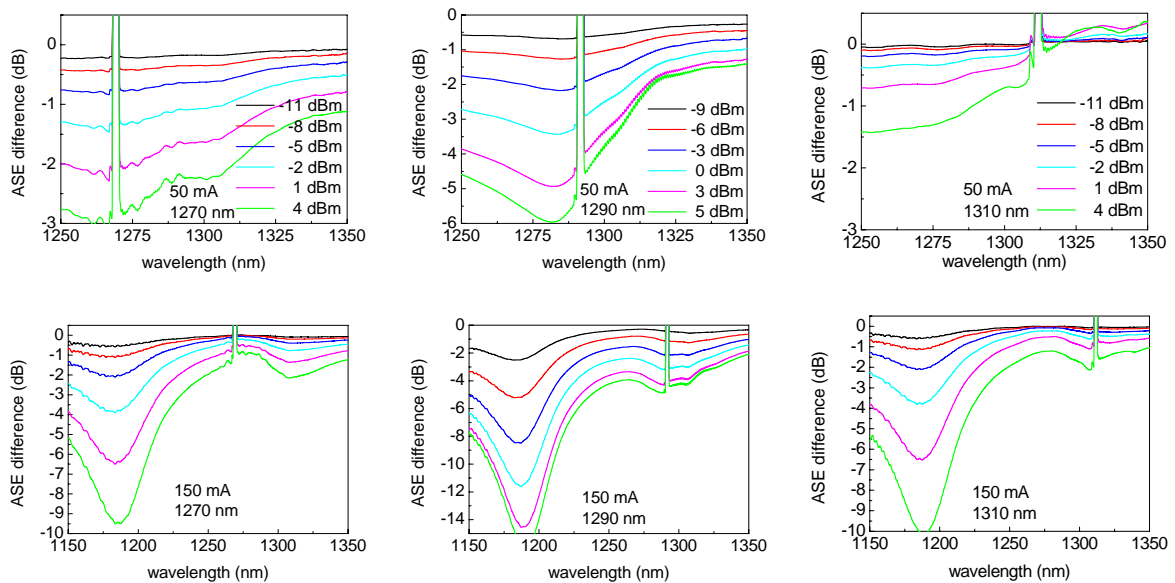


Fig. 5.9: ASE cross gain modulation for 50 mA (upper row) and 150 mA (lower row). Pump wavelength is varied from 1270, 1290 to 1310 nm from left to right. In the lower row the spectrum shows also the influence of the excited state at the same input power levels as the graphs above.

For 150 mA bias (Fig. 5.9 lower row) the shape of the ASE difference at the GS is different to the case of 50 mA. This is due to the contribution of the ES which serves as an efficient and fast carrier reservoir mediating a large part of the gain saturation by fast refill of the GS. The ES state population was not included in the above described modeling.

From these measurements we can conclude the following:

- We observe only a wide spectral hole due to the limitations of the present signal in the spectra.
- The hole with the shallow slope is due to the general ASE reduction. The hole is more pronounced for larger powers since carrier replenishment in a particular saturated QD

group originates from other, spectrally neighboring, QD groups which is typical for an inhomogeneously broadened gain medium.

- For short wavelengths, the spectral hole is smaller due to the reduced four wave mixing efficiency and the strong coupling to the ES and wetting layer. For long wavelengths, the spectral hole is also smaller than the one at the gain peak because of the larger saturation power.

5.1.4 Polarization dependence of QD SOAs

The polarization sensitivity of SOAs must be examined in order to improve the performance of these elements in optical systems. From a technical point of view a gain difference between the optical TE- and TM-mode of less than 3 dB (1 dB) is desired in data transmission systems.

In literature different terms are used in the framework of polarization of amplifiers and gain media. We adhere to the definition given in chapter 2.3.2. Light which propagates along the xy-plane has two possible polarizations. In the case of the transverse-magnetic (TM)-mode the polarization is aligned with the z-direction. For the transverse-electric (TE)-mode the polarization is along the xy-plane, here we assume it to be parallel to the x-direction. Therefore, the TE- and TM-modes are often referred to as parallel and vertical mode, respectively. The difference between parallel and vertical vector of the polarization specifies the so-called polarization ratio.

In a calibration routine the electrical controllable polarization controller (HP11896A) is scanned until maximum output of TE or TM (set by polarization filter after the taper) is detected (Fig. 5.10a). The positions of four fiber loops inside the polarization controller are recorded. Although all fibers are non-polarization-maintaining SMF the polarization output of the taper is stable and reproducible as long as the fibers remain untouched.

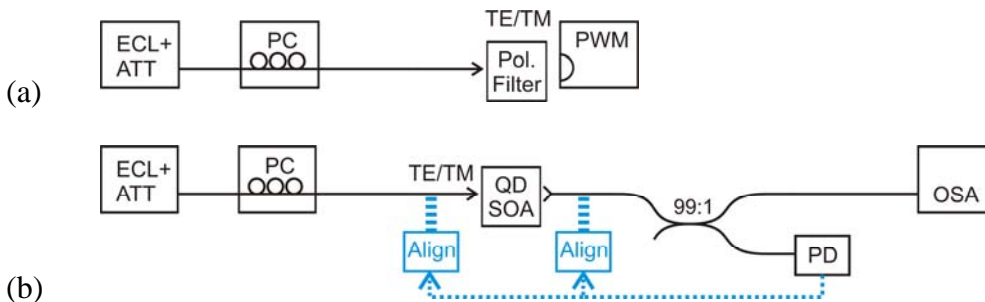


Fig. 5.10: Schematic setup to measure TE/TM polarization dependence of the QD SOA chip. (a) Calibration routine to set the output polarization of the fiber taper. The polarization controller (PC) is controllable via GPIB. (b) Measurement of the polarization dependent gain of the chip under test by setting the input polarization with the PC.

By setting the positions of the polarization controller the input signal into the QD SOA is adjusted to TE or TM when the gain is measured. The alignment of the input and output fiber tapers is controlled by the divided output signal. The gain is calculated from the optical spectrum as described in section 4.2.2.

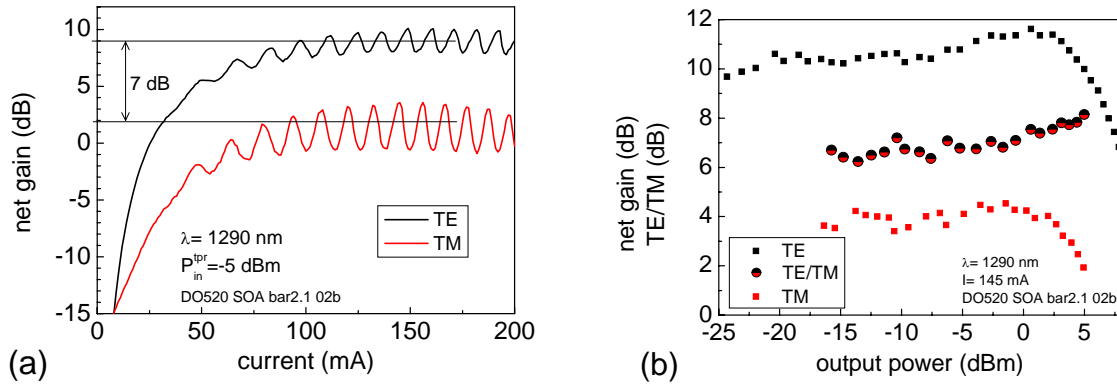


Fig. 5.11: (a) Net gain vs. current for TE and TM polarization (b) Measurement of polarization dependent gain of the QD SOA showing a 6-8 dB TE/TM ratio.

Using TE and TM polarized input we have investigated the polarization dependence of the QD gain. Fig. 5.11 shows the resulting gain measurement versus current and output power. The TE polarized gain is nearly congruent to the measurement with optimized polarization, i.e. the amplifier is dominantly TE polarized.

We find a polarization ratio of 6-8 dB which is slightly varying between the linear and nonlinear region of the amplifier. This can be explained by a larger saturation of the overall smaller TM gain. The ten QD layers of the sample have been grown with a large spacer (see section 3.2) resulting in decoupled QDs which should emit mainly in TE direction as indicated by the modelling described in 2.2.6. The ridge waveguide has a rectangular shape which is also supporting dominantly TE polarized light as can be seen from calculating the optical mode of this structure (section 2.3.1). Therefore, the measured 6 to 8 dB suppression of the TM gain compared to the TE gain is consistent with the structure and epitaxy of the SOA.

5.2 Dynamic amplification experiments with QD SOAs

Typically SOAs are deployed in optical data transmission systems and used as elements in all-optical wavelength processing. For all applications their dynamic performance in the linear and non-linear amplification regime is of importance. In this chapter we have investigated the unique speed properties of QD SOAs with various methods. With mode locked lasers processed from the same QD material we were able to amplify ultrafast pulse trains with an exact match of the gain profile. These experiments demonstrate the bitrate potential of the devices, but no information on patterning or saturation effects is immanent in these results. By pump-probe experiments we get a detailed picture on the recovery and saturation effects of the QD SOA. System performance and patterning effects are analyzed by measurement of eye-patterns and bit error ratios. For the application in optical processing it is essential to investigate the cross gain modulation performance which we have investigated with small-signal modulation experiments.

5.2.1 Amplification of mode-locked laser pulse trains at 20 to 40 GHz

Data transmission is generally done with a modulated signal source that is transmitted through a glass fiber. Due to absorption in the fiber or losses in passive nodes the signal needs to be amplified after a certain range. Three categories of optical sources are available: Directly

electrically modulated lasers, cw lasers combined with an electro-optical modulator, and mode-locked lasers in a combination with a phase or intensity modulator. The first two methods resulting in a non-return-to-zero (NRZ) signal, the second in a return-to-zero (RZ) signal. We have investigated the high frequency suitability of QD SOAs by amplifying a train of mode-locked laser (MLL) pulses. These ultrafast optical combs are emitted from mode-locked lasers based on the same QD material. This is the first important step in understanding the performance of amplification of RZ signals without influence of data patterns.

The samples for mode-locking were processed into two-section devices with a gain (90%¹⁵) and an absorber (10%) section by defining a 20 μm gap in the p-metal and by dry etching through the contact layer in this gap (see section 3.3.1). The MLLs with lengths of 2, 1 and 0.5 mm for 20, 40 and 80 GHz repetition frequency, respectively, were passively (80 GHz) and hybridly (20, 40 GHz) operated at currents from 20 mA to 100 mA and reverse bias voltages between 0 and -10 V. For hybrid mode-locking rf-power up to 14 dBm was applied to the absorber section. For the amplification measurements optimum operating points of the MLLs were selected with regard to stability, pulse width or jitter performance.

In order to evaluate the full performance of the MLL we have conducted parameter scans of the reverse bias vs. gain current to record maps of FWHM pulse width, pulse offset, center frequency, peak intensity and rms jitter at 20, 40 and 80 GHz [86]. This allows choosing the optimum operating point of the devices for the subsequent amplification experiments. The map of the FWHM pulse widths extracted from autocorrelation measurements is shown in Fig. 1 for 80 GHz, representatively. With hybrid mode-locking the shortest deconvoluted pulse width obtained, best fitted by a sech^2 shaped pulse, was 710 fs at 20 GHz, which is the shortest pulse width for all devices we investigated. The maximum repetition frequency we achieved was 80 GHz with a minimum pulse width of 1.9 ps. The corresponding spectrum yields a time-bandwidth product of 1.5, which is well above the Fourier transform limit of 0.32, indicating the large potential to further reduce the pulse width.

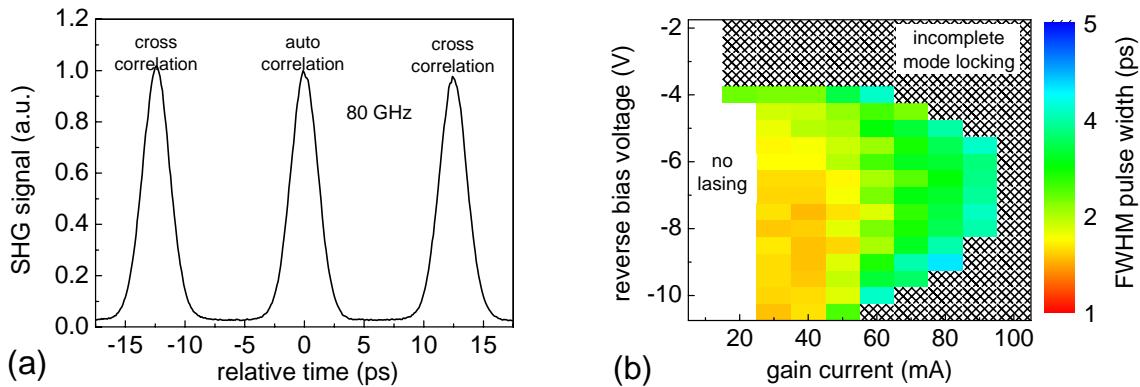


Fig. 5.12: (a) Auto- and cross-correlation trace of a passively mode-locked quantum dot laser at 1.3 μm and 80 GHz repetition rate (sample DO453). (b) Field scan of autocorrelation traces with color-coded FWHM pulse widths and regions of no or incomplete mode-locking. [Courtesy of M. Kuntz [86]]

In order to amplify the pulse train of the MLLs, they were fiber-coupled to a 4000 μm long, 4 μm ridge SOA chip of the same QD gain material and ridge waveguide structure (DO453). The cw characteristics of this chip are analyzed in section 4.2.2. The straight device shows large gain ripples and lasing at currents larger than 80 mA due to insufficient AR coating. The lasing can be suppressed by large optical input, but the gain is clamped at lower values. Both, the MLL and the SOA were actively fiber coupled as described in section 4.2.1. Input and

¹⁵ of the device length

output auto- and cross-correlations of the pulse trains were recorded. The comparison of the normalized input to the output traces could reveal pulse broadening and a change of the background intensity. The pulses were mainly characterized by measuring the second harmonic generation (SHG) signal of an autocorrelator, additional information was gathered with measurements of the integrated power, electrical and optical spectra and jitter measurements. The schematic setup is presented in Fig. 5.13.

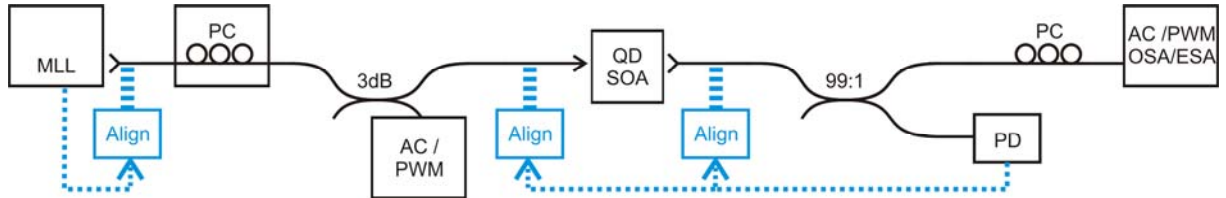


Fig. 5.13: Schematic setup of amplification of QD MLL pulses with a QD SOA and its characterization by auto-correlator (AC), power meter (PWM), optical (OSA) and electrical spectrum analyzer (ESA). The active alignment to couple light in and out of the fibers is sketched in blue.

The 20, 40 and 80 GHz pulse trains were amplified by the QD SOA. Fig. 5.14 shows the corresponding autocorrelation (AC) traces of the input and output signals.

With hybrid mode-locking at 20 GHz the shortest full-width-at-half-maximum (FWHM) AC pulse width obtained was 1.1 ps (convoluted, i.e. obtained from the AC measurement), best fitted by a sech^2 shaped pulse to 710 fs (deconvoluted), which is the shortest pulse width for all devices we investigated. The MLL operated at a gain current of 70 mA and reverse bias voltage of -9.5 V. This pulse train was amplified by the QD SOA at $I_{\text{SOA}} = 70$ mA and we were able to stable measure while all fiber couplings were actively aligned. Within the measurement uncertainty no degradation of the AC pulse shape induced by the SOA could be observed (Fig. 5.14a red). Also, the cross-correlation (not shown) was not significantly deteriorated. This was difficult to quantify as the pulse train showed amplitude jitter (before and after the SOA) which was revealed in the fluctuation of the cross-correlation amplitude. We have investigated the electrical spectrum before and after amplification (Fig. 5.17b). Again, we find no influence of the SOA on the pulse characteristics, the linewidth remains the same. A fiber-to-fiber gain of 10 ± 0.5 dB with respect to the average input/output power was achieved which results in a de-embedded chip gain of 22 dB and a 3dB-saturation output power of 6 dBm after consideration of a 6 dB fiber-to-chip coupling loss per facet.

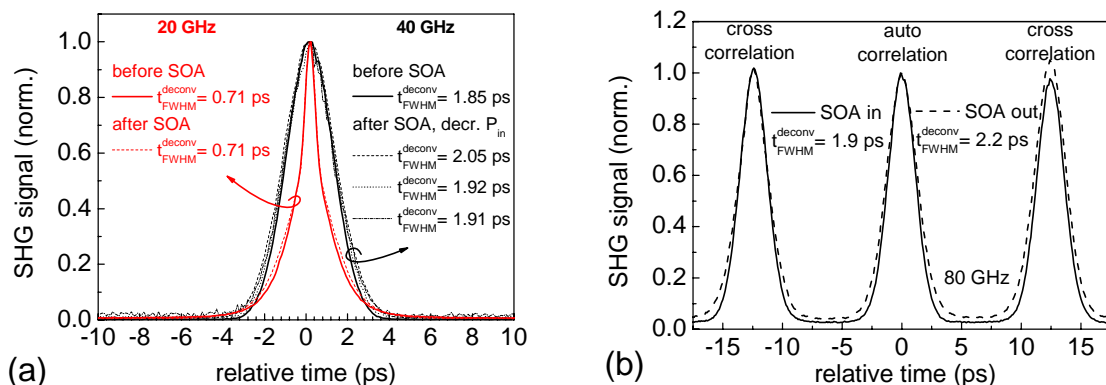


Fig. 5.14: (a) 20 and 40 GHz hybrid mode-locking signals before and after the SOA chip. Solid line (input) and dotted lines (output) for various (decreasing from top to bottom) input powers. (b) Cross- and autocorrelation signal of 80 GHz passive mode-locking at input (solid) and output (dashed) of the SOA.

A 40 GHz signal from a 1 mm long hybridly MLL at a gain current of 40 mA and reverse bias voltage of -7 V (rf-power 14 dBm) was amplified and Fig. 5.14(a) shows the autocorrelation

of the signal before and after the QD SOA. Here we find an increase by 4% in the deconvoluted pulse width from 1.85 ps to 1.92 ps in the linear gain regime. For larger input powers the pulse width further increases up to 2.05 ps for $P_{in} = -8.1$ dBm in the non-linear regime of the amplifier. The optical spectra differ considerably before and after amplification (Fig. 5.15a). The input spectrum of the MLL is modified by the ASE of the QD SOA and the output spectrum exhibits a broad background. But the signal-to-ASE ratio is still up to 30 dB, therefore, we assume that the ASE does not influence the pulse shape. It could contribute to the cw background of the pulse train, but this is not observed in the AC measurement where it would appear as a pulse offset.

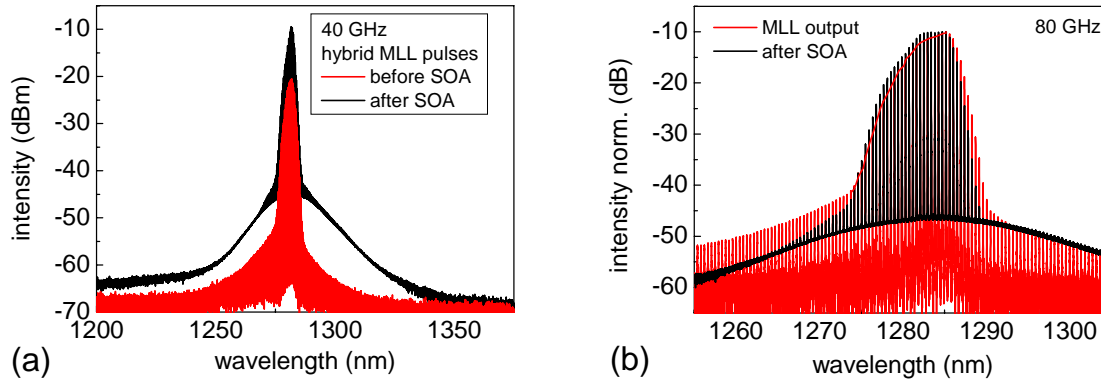


Fig. 5.15: (a) Spectra of 40 GHz MLL pulses before and after amplification. (b) Spectra of 80 GHz MLL before and after amplification. For comparison of the shape, the spectra have been shifted to the same maximum value.

An ultrafast pulse train of 80 GHz was investigated using a 500 μm long passively mode-locked laser at $U_{reverse} = -7$ V and $I_{gain} = 45$ mA. Auto- and cross-correlation of the optical comb before and after the SOA are presented in Fig. 5.14(b). No significant change of the auto-correlation is observed, but the pulse width exhibits a broadening by 15% after amplification. The deconvoluted pulse width increases from 1.9 to 2.2 ps. The graph suggests an offset of the amplified pulse, but the different cw offset of the autocorrelation traces is an artifact due to the normalization of the signal in different measurement ranges of the autocorrelator. The cross-correlation also remains unchanged within the measurement margin. This indicates an undisturbed correlated jitter performance. More detail jitter measurements are presented below. Fig. 5.17 summarizes measurements for different SOA bias currents. The pulse widths before the amplification range between 1.9 and 2.0 ps, whereas the pulse widths after the SOA show a fluctuation from 2.05 to 2.4 ps with no clear trend with regards to the increasing current. This result suggests that the individual operating conditions of the QD SOA have also a significant influence on the dynamic performance of the device.

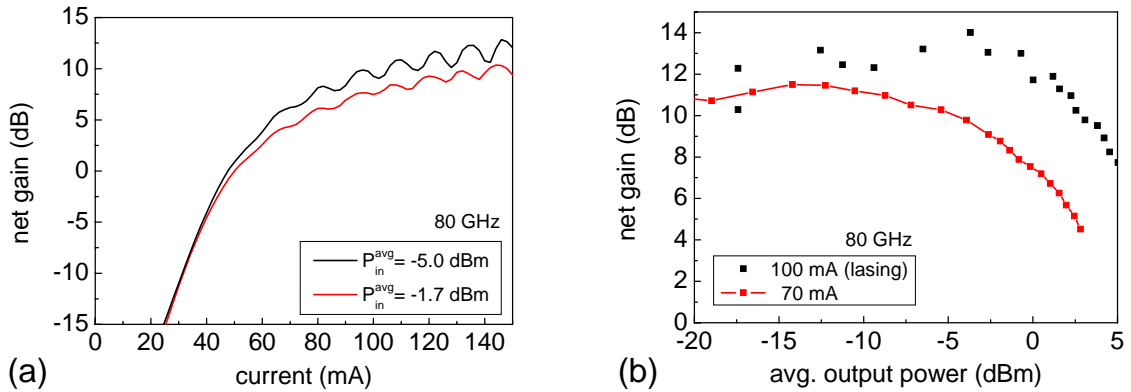


Fig. 5.16: (a) Net gain vs. current for two different input powers at 80 GHz. The fiber-to-fiber gain is computed from average pulse power. (b) Net gain vs. output power for two different current settings at 80 GHz. Note, for $I > 80$ mA the device is lasing for low input power.

In order to find an explanation of the broadening we have compared the shape of the optical spectra of the MLL and after the SOA (Fig. 5.15b). Besides the addition of the ASE spectrum and a shift by ~ 0.8 nm, the shape of the optical spectra are congruent and do not explain the change of the pulse width. Fig. 5.16 summarizes the fiber-to-fiber gain we have measured for varying current and input power. The gain is computed from averaged pulse powers as measured with a powermeter. In Fig. 5.16(a) we observe a gain ripple, but the magnitude is smaller than for cw measurements because the optical spectrum of the pulses is much broader than the monochromatic signal in the cw case. For currents larger than 80 mA and low input powers the SOA shows lasing which results in a suppressed gain that deviates from the typical gain-power dependence (Fig. 5.16b). A linear net gain of 11 dB was achieved which results in a de-embedded chip gain of 23 dB after consideration of a 6 dB fiber-to-chip coupling loss.

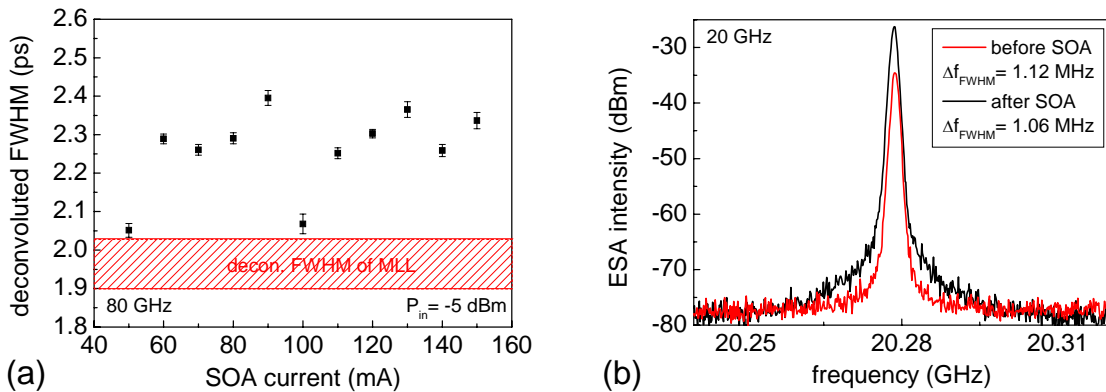


Fig. 5.17: (a) Deconvoluted pulse widths from autocorrelation measurements for different SOA bias current. The error bar is deduced from the Gaussian fit of the AC pulse. (b) ESA spectra of mode-locked pulse train at 20 GHz before and after amplification. The linewidth remains the same within measurement error.

Additionally to the measurement of the SHG AC signal, OSA and ESA spectra, and the gain measurement we have investigated the influence of the QD SOA on the timing jitter of the pulse train. The jitter of the amplified pulse trains was evaluated at 20 and 40 GHz for hybrid mode-locking with a 70 GHz Agilent Infiniium DCA-86100B sampling oscilloscope comprising a precision timebase (200 fs eigenjitter). It is necessary to have a hybridly mode-locked signal to lock to the timebase. This equipment was not available for the ultrashort 710 fs pulses at 20 GHz and for the passive MLL repetition frequency of 80 GHz. A rms jitter

5 Application Oriented Experiments with QD SOAs

of 0.60 ± 0.05 ps at 20 GHz was obtained with a corresponding deconvoluted pulse width of 3.3 ps. After passing through the SOA the jitter remained the same within the error margins and the pulse width was unchanged as seen before. At 40 GHz we determined a rms jitter of 1.4 ps for the QD MLL source. After amplification with the QD SOA the jitter was measured at various input powers (-9 dBm, -14 dBm) and bias currents (70 mA, 80 mA). Within the measurement accuracy the jitter remained unchanged at 1.4 ps, i.e. the amplifier does not affect the jitter characteristics of the pulse train. Measurements of the jitter with the optical sampling setup of H. Quast [191] have confirmed the above results.

Table 1 shows an overview of the amplification of MLL pulses and the obtained parameters like deconvoluted pulse width before and after the SOA, spectral width and time-bandwidth product of the MLLs, saturation output power (averaged and peak) of the pulses after the SOA, net gain, and jitter if applicable.

Table 8: Amplification of QD MLL pulses with QD SOA summarized with the values of mode-locking frequency and mode, deconvoluted pulse width of the MLL and after the SOA, spectral width and time-bandwidth product of the MLL, averaged and peak saturation output power of the pulses after the SOA, maximum achieved fiber-to-fiber net gain, and jitter if applicable.

f_{MLL}	mode	$\tau_{\text{decon}}^{\text{MLL}}$	$\tau_{\text{decon}}^{\text{SOA}}$	$\Delta\lambda_{\text{MLL}}$	$\Delta\tau\Delta\nu$	$P_{\text{avg}}^{\text{out,max}}$	$P_{\text{peak}}^{\text{out,max}}$	$G_{\text{net}}^{\text{max}}$	$\sigma_{\text{rms}}^{\text{jitter}}$
GHz		ps	ps	nm		dBm	mW	dB	ps
20	hybrid	0.7	0.7	8.5	1.1	2.7	130	10	n/a
20	hybrid	3.3	3.3	6.5	3.9	2.3	26	10	0.6
40	hybrid	1.8	1.9	2.2	0.7	0.7	14	10	1.4
80	passive	1.9	2.2	4.2	1.5	2.8	11	10	n/a

In summary, in this section we have presented mode-locked lasers and semiconductor optical amplifiers based on the same quantum dot material, i.e. their gain profile was matched within the variation of different bias and operating conditions perfectly. By investigating the amplification of fast pulse trains with repetition frequencies from 20 to 80 GHz and pulse widths as short as 710 fs, we have gained insight in the capabilities of the QD SOA to amplify RZ data patterns – while neglecting the influence of the pattern and transmitting only a series of ones.

The mode-locked pulse trains are essentially undistorted by the amplifier, no significant deviation in the optical and electrical spectra was found. A jitter analysis showed no increase of the rms jitter by a contribution of the SOA. Only a small increase of the AC pulse width is observed at high repetition rates; at 40 GHz the pulse width increases by 4-10% depending on the input power and at 80 GHz we estimate an increase of 15%. The broadening of the pulses at 40 and 80 GHz might be attributed to the 2nd slower term in the bi-exponential recovery of the QD SOA gain which is on the order of 10-100 ps, implying a broadening of the pulses at repetition rates larger than 10-100 GHz [42, 45, 52]. Detailed pump-probe measurements on the recovery of the gain are presented in section 5.2.2 where a complete ultrafast recovery of the GS is found under the suitable operating conditions of the amplifier.

These results emphasize the potential of ultrafast dynamics of QD SOAs for their application in optical high-bitrate transmission systems. Ultrafast amplification at 80 GHz and excellent jitter performance makes QD SOAs ideal candidates for future 100 GBit Ethernet.

But due to the pulse train no information on patterning or saturation effects is immanent in these results. Experimentally there are two ways to acquire this information. Pump-probe experiments where not only the gain recovery of a single pump pulse is probed, but the pump

consists of two short pulses with a small delay, create a detailed picture on the recovery and saturation effects within the ground and excited states of the QD SOA. System performance and patterning effects can be analyzed by the measurement of data and eye-patterns and the bit error ratios of a transmission line including a QD SOA. These complementing experiments are presented in the following sections.

5.2.2 Double pulse pump- and probe measurements

The gain dynamics of our samples were measured in the group of U. Woggon, Universität Dortmund, by a femtosecond pump-probe technique with heterodyne detection as described in section 4.3.2. In this experiment two consecutive pump pulses are probed, therefore, the results provide key information in understanding the amplification of pulse trains as investigated in section 5.2.1. The results described here have been submitted for joint publication [189].

The samples were of structure DO453 with $2\ \mu\text{m}$ width, 1 mm length and AR-coating. The experiment was carried out at room temperature. ASE spectra for different bias currents are shown in Fig. 5.18(a). The ground state excitonic emission can be identified with its peak at 965 meV ($1.285\ \mu\text{m}$) for low current values up to 954 meV ($1.3\ \mu\text{m}$) for large currents with an inhomogeneous broadening of 33 meV. The excited state emission peak at 1030 meV ($1210\ \text{nm}$) dominates at currents larger than 80 mA. The transition from absorption to gain, i.e. the transparency current (density), has been determined to 7.5 mA ($375\ \text{A}/\text{cm}^2$) and 37.5 mA ($1875\ \text{A}/\text{cm}^2$) for the ground and excited state, respectively.

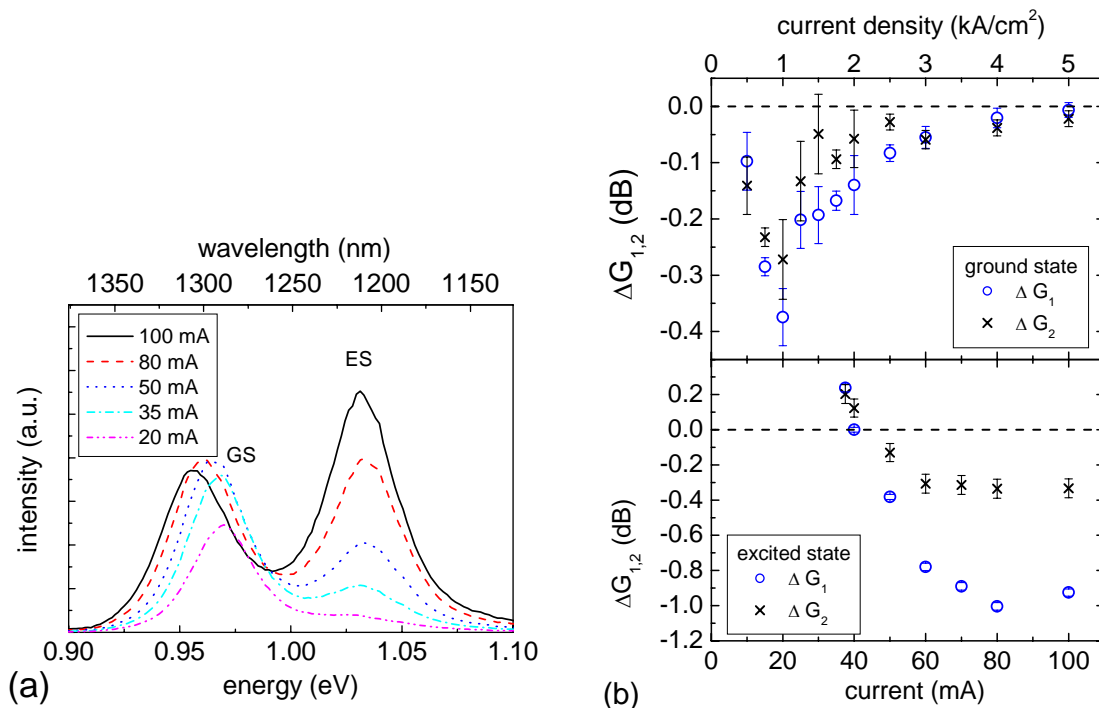


Fig. 5.18: (a) Amplified spontaneous emission (ASE) spectra at different bias currents. GS: ground state, ES: excited state. (b) Gain reduction ΔG_1 and ΔG_2 induced by the first and second pump pulse in the ground and excited state. Adopted from [189].

The gain change ΔG induced by the double pump pulse in the ground and the excited states is reproduced for its temporal evolution for different bias currents in Fig. 5.19. At large injection (100 mA or 5 kA/cm²) the ground state gain recovers ultrafast (<1 ps) and completely after both pump pulses. For lower currents the gain recovery time shows a fast component <1 ps and a longer recovery >5 ps, which leads to a partial gain reduction for the second pump pulse. The excited state does not recover completely at any of the applied bias currents (Fig. 5.19b).

In order to quantify the results described above we introduce the gain reduction factors $\Delta G_1 = \Delta G(\tau = 5\text{ps})$ and $\Delta G_2 = \Delta G(\tau = 10\text{ps}) - \Delta G_1$ induced by the first and the second pump pulse, respectively (depicted in Fig. 5.19). Fig. 5.18b summarizes the gain changes for ground and excited state according to these gain reduction factors. The course of the ground state recovery shows a decrease of ΔG_1 and ΔG_2 for low currents, a minimum around $I_0 = 20$ mA and a return to zero at high currents around 100 mA when a complete gain recovery is achieved. I_0 corresponds to the onset of the excited state emission (Fig. 5.18a) which indicates the important role of the excited state population for the ultrafast refilling of the ground state [192]. In the excited state ΔG_1 and ΔG_2 decrease for increasing currents until they reach a constant value at $I \approx 80$ mA. $|\Delta G_1| > |\Delta G_2|$ is true both for ground and excited state (Fig. 5.18). If the ground state was refilled only by intradot relaxation from the excited state, a partial depletion of the excited state by the first pulse would cause an increase of the accumulated gain reduction after the second pulse, which is in contradiction with our observations.

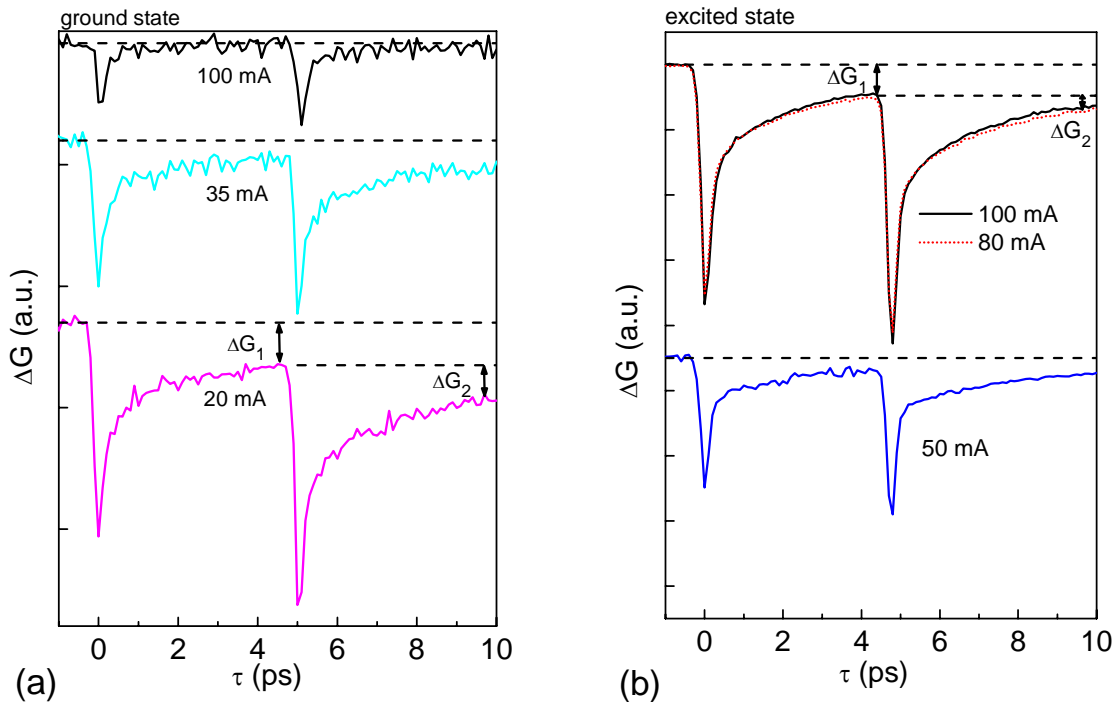


Fig. 5.19: Dynamics of gain recovery (a) in the ground state and (b) in the excited state, at different bias current (Color coding congruent to ASE in Fig. 5.18a). Adopted from [189].

Therefore, the direct capture from the wetting layer must contribute to the ground state gain recovery as well and, together with the ultrafast refilling from the excited state, results in the complete gain recovery we observed for large injection currents. This substantiates our conclusion that there are no physical restrictions for an above 200 GHz operation (according

to the 5 ps pulse delay) of the studied QD based SOA in the presence of significant excited state population.

5.2.3 Eye-pattern and bit-error-ratio measurements

The potential of QD SOAs for high speed transmission is demonstrated in sections 5.2.1 and 5.2.2, but the amplification of optical combs does not give information about the occurrence of patterning effects for data signal amplification. Therefore, the amplification of PRBS data patterns at 40 Gb/s and bit error ratio measurements using the SOA module were carried out in collaboration with the group of C. Schubert, Fraunhofer Institut für Nachrichtentechnik Heinrich-Hertz-Institut. Setup details, measurement parameters and the equipment we used are described in section 4.3.3.

In the first BER measurement session we compared the performance of the QD SOA in a booster configuration for different operating conditions. Fig. 5.20 presents the BER at 40 Gb/s for 100 and 120 mA. For 120 mA a smaller penalty compared to 100 mA, a BER of 10^{-11} (limited by measurement time) and no error floor is observed. At 100 mA an error floor at a BER of about 10^{-9} is observed. The inset in the figure presents the eye-diagram at 120 mA and a BER of 10^{-9} where we observe a clearly open eye with negligible patterning, i.e. a straight “1” level, although the input power of -5.8 dBm and a gain of 8 dB suggest from cw characterization that the module is in the non-linear operation regime. It was not possible to evaluate the back-to-back measurement because once the QD SOA was taken out of the setup the BER degraded to 10^{-4} while an improvement would be expected. Possible reasons could be

- the non-optimized input polarization of QW SOA which was used as pre-amplifier. But although it was not optimized, the output signal had the same amplitude with the input set to the same value as with the QD SOA. Another reason could be
- a jitter reduction from the QD SOA because of a dynamic feature of the QDs. This has not been observed before and is not indicated by our jitter measurements of amplified pulse trains, or
- signal reflections at QW SOA, after the QD SOA was removed, could disturb the EO modulator which featured an automatic bias control to set its modulation point.

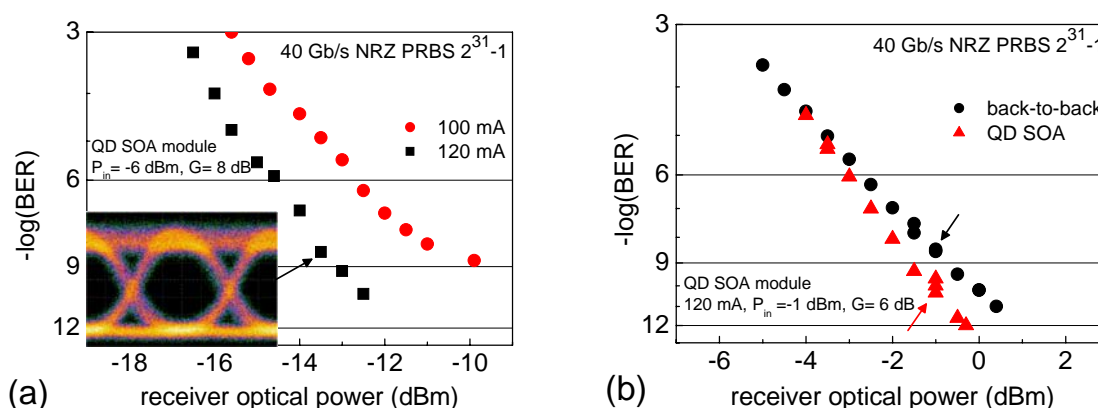


Fig. 5.20: (a) BER vs. attenuated optical receiver power for two SOA bias currents for 40 Gb/s NRZ PRBS 2³¹-1. The arrow indicates the measurement point of the inset: Eye-diagram of the amplified data signal at BER 10⁻⁹, 120 mA with jitter 1.4 ps and extinction ratio 5.9 dB. (b) BER vs. attenuated optical receiver power for back-to-back measurement and including a QD SOA at 120 mA.

5 Application Oriented Experiments with QD SOAs

In the next BER session we modified the setup, used the QW SOA only in the cw part as booster of the ECL, and compensated the sensitivity problem at the receiver side with a broadband electrical amplifier. In this configuration it was possible to measure the back-to-back performance of the setup and compare it with the influence of the QD SOA module. The BER traces of back-to-back and QD SOA are concurrent within error margins (Fig. 5.20b) and we observe error-free transmission down to a BER of 10^{-12} . The QD SOA exhibits even a small negative penalty, but that is compensated by its degraded optical signal to noise ratio as can be inferred from the eye-diagrams presented in Fig. 5.21. In a next measurement session it would be ideal to compare the BER as a function of optical SNR to undermine this conclusion. The degraded optical SNR stems from an increased patterning which we observe in the eye-diagram at a BER of $5 \cdot 10^{-11}$ when the amplifier is driven at 120 mA and in saturation with an optical input power of -1 dBm.

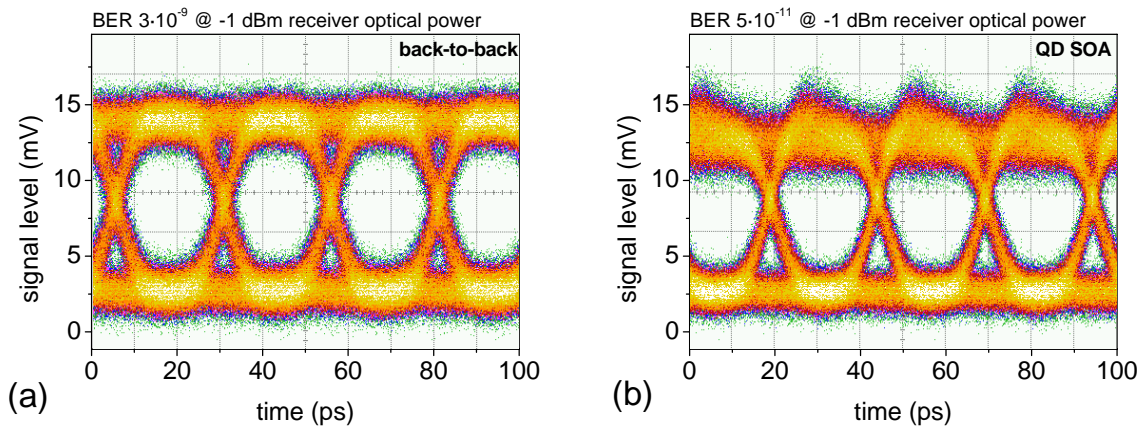


Fig. 5.21: Eye diagrams 40 Gb/s NRZ PRBS $2^{31}-1$ corresponding to a BER data point of Fig. 5.20-b (indicated by an arrow) at -1 dBm receiver optical power. (a) back-to-back transmission, BER $3 \cdot 10^{-9}$ (b) QD SOA amplification, BER $5 \cdot 10^{-11}$

The patterning dependence was further investigated by recording the direct patterns after amplification with the QD SOA for different input powers with a 70 GHz sampling oscilloscope. The same pattern sections from a 40 Gb/s NRZ PRBS with 2^7-1 bit length are depicted in Fig. 5.22 for strongly saturating input (+3.5 dBm) and for -4 dBm which is close to the cw 3dB saturation input power of -5 dBm. In the first case large overshoots of the ones I_{peak} after a gain recovery during the zero levels are found which relax to a saturated “1” intensity I_{sat} . In the case with lower input power we find no such overshoot, the remaining patterns are also observed in the back-to-back measurement.

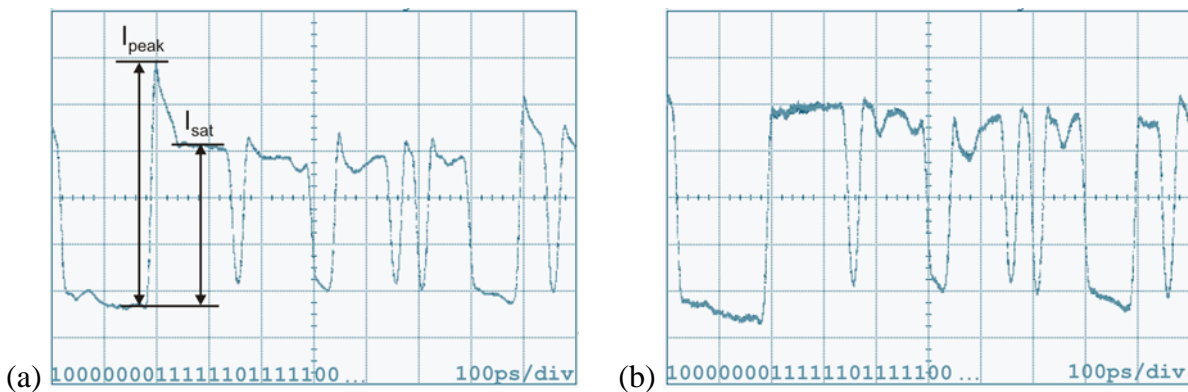


Fig. 5.22: Patterning effects after amplification using the QD SOA in 40 Gb/s NRZ PRBS 2^7-1 data pattern: 100000001111110111110011110101110001101. Patterns for input power levels of +3.5 dBm (a) and -4 dBm (b).

In order to quantify the patterning effect we have evaluated the ratio $I_{\text{peak}}/I_{\text{sat}}$ as a function of input power and as a function of recovery time given by the number of zeros times the bit period of 25 ps. We have defined a “no patterning” region for an overshoot which has a ratio within 1.0 ± 0.1 . From Fig. 5.23(b) we also find that if input power is lowered even a long recovery time does not influence the overshoot magnitude. It is evident from Fig. 5.23 that below an input power of -3 dBm we observe no patterning, yet the amplifier operates in a regime that is still non-linear. This is consistent with the eye-pattern we have presented in the inset of Fig. 5.20(a) which also shows no patterning at an input of -5.8 dBm slightly below the cw 3dB saturation input power.

It should be investigated in further measurements whether the patterning is bias current dependent. As suggested from the comparison of the BER for 100 and 120 mA and from theoretical calculations [101] the patterning effects can be suppressed at large current densities where the ES is significantly populated.

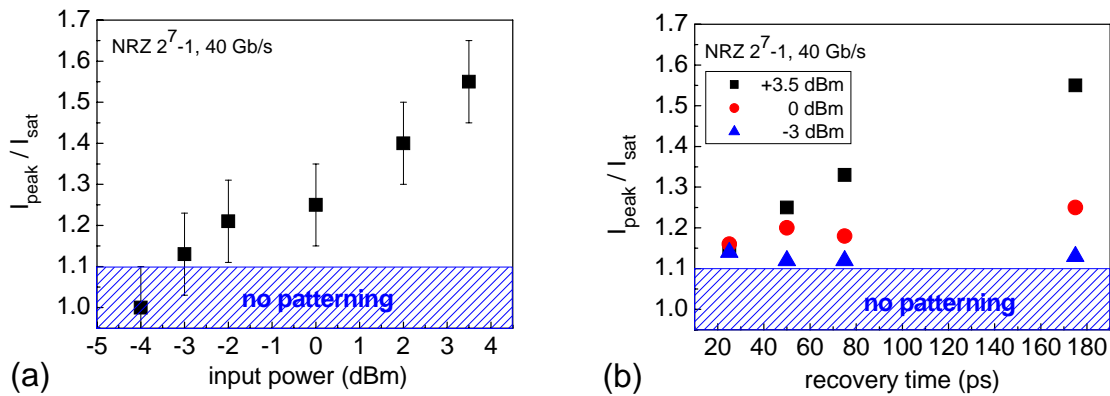


Fig. 5.23: Ratio of peak intensity to saturated intensity as defined in Fig. 5.22. The “no patterning” area was defined as the region where the over/undershoot is less than 10%. (a) For various input power levels at the “long zero – long one” pattern (recovery time 180 ps). (b) Dependency of the overshoot ratio on the recovery time for three different input powers.

In summary, a 40 Gb/s NRZ PRBS data transmission with a QD SOA module was presented. BER measurements have shown the penalty free communication as compared to a back-to-back measurement, and error-free amplification down to a BER of 10^{-12} was demonstrated. The patterning behavior was assessed in detail and large patterning effects of the QD SOA under strong saturation were found, but it was also shown that the QDs facilitate a pattern-free operation in the linear and weakly saturated SOA regime.

5.2.4 Small-signal cross gain modulation of QD SOAs

In the preceding section it was shown that QD SOAs work at 40 Gb/s in dynamic data transmission systems. These measurements were conducted at one input wavelength. In this section the performance of QD SOAs in multi-wavelength amplification are investigated. When an amplifier operated in the saturated regime has multiple inputs at different wavelengths, a crosstalk, i.e. the transfer of modulation from one channel to another, occurs which limits the use of the amplifier in multichannel transmission systems, but also offers the possibility to deploy the SOA for wavelength conversion in optical processing.

We have investigated the small-signal XGM in our QD SOA with the setup described in section 4.3.4. For three pump wavelengths at 1270, 1290 and 1310 nm the probe signals in adjacent CWDM channels were analyzed with regard to their frequency response. In Fig.

5 Application Oriented Experiments with QD SOAs

5.24(a) this measurement is presented for the pump wavelength in the gain maximum at 1290 nm. The measured data was compared with the theory from section 2.2.7. From cw measurements we know the saturation output power and the small signal (i.e. linear) gain of the SOA as $P_{\text{sat}}^{\text{3dB}} = 1$ dBm and $G = 6$ dB at a bias current of 50 mA. The optical power of the probe was -10 dBm. We assume a spontaneous emission carrier lifetime of $\tau_{\text{se}} = 200$ ps and get for the parameters in the theoretical calculation $gL = G/10 \log e = 4.1$, $E_{\text{sat}} = \tau_{\text{se}} \cdot P_{\text{sat}}^{\text{3dB}} / \ln 2 = 2.88 \cdot 10^{-13}$ J and for the stimulated emission carrier lifetime $\tau_s = E_{\text{sat}} / P_p = 2.88$ ns. Substituting these numbers in equation (2.38) yields the calculated curve in Fig. 5.24(a). It matches the experimental data well, but can be only rough approximation as the theory does not include the wavelength detuning magnitude. A more detailed theory would have to be applied in order to explain the experimental data which is beyond the scope of this thesis.

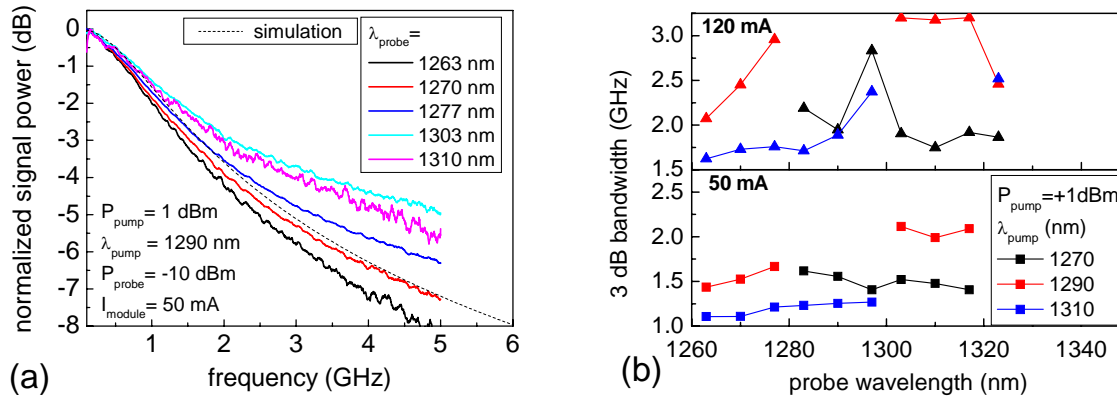


Fig. 5.24: (a) XGM frequency response in the QD SOA module for different probe wavelengths at $\lambda_{\text{pump}} = 1290$ nm. The dashed line is a theoretical calculation according to equation (2.38). (b) 3 dB bandwidth of a set of XGM measurements for different pump wavelengths as a function of probe wavelength. The measurements were done at 50 mA (only GS populated) and at 120 mA (ES and GS populated).

The 3dB-bandwidth of all XGM measurements is in the range of 1-3.5 GHz. All values have been plotted in Fig. 5.24(b) separated for measurements at 50 and 120 mA as a function of the probe wavelength. In the case of 50 mA where mainly GS population is observed, a generally smaller bandwidth than for 120 mA is found.

The bandwidth is more or less independent of the probe wavelength, only in the case of $\lambda_{\text{pump}} = 1290$ nm there is a slight increase from 1.5 to 2 GHz. If we follow the arguments of [79], where also the case of pure GS population was considered, this would mean that the XGM process is mediated by the wetting layer and its bandwidth increases when the energy corresponding to the probe wavelength is far from the wetting layer energy, and therefore the carrier escape time is reduced. As the probe energy decreases the escape time decreases and the carrier replenishment becomes more efficient, which amounts to a wider bandwidth. This dynamic process together with the gain at the wavelength of interest determines the overall XGM efficiency.

The observation that the bandwidth is largest for the pump at the gain maximum (which is true for both currents) supports this argument. In the case of 120 mA with ES and GS populated we find a larger bandwidth than for 50 mA. If we assume that through the presence of the ES the carrier relaxation into the GS is faster than in the case where the carriers relax from the WL, our observation is in contradiction to the calculation reported for p-doped QDs in [80] which states that a faster intersubband relaxation results in a smaller XGM bandwidth.

Possibly the increase through larger current and stimulated emission shields this effect in our experiment. Note, one data point (at $\lambda_{\text{pump}}=1270\text{nm}$, $\lambda_{\text{probe}}=1297\text{nm}$, $I=120\text{mA}$) does not follow the general trend which might be due to a too large probe power having a strong influence in the maximum gain region.

In conclusion, we have described small signal XGM in a QD SOA and investigated its modulation bandwidth. We have found only little dependence on the pump-probe wavelength detuning. The largest effect is the increase of the bandwidth with the bias current which is attributed to the presence of the populated ES at larger injection. Our measured bandwidths between 1 and 3.5 GHz are in agreement with other small signal measurements on quantum dot and quantum dash samples and demonstrate the potential for multi-wavelength amplification without crosstalk in the region outside the homogeneous broadening.

6 Summary

This work is a comprehensive report of the realization and characterization of GaAs based semiconductor optical amplifiers (SOA) using self-organized InGaAs quantum dots (QD) as an active gain medium for optical amplification in the 1.3 μm wavelength regime.

A part of the thesis was devoted to simulation and modeling of the device properties like the modal structure of the waveguide, the behavior of tilted waveguides and other means of reduction of the crystal facet reflectivity like anti-reflection coatings or facet windows. These simulations provided the input for design considerations to realize traveling wave amplifiers. The transfer matrix method was applied to study the propagation of an optical field through an amplifier. In this model the general gain and saturation behavior of a SOA was illustrated to understand the propagation dependent mechanisms of the carrier density and the modal gain along the device.

The theory part builds the background to understand the unique properties of the quantum dots and the important characteristics of a semiconductor optical amplifier. SOA relevant features of InGaAs quantum dots like p-doping, the linewidth enhancement factor, inhomogeneous broadening of the emission, gain saturation mechanisms and gain recovery were discussed. Theoretical fundamentals of SOAs were briefly reviewed and the concepts of gain, gain bandwidth, and saturation of gain were explained. The gain ripple, which stems from the residual reflectivity of the Fabry-Perot cavity, was discussed in detail as it causes a wavelength dependent deterioration of the performance of the device. Amplified spontaneous emission is the main origin of noise in the amplifier and adds to the noise figure. These key parameters were investigated considering the influence of polarization and QD properties.

Higher order effects govern the behavior of the SOA in the non-linear gain regime. Cross gain modulation in general and with respect to QDs was described as it is important to explain multi-wavelength cw or dynamic experiments.

The theory part was topped off with a review on available models for QD SOAs and subsumed important results that predict excellent performance of QD based SOAs in comparison to conventional SOAs.

The growth of QDs and the epitaxial structure of the samples was not a development of this work; the QD samples were optimized for 1.3 μm laser applications, but suited also for the first time realization of SOAs and their use. For future improvement of the QD SOA performance the growth of the quantum dot gain medium and the waveguide structure of the devices need to be tailored to the specific amplifier requirements like large bandwidth, polarization independence and low far field divergence for high coupling efficiencies.

In order to realize a single mode amplifier with a strong guiding of the input signal, the narrow ridge waveguide processing applied for QD lasers was re-designed. With the new processing scheme deeply dry etched (through the active layer) ridge waveguides were realized and a new top contact scheme was implemented enabling easy access to the top contacts with a ground-signal-ground probe head. This allowed for quick bar testing without the need of wire-bonding and was successfully adopted for contacting high speed lasers for direct modulation or hybrid mode-locking applications as well. The processed ridge waveguides feature a natural reflectivity from the crystal end facets, which needed to be suppressed to make a traveling wave amplifier. The concept of tilted waveguides in

combination with two-layer anti-reflection coatings was applied and reflectivities below 10^{-3} were achieved. The mounting of the SOA chips was expanded from simple copper heatsinks to test bars with several devices to a full packaging of two devices where temperature controlled fiber-pigtailed SOA modules were realized.

The amplifiers were characterized and optimized with regard to their internal device performance. The far field measurement verified that by processing ridges with only $1\ \mu\text{m}$ width a quasi-symmetric far field was realized, which minimizes coupling losses due to mode ellipticity. Using the Hakki-Paoli method the gain-reflectivity product from the ASE ripple of the spectrum was measured. In combination with a spectrally resolved gain measurement we were able to evaluate the combined reflectivity of tilted waveguide and anti-reflection coating to values well below 10^{-3} . The coupling losses from the fiber to the waveguide determined the net amplifier performance from fiber input to fiber output. The lowest coupling loss to our $4\ \mu\text{m}$ wide ridge waveguide structure was 4 dB using a tapered fiber, which is a good value for ridge waveguide structures, but far from values below 1 dB that are achieved with buried heterostructures.

The cw performance of the QD SOAs was comparable to commercial QW based amplifiers at $1.3\ \mu\text{m}$ with a chip gain up to 25 dB limited by the onset of lasing, a spectral amplifier bandwidth of 30 nm indicating that these QDs were relatively homogeneous in size, and a minimum chip noise figure of 4 dB which was close to the theoretical limit of 3 dB. In the linear regime of the QD SOA, i.e. at low input power, negligible influence of three CWDM wavelengths amplified in the SOA was found, which shows the potential for multi-wavelength data transmission.

The ASE cross gain measurement displayed a spectral hole with a shallow slope since carrier replenishment in a particular saturated QD group originated from other, spectrally neighboring, QD groups, which is typical for an inhomogeneously broadened gain medium. Polarization resolved measurements evidenced a polarization ratio of 6-8 dB. This dominant TE polarization was expected from the modeling of the decoupled QD layers. The rectangular ridge waveguide also favors TE polarized light. Modeling of QD polarization dependence showed that it should be possible to achieve polarization insensitive SOAs with a balanced TE/TM ratio using vertically coupled QD stacks.

In dynamic measurements the QD SOAs demonstrated excellent performance. The amplification of fast pulse trains from mode-locked lasers with identical QD gain medium, repetition frequencies from 20 to 80 GHz, and pulse widths as short as 710 fs was investigated. Thereby, insight in the capabilities of the QD SOA to amplify a high speed pulse sequence was gained. The mode-locked pulse trains were essentially undistorted by the amplifier and only a small increase of the auto-correlation pulse width was observed at high repetition rates of 40 and 80 GHz. The broadening of the pulses at these frequencies was attributed to the 2nd slower term in the bi-exponential recovery of the QD SOA gain which is on the order of 10-100 ps, implying a broadening of the pulses at repetition rates larger than 10-100 GHz. These results emphasize the potential of ultrafast dynamics of QD SOAs for their application in optical high-bitrate transmission systems. Ultrafast amplification at 80 GHz and excellent jitter performance make QD SOAs ideal candidates for future 100 GBit Ethernet.

Using ultrafast pump-probe spectroscopy the gain recovery dynamics in a QD based SOA after amplification of double femtosecond pump pulses was investigated. A distinct change in gain recovery in the ground state was observed when a significant excited state population

6 Summary

was achieved. A complete gain recovery was found when two 150 fs pulses with 5 ps time delay passed through the SOA in resonance to the ground state under high injection currents of 80 to 100 mA. The results indicate that the overall gain recovery dynamics were accelerated in the presence of significant excited state population. This opens the way for ultrafast (> 200 GHz) operation in p-doped QD based SOAs at 1.3 μm telecom wavelengths.

With measurements of small signal cross gain modulation, the modulation bandwidth in a QD SOA was investigated. Only little dependence on the pump-probe wavelength detuning was found. The largest effect was the increase of the bandwidth with the bias current, which was attributed to the presence of the populated ES at larger injection. The measured XGM bandwidths between 1 and 3.5 GHz were in agreement with other small signal measurements on quantum dot and quantum dash samples and demonstrate the potential for multi-wavelength amplification without crosstalk in the region outside the homogeneous broadening of the QDs.

A 40 Gb/s NRZ PRBS data transmission with a QD SOA module was measured. Bit-error-ratio measurements showed penalty free communication as compared to a back-to-back measurement without the QD SOA, and error-free amplification down to a BER of 10^{-12} was demonstrated. The patterning behavior was assessed in detail and large patterning effects of the QD SOA under strong saturation were found, but it was also shown that the QDs facilitate a pattern-free operation in the linear and weakly saturated SOA regime.

Despite these encouraging results, the QD SOAs presented in this work still lack from some device limitations like insufficient reduction of reflectivity resulting in the onset of lasing, polarization dependence, and large coupling losses. But these limitations can be overcome by further design improvements, e.g. larger waveguide tilt angle and growth modifications like coupled QD stacks and re-growth for buried heterostructures, respectively. The dynamic behavior of the quantum dot based SOAs was proven to be state of the art enabling ultrafast, beyond 100 GHz operation at 1.3 μm telecom wavelengths. Using QDs as a gain medium opens up the road for future high speed all-optical networks employing QD SOAs as ultrafast amplifying elements or functional elements in all-optical signal processing.

7 Technical Annex

7.1 Abbreviations and acronyms

The following table shows the abbreviations and acronyms used in this text.

1D, 2D, 3D	One-, two-, three-dimensional	PBC	Photonic bandgap crystal
3R	Re-amplification, re-shaping, re-timing	PD	Photodetector
AC	Auto-correlation	PRBS	Pseudo random bit sequence
AMP	Electrical amplifier	PWM	Powermeter
AR	Anti-reflection	QD	Quantum dot
ASE	Amplified spontaneous emission	QDash	Quantum dash
ATT	Attenuator	QW	Quantum well
BCB	Bencocyclobutene	RHEED	Reflection high energy electron diffraction
BER(T)	Bit error ratio (tester)	RIE	Reactive ion etching
BPG	Bit pattern generator	RTA	Rapid thermal annealing
BPM	Beam propagation method	RZ	Return to zero
CAIBE	Chemical assisted ion beam etching	SC	Separate confinement
CAD	Computer aided design	SEM	Scanning electron microscope
CWDM	Coarse wavelength division multiplexer	SGM	Self gain modulation
DC BIAS	Direct current bias	SHG	Second harmonic generation
DEMUX	De-Multiplexer	SMF	Single mode fiber
DHS	Double heterostructure	SNR	Signal to noise ratio
DI	Direct interpolation	SOA	Semiconductor optical amplifier
DWELL	Dots-in-a-well	SOG	Spin-on glass
ECL	External cavity laser	SPM	Self phase modulation
EOM	Electro optical modulator	SSE	Source spontaneous emission
ES	Excited state	T-Control	Temperature control
ESA	Electrical spectrum analyzer	TE	Transverse electric
FBH	Ferdinand Braun Institut für Höchstfrequenzmesstechnik	TEM	Transmission electron microscope
FWHM	Full width at half maximum	TM	Transverse magnetic
FWM	Four wave mixing	TMM	Transfer matrix method
GPIB	General purpose interface bus	TU(B)	Technische Universität (Berlin)
GS	Ground state	VOA	Variable optical attenuator
GSG	Ground-signal-ground	WL	Wetting layer
HH	Heavy hole	XGM	Cross gain modulation
HRI	High refractive index (material)	XPM	Cross phase modulation
LH	Light hole		
LOC	Large optical cavity		
LRI	Low refractive index (material)		
MBE	Molecular beam epitaxy		
ML	Monolayer		
MOCVD	Metal organic chemical vapor deposition		
MPI	Multi-path interference		
MUX	Multiplexer		
NF	Noise figure		
NRZ	Non return to zero		
OSA	Optical spectrum analyzer		

7.2 OSA calibration

The OSA (Ando AQ6317B) can be optically aligned and wavelength calibrated using an implemented routine and its internal acetylene gas source as a reference. According to its specification the OSA power level is accurate to ± 0.3 dB. The wavelength accuracy is specified as ± 0.04 nm. For exact gain and noise measurements it is important to carry out an external calibration to check the power reading from the OSA. The resolution bandwidth of the OSA has to be calibrated, too. Both can be done following the calibration procedures from [64]:

Power calibration

1. The signal source (e.g. Agilent ECL) is set to the signal wavelength λ_{sig} and connected to an optical powermeter (e.g. ILX OMM-6810B) to measure P_{PWM} in dBm.
2. Then the source is connected to the OSA and the integrated power $P_{\text{OSA}}^{\text{int}}$ is evaluated. This has to be done carefully by considering the following:
 - a. The implemented OSA power meter routine is unreliable for precise measurements as the underlying resolution bandwidth (RB) and integration procedure are unknown.
 - b. Simple integration of the spectrum and correction of the integrated power sum with the RB is inaccurate due to the finite measurement resolution and the general problem of having an extremely narrowband source within a considerably larger RB. This even leads to unphysical results like an integrated power that is smaller than the peak power at the signal wavelength.
 - c. Using a sum of the (interpolated RB corrected) integration of the ASE signal and the (ideally sharp) contribution of the peak power yields the most realistic $P_{\text{OSA}}^{\text{int}}$.
3. The power calibration factor (PCF) in dB is then simply $\text{PCF}(\lambda_{\text{sig}}) = P_{\text{PWM}} - P_{\text{OSA}}^{\text{int}}$. It should be applied accordingly to all OSA power measurements.

Following this calibration routine for the utilized Ando OSA the PCF was found to be 0.66 (0.44) dB comparing an ILX (Agilent) powermeter (Fig. TA1a). The power accuracy of the OSA and of the powermeters is ± 0.3 dB and ± 0.15 (± 0.18) dB, respectively. It is therefore difficult to decide which calibration (OSA or powermeter) is more trustworthy. Consequently the OSA power reading was used for all measurements without applying the PCF.

Resolution bandwidth calibration

1. The signal source (e.g. Agilent ECL 8164B) is set to the signal wavelength λ_{sig} and connected to the OSA.
2. The OSA span is set to zero. The resolution bandwidth (RB) is set to the desired value.
3. The source wavelength is scanned from/to $\lambda_{\text{sig}} \pm (\text{RB}/2 + \delta)$ and for each wavelength λ_i the power $P(\lambda_i)$ is measured in linear units.
4. The corrected resolution bandwidth (for the fixed RB of the OSA) is calculated as a mean value by

$$\Delta\lambda_{\text{BW}}(\lambda_{\text{sig}}) = \int \frac{P(\lambda_i)}{P(\lambda_{\text{sig}})} d\lambda = \sum_i \frac{P(\lambda_i)}{P(\lambda_{\text{sig}})} \Delta\lambda_i.$$

5. The bandwidth B_0 expressed in Hz is approximately given by

$$B_0(\lambda_{\text{sig}}) \approx \frac{c\Delta\lambda_{\text{BW}}}{\lambda_{\text{sig}}^2}.$$

Fig. TA1 (b) shows an exemplary calibration measurement at a center wavelength of 1280 nm and a RB setting of 0.5 nm. The calibrated resolution bandwidth is determined to $\Delta\lambda_{\text{BW}} = 0.458$ nm which is 8% off (compared to the specified resolution accuracy of $\pm 5\%$ of the Ando OSA).

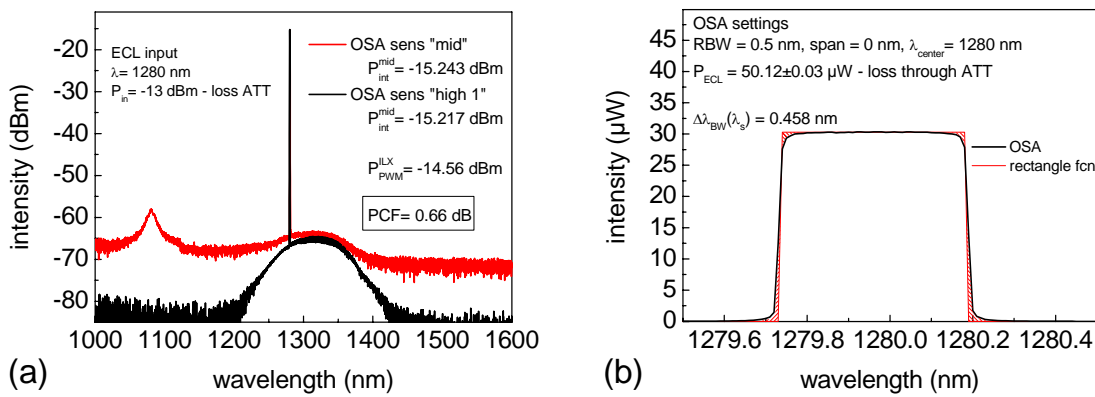


Fig. TA1: (a) Calibration measurement of the optical power. The integrated power value of the OSA for two different resolution settings is compared with the power measurement from the integrated sphere. (b) Calibration measurement of the optical bandwidth of the OSA. The measured data is fitted by a rectangle function with an effective width $\Delta\lambda_{\text{BW}}(\lambda_{\text{sig}})$ which describes the optical bandpass function in a simplified way.

7.3 Small signal modulation

External modulator intensity modulation response (from [61])

The optical transmission response of a Mach-Zehnder modulator is a function of the applied dc bias voltage. The transfer function (Fig. TA2) highlights four parameters: insertion loss I_L , switching voltage V_π , extinction ratio, operating point V_b . The modulator response is linear for small deviations from the nominal operating bias point. The transmitted light power can be written as

$$I(t) = \frac{I_0}{2} \left[1 + m \cdot \cos \left(\pi \frac{V_{\pi, \text{bias}} + E(\omega) V_{\pi, \text{RF}} \cos(\omega t)}{V_\pi} \right) \right] \quad (7.1)$$

with I_0 the maximum transmitted light power, $E(\omega)$ the frequency-dependent modulation efficiency, $V_{\pi, \text{RF}}$ the peak signal voltage applied to the modulator, m the modulation depth.

Linearization at $3/2\pi$

$$I(t) \approx \frac{I_0}{2} \left[1 + \left(\pi \frac{E(\omega) V_{\pi,RF} \cos(\omega t)}{V_{\pi}} \right) \right]_{V_{\pi,bias}/V_{\pi,RF}=3/2} \quad (7.2)$$

$$= \frac{I_0}{2} + \frac{I_0 \pi V_{\pi,RF}}{2 V_{\pi}} E(\omega) \cos(\omega t)$$

Expansion of $\cos(x)$ at $3/2\pi$ which is equivalent to expansion of $\sin(x)$

$$\sin(x) = x - \frac{x^3}{3!} + \frac{x^5}{5!} - \dots \quad (7.3)$$

$$\cos^3(x) = \frac{1}{4} (\cos(3x) + 3\cos(x)) \quad (7.4)$$

$$I(t) = \frac{I_0}{2} \left[1 + \cos \left(\pi \frac{V_{\pi,bias} + E(\omega) V_{\pi,RF} \cos(\omega t)}{V_{\pi}} \right) \right] \quad (7.5)$$

$$\approx \frac{I_0}{2} \left[1 + \left(\pi \frac{E(\omega) V_{\pi,RF} \cos(\omega t)}{V_{\pi}} \right) - \frac{1}{6} \left(\pi \frac{E(\omega) V_{\pi,RF} \cos(\omega t)}{V_{\pi}} \right)^3 \right]$$

Optical extinction ratio $ER = \frac{P_{high}}{P_{low}}$

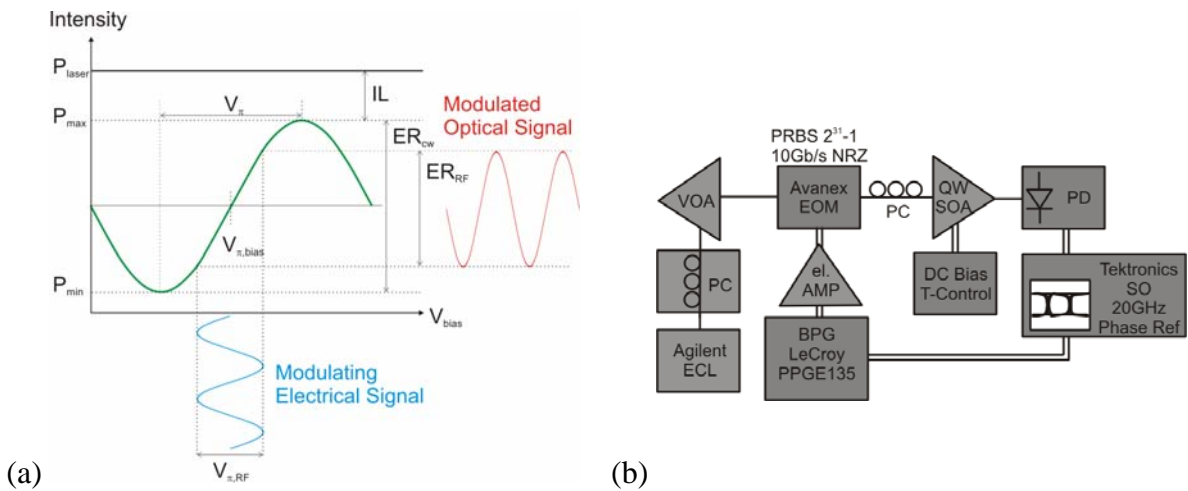


Fig. TA2: (a) Transfer function of a Mach-Zehnder-Interferometer (MZI)-modulator for digital modulation of an optical signal. (b) Setup for dynamic characterization of the Avanex modulator

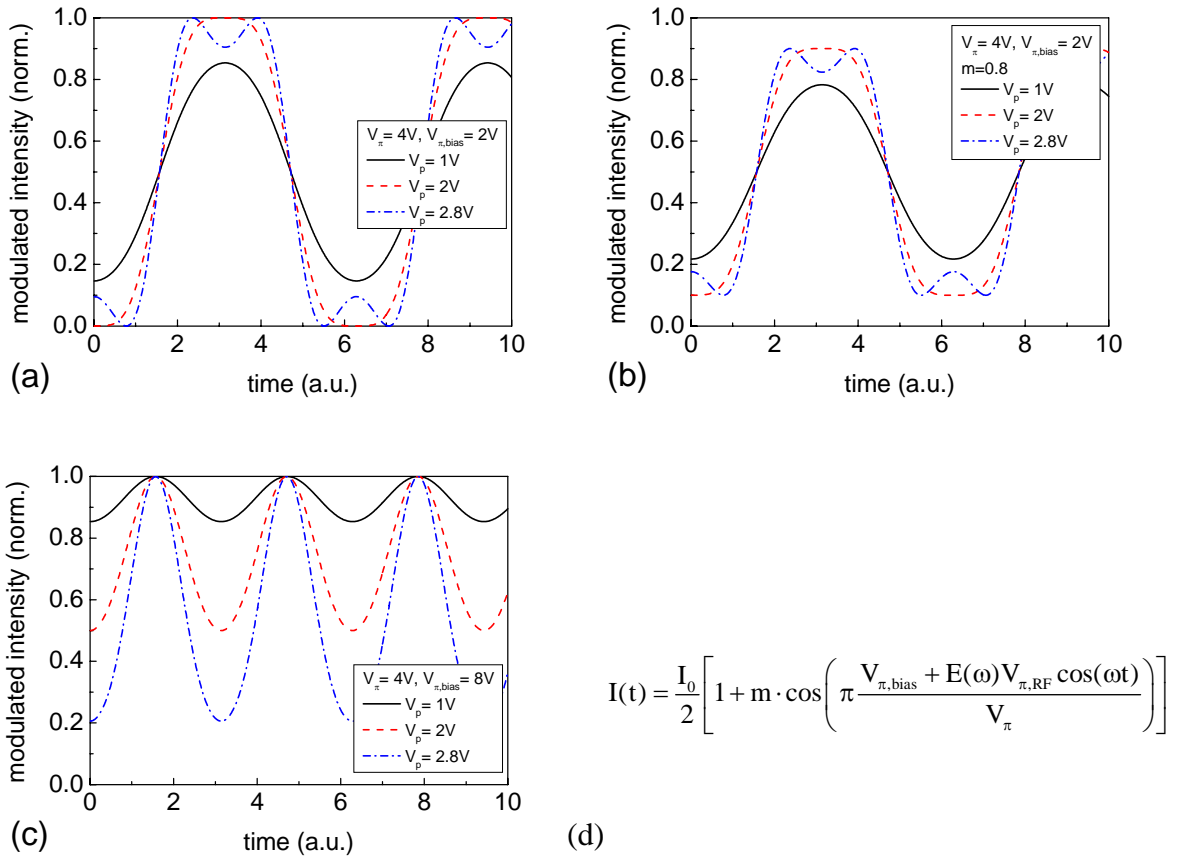


Fig. TA3: Simulation of optical output of a MZI-modulator for sinusoidal input according to equation (d) (7.1) with $I_0 = 1$. (a) $m=1$, (b) $m=0.78$, (c) $V_{\pi,bias}=8V$ (max. bias)

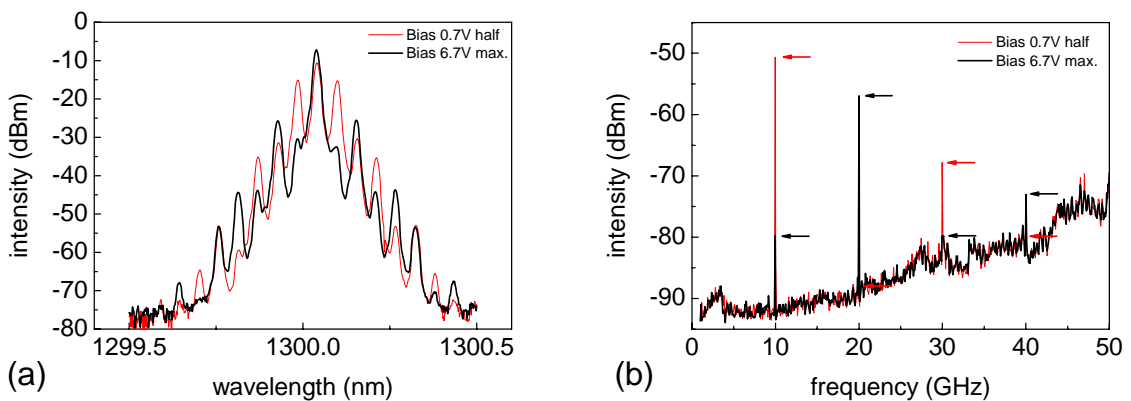


Fig. TA4: Output of a MZI-modulator under sinusoidal modulation at 10 GHz measured with optical spectrum analyzer (a) and with electrical spectrum analyzer (b) for two typical bias points: “half bias point” for normal frequency modulation and “max. bias point” for frequency doubling.

Dynamic characterization of the 40 Gb/s NRZ Lithium Niobate Modulator “PowerBit SD-40” using a bit pattern generator (5 or 10 Gb/s) (for setup see Fig. TA2 (b)) leads to the results presented in Fig. TA5 and TA6.

7 Technical annex

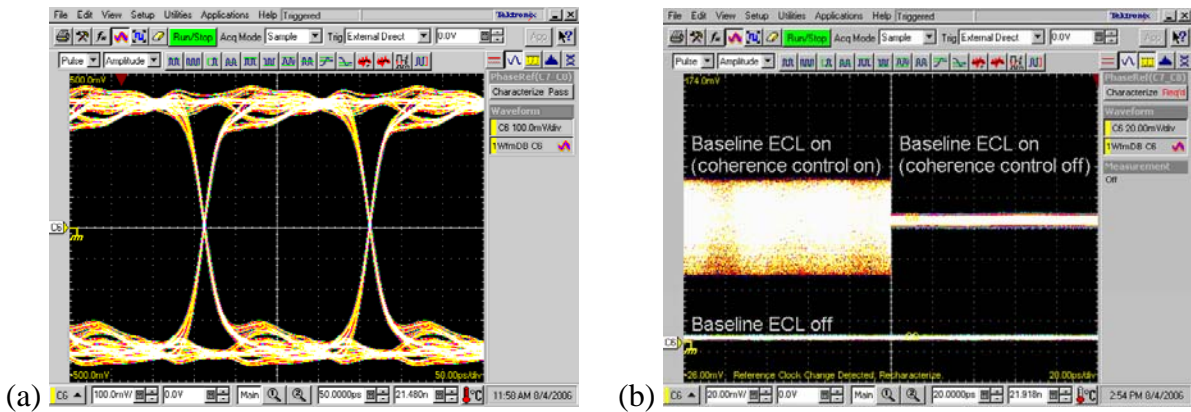


Fig. TA5: (a) PPG electrical eye 5 GHz (b) Comparison of influence of coherence control on baselines with different ECL settings

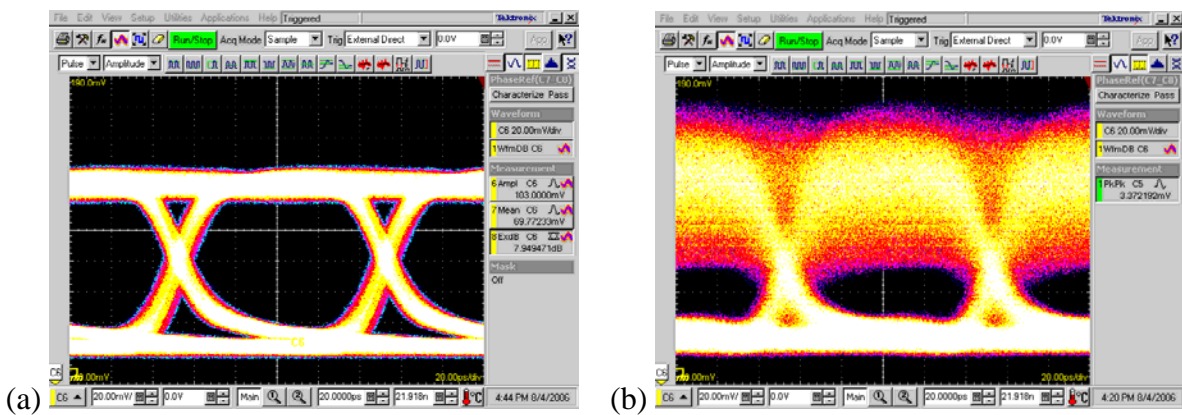


Fig. TA6: (a) PPG+MOD+QWSOA 10 GHz Mod 0.7V ECL 1300nm 3.5dBm coherence on. Dynamic extinction ratio 7.9 dB (b) PPG+MOD+QWSOA 10 GHz Mod 0.7V ECL 1300nm 3.5dBm coherence off

The modulator is further characterized with a sinusoidal input from a frequency synthesizer (setup as in Fig. TA2 (a) with synthesizer instead of BPG) for different input powers and optical wavelength (Fig. TA7 and TA8). The extinction ratio for these measurements is summarized in table TA1.

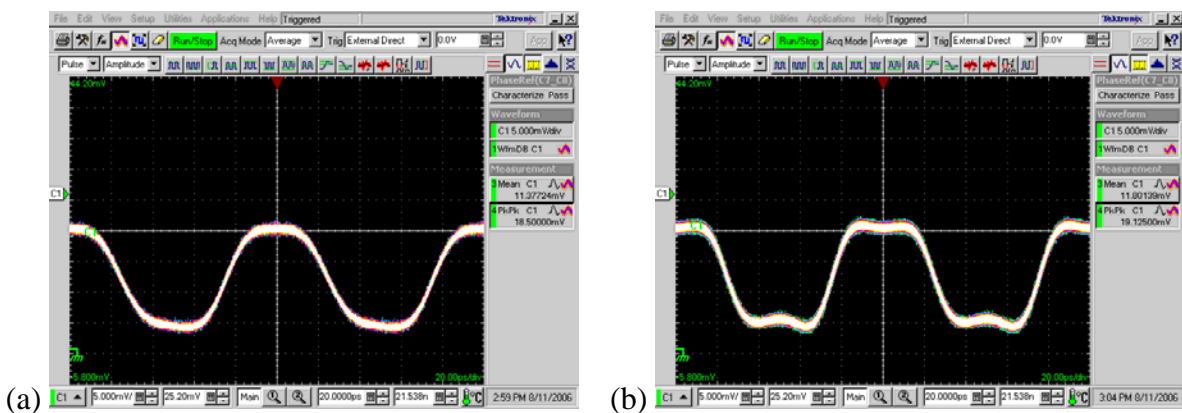


Fig. TA7: SG+AMP+MOD+QDSOA+SampOsz 10 GHz Mod 0.8V ECL 1300nm 3.5dBm (a) $V_{\pi,RF} = 8(19)$ dBm, extinction ratio 5.7 dB (b) $V_{\pi,RF} = 11(22)$ dBm, extinction ratio 5.5 dB.

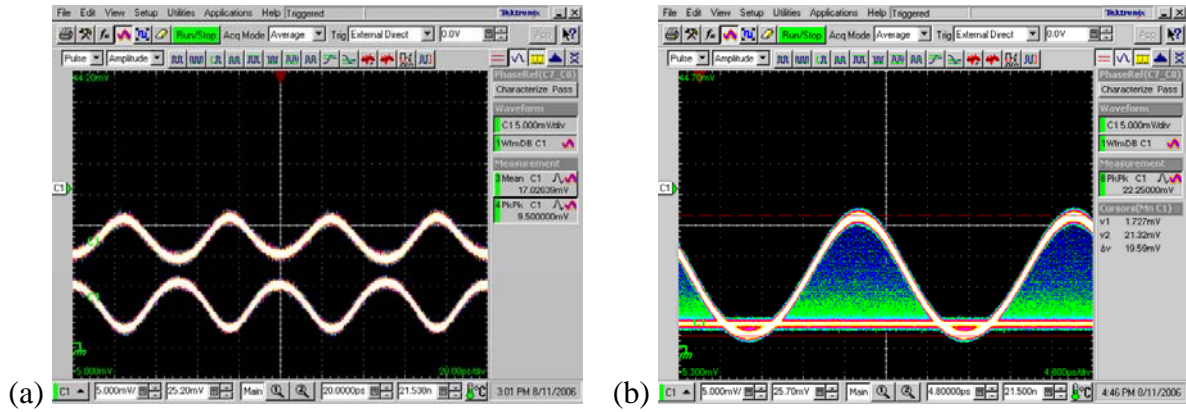


Fig. TA8: (a) SG+AMP+MOD+QDSOA+SampOsz 10 GHz Mod 8(19) dBm ECL 1300 nm 3.5 dBm. Frequency doubling with upper trace 6.5 V (max. bias) and lower trace 2.6 V (min. bias)
 (b) SG+AMP+MOD+EDFA+SampOsz 40 GHz Mod 2.3 V 11(22) dBm FP-LD 1558 nm -1d Bm. Extinction ratio 8.0 dB. The flat trace shows the baseline of the EDFA (setting 25).

Table TA1: Modulator extinction ratio with dependence on wavelength, sinusoidal modulation frequency and RF power. The modulator bias voltage was optimized for maximum ER for each measurement. The RF power is given in readings from the Agilent synthesizer which is followed by a 6 dB divider and a broadband electrical amplifier (SHF 803P) featuring 17 dB gain and 22 dBm saturation output power. This yields in linear extrapolation 17, 19, 22 dBm input to the modulator for 5, 8, 11 dBm RF power of the synthesizer, resp.

wavelength (nm)	frequency (GHz)	bias (V)	RF power (dBm)	extinction ratio (dB)
1300	2	0.8	5	8.3
1300	2	0.65	8	9.4
1300	2	0.65	11	9.4
1300	10	0.8	8	6.7
1300	10	0.7	11	6.9
1300	40	0.7	8	3.3
1300	40	0.8	11	4.2
1300	40	1.5	11	6.3
1558	2	1.3	8	15.1
1558	10	1.4	8	11.7
1558	10	1.0	11	12.3
1558	40	2.3	8	7.6
1558	40	2.3	11	9.7

The Avanex modulator works at 1.55 μm according to its specifications. Yet, at 1.3 μm the specifications can be reached only at a bad operation point (with large insertion loss). Nevertheless the modulator is ideal for small-signal measurements and the large-signal performance should be sufficient even for measurements at 40 Gb/s.

7.4 On the use of the Brewster angle for reduced facet reflectivity of SOA

Here, the use of the Brewster angle for reduced facet reflectivity of a SOA is evaluated. It is shown that for a typical GaAs-air interface the Brewster angle is at 17° which results in a refracted transmitted (parallel polarized) beam at an angle of 73° . Additionally, the angle of total reflection is at 18° giving a narrow processing window. Although the idea of a low reflectivity for the parallel polarized wave at the Brewster angle is intriguing, it is not feasible for tilted ridge waveguides of SOAs.

For SOA it is essential to reduce the facet reflectivity R to a minimum. There are several approaches (as described in chapter 2.3.2) to achieve values $R < 10^{-4}$ needed for efficient suppression of the Fabry-Pérot cavity resonance. Dielectric antireflection coatings of this quality are demanding in their specifications for fabrication. Tilted ridge waveguides lead to a reduced back reflection into the waveguide, thereby reducing the effective feedback, yet introducing a considerable loss. The Brewster angle promises to combine a low reflectivity with full transmission of one polarization direction and at the same time a selection of the modal polarization. Cleaving laser crystals at the Brewster angle is commonly used in solid state lasers with an external cavity. In order to assess the potential of this concept for SOA a detailed investigation is given in the following.

With a simple simulation of the textbook Fresnel formulas

$$r_{\parallel} = \frac{\tan(\theta_i - \theta_r)}{\tan(\theta_i + \theta_r)}; \quad r_{\perp} = -\frac{\sin(\theta_i - \theta_r)}{\sin(\theta_i + \theta_r)} \quad (7.6)$$

the angular dependent reflectivity of a GaAs-air interface is calculated giving $R = |r|^2$ of a parallel or vertical polarized wave with respect to the plane of incidence, respectively. Where θ_i is the incident and θ_r is the refracted or transmitted angle. Simple geometric optics is assumed. Fig. TA9 shows that the simulation code reproduces all typical features of a glass-air interface.

For the calculation of the GaAs-air interface only the refractive index is changed to $n_{\text{eff}}(\text{GaAs}) = 3.25$ which is the effective index of the optical waveguide of a typical GaAs-based SOA. Fig. TA10 shows on the left-hand side the semi-logarithmic plot of the reflectivity versus the incident angle of a wave propagating in the direction GaAs-interface-air. The right-hand side features a schematic of the incident and refracted beam at the Brewster angle condition at 17° . To achieve a reflectivity below 10^{-3} the angular tilt of the waveguide has to be realized in fabrication to an accuracy of $\pm 0.15^\circ$ which is feasible, but difficult. It should be noted that the angle of total reflection is at 18° only one degree away from the Brewster angle in this material system. With the incident beam at the Brewster angle of 17° the refracted beam angle of 73° will affect the coupling to and from the waveguide. Therefore, from distortion of the far field and from geometric restrictions (it is not possible to get very close to the facet with a fiber or a lens at this angle) high coupling losses are anticipated.

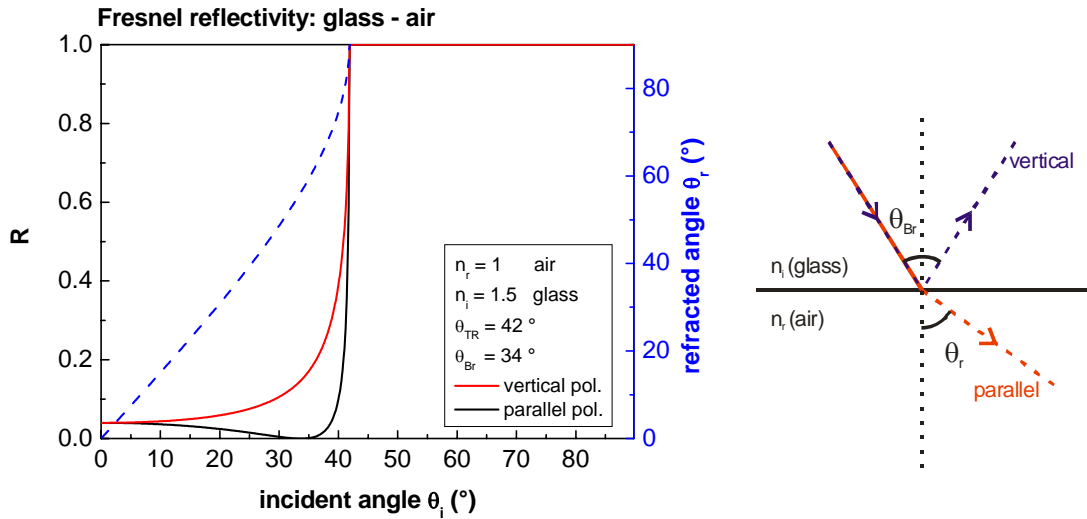


Fig. TA9: Modeling of the well known glass-air interface with the Fresnel formulas (left) and schematic of the Brewster condition (right). The simulation code reproduces all features such as the total refraction angle $\theta_{TR} = 42^\circ$, Brewster angle $\theta_{Br} = 34^\circ$ and normal incidence reflectivity of 4%.

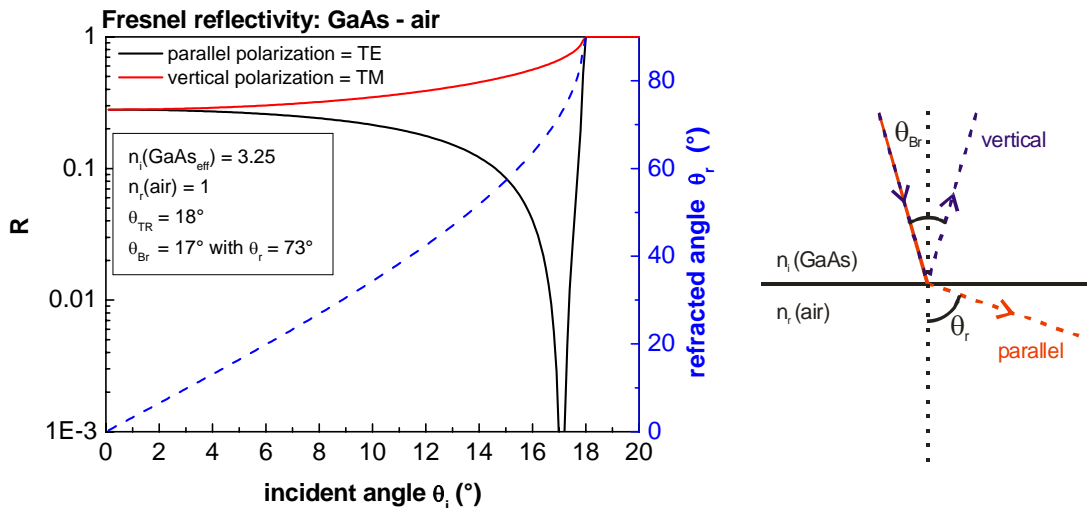


Fig. TA10: Modeling of the GaAs-air interface (left) and schematic of the Brewster condition (right). The reflectivity is plotted semi-logarithmic to indicate the small angular acceptance of low reflectivity at the Brewster angle.

Although tilted ridge waveguides (typically 5-10° tilt angle) are commonly used as a means to reduce laser feedback from facet reflectivity, it can be clearly seen from this evaluation that the use of the Brewster angle is not feasible for GaAs-based SOA.

7.5 Fabry-Perot formulation of the amplifier gain

We follow the derivation of [61] considering a uniform gain profile with a single-pass gain G_s along an amplifier. The output electric field E_{out} is a sum of multiple reflected signals at the facets of the cavity with reflections $R_{1,2}$ and the geometric mean reflectivity $R = \sqrt{R_1 R_2}$

$$E_{\text{out}} = \sqrt{(1-R_1)(1-R_2)G_s} E_0 \exp(-i\beta L) \times \left[1 + \sqrt{R_1 R_2} G_s \exp(-2i\beta L) + R_1 R_2 G_s^2 \exp(-4i\beta L) + \dots \right] \quad (7.7)$$

Using the sum for an infinite geometric progression $\sum_n x^n = 1/(1-x)$ this expression simplifies to

$$E_{\text{out}} = \frac{\sqrt{(1-R_1)(1-R_2)G_s} E_0 \exp(-i\beta L)}{1 - G_s \sqrt{R_1 R_2} \exp(-2i\beta L)} \quad (7.8)$$

Then the output power equals

$$|E_{\text{out}}|^2 = \frac{(1-R_1)(1-R_2)G_s E_0^2 |e^{-i\beta L}|^2}{|1 - G_s \sqrt{R_1 R_2} \exp(-2i\beta L)|^2} = \frac{(1-R_1)(1-R_2)G_s E_0^2}{|1 - G_s \sqrt{R_1 R_2} [\cos(-2\beta L) + i \sin(-2\beta L)]|^2} \quad (7.9)$$

using the well-known relations $|e^{i\phi}|=1$ and Eulers formula $e^{i\phi} = \cos \phi + i \sin \phi$. We use $|a| = |x + iy| = \sqrt{x^2 + y^2}$ to calculate the absolute value of the complex denominator

$$|E_{\text{out}}|^2 = \frac{(1-R_1)(1-R_2)G_s E_0^2}{\sqrt{[1 - G_s \sqrt{R_1 R_2} \cos(-2\beta L)]^2 + [G_s \sqrt{R_1 R_2} \sin(-2\beta L)]^2}^2} \quad (7.10)$$

Further simplifications of the expression make use of $(\cos^2 \phi + \sin^2 \phi) = 1$ and $\sin^2 \phi = \frac{1}{2}(1 - \cos 2\phi)$, as well as $(1^2 - 2b + b^2) = (1 - b)^2$

$$\begin{aligned} |E_{\text{out}}|^2 &= \frac{(1-R_1)(1-R_2)G_s E_0^2}{\left[1 - 2G_s \sqrt{R_1 R_2} \cos(-2\beta L) + G_s^2 \sqrt{R_1 R_2}^2 \cos^2(-2\beta L) \right] + \left[G_s^2 \sqrt{R_1 R_2}^2 \sin^2(-2\beta L) \right]} \\ &= \frac{\sim}{1 + G_s^2 R_1 R_2 (\cos^2(-2\beta L) + \sin^2(-2\beta L)) - 2G_s \sqrt{R_1 R_2} \cos(-2\beta L)} \\ &= \frac{\sim}{(1 - 2G_s \sqrt{R_1 R_2} + G_s R_1 R_2) + 2G_s \sqrt{R_1 R_2} (1 - \cos(-2\beta L))} \\ &= \frac{\sim}{(1 - G_s \sqrt{R_1 R_2})^2 + 4G_s \sqrt{R_1 R_2} \sin^2(\beta L)} \end{aligned} \quad (7.11)$$

Now the amplifier gain is given using $|E_{\text{in}}|^2 = E_0^2$ by

$$G = \left| \frac{E_{\text{out}}}{E_{\text{in}}} \right|^2 = \frac{(1-R_1)(1-R_2)G_s}{(1 - G_s \sqrt{R_1 R_2})^2 + 4G_s \sqrt{R_1 R_2} \sin^2(\beta L)} \quad (7.12)$$

which depends on the phase β further specified in equation (2.23). The maximum and minimum gain is found by equating (7.12) for $\sin^2(\beta L) = 1$ and 0, respectively:

$$G_{\max} = \frac{(1-R_1)(1-R_2)G_s}{(1-G_s\sqrt{R_1R_2})^2} \quad G_{\min} = \frac{(1-R_1)(1-R_2)G_s}{(1+G_s\sqrt{R_1R_2})^2} \quad (7.13)$$

With these expressions we can calculate their ratio as a measure for the gain ripple

$$\xi = \frac{G_{\max}}{G_{\min}} = \left(\frac{1+G_s\sqrt{R_1R_2}}{1-G_s\sqrt{R_1R_2}} \right)^2 \quad (7.14)$$

or solve for the geometric mean reflectivity $R = \sqrt{R_1R_2}$

$$R = \frac{1}{G_s} \left[\frac{\sqrt{\frac{G_{\max}}{G_{\min}} - 1}}{\sqrt{\frac{G_{\max}}{G_{\min}} + 1}} \right] \quad (7.15)$$

Yet, from [13] we have

$$R = \frac{G_{\max} - G_{\min}}{4G_{\max}G_{\min}} \quad (7.16)$$

which gives the reflectivity R from a measured gain spectrum. Using equation (7.14) we can calculate the single pass gain G_s and then verify the measured spectrum using the expression (7.12) for the Fabry-Perot gain G .

7.6 Considerations on contact metallization

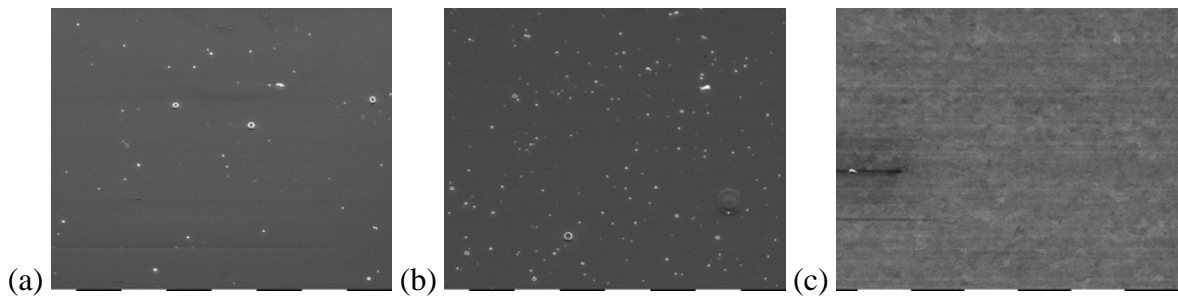


Fig. TA11: REM pictures of Au surfaces for different evaporation techniques. (a) e-beam evaporation: $r = 0.5 \pm 0.1$ Å/s, defect density = $0.01/\mu\text{m}^2$, (b) e-beam evaporation: $r = 1.0 \pm 0.5$ Å/s, defect density = $0.05/\mu\text{m}^2$ (c) thermal evaporation (Veeco): $r = 3-6$ Å/s, defect density = $0.0/\mu\text{m}^2$. [Picture size: (a)+(b) $75 \times 75 \mu\text{m}^2$, (c) $32 \times 32 \mu\text{m}^2$]

A combination of Ni/Au:Ge/Au for the backside contact of the n-doped substrate side provides good ohmic contact. Ni serves as the adhesive layer between semiconductor and metal. Although these contacts show a good ohmic contact, they are not usable for die-

bonding on a diamond heat spreader. During bonding an unknown process – most probably out-diffusion of Ge – prevents a solid connection between the sample and the gold plated diamond. We have tested a number of different n-contacts with the transmission line model [193] for their conductivity after rapid thermal annealing (RTA) and checked their suitability for die-bonding as summarized in Table 9.

Table 9: n-contacts tested for conductivity (with transmission line model) and die-bonding suitability

Contact	Thicknesses (nm)	RTA	Contact	
Ni/Au:Ge/Au	8/80/200	390°, 100s	Ohmic	Standard contact TU (*)
Ti/Pt/Au	20/100/200	390°, 100s	Schottky	Standard contact HHI (*)
Ti/Pt/Au	20/100/200	450°, 90s	Schottky	Kirstädter [186] (*)
Ni/Au:Ge/Ti/Pt/Au	8/45/10/100/200	390°, 100s	Semi-Schottky, Stripewidth-dependent (*)	
Ni/Au:Ge/Ti/Pt/Au	8/80/10/100/200	390°, 100s	Semi-Schottky	(**)

(*) With this contact no stable die-bonding was possible.

(**) This contact showed a very good bonding of the sample to the diamond.

8 Bibliography

- [1] International-Telecommunication-Union, *WORLD INFORMATION SOCIETY REPORT*. 2006, ITU: Geneva.
- [2] AgilentTechnologies, *Optical Amplifier Testing with the Interpolated Source-Subtraction and Time-Domain Extinction Techniques*, in *Application Notes*. 2002. p. 1.
- [3] G.P. Agrawal, *Fiber-Optic Communication Systems*, 2 ed. Microwave and Optical Engineering, ed. K. Chang. John Wiley & Sons, Inc., New York (1997)
- [4] A. Zapata, M. Duser, J. Spencer, P. Bayvel, I. de Miguel, D. Breuer, N. Hanik, and A. Gladisch, *Next-generation 100-gigabit metro Ethernet (100 GbME) using multiwavelength optical rings*, *Journal of Lightwave Technology*, **22**, 2420 (2004).
- [5] U. Feiste, R. Ludwig, C. Schubert, J. Berger, S. Diez, C. Schmidt, H.G. Weber, A. Munk, and B. Schmauss, *160 Gbit/s transmission using 160 to 40 Gbit/s OTDM and 40 to 10 Gbit/s ETDM Demux-Techniques*, *Proceedings of 26th ECOC*, 1.10 (2000).
- [6] S. Shimada, *Optical Amplifiers for Optical Communication Systems*, *IEICE Transactions*, **E 74**, 65 (1991).
- [7] Y. Yamamoto and T. Mukai, *Fundamentals on optical amplifiers*, *Optical and Quantum Electronics*, **21**, S1 (1989).
- [8] ITU-T, *G.694 - Wavelength band definition*: International Telecommunication Union - Telecommunication Standardization Sector.
- [9] S. Sudo, *Progress in optical fiber amplifiers*, *International Journal of High Speed Electronics and Systems*, **7**, 1 (1996).
- [10] J. Bromage, *Raman Amplification for Fiber Communications Systems*, *Journal of Lightwave Technology*, **22**, 79 (2004).
- [11] M.J. O'Mahony, *Semiconductor-Laser Optical Amplifiers for Use in Future Fiber Systems*, *Journal of Lightwave Technology*, **6**, 531 (1988).
- [12] T. Saitoh and T. Mukai, *Recent progress in semiconductor laser amplifiers*, *Journal of Lightwave Technology*, **6**, 1656 (1988).
- [13] N.A. Olsson, *Lightwave systems with optical amplifiers*, *Journal of Lightwave Technology*, **7**, 1071 (1989).
- [14] R. Ludwig, S. Diez, U. Feiste, E. Hilliger, C. Schmidt, and H.G. Weber. *Applications of SOA's for optical signal processing and OTDM*. 124, **Technical Digest, 10th Optical Amplifiers and their Application** (1999)
- [15] K.E. Stubkjaer, *Semiconductor Optical Amplifier-Based All-Optical Gates for High-Speed Optical Processing*, *IEEE Journal of selected topics in quantum electronics*, **6**, 1428 (2000).

8 Bibliography

- [16] T. Whitaker, *Optical Networking*, Compound Semiconductor, **6**, (2000).
- [17] E. Schöll, K. Ketterer, E.H. Bottcher, and D. Bimberg, *Gain-Switched Semiconductor-Laser Amplifier as an Ultrafast Dynamical Optical Gate*, Applied Physics B-Photophysics and Laser Chemistry, **46**, 69 (1988).
- [18] Y. Arakawa and H. Sakaki, *Multidimensional quantum well laser and temperature dependence of its threshold current*, Applied Physics Letters, **40**, 939 (1982).
- [19] A.R. Kovsh, N.A. Maleev, A.E. Zhukov, S.S. Mikhrin, A.P. Vasil'ev, E.A. Semenova, Y.M. Shernyakov, M.V. Maximov, D.A. Livshits, V.M. Ustinov, N.N. Ledentsov, D. Bimberg, and Z.I. Alferov, *InAs/InGaAs/GaAs quantum dot lasers of 1.3 μm range with enhanced optical gain*, Journal of Crystal Growth, **251**, 729 (2003).
- [20] D. Bimberg, M. Grundmann, and N.N. Ledentsov, *Quantum Dot Heterostructures*. John Wiley & Sons Ltd, Chichester (1999)
- [21] U. Woggon, *Optical properties of semiconductor quantum dots*. Springer Tracts in Modern Physics. Vol. 136 (1996)
- [22] M. Grundmann, *Nano-optoelectronics: concepts, physics and devices*. Springer-Verlag, Berlin Heidelberg New York (2002)
- [23] V.A. Shchukin, N.N. Ledentsov, and D. Bimberg, *Epitaxy of Nanostructures*. Springer Verlag (2003)
- [24] D. Bimberg, G. Fiol, M. Kuntz, C. Meuer, M. Lämmlin, N. Ledentsov, and A. Kovsh, *High speed nanophotonic devices based on quantum dots*, phys. stat. sol. (a), **203**, 3523 (2006).
- [25] D. Bimberg, *Quantum dots for lasers, amplifiers and computing*, Journal of Physics D: Applied Physics, **38**, 2055 (2005).
- [26] M. Sugawara, N. Hatori, M. Ishida, H. Ebe, Y. Arakawa, T. Akiyama, K. Otsubo, Y. Yamamoto, and Y. Nakata, *Recent progress in self-assembled quantum-dot optical devices for optical telecommunication: temperature-insensitive 10 Gb s⁻¹ directly modulated lasers and 40 Gb s⁻¹ signal-regenerative amplifiers*, Journal of Physics D: Applied Physics, **38**, 2126 (2005).
- [27] D.J. Mowbray and M.S. Skolnick, *New physics and devices based on self-assembled semiconductor quantum dots*, Journal of Physics D-Applied Physics, **38**, 2059 (2005).
- [28] T.B. Norris, K. Kim, J. Urayama, Z.K. Wu, J. Singh, and P.K. Bhattacharya, *Density and temperature dependence of carrier dynamics in self-organized InGaAs quantum dots*, Journal of Physics D-Applied Physics, **38**, 2077 (2005).
- [29] S. Fathpour, Z. Mi, and P. Bhattacharya, *High-speed quantum dot lasers*, Journal of Physics D-Applied Physics, **38**, 2103 (2005).
- [30] H. Su and L.F. Lester, *Dynamic properties of quantum dot distributed feedback lasers: high speed, linewidth and chirp*, Journal of Physics D-Applied Physics, **38**, 2112 (2005).

- [31] D.G. Deppe, S. Freisem, H. Huang, and S. Lipson, *Electron transport due to inhomogeneous broadening and its potential impact on modulation speed in p-doped quantum dot lasers*, Journal of Physics D-Applied Physics, **38**, 2119 (2005).
- [32] D. Bimberg, M. Kuntz, and M. Laemmlin, *Quantum dot photonic devices for lightwave communication*, Applied Physics a-Materials Science & Processing, **80**, 1179 (2005).
- [33] D. Bimberg, M. Kuntz, and M. Laemmlin, *Quantum dot photonic devices for lightwave communication*, Microelectronics Journal, **36**, 175 (2005).
- [34] P. Borri, W. Langbein, J.M. Hvam, F. Heinrichsdorff, H.-M. Mao, and D. Bimberg, *Ultrafast Gain Dynamics in InAs-InGaAs Quantum-Dot Amplifiers*, IEEE Photonics Technology Letters, **12**, 594 (2000).
- [35] P. Borri, W. Langbein, J.M. Hvam, F. Heinrichsdorff, H.-M. Mao, and D. Bimberg, *Spectral Hole-Burning and Carrier-Heating Dynamics in Quantum-Dot Amplifiers: Comparison with Bulk Amplifiers*, phys. stat. sol. (b), **224**, 419 (2001).
- [36] D.G. Deppe, H. Huang, and O.B. Shchekin, *Modulation characteristics of quantum-dot lasers: The influence of p-type doping and the electronic density of states on obtaining high speed*, IEEE Journal of Quantum Electronics, **38**, 1587 (2002).
- [37] A.V. Uskov, J. Moerk, B. Tromborg, T.W. Berg, I. Magnusdottir, and E.P. O'Reilly, *On high-speed cross-gain modulation without pattern effects in quantum dot semiconductor optical amplifiers*, Optics Communications, **227**, 363 (2003).
- [38] T. Akiyama, N. Hatori, Y. Nakata, H. Ebe, and M. Sugawara, *Pattern-effect-free semiconductor optical amplifier achieved using quantum dots*, Electronic Letters, **38**, 1139 (2002).
- [39] T. Akiyama, H. Kuwatsuka, N. Hatori, Y. Nakata, H. Ebe, and M. Sugawara, *Symmetric Highly Efficient (~0 dB) Wavelength Conversion Based on Four-Wave Mixing in Quantum Dot Optical Amplifiers*, IEEE Photonics Technology Letters, **14**, 1139 (2002).
- [40] T. Akiyama, N. Hatori, Y. Nakata, H. Ebe, and M. Sugawara, *Pattern-effect-free amplification and cross-gain modulation achieved by using ultrafast gain nonlinearity in quantum-dot semiconductor optical amplifiers*, phys. stat. sol. (b), **238**, 301 (2003).
- [41] T. Akiyama, M. Ekawa, M. Sugawara, K. Kawaguchi, H. Sudo, A. Kuramata, H. Ebe, and Y. Arakawa, *An ultrawide-band semiconductor optical amplifier having an extremely high penalty-free output power of 23 dBm achieved with quantum dots*, IEEE Photonics Technology Letters, **17**, 1614 (2005).
- [42] J.P. Reithmaier, A. Somers, S. Deubert, R. Schwertberger, W. Kaiser, A. Forchel, M. Calligaro, P. Resneau, O. Parillaud, S. Bansropun, M. Krakowski, R. Alizon, D. Hadass, A. Bilenca, H. Dery, V. Mikhelashvili, G. Eisenstein, M. Giovannini, I. Montrosset, T.W. Berg, M. van der Poel, J. Moerk, and B. Tromborg, *InP based lasers and optical amplifiers with wire-/dot-like active regions*, Journal of Physics D: Applied Physics, **38**, 288 (2005).

- [43] T. Akiyama, M. Ekawa, M. Sugawara, S. Sudo, H. Kawaguchi, A. Kuramata, H. Ebe, K. Morito, H. Imai, and Y. Arakawa. *An Ultrawide-Band (120 nm) Semiconductor Optical Amplifier Having an Extremely-High Penalty-Free Output Power of 23 dBm Realized with Quantum-Dot Active Layers*. PDP12, *OFC Optical Fiber Communication Conference*. Los Angeles, USA: Optical Society of America (2004)
- [44] T. Akiyama, H. Kawaguchi, M. Sugawara, S. Sudo, M. Ekawa, H. Ebe, A. Kuramata, K. Otsubo, K. Morito, and Y. Arakawa. *A Semiconductor Optical Amplifier with an Extremely-High Penalty-Free Output Power of 20 dBm Achieved with Quantum Dots*. PD22, *ECOC*. Rimini, Italy (2003)
- [45] T.W. Berg, S. Bischoff, I. Magnusdottir, and J. Moerk, *Ultrafast gain recovery and modulation limitations in self-assembled quantum-dot devices*, *IEEE Photonics Technology Letters*, **13**, 541 (2001).
- [46] M. van der Poel, D. Birkedal, J.M. Hvam, M. Laemmlin, and D. Bimberg. *Alpha parameter in quantum-dot amplifier under optical and electrical carrier modulation*. CTuP18, **96**, *Conference on Lasers and Electro-Optics (CLEO)*. San Francisco, USA: Optical Society of America (2004)
- [47] M. van der Poel, E. Gehrig, O. Hess, D. Birkedal, and J.M. Hvam, *Ultrafast gain dynamics in quantum-dot amplifiers: Theoretical analysis and experimental investigations*, *Ieee Journal of Quantum Electronics*, **41**, 1115 (2005).
- [48] S. Schneider, P. Borri, W. Langbein, U. Woggon, R.L. Sellin, D. Ouyang, and D. Bimberg, *Linewidth enhancement factor in InGaAs quantum dot amplifiers*, *IEEE Journal of Quantum Electronics*, **40**, 1423 (2004).
- [49] O.B. Shchekin and D.G. Deppe, *1.3 μm InAs quantum dot laser with $T_0=161$ K from 0 to 80 $^\circ\text{C}$* , *Applied Physics Letters*, **80**, 3277 (2002).
- [50] K. Otsubo, N. Hatori, M. Ishida, S. Okumura, T. Akiyama, Y. Nakata, H. Ebe, M. Sugawara, and Y. Arakawa, *Temperature-insensitive eye-opening under 10-Gb/s modulation of 1.3- μm p-doped quantum-dot lasers without current adjustments*, *Japanese Journal of Applied Physics Part 2-Letters & Express Letters*, **43**, L1124 (2004).
- [51] P. Borri, W. Langbein, J.M. Hvam, F. Heinrichsdorff, H.-M. Mao, and D. Bimberg, *Spectral Hole-Burning and Carrier-Heating Dynamics in InGaAs Quantum-Dot Amplifiers*, *IEEE Journal of selected topics in quantum electronics*, **6**, 544 (2000).
- [52] P. Borri, S. Schneider, W. Langbein, U. Woggon, A.E. Zhukov, V.M. Ustinov, N.N. Ledentsov, Z.I. Alferov, D. Ouyang, and D. Bimberg, *Ultrafast carrier dynamics and dephasing in InAs quantum-dot amplifiers emitting near 1.3 μm -wavelength at room temperature*, *Applied Physics Letters*, **79**, 2633 (2001).
- [53] A.V. Uskov, E.P. O'Reilly, M. Laemmlin, N.N. Ledentsov, and D. Bimberg, *On gain saturation in quantum dot semiconductor optical amplifiers*, *Optics Communications*, **248**, 211 (2005).
- [54] H. Kroemer, *A Proposed Class of Heterojunction Injection Lasers*, *Proceedings of the Ieee*, **51**, 1782 (1963).

- [55] Z.I. Alferov, V.M. Andreev, D.Z. Garbuzov, Y.V. Zhilyaev, E.P. Morozov, E.L. Portnoi, and V.G. Trofim, *Investigation of the influence of the AlAs-GaAs heterostructure parameters on the laser threshold current and realization of continuous emission at room temperature*, Soviet Physics - Semiconductors, **4**, 1826 (1970).
- [56] M. Born and E. Wolf, *Principles of Optics*, 6th ed. Pergamon Press, Oxford (1993)
- [57] N. Dutta and Q. Wang, *Semiconductor Optical Amplifiers*. World Scientific, New Jersey (2006)
- [58] G. Eisenstein, N. Tessler, U. Koren, J.M. Wiesenfeld, G. Raybon, and C.A. Burrus, *Length dependence of the saturation characteristics in 1.5- μm multiple quantum well optical amplifiers*, IEEE Photonics Technology Letters, **2**, 790 (1990).
- [59] T.W. Berg, *Quantum dot semiconductor optical amplifiers - Physics and applications*, in *Department of Communications, Optics & Materials (COM)*. 2004, Technical University of Denmark: Lyngby. p. 202.
- [60] G.P. Agrawal and N. Dutta, *Semiconductor Lasers*, 2nd ed. Van Nostrand Reinhold, New York (1993)
- [61] H. Ghafouri-Shiraz, *Fundamentals of laser diode amplifiers*. John Wiley & Sons Ltd, Chichester (1996)
- [62] M.J. Adams, J.V. Collins, and I.D. Henning, *Analysis of semiconductor laser optical amplifiers*, IEE Proceedings J - Optoelectronics, **132**, 58 (1985).
- [63] C.Y.J. Chu and H. Ghafourishiraz, *A Simple Method to Determine Carrier Recombinations in a Semiconductor-Laser Optical Amplifier*, Ieee Photonics Technology Letters, **5**, 1182 (1993).
- [64] D. Derickson, *Fiber optic test and measurement*. 1998, Prentice-Hall, Inc.: New Jersey. p. 533 to 540.
- [65] T. Saitoh and T. Mukai, *1.5 μm GaInAsP travelling-wave semiconductor optical amplifier*, IEEE Journal of Quantum Electronics, **23**, 1010 (1987).
- [66] Y. Yamamoto and K. Inoue, *Noise in amplifiers*, Journal of Lightwave Technology, **21**, 2895 (2003).
- [67] L.F. Tiemeijer, P.J.A. Thijs, T. vanDongen, J.J.M. Binsma, and E.J. Jansen, *Polarization resolved, complete characterization of 1310 nm fiber pigtailed multiple-quantum-well optical amplifiers*, Journal of Lightwave Technology, **14**, 1524 (1996).
- [68] DIN-Norm, *61290 Teil 3: Prüfverfahren für Rauschzahlparameter*. 1999: Deutsche Fassung.
- [69] T. Briant, P. Grangier, R. Tualle-Brouri, A. Bellemain, R. Brenot, and B. Thedrez, *Accurate determination of the noise figure of polarization-dependent optical amplifiers: Theory and experiment*, Journal of Lightwave Technology, **24**, 1499 (2006).

8 Bibliography

- [70] W.P. Wong and K.S. Chiang, *Design of Waveguide Structures for Polarization-Insensitive Optical Amplification*, IEEE Journal of Quantum Electronics, **36**, 1243 (2000).
- [71] K. Morito, M. Ekawa, T. Watanabe, and Y. Kotaki, *High-output-power polarization-insensitive semiconductor optical amplifier*, Journal of Lightwave Technology, **21**, 176 (2003).
- [72] Y.-S. Cho and W.-Y. Choi, *Analysis and Optimization of Polarization-Insensitive Semiconductor Optical Amplifiers with Delta-Strained Quantum Wells*, IEEE Journal of Quantum Electronics, **37**, 574 (2001).
- [73] D. Alexandropoulos, M.J. Adams, Z. Hatzopoulos, and D. Syvridis, *Proposed scheme for polarization insensitive GaInNAs-based semiconductor optical amplifiers*, Ieee Journal of Quantum Electronics, **41**, 817 (2005).
- [74] D. Tishinin, K. Uppal, I. Kim, and P.D. Dapkus, *1.3- μ m polarization insensitive amplifiers with integrated mode transformers*, IEEE Photonics Technology Letters, **9**, 1337 (1997).
- [75] A. Schliwa, *Working Title: Electronic and Optical Properties of Quantum Dots and Wires*, in *Institut für Festkörperphysik*. Diss. to be published, Technische Universität Berlin: Berlin.
- [76] I.L. Krestnikov, M. Strassburg, M. Caesar, A. Hoffmann, U.W. Pohl, D. Bimberg, N.N. Ledentsov, P.S. Kop'ev, Z.I. Alferov, D. Litvinov, A. Rosenauer, and D. Gerthsen, *Control of the electronic properties of CdSe submonolayer superlattices via vertical correlation of quantum dots*, Physical Review B, **60**, 8695 (1999).
- [77] P. Yu, W. Langbein, K. Leosson, J.M. Hvam, N.N. Ledentsov, D. Bimberg, V.M. Ustinov, A.Y. Egorov, A.E. Zhukov, A.F. Tsatsul'nikov, and Y.G. Musikhin, *Optical anisotropy in vertically coupled quantum dots*, Physical Review B, **60**, 16680 (1999).
- [78] P. Jayavel, T. Kita, O. Wada, H. Ebe, M. Sugawara, Y. Arakawa, Y. Nakata, and T. Akiyama, *Optical Polarization Properties of InAs/GaAs Quantum Dot Semiconductor Optical Amplifier*, Japanese Journal of Applied Physics, **44**, 2528 (2005).
- [79] R. Alizon, A. Bilenca, H. Dery, V. Mikhelashvili, G. Eisenstein, R. Schwertberger, D. Gold, J.P. Reithmaier, and A. Forchel, *Cross-gain modulation in inhomogeneously broadenend gain spectra of InP-based 1550 nm quantum dash optical amplifiers: small-signal bandwidth dependence on wavelength detuning*, Applied Physics Letters, **82**, 4660 (2003).
- [80] J. Kim and S.L. Chuang, *Small-Signal Cross-Gain Modulation of Quantum-Dot Semiconductor Optical Amplifiers*, Photonics Technology Letters, **in press**, (2006).
- [81] *Beam Propagation Method BPM CAD*. 1997, Optiwave Corp.
- [82] S. Kim, A.C. Bryce, D.A. Yanson, and J.H. Marsh. *Low-divergence large-optical-cavity InGaAs quantum-dot laser with distributed active layers*. 691, **2**, LEOS 2004. *The 17th Annual Meeting of the IEEE* (2004)

- [83] N.N. Ledentsov, V.A. Shchukin, S.S. Mikhlin, I.L. Krestnikov, A.V. Kozhukhov, A.R. Kovsh, L.Y. Karachinsky, M.V. Maximov, I.I. Novikov, and Y.M. Shernyakov, *Wavelength-stabilized tilted cavity quantum dot laser*, *Semiconductor Science Technology*, **19**, 1183 (2004).
- [84] N. Ledentsov and V.A. Shchukin, *Novel concepts for injection lasers*, *Optical Engineering*, **41**, 3193 (2002).
- [85] V.A. Shchukin and N. Ledentsov, *Semiconductor laser based on the effect of photonic band gap crystal-mediated filtration of higher modes of laser radiation and method of making the same*. 2001, PBC Lasers, Ltd.: United States Patent, US 6,804,280 B2.
- [86] M. Kuntz, *Modulated InGaAs-GaAs quantum dot lasers*, in *Institut für Festkörperphysik*. 2006, Technische Universität Berlin: Berlin. p. 166.
- [87] *MATLAB 6*. 2002, The MathWorks, Inc.
- [88] W.B. Joyce and B.C. Deloach, *Alignment of Gaussian Beams*, *Applied Optics*, **23**, 4187 (1984).
- [89] C.E. Zah, J.S. Osinski, C. Caneau, S.G. Menocal, L.A. Reith, J. Salzman, F.K. Shokoohi, and T.P. Lee, *Fabrication and Performance of 1.5-Mu-M Gainasp Traveling-Wave Laser-Amplifiers with Angled Facets*, *Electronics Letters*, **23**, 990 (1987).
- [90] D. Marcuse, *Reflection Loss of Laser Mode from Tilted End Mirror*, *Journal of Lightwave Technology*, **7**, 336 (1989).
- [91] D. Marcuse, *Tilt, Offset, and End-Separation Loss of Lowest-Order Slab Wave-Guide Mode*, *Journal of Lightwave Technology*, **4**, 1647 (1986).
- [92] D.T. Cassidy, *Comparison of Rate-Equation and Fabry-Perot Approaches to Modeling a Diode-Laser*, *Applied Optics*, **22**, 3321 (1983).
- [93] D. Marcuse, *Computer-Model of an Injection-Laser Amplifier*, *Ieee Journal of Quantum Electronics*, **19**, 63 (1983).
- [94] C.Y.J. Chu and H. Ghafourishiraz, *Analysis of Gain and Saturation Characteristics of a Semiconductor-Laser Optical Amplifier Using Transfer-Matrices*, *Journal of Lightwave Technology*, **12**, 1378 (1994).
- [95] J.W. Wang, H. Olesen, and K.E. Stubkjaer, *Recombination, Gain and Bandwidth Characteristics of 1.3-Mu-M Semiconductor-Laser Amplifiers*, *Journal of Lightwave Technology*, **5**, 184 (1987).
- [96] C.Y.J. Chu and H. Ghafourishiraz, *Equivalent-Circuit Theory of Spontaneous Emission Power in Semiconductor-Laser Optical Amplifiers*, *Journal of Lightwave Technology*, **12**, 760 (1994).
- [97] M. Grundmann, O. Stier, and D. Bimberg, *InAs/GaAs pyramidal quantum dots: Strain distribution, optical phonons, and electronic structure*, *Physical Review B*, **52**, 11969 (1995).

8 Bibliography

- [98] O. Stier, M. Grundmann, and D. Bimberg, *Electronic and optical properties of strained quantum dots modeled by 8-band- $k\cdot p$ theory*, Physical Review B, **59**, 5688 (1999).
- [99] O. Stier, *Electronic and Optical Properties of Quantum Dots and Wires*, in *Institut für Festkörperphysik*. 2000, Technische Universität Berlin: Berlin. p. 190.
- [100] A.V. Uskov, Y. Boucher, J. Le Bihan, and J. McInerney, *Theory of a self-assembled quantum-dot semiconductor laser with Auger carrier capture: Quantum efficiency and nonlinear gain*, Applied Physics Letters, **73**, 1499 (1998).
- [101] A.V. Uskov, T.W. Berg, and J. Mork, *Theory of pulse-train amplification without patterning effects in quantum-dot semiconductor optical amplifiers*, Ieee Journal of Quantum Electronics, **40**, 306 (2004).
- [102] O. Qasaimeh, *Optical gain and saturation characteristics of quantum-dot semiconductor optical amplifiers*, Ieee Journal of Quantum Electronics, **39**, 793 (2003).
- [103] M. Sugawara, K. Mukai, Y. Nakata, H. Ishikawa, and A. Sakamoto, *Effect of homogeneous broadening of optical gain on lasing spectra in self-assembled $In_xGa_{1-x}As/GaAs$ quantum dot lasers*, Physical Review B, **61**, 7595 (2000).
- [104] M. Sugawara, H. Ebe, N. Hatori, M. Ishida, Y. Arakawa, T. Akiyama, K. Otsubo, and Y. Nakata, *Theory of optical signal amplification and processing by quantum-dot semiconductor optical amplifiers*, Physical Review B, **69**, 235332 (2004).
- [105] H. Huang and D.G. Deppe, *Rate equation model for nonequilibrium operating conditions in a self-organized quantum-dot laser*, Ieee Journal of Quantum Electronics, **37**, 691 (2001).
- [106] M. Grundmann and D. Bimberg, *Theory of random population for quantum dots*, Physical Review B, **55**, 9740 (1997).
- [107] M. Grundmann and D. Bimberg, *Gain and Threshold of Quantum Dot Lasers: Theory and Comparison to Experiments*, Japanese Journal of Applied Physics, **36**, (1997).
- [108] J. Moerk and A. Mecozzi, *Theory of the ultrafast optical response of active semiconductor waveguides*, Journal of the Optical Society of America B-Optical Physics, **13**, 1803 (1996).
- [109] T.W. Berg, J. Mork, and J.M. Hvam, *Gain dynamics and saturation in semiconductor quantum dot amplifiers*, New Journal of Physics, **6**, (2004).
- [110] O. Qasaimeh, *Theory of four-wave mixing wavelength conversion in quantum dot semiconductor optical amplifiers*, IEEE Photonics Technology Letters, **16**, 993 (2004).
- [111] O. Qasaimeh, *Characteristics of Cross-Gain (XG) Wavelength Conversion in Quantum Dot Semiconductor Optical Amplifiers*, IEEE Photonics Technology Letters, **16**, 542 (2004).

- [112] A. Bilenca and G. Eisenstein, *On the Noise Properties of Linear and Nonlinear Quantum-Dot Semiconductor Optical Amplifiers: The Impact of Inhomogeneously Broadened Gain and Fast Carrier Dynamics*, IEEE Journal of Quantum Electronics, **40**, 690 (2004).
- [113] M. Sugawara, N. Hatori, T. Akiyama, Y. Nakata, and H. Ishikawa, *Quantum-Dot Semiconductor Optical Amplifiers for High Bit-Rate Signal Processing over 40 Gbit/s*, Japanese Journal of Applied Physics, **40(2)**, L488 (2001).
- [114] A.V. Uskov, E.P. O'Reilly, R.J. Manning, R.P. Webb, D. Cotter, M. Laemmlin, N.N. Ledentsov, and D. Bimberg, *On ultrafast optical switching based on quantum-dot semiconductor optical amplifiers in nonlinear interferometers*, Ieee Photonics Technology Letters, **16**, 1265 (2004).
- [115] M. Sugawara, T. Akiyama, N. Hatori, Y. Nakata, H. Ebe, and H. Ishikawa, *Quantum-dot semiconductor optical amplifiers for high-bit-rate signal processing up to 160 Gb s⁻¹ and a new scheme of 3R regenerators*, Measurement Science & Technology, **13**, 1683 (2002).
- [116] N.N. Ledentsov, *Growth Processes and Surface Phase Equilibria in Molecular Beam Epitaxy*. Springer Tracts in Modern Physics, ed. G. Köhler. Vol. 156. Springer, Berlin-Heidelberg (1999)
- [117] R.L. Sellin, *Metalorganic Chemical Vapor Deposition of High-Performance GaAs-Based Quantum-Dot Lasers*, in *Institut für Festkörperphysik*. 2003, Technische Universität Berlin: Berlin. p. 144.
- [118] R.L. Sellin, I.N. Kaiander, D. Ouyang, T. Kettler, and D. Bimberg, *Alternative-precursor metalorganic chemical vapor deposition of self-organized InGaAs/GaAs quantum dots and quantum-dot lasers*, Applied Physics Letters, **82**, 841 (2003).
- [119] O.G. Schmidt, S. Kiravittaya, Y. Nakamura, H. Heidemeyer, R. Songmuang, C. Muller, N.Y. Jin-Phillipp, K. Eberl, H. Wawra, S. Christiansen, H. Grabeldinger, and H. Schweizer, *Self-assembled semiconductor nanostructures: climbing up the ladder of order*, Surface Science, **514**, 10 (2002).
- [120] M.V. Maximov, B.V. Tsatsul'nikov, B.V. Volovik, D.S. Sizov, Y.M. Shernyakov, I.N. Kaiander, A.E. Zhukov, A.R. Kovsh, S.S. Mikhrin, V.M. Ustinov, Z.I. Alferov, R. Heitz, V.A. Shchukin, N.N. Ledentsov, D. Bimberg, Y.G. Musikhin, and W. Neumann, *Tuning quantum dot properties by activated phase separation of an InGa(Al)As alloy grown on InAs stressors*, Physical Review B, **62**, 16671 (2000).
- [121] R.L. Sellin, C. Ribbat, D. Bimberg, F. Rinner, H. Konstanzer, M.T. Kelemen, and M. Mikulla, *High-reliability MOCVD-grown quantum dot laser*, Electronics Letters, **38**, 883 (2002).
- [122] R.L. Sellin, C. Ribbat, M. Grundmann, N.N. Ledentsov, and D. Bimberg, *Close-to-ideal device characteristics of high-power InGaAs/GaAs quantum dot lasers*, Applied Physics Letters, **78**, 1207 (2001).
- [123] R.L. Sellin, I. Kaiander, D. Ouyang, T. Kettler, U.W. Pohl, D. Bimberg, N.D. Zakharov, and P. Werner, *Alternative-precursor metalorganic chemical vapor*

deposition of self-organized InGaAs/GaAs quantum dots and quantum-dot lasers, Applied Physics Letters, **82**, 841 (2003).

- [124] A.R. Kovsh, A.E. Zhukov, N.A. Maleev, S.S. Mikhrin, V.M. Ustinov, A.F. Tsatsul'nikov, M.V. Maksimov, B.V. Volovik, D.A. Bedarev, Y.M. Shernyakov, E.Y. Kondrat'eva, N.N. Ledentsov, P.S. Kop'ev, Z.I. Alferov, and D. Bimberg, *Lasing at a wavelength close to 1.3 μm in InAs quantum-dot structures*, Semiconductors, **33**, 929 (1999).
- [125] M.V. Maximov, Y.M. Shernyakov, I.N. Kaiander, D.A. Bedarev, E.Y. Kondrat'eva, P.S. Kop'ev, A.R. Kovsh, N.A. Maleev, S.S. Mikhrin, A.F. Tsatsul'nikov, V.M. Ustinov, B.V. Volovik, A.E. Zhukov, Z.I. Alferov, N.N. Ledentsov, and D. Bimberg, *Single transverse mode operation of long wavelength (similar to 1.3 μm) InAsGaAs quantum dot laser*, Electronics Letters, **35**, 2038 (1999).
- [126] G. Park, O.B. Shchekin, S. Csutak, D.L. Huffaker, and D.G. Deppe, *Room-temperature continuous-wave operation of a single-layered 1.3 μm quantum dot laser*, Applied Physics Letters, **75**, 3267 (1999).
- [127] A.E. Zhukov, A.R. Kovsh, V.M. Ustinov, Y.M. Shernyakov, S.S. Mikhrin, N.A. Maleev, E.Y. Kondrat'eva, D.A. Livshits, M.V. Maximov, B.V. Volovik, D.A. Bedarev, Y.G. Musikhin, N.N. Ledentsov, P.S. Kop'ev, Z.I. Alferov, and D. Bimberg, *Continuous-wave operation of long-wavelength quantum-dot diode laser on a GaAs substrate*, IEEE Photonics Technology Letters, **11**, 1345 (1999).
- [128] S.S. Mikhrin, A.E. Zhukov, A.R. Kovsh, N.A. Maleev, V.M. Ustinov, Y.M. Shernyakov, I.N. Kayander, E.Y. Kondrat'eva, D.A. Livshits, I.S. Tarasov, M.V. Maksimov, A.F. Tsatsul'nikov, N.N. Ledentsov, P.S. Kop'ev, D. Bimberg, and Z.I. Alferov, *A spatially single-mode laser for a range of 1.25-1.28 μm on the basis of InAs quantum dots on a GaAs substrate*, Semiconductors, **34**, 119 (2000).
- [129] A.F. Tsatsul'nikov, D.A. Bedarev, N.A. Bert, A.R. Kovsh, P.S. Kop'ev, N.A. Maleev, Y.G. Musikhin, M.V. Maximov, V.M. Ustinov, B.V. Volovik, A.E. Zhukov, Z.I. Alferov, N.N. Ledentsov, D. Bimberg, A.A. Suvorova, and P. Werner, *1.3 μm emission from quantum dots formed by 2 ML InAs deposition in a wide band gap (1.5-1.7 eV) InGaAlAs matrix*, Compound Semiconductors 1999, 261 (2000).
- [130] A.F. Tsatsul'nikov, A.R. Kovsh, A.E. Zhukov, Y.M. Shernyakov, Y.G. Musikhin, V.M. Ustinov, N.A. Bert, P.S. Kop'ev, Z.I. Alferov, A.M. Mintairov, J.L. Merz, N.N. Ledentsov, and D. Bimberg, *Volmer-Weber and Stranski-Krastanov InAs-(Al,Ga)As quantum dots emitting at 1.3 μm* , Journal of Applied Physics, **88**, 6272 (2000).
- [131] V.M. Ustinov, A.E. Zhukov, A.R. Kovsh, S.S. Mikhrin, N.A. Maleev, B.V. Volovik, Y.G. Musikhin, Y.M. Shernyakov, E.Y. Kondrat'eva, M.V. Maximov, A.F. Tsatsul'nikov, N.N. Ledentsov, Z.I. Alferov, J.A. Lott, and D. Bimberg, *Long-wavelength quantum dot lasers on GaAs substrates*, Nanotechnology, **11**, 397 (2000).
- [132] V.M. Ustinov, A.R. Kovsh, D.A. Livshits, A.E. Zhukov, A.Y. Egorov, M.V. Maximov, I.S. Tarasov, N.N. Ledentsov, P.S. Kop'ev, Z.I. Alferov, and D. Bimberg, *High output power CW operation of a quantum dot laser.*, Compound Semiconductors 1999, 277 (2000).

- [133] P.G. Eliseev, H. Li, G.T. Liu, A. Stintz, T.C. Newell, L.F. Lester, and K.J. Malloy, *Ground-state emission and gain in ultralow-threshold InAs-InGaAs quantum-dot lasers*, IEEE Journal of Selected Topics in Quantum Electronics, **7**, 135 (2001).
- [134] V.M. Ustinov, A.E. Zhukov, N.A. Maleev, A.R. Kovsh, S.S. Mikhlin, B.V. Volovik, Y.G. Musikhin, Y.M. Shernyakov, M.V. Maximov, A.F. Tsatsul'nikov, N.N. Ledentsov, Z.I. Alferov, J.A. Lott, and D. Bimberg, *1.3 μm InAs/GaAs quantum dot lasers and VCSELs grown by molecular beam epitaxy*, Journal of Crystal Growth, **227**, 1155 (2001).
- [135] A.R. Kovsh, N.A. Maleev, A.E. Zhukov, S.S. Mikhlin, A.P. Vasil'ev, Y.M. Shernyakov, M.V. Maximov, D.A. Livshits, V.M. Ustinov, Z.I. Alferov, N.N. Ledentsov, and D. Bimberg, *InAs/InGaAs/GaAs quantum dot lasers of 1.3 μm range with high (88%) differential efficiency*, Electronics Letters, **38**, 1104 (2002).
- [136] S.S. Mikhlin, A.E. Zhukov, A.R. Kovsh, N.A. Maleev, A.P. Vasil'ev, E.S. Semenova, V.M. Ustinov, M.M. Kulagina, E.V. Nikitina, I.P. Soshnikov, Y.M. Shernyakov, D.A. Livshits, N.V. Kryjanovskaya, D.S. Sizov, M.V. Maksimov, A.F. Tsatsul'nikov, N.N. Ledentsov, D. Bimberg, and Z.I. Alferov, *High efficiency ($h_D > 80\%$) long wavelength ($l > 1.25 \mu\text{m}$) quantum dot diode lasers on GaAs substrates*, Semiconductors, **36**, 1315 (2002).
- [137] A.R. Kovsh, A.E. Zhukov, N.A. Maleev, S.S. Mikhlin, D.A. Livshits, Y.M. Shernyakov, M.V. Maximov, N.A. Pihtin, I.S. Tarasov, V.M. Ustinov, Z.I. Alferov, J.S. Wang, L. Wei, G. Lin, J.Y. Chi, N.N. Ledentsov, and D. Bimberg, *High power lasers based on submonolayer InAs-GaAs quantum dots and InGaAs quantum wells*, Microelectronics Journal, **34**, 491 (2003).
- [138] A.E. Zhukov, A.R. Kovsh, S.S. Mikhlin, A.P. Vasil'ev, E.S. Semenova, N.A. Maleev, V.M. Ustinov, M.M. Kulagina, E.V. Nikitina, I.P. Soshnikov, Y.M. Shernyakov, D.A. Livshits, N.V. Kryjanovskaya, D.S. Sizov, M.V. Maximov, A.F. Tsatsul'nikov, N.N. Ledentsov, D. Bimberg, and Z.I. Alferov, *High external differential efficiency and high optical gain of long-wavelength quantum dot diode laser*, Physica E-Low-Dimensional Systems & Nanostructures, **17**, 589 (2003).
- [139] I.R. Sellers, H.Y. Liu, T.J. Badcock, K.M. Groom, D.J. Mowbray, M. Gutierrez, M. Hopkinson, and M.S. Skolnick, *Lasing and spontaneous emission characteristics of 1.3 μm In(Ga)As quantum-dot lasers*, Physica E-Low-Dimensional Systems & Nanostructures, **26**, 382 (2005).
- [140] S.K. Ray, K.M. Groom, R.A. Hogg, H.Y. Liu, I.R. Sellers, M. Hopkinson, T.J. Badcock, A.J. Ramsay, D.J. Mowbray, and M.S. Skolnick, *Growth, fabrication, and operating characteristics of ultra-low threshold current density 1.3 μm quantum dot lasers*, Japanese Journal of Applied Physics Part 1-Regular Papers Short Notes & Review Papers, **44**, 2520 (2005).
- [141] Y.M. Shernyakov, D.A. Bedarev, E.Y. Kondrat'eva, P.S. Kop'ev, A.R. Kovsh, N.A. Maleev, M.V. Maximov, S.S. Mikhlin, A.F. Tsatsul'nikov, V.M. Ustinov, B.V. Volovik, A.E. Zhukov, Z.I. Alferov, N.N. Ledentsov, and D. Bimberg, *1.3 μm GaAs-based laser using quantum dots obtained by activated spinodal decomposition*, Electronics Letters, **35**, 898 (1999).

8 Bibliography

- [142] V.M. Ustinov, N.A. Maleev, A.E. Zhukov, A.R. Kovsh, A.Y. Egorov, A.V. Lunev, B.V. Volovik, I.L. Krestnikov, Y.G. Musikhin, N.A. Bert, P.S. Kop'ev, Z.I. Alferov, N.N. Ledentsov, and D. Bimberg, *InAs/InGaAs quantum dot structures on GaAs substrates emitting at 1.3 μm* , Applied Physics Letters, **74**, 2815 (1999).
- [143] M.V. Maximov, L.V. Asryan, Y.M. Shernyakov, A.F. Tsatsul'nikov, I.N. Kaiander, V.V. Nikolaev, A.R. Kovsh, S.S. Mikhrin, V.M. Ustinov, A.E. Zhukov, Z.I. Alferov, N.N. Ledentsov, and D. Bimberg, *Gain and threshold characteristics of long wavelength lasers based on InAs/GaAs quantum dots formed by activated alloy phase separation*, IEEE Journal of Quantum Electronics, **37**, 676 (2001).
- [144] A.F. Tsatsulnikov, N.N. Ledentsov, M.V. Maksimov, A.Y. Egorov, A.E. Zhukov, V.M. Ustinov, B.V. Volovik, I.L. Krestnikov, A.R. Kovsh, A.V. Sakharov, N.A. Bert, P.S. Kopev, and Z.I. Alferov, *Photoluminescence of arrays of vertically coupled, stressed InAs quantum dots in a GaAs(100) matrix*, Semiconductors, **30**, 953 (1996).
- [145] M.V. Maximov, A.F. Tsatsul'nikov, B.V. Volovik, D.S. Sizov, Y.M. Shernyakov, I.N. Kaiander, A.E. Zhukov, A.R. Kovsh, S.S. Mikhrin, V.M. Ustinov, Z.I. Alferov, R. Heitz, V.A. Shchukin, N.N. Ledentsov, D. Bimberg, Y.G. Musikhin, and W. Neumann, *Tuning quantum dot properties by activated phase separation of an InGa(Al)As alloy grown on InAs stressors*, Physical Review B, **62**, 16671 (2000).
- [146] G.S. Solomon, S. Komarov, J.S. Harris, and Y. Yamamoto, *Increased size uniformity through vertical quantum dot columns*, Journal of Crystal Growth, **175**, 707 (1997).
- [147] R. Heitz, I. Mukhametzhano, P. Chen, and A. Madhukar, *Excitation transfer in self-organized asymmetric quantum dot pairs*, Physical Review B, **58**, R10151 (1998).
- [148] Z.I. Alferov, N.A. Bert, A.Y. Egorov, A.E. Zhukov, P.S. Kopev, A.O. Kosogov, I.L. Krestnikov, N.N. Ledentsov, A.V. Lunev, M.V. Maksimov, A.V. Sakharov, V.M. Ustinov, A.F. Tsapulnikov, Y.M. Shernyakov, and D. Bimberg, *An injection heterojunction laser based on arrays of vertically coupled InAs quantum dots in a GaAs matrix*, Semiconductors, **30**, 194 (1996).
- [149] Y.M. Shernyakov, A.Y. Egorov, A.E. Zhukov, S.V. Zaitsev, A.R. Kovsh, I.L. Krestnikov, A.V. Lunev, N.N. Ledentsov, M.V. Maksimov, A.V. Sakharov, V.M. Ustinov, C. Chen, P.S. Kopev, Z.I. Alferov, and D. Bimberg, *Quantum-dot cw heterojunction injection laser operating at room temperature with an output power of 1 W*, Technical Physics Letters, **23**, 149 (1997).
- [150] V.M. Ustinov, A.Y. Egorov, A.R. Kovsh, A.E. Zhukov, M.V. Maximov, A.F. Tsatsulnikov, N.Y. Gordeev, S.V. Zaitsev, Y.M. Shernyakov, N.A. Bert, P.S. Kopev, Z.I. Alferov, N.N. Ledentsov, J. Bohrer, D. Bimberg, A.O. Kosogov, P. Werner, and U. Gosele, *Low-threshold injection lasers based on vertically coupled quantum dots*, Journal of Crystal Growth, **175**, 689 (1997).
- [151] S.V. Zaitsev, N.Y. Gordeev, Y.M. Shernyakov, V.M. Ustinov, A.E. Zhukov, A.Y. Egorov, M.V. Maximov, P.S. Kopev, Z.I. Alferov, N.N. Ledentsov, N. Kirstaedter, and D. Bimberg, *Radiation characteristics of injection lasers based on vertically coupled quantum dots*, Superlattices and Microstructures, **21**, 559 (1997).
- [152] S.V. Zaitsev, N.Y. Gordeev, V.I. Kopchatov, A.M. Georgievskii, V.M. Ustinov, A.E. Zhukov, A.Y. Egorov, A.R. Kovsh, N.N. Ledentsov, P.S. Kopev, Z.I. Alferov, and D.

- Bimberg, *Quantum-dot lasers: Principal components of the threshold current density*, Semiconductors, **31**, 947 (1997).
- [153] A.E. Zhukov, A.Y. Egorov, A.R. Kovsh, V.M. Ustinov, M.V. Maksimov, A.F. Tsatsulnikov, N.N. Ledentsov, N.Y. Gordeev, S.V. Zaitsev, P.S. Kopev, Z.I. Alferov, and D. Bimberg, *Thermal stability of vertically coupled InAs-GaAs quantum dot arrays*, Semiconductors, **31**, 84 (1997).
- [154] Y.M. Shernyakov, A.Y. Egorov, B.V. Volovik, A.E. Zhukov, A.R. Kovsh, A.V. Lunev, N.N. Ledentsov, M.V. Maksimov, A.V. Sakharov, V.M. Ustinov, Z. Zhao, P.S. Kop'ev, Z.I. Alferov, and D. Bimberg, *Operating characteristics and their anisotropy in a high-power laser (1.5 W, 300 K) with a quantum-dot active region*, Technical Physics Letters, **24**, 351 (1998).
- [155] A.E. Zhukov, V.M. Ustinov, A.Y. Egorov, A.R. Kovsh, A.F. Tsatsul'nikov, M.V. Maximov, N.N. Ledentsov, S.V. Zaitsev, N.Y. Gordeev, V.I. Kopchatov, Y.M. Shernyakov, P.S. Kop'ev, D. Bimberg, and Z.I. Alferov, *Injection lasers based on InGaAs quantum dots in an AlGaAs matrix*, Journal of Electronic Materials, **27**, 106 (1998).
- [156] A.R. Kovsh, D.A. Livshits, A.E. Zhukov, A.Y. Egorov, M.V. Maksimov, V.M. Ustinov, I.S. Tarasov, N.N. Ledentsov, P.S. Kop'ev, Z.I. Alferov, and D. Bimberg, *Quantum-dot injection heterolaser with 3.3 W output power*, Technical Physics Letters, **25**, 438 (1999).
- [157] A.R. Kovsh, A.E. Zhukov, A.Y. Egorov, V.M. Ustinov, Y.M. Shernyakov, M.V. Maximov, V.V. Volovik, A.F. Tsatsul'nikov, Y.V. Musikhin, N.N. Ledentsov, P.S. Kop'ev, D. Bimberg, and Z.I. Alferov, *Molecular beam epitaxy (MBE) growth of composite (In,Al)As/(In,Ga)As vertically coupled quantum dots and their application in injection lasers*, Journal of Crystal Growth, **202**, 1117 (1999).
- [158] C. Ribbat, R.L. Sellin, I.N. Kaiander, F. Hopfer, N.N. Ledentsov, D. Bimberg, A.R. Kovsh, V.M. Ustinov, A.E. Zhukov, and M.V. Maximov, *Complete suppression of filamentation and superior beam quality in quantum-dot lasers*, Applied Physics Letters, **82**, 952 (2003).
- [159] M. Kuntz, G. Fiol, M. Lämmlin, D. Bimberg, M.G. Thompson, K.T. Tan, C. Marinelli, R.V. Penty, I.H. White, V.M. Ustinov, A.E. Zhukov, Y.M. Shernyakov, and A.R. Kovsh, *35 GHz mode-locking of 1.3 μm quantum dot lasers*, Applied Physics Letters, **85**, 843 (2004).
- [160] M. Kuntz, G. Fiol, M. Laemmlin, N.N. Ledentsov, D. Bimberg, M.G. Thompson, K.T. Tan, C. Marinelli, R.V. Penty, I.H. White, M. van der Poel, D. Birkedal, J.M. Hvam, A.R. Kovsh, and V.M. Ustinov. *35 GHz passive mode-locking of InGaAs/GaAs quantum dot lasers at 1.3 μm with Fourier-limited pulses*. CTuP21, **96**, *Conference on Lasers and Electro-Optics (CLEO)*. San Francisco, USA: Optical Society of America (2004)
- [161] M.G. Thompson, K.T. Tan, C. Marinelli, K.A. Williams, R.L. Sellin, R.V. Penty, I.H. White, M. Kuntz, M. Laemmlin, D. Ouyang, I.N. Kaiander, N. Ledentsov, D. Bimberg, V. Ustinov, A.E. Zhukov, A.R. Kovsh, F. Visinka, S. Jochum, S. Hansmann,

- and D.-J. Kang. *Mode-locked quantum dot lasers for picosecond pulse generation*. 107, **5365**, *Photonics West: Proc. SPIE* (2004)
- [162] M. Laemmlin, G. Fiol, C. Meuer, M. Kuntz, F. Hopfer, A. Kovsh, N. Ledentsov, and D. Bimberg, *Distortion-free optical amplification of 20–80 GHz modelocked laser pulses at 1.3 μm using quantum dots*, *Electronic Letters*, **42**, 697 (2006).
- [163] M. Laemmlin, G. Fiol, M. Kuntz, F. Hopfer, D. Bimberg, A. Kovsh, and N. Ledentsov. *Dynamical Properties of Quantum Dot Semiconductor Optical Amplifiers at 1.3 μm Fiber-Coupled to Quantum Dot Mode-Locked Lasers*. CThGG2, **Technical Digest**, *Conference on Lasers and Electro-Optics (CLEO)*. Long Beach, USA: Optical Society of America (2006)
- [164] M. Laemmlin, G. Fiol, C. Meuer, M. Kuntz, F. Hopfer, D. Bimberg, A. Kovsh, and N. Ledentsov. *Amplification of quantum dot mode-locked lasers with quantum dot semiconductor optical amplifiers at 20, 40 and 80 GHz. II.2, International Workshop on Semiconductor Quantum dot based Devices and Applications*. Paris (2006)
- [165] M. Kuntz, G. Fiol, M. Lämmlin, D. Bimberg, A.R. Kovsh, S. Mikhrin, A.V. Kozhukhov, N.N. Ledentsov, C. Schubert, V.M. Ustinov, A.E. Zhukov, Y.M. Shernyakov, A. Jacob, and A. Umbach. *10 Gb/s data modulation and 50 GHz mode locking using 1.3 μm InGaAs quantum dot lasers*. 79, *Proc. of 13th Int. Symp. Nanostructures: Physics and Technology*. St. Petersburg, Russia: Ioffe Physical Technical Institute (2005)
- [166] M. Kuntz, G. Fiol, M. Lämmlin, D. Bimberg, M.G. Thompson, K.T. Tan, C. Marinelli, A. Wonfor, R.L. Sellin, R.V. Penty, I.H. White, V.M. Ustinov, A.E. Zhukov, Y.M. Shernyakov, A.R. Kovsh, N.N. Ledentsov, C. Schubert, and V. Marembert, *Direct modulation and mode locking of 1.3 μm quantum dot lasers*, *New Journal of Physics*, **6**, 181 (2004).
- [167] K.T. Tan, C. Marinelli, M.G. Thompson, A. Wonfor, M. Silver, R.L. Sellin, R.V. Penty, I.H. White, M. Kuntz, M. Lämmlin, N.N. Ledentsov, D. Bimberg, A.E. Zhukov, V.M. Ustinov, and A.R. Kovsh, *High bit rate and elevated temperature data transmission using InGaAs quantum-dot lasers*, *Ieee Photonics Technology Letters*, **16**, 1415 (2004).
- [168] M. Kuntz, G. Fiol, M. Lämmlin, C. Schubert, A.R. Kovsh, A. Jacob, A. Umbach, and D. Bimberg, *10 Gb/s Data Modulation using 1.3 μm InGaAs Quantum Dot Lasers*, *Electronic Letters*, **41**, 244 (2005).
- [169] D. O'Brien, S.P. Hegarty, G. Huyet, J.G. McInerney, T. Kettler, M. Laemmlin, D. Bimberg, V.M. Ustinov, A.E. Zhukov, S.S. Mikhrin, and A.R. Kovsh, *Feedback sensitivity of 1.3 μm InAs/GaAs quantum dot lasers*, *Electronics Letters*, **39**, 1819 (2003).
- [170] K.T. Tan, C. Marinelli, M.G. Thompson, A. Wonfor, R.L. Sellin, R.V. Penty, I.H. White, M. Kuntz, M. Laemmlin, N.N. Ledentsov, D. Bimberg, V.M. Ustinov, A.E. Zhukov, and A.R. Kovsh. *5 Gb/s elevated temperature data transmission using quantum dot lasers*. CThB4, **96**, *Conference on Lasers and Electro-Optics (CLEO)*. San Francisco, USA: Optical Society of America (2004)

- [171] Y. Chu, R.V. Penty, I.H. White, M. Kuntz, G. Fiol, M. Laemmlin, D. Bimberg, C. Schubert, A. Kovsh, A. Jacob, and A. Umbach. *10Gb/s Data Transmission with a 1.3 μ m InGaAs Quantum Dot Laser*. We4.P.060, *European Conference on Optical Communications*. Glasgow (2005)
- [172] R.L. Sellin, D. Bimberg, V.M. Ustinov, N.N. Ledentsov, I.N. Kaiander, M. Kuntz, M. Lämmlin, K.T. Tan, C. Marinelli, M.G. Thompson, A. Wonfor, R.V. Penty, I.H. White, D. O'Brien, S.P. Hegarty, G. Huyet, J.G. McInerney, and J.K. White, *High-power ultra-fast single- and multi-mode quantum-dot lasers with superior beam profile*, *Semiconductor News*, **13**, (2004).
- [173] R.L. Sellin, D. Bimberg, V.M. Ustinov, N.N. Ledentsov, I.N. Kaiander, M. Kuntz, M. Lämmlin, K.T. Tan, C. Marinelli, M.G. Thompson, A. Wonfor, R.V. Penty, I.H. White, D. O'Brien, S.P. Hegarty, G. Huyet, J.G. McInerney, and J.K. White. *High power ultra-fast single and multi-mode quantum dot lasers with superior beam profile*. 46, **5365**, *Photonics West: Proc. SPIE* (2004)
- [174] M. Laemmlin, M. Kuntz, G. Fiol, D. Bimberg, A.R. Kovsh, and V.M. Ustinov. *InGaAs/GaAs quantum dot based photonic devices for direct modulation, mode-locking and optical amplification at 1.3 μ m*. V.1, *European Semiconductor Laser Workshop (ESLW)*. Särö, Sweden (2004)
- [175] M. Laemmlin, G. Fiol, M. Kuntz, F. Hopfer, A. Mutig, N.N. Ledentsov, A.R. Kovsh, C. Schubert, A. Jacob, A. Umbach, and D. Bimberg. *Quantum dot based photonic devices at 1.3 μ m: Direct modulation, mode-locking, VCSELs and SOAs*. Tu3.3, *32nd International Symposium on Compound Semiconductors ISCS*. Rust, Germany (2005)
- [176] M. Laemmlin, G. Fiol, C. Meuer, M. Kuntz, F. Hopfer, N. Ledentsov, A. Kovsh, and D. Bimberg. *Self-organized quantum dots for 1.3 μ m photonic devices*. 63500M, **6350**, *Workshop on Photonic Components for Broadband Communication 2006*. Stockholm, Sweden: Proceedings of SPIE (2006)
- [177] M. Laemmlin, G. Fiol, M. Kuntz, F. Hopfer, A. Mutig, N. Ledentsov, A. Kovsh, C. Schubert, A. Jacob, A. Umbach, and D. Bimberg, *Quantum dot based photonic devices at 1.3 μ m: Direct modulation, mode-locking, SOAs and VCSELs*, *phys. stat. sol. (c)*, **3**, 391 (2006).
- [178] F. Hopfer, *Oberflächenemittierende Quantenpunktlaser: Design, Technologie und Charakterisierung*, in *Institut für Festkörperphysik*. 2005, Technische Universität Berlin: Berlin. p. 122.
- [179] DIN-Norm, 11146 - *Prüfverfahren für Laserstrahlmessungen, Divergenzwinkel und Beugungsmaßzahlen*. 2005: Deutsche Fassung.
- [180] W. Bludau and R.H. Rossberg, *Low-Loss Laser-to-Fiber Coupling with Negligible Optical Feedback*, *Journal of Lightwave Technology*, **LT-3**, 294 (1985).
- [181] F. Dörfel, S. Nerreter, J.W. Tomm, R. Grunwald, R. Kunkel, and J. Luft. *Micro-Reflectance Inspection of Diode Laser Front Facets*. 48, **4648**, *Photonics West*. San Jose, USA: Proc. SPIE (2002)
- [182] B.W. Hakki and T.L. Paoli, *Gain spectra in GaAs double-heterostructure injection lasers*, *Journal of Applied Physics*, **46**, 1299 (1975).

8 Bibliography

- [183] *LabVIEW 6.1*. 2001, National Instruments.
- [184] DIN-Norm, *61290 Teil 1-1: Prüfverfahren für Verstärkungsparameter Elektrischer Spektralanalysator*. 1998: Deutsche Fassung.
- [185] DIN-Norm, *61290 Teil 3-2: Rauschzahlparameter - Prüfverfahren mit elektrischem Spektralanalysator*. 2003: Deutsche Fassung.
- [186] DIN-Norm, *61290 Teil 3-1: Rauschzahlparameter - Prüfverfahren mit optischem Spektralanalysator*. 2003: Deutsche Fassung.
- [187] P. Borri, W. Langbein, J. Mork, and J.M. Hvam, *Heterodyne pump-probe and four-wave mixing in semiconductor optical amplifiers using balanced lock-in detection*, Optics Communications, **169**, 317 (1999).
- [188] P. Borri, W. Langbein, S. Schneider, U. Woggon, R.L. Sellin, D. Ouyang, and D. Bimberg, *Exciton Relaxation and Dephasing in Quantum-Dot Amplifiers From Room to Cryogenic Temperature*, IEEE Journal of selected topics in quantum electronics, **8**, 984 (2002).
- [189] S. Dommers, V.V. Temnov, U. Woggon, J. Gomis, J. Martinez-Pastor, M. Laemmlin, and D. Bimberg, *Complete ground state gain recovery after ultrashort double pulses in quantum dot based semiconductor optical amplifier*, Applied Physics Letters, submitted (2006).
- [190] Z. Bakonyi, H. Su, G. Onishchukov, L.F. Lester, A.L. Gray, T.C. Newell, and A. Tünnermann, *High-gain quantum-dot semiconductor optical amplifier for 1300 nm*, IEEE Journal of Quantum Electronics, **39**, 1409 (2003).
- [191] H. Quast, *Semiconductor Laser Systems with Advanced Pulse Compression for High-Frequency Measurement Applications*, in *Institut für Festkörperphysik*. 2006, Technische Universität Berlin: Berlin. p. unpublished.
- [192] J. Urayama, T.B. Norris, J. Singh, and P. Bhattacharya, *Observation of phonon bottleneck in quantum dot electronic relaxation*, Physical Review Letters, **86**, 4930 (2001).
- [193] O. Schulz, *Dissertation*, in *Institut für Festkörperphysik*. 2006, Technische Universität Berlin: Berlin. p. unpublished.

9 Acknowledgement

I would like to express my sincere thank to my advisor, Prof. Dieter Bimberg. He has supplied a fertile and challenging subject for my thesis and supported me not only financially, but also professional in the sense of competence, subject and expert knowledge. He has provided the technical resources and the scientific network that made this work successful. It is my pleasure to have Prof. Nicolai Ledentsov refereeing my thesis. I thank him for fruitful discussions about the design and improvements of amplifiers and his unfatigued interest in the progress of my work.

It is great that Christian Meuer has been joining the SOA group and working together with me on the challenging QD SOA business. I thank him for his unimpeachable work and his unselfish helpfulness. I am privileged to work together with so many bright colleagues and I would like to thank some of them by name. I am deeply grateful to Matthias Kuntz for so many laughs and at the same time so many further pursuing professional discussions and brilliant ideas. Friedhelm Hopfer has helped on many important parts of the device processing, offering his valuable family time and his invaluable advice and details on the enduring quest for better processing. I would also like to thank Gerrit Fiol for his reliable and cooperative support in the lab and Andrei Schliwa for his charming explanation of the k-p-theory and his enlightening modeling of polarization properties of QDs. Without the sacrificially work to plan and build a more-than-decent cleanroom of Oliver Schulz and Anatol Lochmann many achievements in the processing of the SOAs would not have been possible. In the cleanroom framework I appreciate also the swabian way of Holger Pfitzenmaier of introducing me to the mysteries of processing. Holger Quast is a keen character; I have enjoyed with him many scientific and also inspiring private discussions, the French language, and Italian espressi. All my colleagues are thanked for creating a pleasant, positive and working atmosphere, and of course I would like to thank our skillful technical staff, the members of our precision mechanics workshop and our always helpful secretary Ulrike Grupe. The university has excellent staff in the project administration and I thank representatively Roswitha Koskinas and Arleta Kraszewski.

Via external collaborations in various projects with creative acronyms like AGENT-DE (in future), INTAS, DOTCOM, MonoPic, NanOp, OptiDot, SANDiE, TOB, and TRIUMPH I had the pleasure to work with stimulating colleagues. Notably, I thank my Russian co-workers Alexey Kovsh (NL Nanosemiconductor) for the growth of wonderful quantum dot wafers and Sasha Uskov (Lebedev Physical Institute, Moscow) for helping me in theoretical understanding, supporting me with prolific collaboration and introducing me to stogramm. I am grateful to Gadi Eisenstein (Technion, Haifa) for superb ideas and stimulating discussions. It is a pity that he joined our team only at a late point of my thesis. I would like to acknowledge Peter Ressel (FBH Institut) for not giving up in fabricating a really good anti-reflection coating and Sabine Dommers and Ulrike Woggon (Universität Dortmund) for their very nice pump-probe measurements and some extra traveling to Berlin. Many thanks to Colja Schubert and Sebastian Ferber (FhG Heinrich Hertz Institut) for letting me smell the flavor of the big system world and the impressive instrumentation of the HHI. I thank Andreas Steffan and Andreas Umbach (u²t photonics) for an unpretentious collaboration resulting in a great module with attached fibers resembling the ring-tailed end of a swine.

Of course I would like to thank all friends and family for supporting me and believing in me on the way through my studies and my PhD in good and also in rough times. Vor allem dank ich au miene Eltre. Si hän immer, obwohl 's iehne sicher schwer gfallt isch, mi Entscheidig fürd Physik reschpektiert un mi lange Wäg voller Lieäbi unterschützt. Especially my wife, Nicola, I would like to express my gratitude. She has gone through this experience "Doktorarbeit" with me, encouraging and motivating me, even in times when I did not believe. Hopefully, I will be able to give back some of her love.